Cis-Trans Isomerisation of Azobenzenes Studied by NMR Spectroscopy with *In situ* Laser Irradiation and DFT Calculations

NUHA WAZZAN

Doctor of Philosophy

2009

Abstract

NMR spectroscopy with *in situ* laser irradiation has been used to investigate the photo- and thermal isomerisation of eight azobenzene derivatives; diphenyldiazene (azobenzene), *p*-phenylazoaniline (*p*-aminoazobenzene), 4-(dimethylamino)azobenzene (Methyl Yellow), 4-dimethylamino-2-methylazobenzene (*o*-Methyl-Methyl Yellow), *p*-nitroazobenzene, 4-nitro-4'-dimethylaminoazobeneze (Dimethyl-nitroazobenzene), 4-(4-nitrophenylazo)aniline (Disperse Orange 3) and N-ethyl-N-(2-hydroxyethyl)-4-(4-nitrophenylazo) (Disperse Red 1).

The rate constants and activation parameters of the thermal *cis*-to-*trans* isomerisation have been measured experimentally and correlated to the mechanism of isomerisation in two solvents. The experimental data show that the values of the activation energy (related to the enthalpy of activation) and the entropy of activation (related to the Arrhenius pre-exponential factor) vary significantly from molecule to molecule and thus both of these parameters influence the inter-molecule variation of the rate constant. Similarly, both of these parameters influence the solvent-dependence of the rate constant.

Complementary computational studies have been carried out in the gas phase and in solution using density functional theory (DFT) to predict the structures of the *cis* and *trans* isomers and the transition state, and to explore the reaction coordinate. The theoretically predicted activation parameters are compared with those determined experimentally, and the utility of DFT calculations in predicting the effects of molecular structure and solvation on the kinetics of *cis*-to-*trans* isomerisation assessed.

The DFT-predicted values of the activation energy and Gibbs free energy of activation in DMSO are in good agreement with the experimental values, while the values in benzene tend to be in less good agreement. The DFT calculations are unsuccessful at predicting the entropy of activation, where in all cases there is a large discrepancy between the theoretical and experimental values.

The DFT- calculated energy differences between the activation energies of the two inversion pathways for the asymmetric azobenzenes suggests the favourable phenyl ring for inversion. The formation of a linear transition state from a dihedral rotation potential energy curve is explained in terms of the lower activation barrier of the more favourable inversion route (α-inversion) than that of the dihedral rotation pathway, and suggests the inversion through the α-phenyl ring to be the favoured pathway for substituted azobenzene. DFT calculations are

able to obtain a transition state corresponding to pure rotation pathway for two azobenzene derivatives. The higher activation barrier for the formation of the transition state corresponding to this pathway compared to that of the formation of the α-transition state confirmed the previous conclusion.

DFT predictions of the effect of protonation on the thermal rates of isomerisation of azobenzenes substituted with electron-donating group were in good agreement with the experimental results; both conclude faster isomerisation and lower activation barriers on protonation. However, DFT calculations could not confirm the postulation of rotational transition state for the isomerisation of the protonated molecule, as a result of weakening of the N=N bond by protonation.

Declaration

I declare that the work presented in this thesis is my own unless otherwise stated by a reference.

Nuha Wazzan

Acknowledgments

First of all, all thanks are to God. May your name be exalted, honoured, and glorified.

This work would not have been possible without the support of many people. I am deeply grateful to my supervisor Dr. Anita Jones whose expertise, support, and guidance added considerably to my graduate experience.

I would like to express my gratitude to the kindest people I ever met, Dr. David Gibson for the great assistance he provided me with NMR spectroscopy during the first stage of this work, Dr. Patricia Richardson for being there in almost each step of my computational work, Mr. Juraj Bella for the NMR technical support, and Dr. Andrew Turner for the computational technical support.

Thanks to the occupants, past and present, of room 252 who have given me friendship and support. Thanks to all the occupants, staff and students, of JBB for assisting me in many different ways. Special thanks go out to my dear friend, Diana Castro-Spencer, for enjoyable times, and exchange of knowledge which helped enrich the experience.

In a personal note, I would like to thank my family for the support they provided me through my entire life. In particular, my mother, your continuous prayers and moral support lights the dark times during this thesis, and my elder sister, Hana, who is and will always be a second mother for me, I never imagine one having a heart full of love and philanthropy as you. My full gratitude goes to my brother, Wajdi; you are my teacher, counsellor, and ideal, my brother-in-law, Fayeq, for acting as a real brother, and my brother, luwai, for the encouragement and assistance.

For my kids, Mohammed, Omar and Areeb, thank you for giving me unlimited happiness and pleasure, God bless you. Last but definitely not least, thank you to my soul twin and my best friend, Suha, your great support during my time here indeed sustained me, and enabled me to accomplish this work; my love and gratitude are beyond the words.

I dedicate this thesis to the absent from my life and present always in my heart my father,
Ahmed Wazzan (1937-2001).
The endless love that you through and the principles that you installed in me have created my views toward life and learning. I am sure this achievement would make you proud.

Abbreviations

AM1	Austin Model 1
B3	Becke's 3-Parameter Exchange Functional
CGTO	Contracted Gaussian Type Orbital
CIDNP	Chemically Induced Dynamic Nuclear Polarisation
CW	Continuous Wave
DFT	Density Functional Theory
DMSO	Dimethyl Sulfoxide
FC	Franck Condon
FID	Free Induction Decay
GED	Gas Electron Diffraction
GGA	Generalised Gradient Approximation
GS	Ground State
GTO	Gaussian Type Orbital
HF	Hartree-Fock
HOMO	Highest occupied molecular orbital
IC	Internal Conversion
ISC	Intersystem Crossing
LUMO	Lowest unoccupied molecular orbital
LYP	Lee-Yang-Parr Correlation functional
MO	Molecular Orbital
NDDO	Neglect of Differential Diatomic Overlap
NMR	Nuclear Magnetic Resonance
PCM	Polarisable Continuum Model
PEC	Potential Energy Curve
PES	Potential Energy Surface
PM3	Parameterised Model number 3
RF	Radio Frequency Radiation
RHF	Restricted Hartree-Fock
ROHF	Restricted Open Shell Hartree-Fock
S_0	Ground State
S_1	First Excited Singlet State
SCRF	Self Consistent Reaction Field
STO	Slater Type Orbital
T_1	First Excited Triplet State
TMS	Tetramethyl Silane
TS	Transition State
UV/Vis	Ultra violet and visible light
VR	Vibrational Relaxation

Table of Contents

1 Introduction

Hartley in 1937[1] published the first piece of work characterising the species resulting from the exposure of a solution of azobenzene to light, thus identifying for the first time the photochemical *trans*-to-*cis* isomerisation of azobenzene. Since then the photoisomerisation of azobenzene has become one of the most well known and studied photochemical phenomena. Azobenzene and a large number of its derivatives exist predominately in the *trans* form, thus the *trans* isomer is the thermodynamically favoured species and the isomerisation to the *cis* form is a photochemical process. The reverse isomerisation, *cis*-to-*trans,* is driven photochemically and thermally.

Azo dyes are characterised by the azo linkage (-N=N-), which is in most molecules bridges two aromatic components, thus the parent molecule of azo dyes is azobenzene. Azo dyes gained their importance from their extensive applications in textile dyeing and as colourants in ink, and recently from their new applications in optical switching and optical data storage techniques.[2,3] The longevity of the photogenerated *cis* isomer is of relevance in both traditional and new applications. In dyeing and printing, the formation of a *cis* product that is long-lived is disadvantageous since it results in a pronounced photochromic effect and thus the constancy of the colour is weakened. On the other hand, the synthesis of azo dyes with long-lived *cis* isomers is required, since the change in the geometric, optical and chemical properties of them on photoisomerisation form the basis of the new applications, such as memories and switches in new electronic and photonic systems and photoswichable enzymic cleavage as a drug delivery system.

The investigation of both the photochemical processes (*trans*-to-*cis* and *cis*-to *trans*) and the thermal *cis*-to-*trans* isomerisation has been conducted extensively, experimentally, using UV/Vis absorption spectroscopy and, recently, using NMR spectroscopy with *in situ* laser irradiation, and of course computationally.

UV/Vis absorption spectroscopy has been applied as a qualitative analytical technique. However, while the sensitivity of this technique is reasonably high, the technique suffers as a result of the low spectral resolution. The absorption spectra from structurally similar species within the same sample are so overlapped that it is virtually impossible to separate without employing curve fitting procedures, which introduces inaccuracies. In addition, features of UV/Vis spectra fail to reveal any structural information about the sample under

investigation, and identification can only be completed by comparison with the spectra of known molecules. UV/Vis absorption spectroscopy has been applied as a quantitative technique for kinetic measurements of the thermal recovery of the *trans* isomer absorption band after irradiation, whilst flash photolysis allows more short-lived transient species to be monitored. In NMR spectroscopy coupled with *in situ* laser irradiation, the laser light through an optical fibre is directly in contact with the sample inside the NMR probe. This technique is a powerful technique due to the high resolution of the NMR spectra, and the detection of short-lived *cis* isomer as a result of the *in situ* irradiation. In contrast with UV/Vis, NMR spectroscopy provides information for each species present, which can be then interpreted.

The pioneering use of NMR coupled with *in situ* laser irradiation in the study of photoisomerisation of azo dyes was carried out for simple azobenzenes and for more complex azo molecules.[4-8] The coupling between NMR spectra recording and laser irradiation allows monitoring of the system under study, and thus acquiring the kinetic information. The kinetics of the photo- and thermal isomerisation of a number of complex dyes have been investigated.[4,5]

The work presented in this thesis involved the investigation of the kinetics of the photo- and thermal isomerisation of simple azo dyes molecules, in addition to obtaining the activation parameters from the temperature dependence of the thermal *cis* decay. DFT calculations were carried out on these molecules. The relatively small size of the studied molecules allows the calculation of not only the structural geometries of the *trans* and *cis* isomers but also permits exploration of the ground state potential energy surfaces in the gas phase and in solution, and calculations of the geometries of the transition states involved in the thermal isomerisation. Furthermore, frequency calculations for the *cis* isomer and the transition state allow the prediction of the activation parameters of this isomerisation. The kinetic and activation parameters that were obtained theoretically were compared with the experimental values. These comparisons allow judgment on the performance of DFT calculations.

The mechanism of the thermal isomerisation has always been difficult to interpret given that there are two competing mechanisms and the domination of one over the other depends on many factors including solvent properties and substituents. The extensive data that were obtained from experimental and computational work in the present study were used in combination to investigate the mechanism of this isomerisation.

The results of the work are gathered in Chapters 4 and 5. In Chapter 4, the study a series of azobenzenes molecules by NMR spectroscopy with *in situ* laser irradiation is reported and their kinetics of photo- and thermal isomerisation is examined. Chapter 5 then presents the results of DFT calculations of the thermal *cis*-to-*trans* isomerisation. Finally, Chapter 6 presents overall conclusions of the work in Chapters 4 and 5. Appendices of relevant observations, Cartesian coordinates of the optimised geometries and the potential energy curves are available at the end of the thesis.

2 Background and Theoretical Aspects

2.1 Photochemistry

The interaction of visible and ultraviolet light with molecules is an important aspect of modern chemistry, which is relevant to atmospheric chemistry, biology (e.g. photosynthesis), laser, organic synthesis, reaction kinetics, and more.

This section is based on material presented previously in the thesis of Tait / Gibson.[4,5]

2.1.1 The Interaction of Light with Matter

2.1.1.1 The Transition Dipole Moment

Energy levels in matter are quantised, *i.e.* species can exist only in certain defined, discrete energy states. A transition between two such states of specific energy must have associated with it a definite energy. Thus, a direct result of the quantisation of energy levels is that for each individual species only specific energies and therefore frequencies, of radiation can be absorbed or emitted. The characteristic line and band spectra of chemical species are a consequence of this behaviour.

An oscillating electric or magnetic moment can be induced in an atom or molecular entity by an electromagnetic wave. Its interaction with the electromagnetic field is resonant if the frequency of the latter corresponds to the energy difference between the initial and final states of a transition $\Delta E = h\nu$. The amplitude of this moment is referred to as the transition moment, μ_{fi}. It can be calculated from an integral taken over the product of the wavefunctions of the initial (i) and final (f) states of a spectral transition, ψ_i and ψ_f^* and the appropriate dipole moment operator, $(\hat{\mu})$ of the electromagnetic radiation:

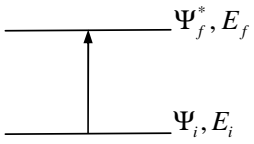

$$\mu_{fi} = \langle f | \mu | i \rangle = \int \psi_f^* \hat{\mu} \psi_i \, d\tau$$

In order for a transition to proceed, the amplitude of the transition moment must be non-zero, leading to a dipolar redistribution of charge. The intensity of the transition is proportional to the square of the transition moment $\left|\mu_{if}\right|^2$.

2.1.1.2 The Franck-Condon Principle

The nuclei are enormously heavy as compared to the electrons, thus during light absorption which occurs in femtoseconds (fs, fs = 10^{-15} s) electrons can move but not the nuclei. This results in a state known as the Franck-Condon state. The transition is vertical promoting the molecule from the lowest vibrational state of its electronic ground state (S_0) to a vibrational state of an electronically excited state (e.g. S_1), Figure 2-1. The vertical transition depicted in Figure 2-1 occurs from the lowest vibrational energy level in the ground state to the vibrational energy level in the excited state that demonstrates the greatest overlap integral of its wave function with that of the initial state, in this case, the transition is from S_0, v''=0 to S_1, v'=3. This does not rule out other possible transitions that have considerable overlap. Figure 2-1 applies to diatomic molecules.

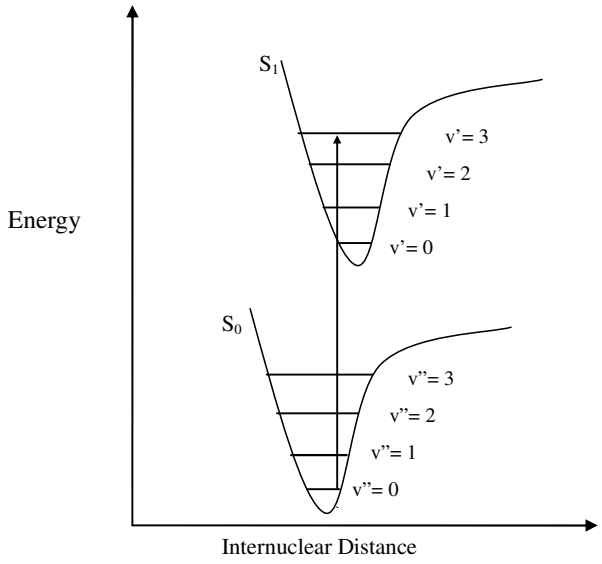

Figure 2-1 Illustration of the Franck-Condon principle for a diatomic molecule.

For polyatomic molecules, there are more transitions over a range of energies. The merging of these transitions leads to an absorption curve. This curve is described as the Franck-Condon envelope.

2.1.1.3 The Beer-Lambert Law

The Beer-Lambert law is a linear relationship between the absorbance and concentration of absorbing molecules, the Beer-Lambert law is written as:

$$A = \varepsilon bc$$ **Equation 2-1**

Where ε is the wavelength-dependent molar decadic absorption coefficient (or the extinction coefficient) with units of M^{-1} cm^{-1}: ε is a characteristic parameter for particular molecule under irradiation of light of specific wavelength and its value indicates the ability of molecules to absorb light of a given frequency: b is the path length of the sample and c is the molar concentration of the sample. The transmittance is defined as:

$$T = \frac{I}{I_0} = 10^{-\varepsilon bc}$$ **Equation 2-2**

Where I is the light intensity after it passes through the sample and I_0 is the incident light intensity. The relation between A and T is given by:

$$A = -\log_{10} T = -\log_{10} \frac{I}{I_0}$$ **Equation 2-3**

2.1.2 Relaxation Mechanisms for Electronically Excited Molecules

The absorption of radiation by a molecule results in most cases in the production of an electronically excited molecule that can exhibit different configuration and excess energy compared to the parent, ground state molecule. There are several routes by which the excited molecule can lose its excess energy and some of the most important routes are represented by a Jablonski diagram, Figure 2-2. Since this work is not concerned with radiative processes (the molecule loses its excess energy as an emission of a photon with an energy equal to energy gap between the ground state (S_0) and the excited state (S_1)) such as fluorescence and phosphorescence, no further discussion of these processes will be undertaken. However, the non-radiative routes (the energy is lost without emission of a photon) are relevant in parts of this work, and are described briefly in the following sections.

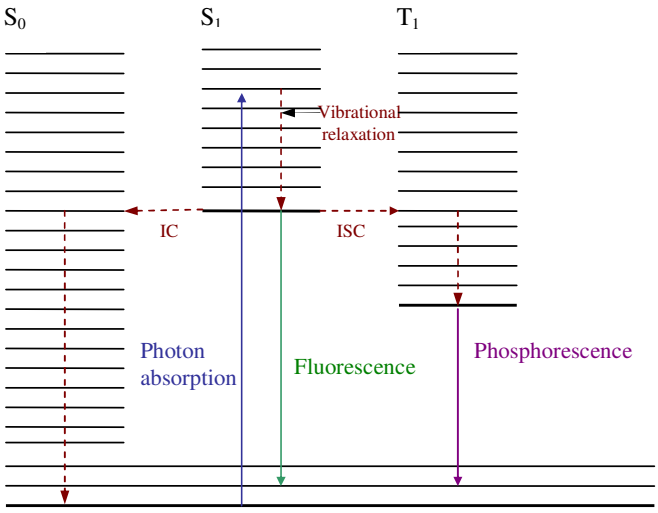

Figure 2-2 Jablonski diagram showing the different routes of deactivation (radiative and non-radiative) of the electronically excited molecule.

2.1.2.1 Vibrational Relaxation

Vibrational relaxation, is the process whereby the excited molecule loses its excess vibrational energy very quickly (< 1 x 10^{-12} s) through collisions with other particles, e.g. molecules of the same species or solvent molecules.

2.1.2.2 Intersystem Crossing

Intersystem crossing (ISC) is an intramolecular, iso-energetic, non-radiative transition between two electronic states having different multiplicities. The spin of the electron must invert for this transition to occur, this forbidden transition is induced through spin-orbit coupling. Spin-orbit coupling involves the interaction between the electron spin and its motion around an atomic nucleus. The singlet and triplet states that the molecule occupies are blurred by this coupling. This allows the electron to change its spin and decay through change of multiplicity rather then through one of the spin-allowed pathways.

2.1.2.3 Internal Conversion

Internal conversion (IC) is an intramolecular, iso-energetic, non-radiative transition between two electronic states having the same multiplicities. In IC the spin state remains the same during the transition. After IC occurs, the vibrationally excited molecule will release this energy to its surrounding through vibrational relaxation.

2.1.2.4 Quenching

Quenching is intermolecular energy transfer between an excited molecule, M*, and a quenching species, Q.

$M^* + Q \rightarrow M + Q$

Quenching is especially important in the liquid phase where collisions are very frequent. At low pressure in the gas phase, quenching process may not be competitive with emission or energy transfer, and in solids quenching may be hindered by the rigidity of the structure. The electronic excitation in M* becomes degraded to vibrational, translational or sometimes rotational energy in Q since in most cases the transfer energy is not enough to induce an electron excitation in the quenching species.

2.1.2.5 Photochemical Isomerisation

Photochemical isomerisation (photoisomerisation) is an intramolecular process in which structural change between isomers is caused by photon excitation. Both reversible and irreversible photoisomerisation reactions exist; examples include photo-induced rotation around a C=C or N=N double bond. Such photochemical processes differ from photophysical phenomena in that the initial and final states are chemically different. The process of photoisomerisation will be discussed with reference to the simple and well characterised example of ethene ($H_2C=CH_2$).

The ethene molecule plays a fundamental role in the understanding of photoisomerisation processes. Ethene contains two sp^2 hybridised carbon atoms, joined by a double bond. Each carbon is attached to two hydrogen atoms. The ground state of this system has planar geometry. Photo excitation of an electron from the double bond will result in a transition of the ethene molecule from the ground state into an excited state potential energy surface. Since this transition is from the HOMO (highest occupied molecular orbital) π orbital to the LUMO (lowest unoccupied molecular orbital) π^* anti-bonding orbital, the excited state is labelled as a $\pi\pi^*$ state.

Figure 2-3 illustrates the potential energy diagram as a function of the torsional angle of the C=C in ethene in the ground (S_0), first excited singlet (S_1), and first excited triplet (T_1) states. Plots of the potential energy of the structure as a function of the rotational angle (0^0-180^0) of C=C bond for each state appear as an energy curve. In order to understand the behaviour of an excited ethene molecule, it is very important to understand the potential energy curves presented. This diagram shows for the ground state potential energy curve an increase in

energy until each end of the molecule is twisted by 90^0 to each other, and a maximum energy is reached at this torsional angle. However, the excited states, S_1 and T_1, contain an electron in an anti-bonding orbital, reducing the order of the double bond. This change in bond character leads to a preferred twisted conformation in S_1 and T_1 in order to reduce the repulsion between electrons in bonding and anti-bonding orbitals. This explains the minimum energy point that appears at a 90^0 torsional angle. At the minimum of these curves, where they are close to the maximum energy of the ground state, crossing may occur by internal conversion from S_1 or inter-system crossing from T_1, into the S_0 potential energy curve. Relaxation may occur in either direction from this maximum, leading to the formation of the initial geometry, or the formation of a geometry that has rotated by 180^0. The above explanation can be generalised to extended C=C, and N=N systems that undergo photoisomerisation.

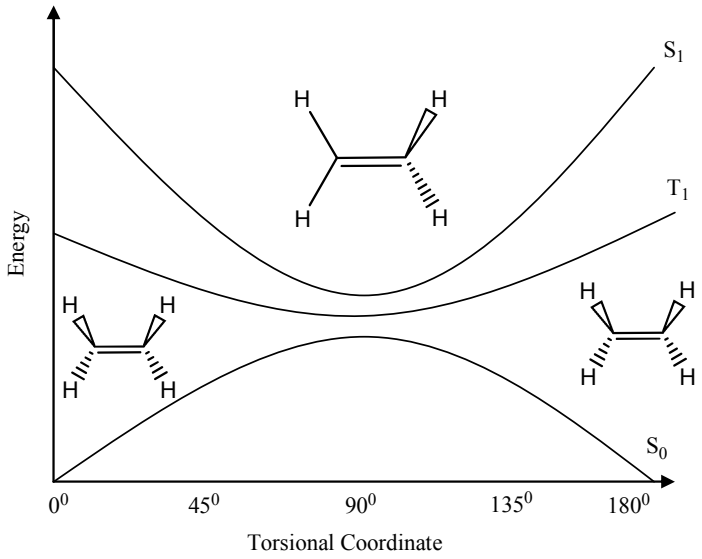

Figure 2-3 Illustration of the S_0, S_1 and T_1 potential energy curves as a function of the rotational angle of C=C in ethene.

2.1.3 Quantum Yield

The quantum yield, Φ, simply defines the efficiency of a photo-induced event. This event may be anything that is observed after photo-excitation, such as fluorescence, phosphorescence, or isomerisation. It is described as:

$$\Phi = \frac{\text{number of events}}{\text{number of photons absorbed}}$$ **Equation 2-4**

The closer Φ is to unity, the more efficient a process will be since it reflects a high probability of an event occurring following the absorption of a photon.

2.2 NMR Spectroscopy

Spectroscopy is the study of the interaction of electromagnetic radiation with matter. Nuclear magnetic resonance spectroscopy is the use of the NMR phenomenon to study physical, chemical, and biological properties of matter. As a consequence, NMR spectroscopy finds applications in several areas of science. NMR spectroscopy is routinely used by chemists to study chemical structure using simple one-dimensional techniques. Two-dimensional techniques are used to determine the structure of more complicated molecules.

In nuclear magnetic resonance (NMR) a magnetic nucleus, like ^{1}H, can absorb radio frequency (RF) radiation when placed in a magnetic field of a strength specific to the identity of the nuclei. When this absorption occurs, the nucleus is described as being in resonance. Different atoms within a molecule resonate at different frequencies at a given field strength. The observation of the resonance frequencies of a molecule provides structural information about the molecule, since the resonant frequencies of the different protons arise from differences in the electronic environment for each proton.

Acquiring an NMR spectrum for a sample requires RF transmitter, static magnetic field, and RF receiver. There are two methods to acquire a spectrum (a) sweeping the magnetic field while the frequency of irradiation is kept constant, or (b) sweeping the frequency of irradiation while the magnetic field is kept constant; the resultant spectra are called the continuous wave (CW) spectra.

One of the disadvantages of CW method is its low efficiency because it probes the NMR response at individual frequencies sequentially. In modern spectrometers, Fourier transform NMR (FT-NMR) is applied; in FT-NMR all the nuclei irrespective of their electronic environment are irradiated simultaneously. A short and strong RF pulse (pulsed NMR) containing all the required frequencies for nuclei excitation is applied (for about 5-10 s). As the pulse is terminated the nuclei return back to the equilibrium through the relaxation.

In pulsed NMR a coincident group of signals from all the excited nuclei is obtained, these signals decrease (decay) with time; this decay is called the free induction decay (FID). The FID contains all the information required to acquire the NMR spectrum. The FID is transformed by the software into the spectrum using Fourier transformation (FT); the FT is a mathematical technique for converting time domain data to frequency domain data. Hence, the name 'FT-NMR' for modern nuclear magnetic resonance spectrometers. NMR is 70 years old, yet it has shown an extraordinary growth during this time. Whenever NMR seemed to have reached a plateau, someone managed to discover a completely new aspect of the subject.

2.2.1 One-Dimensional NMR

As a result of the spin of the protons inside the nuclei of atoms a dipolar magnetic field is generated, Figure 2-4.

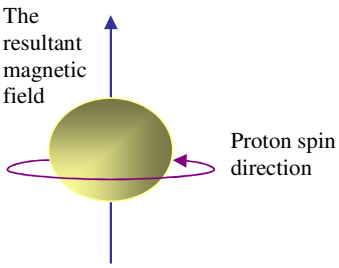

Figure 2-4 The generated magnetic field due to the spin of protons inside the nuclei of atoms.

Nuclei such as ^{1}H, ^{13}C, ^{19}F, and ^{31}P are characterised with an odd number of protons or neutrons and thus exhibit a nuclear spin quantum number, I, of ½. Nuclei such as ^{2}H and ^{14}N characterised with an odd numbers of both protons and neutrons and thus have a nuclear spin quantum number, I, of 1. Also there are nuclei with I = 3/2, 5/2, and 7/2 as a result of the total number of odd protons and neutrons, all of these nuclei with a net spin quantum number are magnetically active. While nuclei such as ^{12}C, ^{16}O, and ^{32}S with even number of both protons and neutrons and a spin quantum number I = 0 are magnetically inactive.

If a nucleus with a spin quantum number I = ½ (^{1}H as example) is placed in a magnetic field, the nucleus will arrange herself into two orientations; the magnetic field generated by the proton will be in the same direction of the applied magnetic field, B_0, (low energy state) or

opposite to it (high energy state). At equilibrium the number of nuclei with lower energy (N_1) is greater than that of nuclei with higher energy (N_2), Figure 2-5.

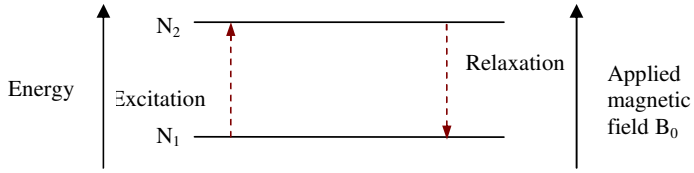

Figure 2-5 Impact of applied magnetic field B_0 on nuclei with a net nuclear spin.

The energy difference between the two energy states, N_1 and N_2, is given by:

$$\Delta E = \frac{h\gamma B_0}{2\pi} = h\nu \qquad \textbf{Equation 2-5}$$

Where h is Planks constant, γ is the gyromagnetic ratio for the studied nucleus and considered as a measure of nuclear magnetic strength, B_0 is the applied magnetic field strength, ν is the frequency of RF used. The relationship between the frequency of RF, ν, and the applied magnetic field strength, B_0, for nucleus with a gyromagnetic ratio, γ, can be written as follows:

$$\nu(Hz) = \frac{\gamma B_0}{2\pi} \qquad \textbf{Equation 2-6}$$

Thus if the applied magnetic field has a strength from 10-100 kG, this requires a RF of frequency of 50-500 MHz to induce a transition between E_1 and E_2.

When RF of a specific frequency is applied it reduces the difference between N_1 and N_2, *i.e.* ΔN and if the intensity of the applied RF is too strong ΔN will go to the zero value, and consequently the NMR signal will disappear and this is called the saturation. On the other hand, if the applied RF has intensity smaller than that required for the saturation so ΔN will remain constant due to so-called relaxation. During the relaxation process the difference in energy, $\Delta E=N_2-N_1$, that was acquired from the RF is lost to the environment. The average lifetime of nuclei in the higher energy state is called the relaxation time and ranges from 10^{-1}-10^{-2} s for different nuclei. Although ΔE is principally related to the magnetic field strength and the type of nucleus, minute variations in the local electronic environment experienced by each nucleus lead to a difference in the energy at which each is brought to resonance. Therefore, identical nuclei in different environments can still be distinguished from one another.

2.2.1.1 Interpretation of One-Dimensional NMR Spectra

A Fourier transformed FID produces a plot of intensity versus frequency. Consider two protons within the molecule that resonate at two different frequencies. The difference between the frequencies depends on the strength of the magnetic field, B_0, used to perform the NMR experiment, *i.e.* the greater the value of B_0, the greater the frequency difference. This relationship could make it difficult to compare NMR spectra taken on spectrometers operating at different field strengths. The term chemical shift was developed to avoid this problem. The chemical shift of a nucleus, δ, is the difference between the resonance frequency of the nucleus and a reference. This quantity is reported in parts per million (ppm) and is given by:

$$\delta = \frac{(\nu_{sig} - \nu_{ref})}{\nu_{ref}} \times 10^6 \qquad \textbf{Equation 2-7}$$

Where ν_{sig} and ν_{ref} are the signal and reference frequencies, respectively, both quoted in Hz. The frequency difference ν_{sig} - ν_{ref} is divided by ν_{ref}, so that δ is a molecular property, independent of the magnetic field used to measure it. For ^1H and ^{13}C, the reference is often tetramethyl silane, Si $(CH_3)_4$, abbreviated to TMS. This reference is an inert and volatile liquid at room temperature that does not interfere with the sample's protons. Thus TMS is the zero point in the chemical shift scale.

The chemical shift is a very precise measurement of the chemical environment around a nucleus. Thus a small molecule with a limited number of protons in different environments should display discrete peaks in a ^1H NMR spectrum. For example aliphatic protons appear at a shielded position in the spectrum (δ (^1H) = 0-5 ppm) close to the TMS reference, whereas aromatic proton signals appear more deshielded (δ (^1H) = 7-9 ppm).

2.2.2 Pseudo Two-Dimensional NMR

This section is based on material presented previously in the thesis Tait / Gibson.[4,5]

In one-dimensional NMR (1D NMR) experiments the signal intensity is recorded as a function of one time variable and then Fourier transformed to give a spectrum which is a function of one frequency variable. In two-dimensional NMR (2D NMR) experiments the signal intensity is recorded as a function of two time variables, t_1 and t_2, and the resulting data Fourier transformed twice to yield a spectrum as a function of two frequency variables. Pseudo two dimensional NMR (pseudo 2D NMR) experiments, as suggested by the name,

only partially fulfil the characteristics of a 2D NMR experiment. The modulation in the second dimension that arises from the variation in t_2 in the 2D NMR remains constant throughout the pseudo-2D experiment, so there is no modulation in the second dimension. The resultant 2D file containing the FIDs is processed only in the first dimension, represented by a two-dimensional plot of a series of 1D experiments. This technique is effective in monitoring the signal intensities change over a period of time, and the pseudo 2D experiment is therefore a compact method for accurate monitoring of the kinetics of a sample.

2.2.2.1 Definition of Integrals in Pseudo 2D Experiments

Integration of the NMR signal is performed in order to count the number of nuclei associated with a peak. Integration of different peaks within the NMR spectrum and comparison of these values allow the determination of how many nuclei each peak corresponds to. For the kinetic work that is presented in Chapter 4, a comparison of the same peak integral between successive runs in a pseudo 2D experiment forms the basis of monitoring photochemical and thermal rates of isomerisation. For such work the integration must be both accurate and reproducible.

In a pseudo 2D experiment the number of scans for each row must be optimised in order to maximise the signal to noise ratio and at the same time should not be so lengthy as to give insufficient resolution for the kinetic measurement. The contribution from noise and possible fluctuation of the baseline can become problematic in the case of low intensity signals, and as the signal decays to zero in the kinetic process. It is possible to overcome this problem by accurate definition of the area that should be integrated and by correcting the baseline for each individual row prior to integration. Figure 2-6 shows two possible integrations of the same peak. In (a) the baseline has been excluded and the area is determined above it, while in (b) some of the baseline noise on each side of the peak is included in the area defined for integration.

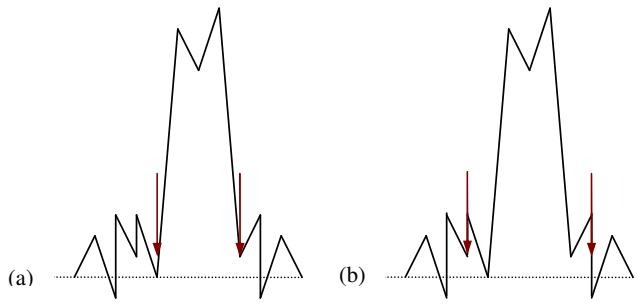

Figure 2-6 Two possible methods of defining peak integrals: (a) without any of baseline noise, (b) includes some of the baseline noise. Dotted line represents the baseline and arrows define the integration limit.

2.3 NMR with *in situ* Irradiation

Tait and Gibson[4-8] demonstrated the use of the NMR spectrometer coupled with *in situ* irradiation to observe and characterise short-lived azo *cis* isomers through continuous irradiation of the sample at the photostationary state (PSS).[4,5] A kinetic study of the photo- and thermal isomerisation processes occurring during irradiation of azo samples was also carried out successfully. During their work they used an optical fibre to deliver light from the laser source to the sample inside the NMR probe. The advantage of using this optical fibre is that it does not require an open laser beam in the laboratory area, and does not require complex or expensive modification of the NMR apparatus. It has also the advantage of portability of the laser source to different NMR spectrometers. One of the greatest advantage of this technique for the thermal decay measurements is that there is no requirement to transfer the sample from the irradiation source to the spectrometer (as in the case of *ex situ* irradiation), obviously this is very important especially for samples where thermal decay is rapid.

The research contained in this thesis employs the NMR spectrometer with *in situ* irradiation *via* an optical fibre for studying photo-induced *cis* isomers of simple azo dyes, and the kinetics of their formation and decay. Experimental details for these studies can be found in Chapter 3, and the results in Chapters 4, 5, and 6.

2.4 Computational Aspects

Section 2.4 -to- Section 2.4.2 are quoted from thesis of Gibson.[5]

This section will provide a short summary of computational methods with relevance to the work presented in Chapter 5. Quantum chemical calculations are employed by chemists and physicists with the aim of solving the time-independent Schrödinger equation for a system. This yields useful information on the system that will either support current experimental findings, or make available properties that are inaccessible by experimental means. Since the Schrödinger equation can only be solved analytically for a one-electron system, this makes the task not a straightforward one. To solve this obstacle, approximations of Schrödinger equation are employed.

The first approximation that must be considered relates to the interaction of nuclear and electronic motion. Because of the difference in mass between nuclei and electrons, the electrons are likely to respond instantaneously to any change in the nuclear framework. Therefore, the electrons are reliant upon the spatial position of the nuclei, but not on the nuclear motion. This assumption allows the terms for nuclear and electronic motion in a molecular wavefunction to be separated, and is known as the Born-Oppenheimer approximation. Following this assumption, the electronic Schrödinger equation for a fixed set of nuclear positions is shown in Equation 2-8, where $\Psi_{el}(r:R)$ is the electronic wavefunction and $E(r:R)$ is the electronic energy of the system, where r corresponds to the electronic positions, and R denotes the location of nuclei. The so-called clamped nucleus Hamiltonian describing this system is defined in Equation 2-9.

$$\hat{H}_{el}\,\Psi_{el}(r:R) = E(r:R)\Psi_{el}(r:R) \qquad \textbf{Equation 2-8}$$

$$\hat{H}_{el} = \hat{T}_{e} + \hat{V}_{en} + \hat{V}_{nn} + \hat{V}_{ee} \qquad \textbf{Equation 2-9}$$

In the Hamiltonian (Equation 2-9), $\hat{T}_{e}$ describes the kinetic energy of the system of electrons, $\hat{V}_{en}$ describes the Columbic attraction between the nuclei and electron, $\hat{V}_{nn}$, the classical term for nuclear-nuclear repulsion energy, is conventionally added at the end of calculation. The final term to mention is $\hat{V}_{ee}$, the electron-electron repulsion. This coupling of electronic motion prevents the facility of writing a many-body wavefunction as a

combination of one-electron functions. This in turn makes the Schrödinger equation extremely difficult to deal with and, except for the most simple of systems, it has not been solved. In the approach to this problem, approximations must be applied to reach a solution. With any approximation, a certain degree of error will be present in the final solution and the amount of acceptable error must be decided upon by the computational chemist when embarking on a study. Two main considerations arise at this point:

1) At what level of theory will the calculation be conducted?
2) What basis set should be applied to the system in order to represent the electrons?

These two points are reviewed in the sections that follow.

2.4.1 Level of Theory

As mentioned above, it is the electron-electron repulsion term, $\hat{V}_{ee}$, in Equation 2-9 that obstructs the solution of the Schrödinger equation for systems containing more than one electron. The theories that underpin computational chemistry must approach this by approximation. Firstly, consider the Pauli Exclusion Principle which infers that no two electrons can be characterised by the same four quantum numbers. Hence, the electronic wavefunctions must change sign whenever the coordinates of two electrons are interchanged. Exchange symmetry states that no observable physical quantity should change after exchanging two identical particles. In this case it is fulfilled, since observable are proportional to $|\Psi|^2$. Any electrons bearing the same spin quantum number occupy different orbitals, staying away from each other and experiencing reduced repulsion, termed the exchange energy. The Hartree-Fock (HF) method includes exchange energy by applying mean-field theory in the calculation, *i.e.* the electron under examination moves in an electric field generated by averaging all the other electrons and nuclei in the system. Treating all other electrons as a smooth distribution of negative charge is a simplification in the HF method that inevitably leads to calculated structures being higher in energy than experimentally determined values. This variation decreases as the accuracy of the basis set increases (Section 2.4.2). Although, even with an infinite number of basis functions, the method will never achieve perfect solution of the Schrödinger equation due to the approximations made with the mean-field approach. This is known as the Hartree-Fock limit.

Improvement to HF method is required in order to improve the accuracy of the results. The approximation of electron exchange included in HF theory partly represents electron correlation through avoiding electrons with parallel spins appearing at the same point in space. However, it does not consider the correlation of electrons with opposing spin, neglecting important Coulomb repulsion energy. Therefore, instantaneous repulsion between electrons is not considered. Many expressions have been derived from HF theory to accommodate electron correlation. Two widely used methods are Configuration Interaction (CI) and Møller-Plasset (MP) perturbation theory. The CI method provides virtual orbitals that the electrons may occupy, effectively expanding the space the electrons can fill. This allows them to relax from the strict HF picture so they are better placed to avoid each other. The MP approach applies a perturbation to the HF system in order to represent electron correlation. The order of perturbation is generally quite small, and this theory is usually represented by MP_n, where n is the order of perturbation. The modifications apply an approximation of the electron configuration to the basic HF model, thus improving the accuracy. However, the increases in accuracy bear elevated computational costs due the presence of two-electron integrals. The computational cost of experiments scales upwards by N^4, where N is the number of basis functions used.[9] As a result of this additional expense, these theories are generally applied to small systems only. As this work has exclusively used density functional theory (DFT) calculations, no further discussion of these methods will be presented. The benefits of DFT are discussed in Section 2.4.1.2.

2.4.1.1 Semi-empirical Methods

Semi-empirical methods can be used to calculate material properties at a much lower computational price. Semi-empirical methods are based on the HF formalism but are adapted to include parameters that fit experimental data in order to simplify the calculation. The Austin Model 1 (AM1) and Parameterised Model number 3 (PM3) are two of many semi-empirical methods. Both methods are based on the Neglect of Differential Diatomic Overlap (NDDO) approximation,[10] which removes all 3 and 4 centre two-electron integrals. The difference between the two methods is that PM3 uses two Gaussian functions per core, and AM1 uses 1-4 depending on the atom. The numerical values of these parameters are also different: where AM1 uses spectroscopic data in its parameters, PM3 treats them as optimisable.

2.4.1.2 Density Functional Theory

The fundamental difference between Density Functional Theory (DFT) and other theories is that DFT optimises an electron density, rather than a wavefunction. The initial DFT theorem was published by Hohenberg and Kohn in 1964,[11] a pure observation that the ground state electron density and the ground state wavefunction could be mapped 1:1 in a many-particle system. Therefore, the total energy of a system of electrons at a given position in space, $E(r)$, is a function of the electron probability density at that exact position, $\rho(r)$. The total energy of the system becomes a functional of the electron probability density, denoted $E[\rho(r)]$.

After one year, Kohn and Sham formulated a method for calculating the ground state electron density by assuming the system of electrons was non-interactive in a static potential field.[12] For this system of non-interacting electrons, the electron density in the ground state will be the same as a real system where electronic interaction is present. The total energy of the ground state is found by varying the electron distribution until a minimum is returned. This simplification reduces the calculation of electron density, ρ, to a series of one-electron densities that are composed of one-electron wavefunctions, Ψ_i. The exact ground state electron density, ρ, at position (r) is given by Equation 2-10 , where Ψ_i (i=1, 2, 3…n) are the Kohn-Sham orbitals for the n electron system.

$$\rho(r) = \sum_{i=1}^{n} |\Psi_i(r)|^2 \qquad \textbf{Equation 2-10}$$

The total energy of a system is expressed in Equation 2-11.

$$E[\rho] = V_{en}[\rho] + T_{ni}[\rho] + V_{ee}[\rho] + E_{xc}[\rho] \qquad \textbf{Equation 2-11}$$

The first term, V_{en}, describes the potential due to nuclear-electron attraction, T_{ni} is the kinetic energy of the non-interacting electron, V_{ee} is the Columbic electron-electron repulsion, and the final term, E_{xc}, contains the electron exchange and correlation terms. Modelling the correlation and interaction is the difficult component of DFT, and approximations must be applied. The applied approximation is the Local-Density approximation (LDA) which is based upon exact exchange, and fits to the correlation energy, for a homogenous electron gas of constant density. The LDA is described by Equation 2-12 , where $\varepsilon_{xc}(\rho(r))$ is the exchange correlation energy of an electron in the uniform electron gas.

$$E_{xc}[\rho(r)] = \int \rho(r)\varepsilon_{xc}(\rho(r))dr$$ **Equation 2-12**

Use of the LDA will essentially lead to errors in the final result, since a molecule will not contain a homogenous distribution of positive or negative charge. Despite the approximation, LDA has been shown to give good results in solid state systems, but slightly less for molecular systems. Further improvements in DFT require the inhomogeneity for a molecular system to be reviewed, which in turn requires approximations in the exchange and correlation energy to be modified. To account for this inhomogeneity, non-local (gradient) correction can be applied to the parameterisation of the exchange correlation energy. Different forms of this are available, and are known as Generalised Gradient Approximation (GGA). The development of new GGA occurred in the late 80's and early 90's and increases the efficiency of DFT calculations.[13,14] Hybrid models have been developed. Combination of Becke's three parameters exact exchange functional (B3),[15] and the Lee-Yang-Parr (LYP) correlation functional,[16] allowed the B3LYP functional to be achieved. Since this functional has been shown to be useful for a broad range of molecular systems, it has been used to perform all the DFT studies within this thesis.

2.4.2 Basis Sets

The accuracy of a calculation depends upon the number and type of functions used to describe the electrons in the system being studied. The positions of nuclei and electrons in a molecule are described by the molecular orbitals (Ψ_i). However, since the Born-Oppenheimer approximation considers the nuclei as static, the wavefunction need only consider electron motion in space. In quantum chemical calculation, the wavefunctions are constructed from a linear combination of a set of known one-electron functions: $\emptyset_n(x,y,z)$. Equation 2-13 describes the linear combinations of these functions, where $\emptyset_\mu$ represents each one-electron basis function, and $c_{\mu i}$ is the coefficient for basis function $\emptyset_\mu$. These basis functions collectively from the basis set.

$$\Psi_i = \sum_{\mu=1}^{N} c_{\mu i}\phi_\mu$$ **Equation 2-13**

The greater the number of the basis functions that formed the basis set, the closer to the optimum description of the electron probability density is achieved. On the other hand, keeping the number of basis functions as minimal as possible is computationally more favourable. The functions used to represent the wavefunction must describe it well in order

to be effective, *i.e.* they will have large amplitude in the regions of space where electron probability density is high, and vice versa.

The accuracy of a calculation is dependent upon the mathematical form of the basis function used. A Slater Type Orbital (STO) appears ideal for the modelling of a basis function. Since the analytical solution to the general four-index integral of an STO does not exist, this causes a significant problem when using STOs for system of more than three or more atoms. A solution to this problem comes in the form of a Gaussian Type Orbital (GTO). However, the utility of a GTO as a basis function is diminished with respect to STOs due to its poor fit when modelling the radial distribution. The GTO has zero slope at the nucleus, and falls off too rapidly as the distance from the nucleus increases. This problem can be identified through a linear combination of several different GTOs in order to represent the STO, the terminology for which is a contracted Gaussian Type Orbital (CGTO).

The early basis sets were called minimal basis sets. As a compromise between accuracy and computational cost, a CGTO composed of three GTOs was found to model the STO orbital well. This basis set is formally named STO-3G (generally STO-*N*G where *N*= number of GTOs) and, as a result of its success in modelling the STO, basis sets have been defined for the majority of the periodic table using this model. Although the computational costs involved are cheap, results using these basis sets are generally not suitable for research publication. In most situations where molecular bonding occurs, it is principally the valence electrons that take part. The STO-*N*G basis sets contain the definition of a single basis function for all the core and valence orbitals. For a more accurate description, split-valance basis functions can be used. In a 3-21G basis set. The core consists of a CGTO comprising three GTOs, as for the STO-3G basis set. However, the valence functions are split, one basis function comprising two GTOs, the other a single GTO. Using two basis functions to describe an orbital can be described a double-ζ basis set. The 3-21G basis set is split-valence with a single- ζ basis set describing the core, and double- ζ describing the valence electrons. This allows a greater degree of accuracy when modelling systems where the bonding is different in opposite directions, for example the carbon atom in H-C≡N.

When the basis functions are centred on the nucleus, there is insufficient mathematical flexibility for the wavefunction to describe the bonding in highly polar molecules. Additional flexibility can be achieved by adding to the basis functions one quantum number of higher angular momentum than the valence orbitals. This allows for small displacements of the centre of electronic charge. Known as polarisation functions, these are often noted following

the standard basis set nomenclature. For example, 6-31G* (synonymous with 6-31G(d)) implies a set of *d* functions is added to polarise the *p* functions on first row atoms C, N, O and F, and 6-31G** (synonymous with 6-31G(d,p)) implies a set of d functions is added to polarise the *p* functions on first row atoms, and a set of *p* functions is added to H and He.[17]Another common addition to basis sets is the addition of diffuse functions, denoted by a plus sign. Two plus signs indicate that diffuse functions are also added to light atoms (hydrogen and helium). These functions allow the electron density to expand into a larger volume; this means that they accurately represent the atomic orbitals which are distant from the atomic nuclei. These additional basis functions can be important when considering anions and molecules with many adjacent lone pairs of electrons. The diffuse functions are a full set of additional functions of the same type as present in the valence space. For example, 6-31+G(d) implies for the C atom a set of *s* basis function and a set of *p* functions are added.

2.4.3 Computational Approaches to Solvation

Standard quantum chemical computations are performed on a single molecule or complex. This isolated species represents a molecule in the gas phase. Although gas phase chemistry covers important chemical topics, the vast majority of chemical reactions occur in solution. Neglecting solvent effects is extremely hazardous. It is a fact that equilibrium and kinetics can be dramatically altered by the nature of the solvent.

Through the 1980s, computational chemists did neglect solvent effects, either because they hoped it would not matter or they had no real way to effectively treat solvation. In terms of the former case, modelling reactions involving non-polar molecules with non-polar transition states in non-polar solvents as gas phase chemistry might be appropriate. This, however, covers a very small subset of chemistry, and even small changes in charge distribution can be manifested in large solvent effect. Over the past 20 years, a number of significant theoretical and algorithmic advances have been proposed towards incorporating solvent effects into quantum chemical computations.

The modelling of a solvent (a liquid phase) is especially challenging. In the gas phase, the molecules can be treated as isolated species that are easily modelled using quantum mechanics or molecular mechanics. On the other hand, a liquid is a challenging medium. Liquids are dynamic by their nature, and any model that does not take this into account will likely be inadequate. The challenges are clear, and there are two fundamentally different strategies to modelling solution. In continuum (or implicit) models, the solvent is treated as a

homogenous medium that surrounds the solute molecule. Computationally, this is implemented as fairly simple set of adjustments to the basic molecular mechanics (or quantum mechanics) model. In explicit solvation models, a large numbers of individual solvent molecules are added to a single solute molecule, and the entire system is treated by molecular mechanics. These methods have the advantage of being closer to physical reality, and being more easily interpreted. However, these benefits are achieved at the price of an enormous increase in computational complexity.

2.4.3.1 The Polarisable Continuum Model

The Polarisable Continuum Model (PCM) by Tomasi *et al.*[18-20] is one of the most frequently used continuum solvation methods and has seen numerous variations over the years. In this model the solvent is represented as a continuum of dielectric constant ε, the solute is placed in a cavity within the solvent. The cavity is defined as the union of a series of interlocking spheres centred on the atoms, and uses a numerical representation of the polarization of the solvent. The PCM model calculates the molecular free energy in solution as the sum over three terms, Equation 2-14:

$$G_{sol} = G_{es} + G_{dr} + G_{cav} \qquad \textbf{Equation 2-14}$$

These components represent the electrostatic (es) and the dispersion-repulsion (dr) contributions to the free energy, and the cavitation energy (cav). All three terms are calculated using a cavity defined through interlocking van der Waals-spheres centred at atomic positions. The reaction field is represented through point charges located on the surface of the molecular cavity.

2.4.4 Potential Energy Surfaces/Curves

Ab initio methods can calculate the energy of a molecule by finding the energies of the molecular orbitals (MOs), assigning the electrons to these MOs, and hence compute the overall electronic energy of the system.

As two molecules A and B come together and start to interact, computing the total energy of the system takes the following steps: when A and B are far apart, the energy will simply be the sum of the energies of A and B. However, as they approach the energy will depend on the details of how the atoms and orbitals in A and B are interacting; eventually the transition state will be reached, whose energy could be calculated. Finally, as the product molecules move apart, the energy will tend to the sum of the energies of the products. So the total

energy of the system varies continuously throughout the reaction. The problem is that the energy will depend on the precise arrangement of atoms, and if A and B have any complexity there will be different number of ways in which the two molecules can approach one another and interact. In principle the energy of each of these arrangements of the atoms in A and B as they interact could be calculated. The end result is a potential energy surface (PES) which gives the energy (the potential energy) as a function of the positions of all the atoms in the system.

For the simplest molecules, such a surface can be simply visualized as energy as of a function of the x- and y-coordinates, and thus referred to as the potential energy curve (PEC), since only one parameter is varied. The key to the understanding of reactions is the PES/PEC. We imagine the atoms as "moving" on this potential energy surface. They start out at one position which corresponds to reactants, move along the reaction path as they rearrange themselves, and then end up at a position which corresponds to products. Apply this to an azobenzene molecule, the isomerisation of the molecule starts at *trans* isomer, this geometry will rearrange itself along the PEC through a specific mechanism (namely rotation or inversion) and end up at the *cis* geometry.

2.5 Azobenzenes

The term ‘azobenzene’ or simply ‘azo’ is often used to refer to a wide class of molecules that share the core azobenzene structure, with different chemical functional groups extending from the phenyl rings. The azo linkage is isosteric with the ethylene linkage, two stable configurations thus can be anticipated, the *trans* and *cis*. Indeed, Hartley [1937][1] isolated *cis*-azobenzene and characterised it, and Hutton and Steel [1964][21] prepared the first aliphatic *cis* azo compound. Azo compounds strongly absorb light and were historically used as dyes in a variety of industries.

2.5.1 Photochromism of Azo Compounds

Photochromism is the reversible interconversion of a chemical species between two states with different absorption spectra. Azo compounds can exhibit photochromism when they are exposed to light of a suitable frequency. An azo compound may exist in two separate forms, namely *trans* and *cis* forms. The *trans* isomer is the thermally stable isomer, absorption of a photon of a suitable frequency can induce isomerisation to form the *cis* isomer. This

geometrical change alters the absorption spectrum from the one corresponding to pure *trans* form to one corresponding to the *cis* isomer or a mixture of both isomers, (since in most cases it is impossible to obtain a sample of 100 % *cis* isomer) and this results in a change of the colour. The *cis* isomer can also undergo photoisomerisation back to the *trans* isomer. If both the *trans* and *cis* isomer absorb light at the incident frequency, a photostationary state (PSS) where equilibrium exists between the two isomers is generated (see Section 2.7). For a variety of reasons, the *cis* isomer is less stable than the *trans* (such as, it has a distorted configuration and is less delocalized than the *trans* configuration). Thus, *cis*-azobenzene will thermally relax back to the *trans*. The *trans* isomer is more stable by approximately 50 kJ/mol, and the barrier to photoisomerisation is approximately 200 kJ/mol,[22] this means that in darkness azobenzene exists predominately as 100 % *trans* isomer. These processes are summarised in Figure 2-7. Compounds that may be readily switched in this way find utility in devices such as molecular switches and optical data storage.

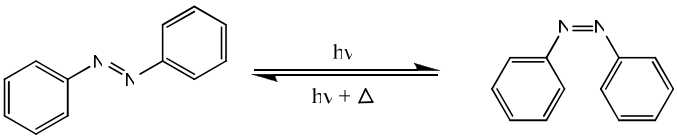

Figure 2-7 The process of photochromism (photo-isomerism) in azobenzene.

2.6 UV/Vis Spectroscopy

Many molecules absorb ultra violet and visible (UV/Vis) light, different molecules absorb light of different frequencies. An absorption spectrum will show a number of absorption bands corresponding to structural groups within the molecule. Most absorption bands of organic compounds are due to excitation of n or π electrons to a π* excited state. The absorption peaks for these transitions fall in an experimentally convenient region of the spectrum (200-700 nm). These transitions need an unsaturated group in the molecule to provide the π orbital.

2.6.1 UV/Vis Spectroscopy of Azo Compounds

For a full understanding of the photochemical isomerisation of an azo compound, knowledge of its excited states and the corresponding UV/Vis spectrum is essential. Azo compounds can be classified into three categories, namely azobenzene, aminoazobenzenes, and

pseudostilbene azobenzenes, a summary of these structural classes is given in Figure 2-8. The spectroscopy of each type is discussed in the following sections.

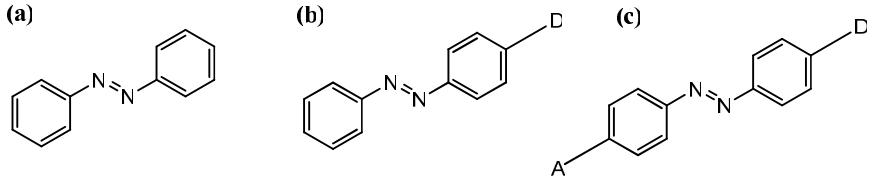

Figure 2-8 Classification of azo molecules: (a) azobenzene, (b) aminoazobenzene, and (c) pseudostilbene. A and D represent acceptor and donor electron groups, respectively, and may be substituted *ortho* or *para* to the azo bond.

2.6.2 Spectroscopy of Azobenzene

Cis- and *trans*-azobenzene have three available excited singlet states, corresponding to three absorption bands in the UV/Vis region of the spectrum,[22-24] and this can best be discussed with reference to the simple molecular orbital diagram shown in Figure 2-9. Figure 2-9 shows the three highest unoccupied and the three lowest occupied π-orbitals and the non-bonding atomic orbitals of the azo-nitrogen atoms, represented by n_a and n_b.

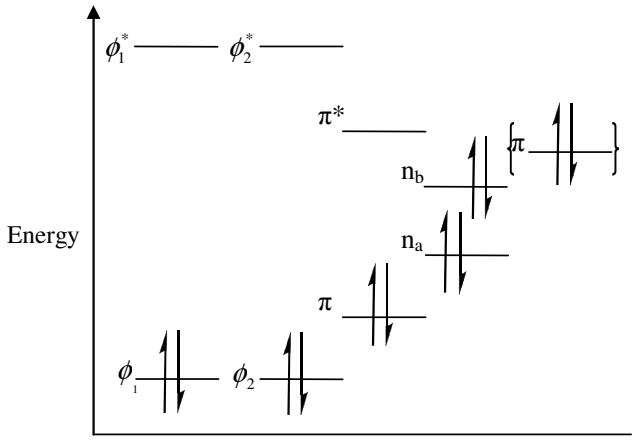

Figure 2-9 Molecular orbital diagram for azobenzene system. Presented the π-lone pair of electrons of azobenzenes substituted with electron donating groups in the positions *ortho* or *para* to the azo bond (additional bracketed orbital). Reproduced from refrence.[23]

The lowest energy transition denoted as $S_1(n\rightarrow\pi^*)$ occurs in the visible region of the spectrum most probably due to the parity forbidden $n_b\rightarrow\pi^*$ process. The second transition

denoted as S_2 occurs in the UV region of the spectrum, the transition is allowed and is due to $\pi \rightarrow \pi^*$ process. The highest energy transition is due to the process $\Phi \rightarrow \Phi^*$, and because of the close association of the Φ orbital with the benzene ring, the transition may be considered as restricted to this ring, the corresponding singlet state is unlikely to be involved in the solution phase reaction of azobenzene.

Absorption bands at approximately 440 nm (ε = 500 M^{-1} cm^{-1}) and 430 nm (ε = 1500 M^{-1} cm^{-1}) in *trans*- and *cis*-azobenzene, respectively, corresponding to the parity forbidden $n \rightarrow \pi^*$ transition. The second band occurs in the UV region of the spectrum, *cis*-azobenzene absorbing at *ca*. 280 nm (ε = 5100 M^{-1} cm^{-1}), and *trans*-azobenzene at 314 nm (ε = 17000 M^{-1} cm^{-1}). The marked difference between the two isomers is due to the non-planar configuration of the *cis*-isomer. The transitions are allowed and are due to $\pi \rightarrow \pi^*$ process. Irradiation of azobenzene by UV light (300 nm) induces a decrease of the high-intensity absorption band centred in the wavelength 317 nm, due to the $\pi \rightarrow \pi^*$ transition, and an increase in the low-intensity band at about 430 nm, due to the $n \rightarrow \pi^*$ transition.

2.6.3 Spectroscopy of Aminoazobenzene and Pseudostilbenes

The aminoazobenzenes category of molecules consists of azobenzenes substituted with electron donating groups in the positions *ortho* or *para* to the azo bond, these groups containing a π-lone pair of electrons in conjugation with the azobenzene π system (represented by the additional bracketed orbital in Figure 2-9). This is a high energy π orbital, since its electrons may be regarded as non-bonding, and consequently the $\pi \rightarrow \pi^*$ transition will be of much lower energy than in azobenzene itself.[22-25] Thus the overall effect of such substituents, or auxochromes, is to provide intense absorption bands in the visible region. In many cases the $\pi\,\pi^*$ band may in fact be lower in energy than the $n\pi^*$ band (which is insensitive to substituent effects), and thus the photochemical properties differ from those of azobenzene. The position of the $\pi\pi^*$ band is sensitive to the substituent. In general, the more electron donating the substituent, the greater the bathochromic shift that is produced. For example, the energy of the $\pi\pi^*$ band of *p*-aminoazobenzene (AAB) will be greater than that of 4-(dimethylamino)azobenzene (MY). The bathochromic shift of the $\pi\pi^*$ band in the corresponding *cis* isomer is less pronounced since the electron donating groups are unable to fully conjugate across the entire molecule due to disruption of the π system by the non linearity of the *cis* form.

The pseudostilbene category of molecules is generally 4-donor-4'-acceptor substituted azobenzenes molecules (push-pull azobenzenes), the electron donating and accepting groups in resonance with the azobenzene π system. Of course, adding another substituent to the molecule will result in even greater differences in the spectral characteristics. This resonance is sufficiently effective to reduce the energy of the ππ* band below that of nπ* band.

Azobenzene compounds containing an additional substituent become even more solvent dependent than the parent molecule, increased polarity causing a bathochromic shift in the absorption band.

2.7 Photochemistry of Azobenzenes

It is well known that azobenzene exists predominately in the *trans* geometry, and in darkness it will always relax back to this geometry. However, upon irradiation, the *trans* isomer may isomerise to a *cis* isomer. The photoisomerisation of azobenzene is reversible, this process is considered one of the cleanest photochemical reactions.[23,26] After photo-excitation of the *trans* isomer with light of suitable frequency, Section 2.6, it will decay to the ground state (S_0) potential energy surface (PES) of either the *trans* or *cis* geometry. In the same manner the photo-excitation of the *cis* isomer is followed by decaying to either the *cis* or *trans* ground state. A simple diagram of this is shown in Figure 2-10.

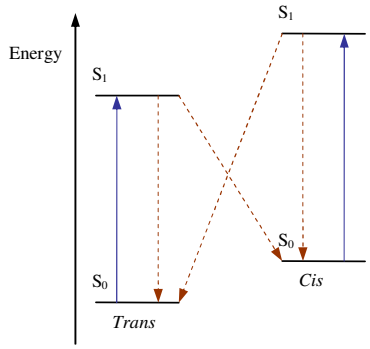

Figure 2-10 Simplified diagram of the excitation and decay routes for the *trans* and *cis* isomers of azobenzene. Reproduced from refrences.[4,5]

If both isomers absorb radiation of the same frequency, an equilibrium state between the *trans* and *cis* isomer will be reached, this state is known as the photostationary state (PSS). The PSS is the equilibrium chemical composition at a single wavelength of visible or UV

light. It is a property of particular importance in photochromic compounds, used as a measure of their practical efficiency, and usually quoted as a ratio or percentage. The PSS is a function of the irradiation parameters, the absorbance properties of the *trans* or *cis* isomer, and the quantum yields of the photochemical reactions.

Placing an irradiated sample in darkness will lead to complete return to 100% *trans* isomer. This first-order rate for this reaction is dependent upon the ground state potential energy barrier between the *cis* and *trans* isomer. The discussion of the proposed mechanisms for the photoisomerisation process is detailed in Section 2.7.1. While, the discussion of those proposed for the thermal isomerisation is delayed to Section 4.1 where it is linked to the thermal kinetics.

2.7.1 Photoisomerisation Mechanism for Azobenzene

The photoisomerisation of azobenzenes proceeds extremely rapidly and it is only recently that ultra fast spectroscopic techniques have become available with the time resolution required to observe the reaction directly in real time, thus most of the literature investigations of the kinetic parameters for the photoisomerisation processes were carried out computationally.

The mechanism of the photoisomerisation has been a fundamental subject for many years. The postulated mechanisms are the rotation and inversion mechanism. The first mechanism involves rotation about the nitrogen-nitrogen bond weakened by electronic excitation (a reduction in π bond order). The second mechanism is by inversion, in which the nitrogen atom can be formally considered to undergo rehybridisation from an sp^2 state to an sp^1 state, with only minor change in the azo π bond order. Both mechanisms are illustrated in Figure 2-11.

The discussion of the mechanism of photoisomerisation that carried out in the following paragraph is based on material presented previously in the thesis Tait / Gibson.[4,5]

The controversy regarding the mechanism can be summarised in three points:

1. In contravention of Kasha's rule, the quantum yields of isomerisation, Φ_{isom}, are wavelength-dependent. Average quantum yields of isomerisation in azobenzene have been reported as $\Phi_{trans \rightarrow cis} = 0.25$, $\Phi_{cis \rightarrow trans} = 0.52$ following S_1 excitation, and $\Phi_{trans \rightarrow cis} = 0.11$, $\Phi_{cis \rightarrow trans} = 0.44$ following S_2 excitation.[27]

2. On the other hand, the wavelength dependence of the quantum yields of isomerisation (point 1) is not observed if the rotational mechanism is inhibited by restraining the azobenzene molecule in a cyclophane structure. This results in equality of Φ_{isom} from both excited states.[28]
3. Efficient electronic relaxtion of S_2 to S_1 was observed for azobenzene and evidence was found suggesting that S_1 has a planar equilibrium geometry.[29]

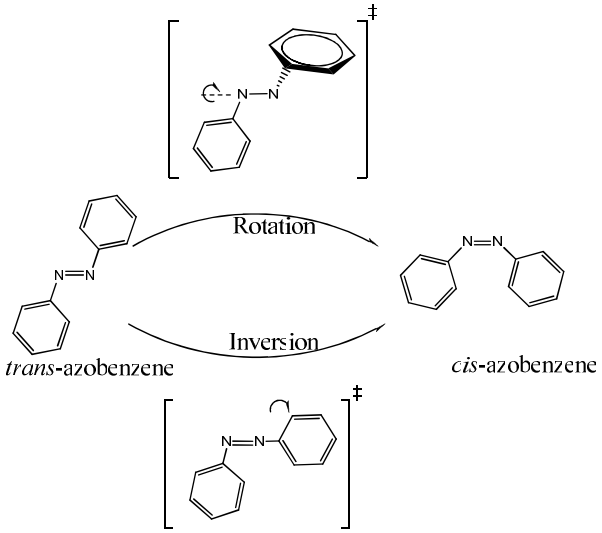

Figure 2-11 The two proposed mechanisms through which azobenzene can photo-isomerise.

Many researches have been published trying to explain the above three points. Point 1 is interpreted as indicating the involvement of a different mechanism (inversion or rotation) after excitation to the different electronically excited states. Point 2 implies that S_1 deactivates *via* an inversion pathway, since the inhibition of the rotational pathway by introducing the cylophane structure into the azobenzene molecule results in an increase in Φ_{isom} upon excitation to the S_2 state, which becomes equal to that on S_1 excitation. Inhibition of the rotation pathway leads to relaxation of S_2 to the S_1 state, followed by normal deactivation of S_1, *via* inversion. This interpretation is consistent with point 3.

Monti *et al.* [1982][30] formulated potential energy diagrams of the inversion and rotation pathway, which constitute the leading theoretical reference for the interpretation of azobenzene photochemistry. Using an early *ab initio* method with configuration interaction (CI), they were able to report calculated potential energy curves for the S_0, S_1 and S_2 states of azobenzene. Because they calculated a significant barrier to rotation on the S_1 curve, and a

much shallower curve on the inversion coordinate containing a minimum half way between the *trans* and *cis* isomer, rotation along S_1 was rules out in favour of an inversion mechanism. After excitation of each isomer to the S_2 state, only the rotational pathway provides an energetic downwards change, avoided crossings with the S_1 rotational pathway producing a minimum on both the *trans* and *cis* sides. These minima are postulated to undergo a bifurcation; the deactivation channelled 1:1 in to the S_1 and S_0 states. This predication that the S_1 state is partially bypassed correlates well with observations of smaller photoisomerisation quantum yields following S_2 excitation, satisfying point 1. Cattaneo and Persico [1999][31] with a greater level of theory, reached the same conclusion about the S_1 excitation, and were also able to conclude using similar arguments that the rotation mechanism would be operated after S_2 excitation; these observations are satisfying point 1.

Experimental investigations, using ultrafast spectroscopic techniques, by Lednev *et al.* [1996 and 1998][32-34] supported the previous experimental and computational work. The first study employed the use of femtosecond time-resolved UV/Vis spectroscopy, their conclusions supported the earlier studies that an inversion mechanism operates on the S_1 surface following $^1(n\pi^*)$ excitation, and at least partial rotation, occurs following S_2 excitation. In the second study applying the same technique, they examined a system in which the rotation pathway is totally inhibited, an azocrown ether-capped azobenzene system. The obtained results obtained after UV excitation were much more similar to those for excitation to S_1 rather than S_2 in azobenzene. This led them to suggest extremely fast (< 0.5 ps) internal conversion from S_2 to S_1. In a third study of the photochemistry of azobenzene in n-hexane, an extremely fast (< 200 fs) component has been observed in the decay of the initially excited S_2 state, and has been found to occur both near and above the electronic origin; it has been attributed to motion along the rotation coordinate. The S_1 state has been observed to decay with a lifetime of 2.5 ps when excited close to origin, attributed to motion along the inversion coordinate, and to decay with an additional fast component ($\leq$ 600 fs), when exited at $\geq$ 6000 cm^{-1} above the origin. This was taken as clear evidence that rotation occurs in azobenzene following excitation to the S_2 potential energy surface, and that inversion follows excitation to S_1, as predicted by earlier studies, and this supporting point 1.

Fujino *et al.* [2000, 2001, and 2002][29,35,36] studied photoisomerisation of *trans*-azobenzene after S_2 $(\pi\pi^*) \leftarrow S_0$ photo excitation using picosecond time-resolved Raman and femtosecond fluorescence spectroscopes. The first Raman study, demonstrated that the $S_2 \rightarrow S_1 \rightarrow S_0$ relaxation observed after S_2 photo-excitation is the process taking place in the molecule that retains essentially planar structure around the NN bonding. Moreover, in the

second study, the femtosecond time-resolved fluorescence spectroscopy indicated that the photoexcited S_2 state is almost exclusively relaxed to the planar S_1 state and that the rotational isomerisation pathway starting directly from the S_2 ($\pi\pi^*$) state does not exist. In the third study, they combined the results from three time-resolved spectroscopes, femtosecond absorption, picosecond Raman and femtosecond fluorescence. They concluded that the S_2 state has a planar structure. Then, the S_1 is relaxed to the S_0 state through the three different relaxation pathways, (1) the inversion isomerisation, (2) a *trans* $S_1 \rightarrow$ *trans* S_0 relaxation channel that is open even in the cold S_1 state, and (3) a *trans* $S_1 \rightarrow$ *trans* S_0 relaxation channel that is open only in the vibrationally excited S_1 state.

Diau [2004][37] proposed a new mechanism, a concerted inversion mechanism. On the basis of the CASSCF calculations for the excited state relaxed surface scan along the C-N=N bending (inversion), the C-N=N-C torsion (rotation), and the concerted CNN bending (concerted inversion) reaction pathways. According to the calculated results he argued that the inversion channel involves a substantial energy barrier and a large S_0–S_1 energy gap so that it is a highly unfavourable channel to be considered for an efficient electronic relaxation. The rotation channel is essentially barrierless with a conical intersection close to the midpoint of the pathway to reasonably account for the subpicosecond to picosecond relaxation times observed in the recent ultrafast experiments. Along the concerted inversion reaction path, a sloped conical intersection (S_0/S_1 CI_{inv}) was found to have the geometry close to the linear CNNC configuration. When the photoexcitation occurs in the S_2 state, the concerted inversion channel may open and the S_0/S_1 CI_{inv} would become energetically accessible to produce more *trans*-S_0 isomer.

Crecca and Roitberg [2006][38] studied a series of azobenzenes using *ab initio* methods to determine the substituent effects on the isomerisation mechanism. They determined the energy barriers from three-dimensional potential energy surfaces of the ground and electronically excited states. They found that the inversion pathway is preferred in the ground state S_0. They show that electron donating substituent increase the isomerisation barrier along the inversion pathway, whereas electron withdrawing substituent decreases it. They found the concerted inversion mechanism to operate in the parent azobenzene.

Wang and Wang [2007][39] used CASSCF calculations to map the potential energy surfaces of the ground state (S_0) and the first excited state (S_1) along the CN=NC rotational coordinate for Disperse Orange 3 (DO3). The result indicated that the photoisomerisation on the S_1 state mainly involved the rotation mechanism. A conical intersection with a twisted configuration

(CI_{rot}) locates on the middle of the PESs along the CN=NC rotational coordinate. Another decay channel (inversion pathway or concerted inversion pathway), characterised by the evolution of two C-N=N angles bending to deactivate the excite molecules also exists. Upon excitation to the S_2 state, the inversion channel could be accessible to decay the excited electron energy.

2.8 Chemical Kinetics

Consider the reversible photoisomerisation process of *trans*-azobenzene to form *cis*-azobenzene, as illustrated in Equation 2-15.

$$Trans \underset{k_{-1}(h\nu+\Delta)}{\overset{k_1(h\nu)}{\rightleftharpoons}} Cis \qquad \textbf{Equation 2-15}$$

If we irradiate a sample of pure *trans*-azobenzene, we find that the isomerisation to the *cis* form does not go to completion but generates an equilibrium mixture (PSS) between the two geometrical isomers. The concentrations of the two isomers are dictated by the equilibrium constant for the isomerisation. Since the photoisomerisation occurs in both directions, the reaction is reversible. For any initial concentration of the *trans* isomer, $[trans]_0$, during the irradiation process the chemical system must go to PSS. At the PSS, the ratio of the concentrations of *trans* and *cis* is given by the equilibrium constant expression,

$$K = \frac{[cis]_{PSS}}{[trans]_{PSS}} \qquad \textbf{Equation 2-16}$$

where $[trans]_{PSS}$ and $[cis]_{PSS}$ are the concentrations of the *trans* and *cis* isomers at the PSS. For the concentrations of the *trans* and *cis* to remain constant at their equilibrium values, both $d[trans]_t / dt$ and $d[cis]_t / dt$ must equals zero. Thus, the kinetic conditions for Equation 2-16 to be at equilibrium is that:

$$-\frac{d[trans]_t}{dt} = \frac{d[cis]_t}{dt} = 0 \qquad \textbf{Equation 2-17}$$

The rate law for Equation 2-15 is first order in both [*trans*] and [*cis*]. The rate is then given by Equation 2-18:

$$-\frac{d[trans]_t}{dt} = k_1[trans]_t - k_{-1}[cis]_t \qquad \textbf{Equation 2-18}$$

If $[trans]_t = [trans]_0$ and $[cis]_t = 0$ at time=0, the stoichiometry of Equation 2-15 requires that $[cis]_t = [trans]_0 - [trans]_t$, and Equation 2-18 replaced by Equation 2-19:

$$-\frac{d[trans]_t}{dt} = (k_1 + k_{-1})[trans]_t - k_{-1}[trans]_0 \qquad \textbf{Equation 2-19}$$

Integrating this rate law subject to the above initial conditions gives:

$$[trans]_t = ([trans]_0 - [trans]_{PSS})e^{-(k_1+k_{-1})t} + [trans]_{PSS} \qquad \textbf{Equation 2-20}$$

By bringing $[trans]_{PSS}$ to the left side and then rearrange the equation, Equation 2-20 can be written as:

$$\frac{[trans]_t - [trans]_{PSS}}{[trans]_0 - [trans]_{PSS}} = e^{-(k_1+k_{-1})t}$$ **Equation 2-21**

Since the sum $(k_1 + k_{-1}) = k_{PSS}$, k_{PSS} is the rate of the photoisomerisation upon irradiation to attain the PSS, Equation 2-19 could be written as:

$$\frac{[trans]_t - [trans]_{PSS}}{[trans]_0 - [trans]_{PSS}} = e^{-k_{PSS}t}$$ **Equation 2-22**

Similarly, for the *cis* isomer

$$\frac{[cis]_t - [cis]_{PSS}}{[cis]_0 - [cis]_{PSS}} = e^{-k_{PSS}t}$$ **Equation 2-23**

2.8.1 Temperature Dependent of Rate Constant

The rate of a chemical reaction almost always depends strongly upon the temperature. The temperature dependence of the rate of a reaction is due to the temperature dependence of the rate constant of the reaction. The temperature dependence of the rate constant is described by:

$$\frac{d \ln k}{dT} = \frac{E_a}{RT^2}$$ **Equation 2-24**

Where, E_a has the units of energy. If E_a is independent of temperature, Equation 2-24 can be integrated to give Equation 2-25:

$$\ln k = \ln A - \frac{E_a}{RT}$$ **Equation 2-25**

Where, A is a constant. The constant A is commonly called the pre-exponential factor, and E_a is called the activation energy. Equation 2-25 predicts that a plot of lnk as a function of 1/T is linear with intercept of lnA and a slope of $-E_a/R$.

Arrhenius [1880s] found that Equation 2-25 describes the temperature dependence of the rate constants for many reactions, and he used it to develop a general model for how reactions occur. Arrhenius noticed that the magnitude of the temperature effect on reaction rates was much too large to be explained in terms of only a change in the translational energy of the reactants. Thus for a reaction to occur it requires more than just a collision between reactants. Because of his contribution to the field of chemical kinetics, Equation 2-25 is now called the Arrhenius equation.

The activation energy is the energy that must be provided to enable the reactant/s to react; a chemical reaction can be described in terms of the simple energy diagram shown in Figure

2-12. The chemical reaction proceeds from reactant to product along a reaction coordinate (specific bond lengths or bond angles).

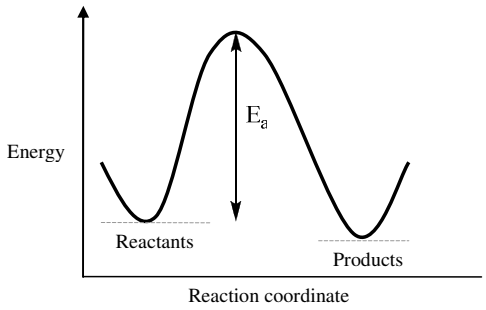

Figure 2-12 A schematic drawing of the energy profile of a chemical reaction. To transform into products the reactants must acquire energy in excess the activation barrier. The reaction coordinate represents the changes in bond lengths and bond angles that occur as the chemical reaction proceeds from reactants to products.

2.9 Transition State Theory

In this section will briefly discuss a theory of reaction rates called activated-complex theory or transition state theory. This theory was developed in the 1930s, principally by Henry Eyring, and focuses on the transient species in the vicinity of the top of the activation barrier. This species is called the transition state or activated complex, from which the theory derives its name. Consider the reaction $A + B \rightarrow P$, where the rate law is given by:

$$\frac{d[P]}{dt} = k[A][B] \qquad \textbf{Equation 2-26}$$

Transition state theory proposes that the reactants and the transition state are in equilibrium with each other. The reaction can be modelled by a two step process:

$$A + B \leftrightarrow AB^{\#} \rightarrow P \qquad \textbf{Equation 2-27}$$

The species $AB^{\#}$ is the transition state. The equilibrium constant expression between the reactants and the transition state is given by:

$$K_c^{\#} = \frac{[AB^{\#}]/c^0}{[A]/c^0[B]/c^0} = \frac{[AB^{\#}]c^0}{[A][B]} \qquad \textbf{Equation 2-28}$$

Where, c^0 is the standard-state concentration (often taken to be 1.00 mol.dm^{-3}). $K_c^{\#}$ may be written in terms of partition functions

$$K_c^{\#} = \frac{(q^{\#}/V)c^0}{(q_A/V)(q_B/V)}$$ **Equation 2-29**

Where, the q_A, q_B and $q^{\#}$ are the partition functions of A, B and $AB^{\#}$, respectively. The transition state is assumed to be stable throughout a small region of width δ centred at the barrier top in Figure 2-13.

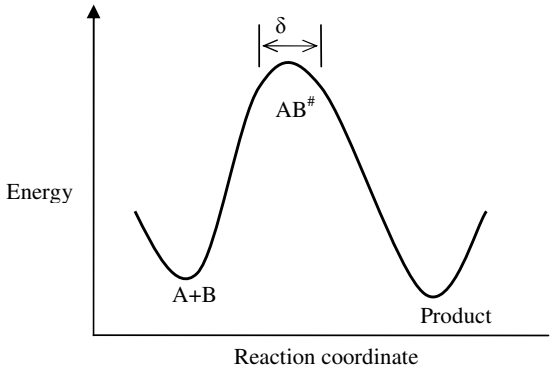

Figure 2-13 A one-dimensional energy diagram. The transition state, $AB^{\#}$, is defined to exist in the small region δ, centred on the barrier top.

The two step process given by Equation 2-27 predicts that the rate of the reaction will be the product of the concentration of the transition state $[AB^{\#}]$ and ν_c, the frequency with which these complexes cross over the barrier top, or

$$\frac{d[P]}{dt} = \nu_c [AB^{\#}]$$ **Equation 2-30**

Equation 2-30and Equation 2-26 give two different, yet equivalent expressions for the reaction rate. Solving Equation 2-28 for $[AB^{\#}]$ and substituting the resulting expression into Equation 2-30, and then equating the result to Equation 2-26 gives:

$$\frac{d[P]}{dt} = k[A][B] = \nu_c [AB^{\#}] = \nu_c \frac{[A][B]K_c^{\#}}{c^0}$$ **Equation 2-31**

or

$$k = \frac{\nu_c K_c^{\#}}{c^0}$$ **Equation 2-32**

Equation 2-30 implies that the motion of the reacting system over the barrier top is a one-dimensional translational motion. The translational partition function, q_{trans}, corresponding to one-dimensional motion is

$$q_{ttrans} = \frac{\left(2\pi m^{\#} k_B T\right)^{1/2}}{h}\delta$$ **Equation 2-33**

where $m^{\#}$ is the mass of the transition state. The partition function of the transition state can be written as $q^{\#} = q_{trans} q^{\#}_{\text{int}}$, where $q^{\#}_{\text{int}}$ accounts for all the remaining degrees of freedom of the transition state. Equation 2-29 can be written as

$$K^{\#} = \frac{\left(2\pi m^{\#} k_B T\right)^{1/2}}{h}\delta\frac{\left(q^{\#}_{\text{int}}/V\right)c^0}{\left(q_A/V\right)\left(q_B/V\right)}$$ **Equation 2-34**

Substituting Equation 2-34 into Equation 2-32 gives the following expression for the reaction rate constant

$$k = \nu_c \frac{\left(2\pi m^{\#} k_B T\right)^{1/2}}{hc^0}\delta\frac{\left(q^{\#}_{\text{int}}/V\right)c^0}{\left(q_A/V\right)\left(q_B/V\right)}$$ **Equation 2-35**

Equation 2-35 contains two quantities, ν_c and δ, that are not well defined and are difficult to determine. Their product, however, can be equated to the average speed with which the transition state crosses the barrier, $\langle u \rangle$, where $\langle u \rangle = \nu\delta$. Because of the assumption that the reactants and the transition state are in equilibrium, the (one-dimensional) Maxwell-Boltzmann distribution can be used to calculate $\langle u \rangle$, or

$$\langle u \rangle = \int_0^\infty u f(u) du = \left(\frac{m^{\#}}{2\pi k_B T}\right)^{1/2} \int_0^\infty u e^{-m^{\#}u^2/2k_B T} du = \left(\frac{k_B T}{2\pi m^{\#}}\right)^{1/2}$$ **Equation 2-36**

The integration is carried over only positive values of u because only those transition states that pass over the barrier in the direction of the reactants to products are considered. Substituting Equation 2-36 into Equation 2-35 for $\nu_c\delta$ gives the transition state theory expression for the rate constant

$$k = \frac{k_B T}{hc^0}\frac{\left(q^{\#}_{\text{int}}/V\right)c^0}{\left(q_A/V\right)\left(q_B/V\right)} = \frac{k_B T}{hc^0}K^{\#}$$ **Equation 2-37**

where $K^{\#}$ is the equilibrium constant for the formation of the transition state from the reactants, and the motion along the reaction coordinate is excluded in $q^{\#}_{\text{int}}$.

The Gibbs free energy of activation, $\Delta G^{\#}$, is defined as the change in Gibbs energy in going from the reactants to the transition state (when $c^0 = 1.00$ mol.dm^{-3}). The relation between $\Delta G^{\#}$ and $K^{\#}$ is

$$\Delta G^{\#} = -RT \ln K^{\#}$$ **Equation 2-38**

Equation 2-38 can be used to express the rate constant k in term of $\Delta G^{\#}$. Solving Equation 2-38 for $K^{\#}$ and substituting the result into Equation 2-37 gives:

$$k(T) = \frac{k_B T}{h} e^{-\Delta G^{\#}/RT}$$ **Equation 2-39**

$\Delta G^{\#}$ can be expressed in terms of $\Delta H^{\#}$, the enthalpy of activation, and $\Delta S^{\#}$, the entropy of activation, by introducing

$$\Delta G^{\#} = \Delta H^{\#} - T\Delta S^{\#}$$ **Equation 2-40**

This upon substitution into Equation 2-39 gives

$$k(T) = \frac{k_B T}{h} e^{\Delta S^{\#}/R} e^{-\Delta H^{\#}/RT}$$ **Equation 2-41**

The Arrhenius activation energy, E_a, can be expressed in terms of $\Delta H^{\#}$ and the Arrhenius A factor in terms of $\Delta S^{\#}$. Differentiating the logarithm of Equation 2-37 with respect to temperature gives:

$$\frac{d\ln k}{dT} = \frac{1}{T} + \frac{d\ln K^{\#}}{dT}$$ **Equation 2-42**

Using the fact that $d\ln K / dT = \Delta U / RT^2$ for an ideal gas system, Furthermore, $\Delta H^{\#} = \Delta U^{\#} + \Delta PV^{\#} = \Delta U^{\#} + RT\Delta n^{\#} = \Delta U^{\#} - RT$, Equation 2-42 could be rewritten as:

$$\frac{d\ln k}{dT} = \frac{\Delta H^{\#} + 2RT}{RT^2}$$ **Equation 2-43**

Comparing Equation 2-43 with Equation 2-24 gives:

$$E_a = \Delta H^{\#} + 2RT$$ **Equation 2-44**

Solving this expression for $\Delta H^{\#}$ and substituting the result into Equation 2-41 gives:

$$k(T) = \frac{e^2 k_B T}{h} e^{\Delta S^{\#}/R} e^{-E_a/RT}$$ **Equation 2-45**

Thus in terms of the thermodynamic interpretation of transition state theory, the Arrhenius A factor is given by:

$$A = \frac{e^2 k_B T}{h} e^{\Delta S^{\#}/R}$$ **Equation 2-46**

2.10 Enthalpy-Entropy Compensation

Enthalpy-entropy compensation is observed when a chemical reaction exhibits a linear relationship between enthalpy and entropy. This could be explained mathematically according to Equation 2-40, where the change in enthalpy of activation, $\Delta H^{\#}$, and the change in entropy of activation, $\Delta S^{\#}$, have opposite signs, thus the Gibbs free energy of activation,

$\Delta G^{\#}$, will change very little if both enthalpy and entropy of activation values increase. For instance, in a reaction where the chemical bonds become stronger or where chemical bonds are being formed throughout the course of a reaction, thus a negative $\Delta H^{\#}$ value will result. At the same time the movement of the molecule will be limited (in terms of the molecule ability to rotate, vibrate, etc.) and hence decrease the entropy of activation. This leads to small $\Delta G^{\#}$ value.

The application of enthalpy-entropy compensation in explaining a reaction are:

- The weak compensation is described when $\Delta H^{\#}$ and $\Delta S^{\#}$ have the same sign. Statistical mechanics shows qualitatively that as a system populates the lower the energy levels, the enthalpy and entropy will both decrease.

- The strong compensation occurs when $\Delta H^{\#}$ and $\Delta S^{\#}$ exhibit a linear correlation. In this case $\Delta G^{\#}$ will be small relative to the change of values expected from the experiment; this application is applied in Section 4.6.6.5.

3 Materials and Methods

3.1 Introduction

This chapter describes the apparatus and procedures used to obtain the results presented in chapters 4, 5 and 6. The main experimental techniques used were NMR and UV/Vis spectroscopy. The method employed for *in situ* laser irradiation of NMR samples is described and the methodology of quantum chemical calculations is outlined.

3.2 Materials

3.2.1 Solvents

Dimethylsulfoxide (DMSO, Aldrich, and spectrophotometer grade), d_6-dimethylsulfoxide (d_6-DMSO, Aldrich, > 99.7 atom % D), d_6-benzene (C_6H_6, Apollo, > 99.5 atom % D), toluene ($C_6H_5.CH_3$, Aldrich, and spectrophotometer grade), cyclohexane ($C_6H_{12,}$ Aldrich, spectrophotometer grade) and d_{12}-cyclohexane (d_{12}- $C_6H_{12,}$ Aldrich, > 99.5 atom % D) were all used as supplied.

All UV/Vis measurements were carried out in toluene, DMSO and cyclohexane. For NMR experiments d_6-benzene, d_6-DMSO and d_{12}-cyclohexane were used.

3.2.2 Azobenzenes

For the azobenzenes studied, the supplier and purity were as follows: azobenzene ($C_{12}H_{10}N_{2,}$ Aldrich, 98%); *p*-aminoazobenzene ($C_{12}H_{11}N_3$, Aldrich, 98%); *o*-methyl-methyl yellow ($C_{15}H_{17}N_3$, Apollo, 98%); *p*-nitro azobenzene ($C_{12}H_9N_3O_2$, Aldrich, 90%); Disperse Orange 3 ($C_{12}H_{10}N_4O_2$, Aldrich, 95%); Disperse Red 1 ($C_{12}H_{18}N_4O_3$, Aldrich, 90%); Methyl Yellow ($C_{12}H_{15}N_3$, Aldrich, no purity stated) and Dimethyl-nitroazobenzene ($C_{12}H_{14}N_4O_2$, Aldrich, no purity stated). All the compounds except Methyl Yellow were used without further purification and the purity of these compounds was taken into account during the preparation calculations of the NMR samples. Methyl Yellow was re-crystallised from water/ethanol mixture.

3.3 NMR Spectroscopy

3.3.1 Spectrometer

A Bruker DMX NMR spectrometer operating at 500.13 MHz (^{1}H) was used. This was equipped with a triple resonance TBI [^{1}H, ^{13}C, X] probehead fitted with an activity shielded z-gradient coil for delivering pulsed field gradients. All spectral data were processed using Xwinnmr software (version 2.0, Bruker Biospin Limited) running on a silicon Graphics Indigo2 XZ workstation operating under Irix 6.2.

3.3.2 *In situ* Laser Irradiation

A schematic diagram of the set up of the NMR with *in situ* laser spectrometer is shown in Figure 3-1. The samples were irradiated using a continuous wave argon/krypton mixed gas laser (Coherent INNOVA 70C) as the laser source, producing monochromatic radiation at wavelengths of 676, 647, 568, 530, 520, 514, 488 and 457 nm along with a multi-line emission from 351-364 nm. Control of sample irradiation was provided by a simple ON/OFF shutter mechanism on the laser.

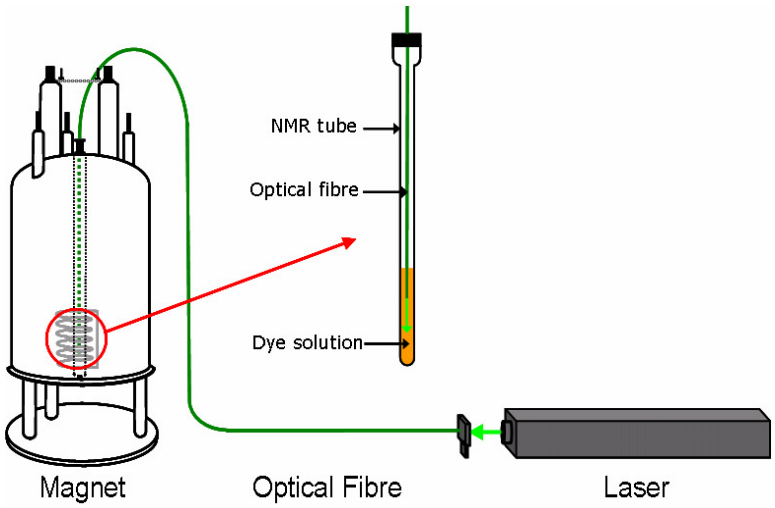

Figure 3-1 Schematic diagram of the set up of NMR spectrometer with *in situ* laser. Provided by A. C. Jones.

An optical fibre was used to couple the output of laser into the NMR sample illustrated in Figure 3-2. The optical fibre (FT-600-UMT, diameter 600 μm: Elliot Scientific Ltd.) carried

the light directly into the NMR sample inside the probe of the magnet. The laser output power from the fibre was adjusted to 30, 20, and 3 mW at 530, 568 and 514 nm, respectively, measured using a power meter (Coherent, FieldMate with O*P*-2 VIS Head) prior to attachment to the NMR tube (Wilmad, 528-TR-7) to insure consistency between sample measurements. The end section of the fibre was securely attached to the 5 mm screw-capped NMR tube *via* an O-ring seal, with the tip of the fibre inserted into the sample solution to a point directly above the detection volume. The position of the fibre inside the tube of NMR sample is described below. The fibre and the attached tube were lowered into the magnet.

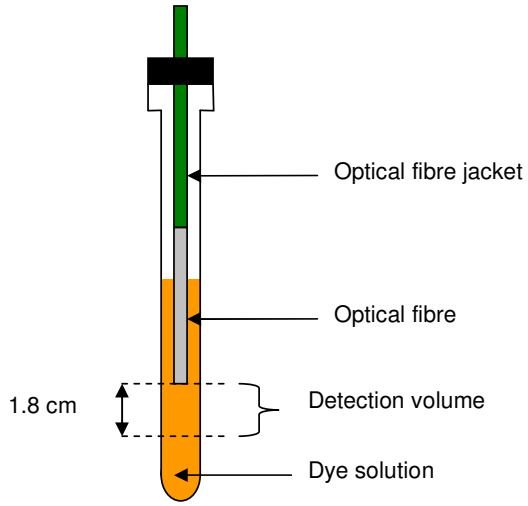

Figure 3-2 Fibre position inside the NMR sample tube.

A typical NMR sample consists of 500-600 µl of solution, leading to a sample depth of 5-6 cm in a 5 mm NMR tube. Since the homogeneity of the sample is essential, only a 200 µl region in the centre of the tube is monitored as other areas suffer from inhomogeneities, either because of the curvature at the base of the tube or the surface effect near the top. The sample section covered by the receiver coils, called the detection volume, begins 2.1 cm from the base of the tube and is only 1.8 cm deep. For the purpose of a normal NMR study it is only necessary to add the correct volume of sample to the tube and run the experiment. In the case on NMR with *in situ* laser irradiation, especially with respect to insuring consistency between kinetic measurements, it is vital that the fibre is placed in the same position for each experiment. The fibre was positioned at the top edge of the detection volume. Placement of the fibre inside the solution at the detection volume allows better application of the light to the solution and greater population of short-lived species. Moreover, there is no apparent

effect on the sample homogeneities as no detrimental effects were observed on the acquired spectra. It was possible to align the optical fibre using a depth gauge. Figure 3-2 illustrates the position of the fibre inside the NMR sample.

3.3.3 Sample Concentration

The sample concentration is a critical parameter when using *in situ* laser irradiation. Two things must be considered in the preparation of the NMR samples; first if the sample is too dilute this will result in poor signal to noise ratio and consequently unclear NMR spectrum, second if the absorption of the sample at the irradiation wavelength is too high, the light is almost totally absorb near the fibre tip, preventing the generation of the *cis* isomer in the detection volume. The sample concentration is strongly related to the pathlength of light, *i.e.* the penetration depth of the laser. Examining the UV/Vis absorption spectra of all the studied azobenzenes show that at most of the laser wavelengths there are strong absorption characteristics, except at the tail of the absorption curves. Applying the Beer-Lambert law (Equation 2-1) which relates absorbance to the molar absorption coefficient, sample concentration and pathlength, irradiation at the tail of the absorption curve allows a high enough sample concentration with low enough molar absorption coefficient. Under these circumstances a satisfactory spectrum was obtained in all cases.

3.3.4 Constant Absorption Condition

The calculations included in this work are quantitative comparisons of the kinetic and of the molecules under the study. Thus the samples must be irradiated under the same conditions, *i.e.* the intensity of light that penetrates each sample should be identical. Each molecule has a different molar absorption coefficient at the chosen irradiation wavelength so it was necessary to control the concentration of the solution using the Beer-Lambert law (Equation 2-1) to guarantee an identical absorption for each dye. This was achieved by adjusting the concentration to give 50% transmission at a path length of 2 mm beyond the tip of the fibre, which had been defined as the constant absorption condition in the previous studies[6,7]. This path length allows photoconversion of the sample within the detection volume, while keeping the concentration of the sample within the limits for NMR.

3.3.5 1D ^{1}H NMR Spectroscopy

1D ^{1}H NMR data were typically acquired over a spectral width of 6 kHz centred at 4.5 ppm into 36000 data points (acquisition time = 3 s) using a standard single pulse-acquire pulse sequence. Data were processed using a line broadening function of 0.2 Hz prior to Fourier transformation and phase correction.

Due to the high concentration of water in the DMSO solvents, for 1D ^{1}H NMR spectra in DMSO it was necessary to suppress the water signal. Since the NMR signal of water is isolated from the aromatic resonance region, the suppression did not require high selectivity. Consequently, a simple pre-saturation pulse program was employed. For these experiments, the spectral width was extended to typically 15 kHz, centred between 3 and 5 ppm. All data were processed using line broadening functions of up to 0.5 Hz prior to Fourier transformation and phase correction.

3.3.6 Pseudo 2D ^{1}H NMR Spectroscopy

Pseudo 2D spectra were recorded for each molecule during approach to the PSS with laser irradiation; the data were extracted and displayed as a graphical plot of integrals with time (decay of the *trans* and rise of the *cis* isomer). Similarly, during the thermal reversal in darkness, the data were extracted and displayed as a graphical plot of signal integrals with time (rise of the *trans* and decay of the *cis* isomer). Data extraction is described in detail in Section 3.3.6.1.

Pseudo 2D NMR experiments were typically acquired between 4 and 28 scans per FID, depending on the concentration of the sample. To preserve resolution in the F2 dimension, 28000 data points were giving an FID acquisition time approximately 1 s. F1 increments were acquired to sufficiently cover the extent of the kinetic process. The spectral width required was typically 15 kHz, centred between 3 and 5 ppm. Pseudo 2D data were processed in the F2 dimension only, with a line broadening function of 0.5 Hz prior to Fourier transformation and phase correction.

3.3.6.1 Data Extraction

This section is based on material presented previously in the thesis of Gibson.[5]

The acquisition of pseudo 2D spectra facilitates the use of a routine within the XWINNMR software that allowed changes in either signal intensity or integral to be monitored during the course of the acquisition period. From the first row of the pseudo 2D spectrum (time zero 1D spectrum) viable signals (those which do not overlap with other signal) are selected. The software than measures the integral and the intensity over the selected frequency channels in each subsequent row of the spectrum. All values are selected relative to those observed in the first, time-zero spectrum, allowing a direct comparison between each row. In all cases, the results are displayed as a graphical plot of integral with time, since, signal integrals showed less spread than signal intensities. Although this routine was designed to determine relaxation times of molecules, this procedure is equally applicable to tracking of the rise and fall of concentration of the two species.

As well as a graphical plot of the change of the concentration of each species with time, the coordinates can be exported as a text file. The data were exported to an Excel spreadsheet where they were fitted to the appropriate kinetic function (these equations are described in Section 4.4) using the non-linear least square fitting procedure. For each isomer the sum of the data for each signal was taken prior to kinetic analysis.

To maximize the time resolution of the measurements, the acquisition time of each row was made as short as possible, while maintaining an acceptable signal to noise ratio. The period of time required to measure each row of the pseudo 2D spectrum depends on the concentration of the sample, in addition to the rate of decay or rise of the two species present. The number of scans per row was varied from 4-32, equating to 10-60 seconds per data point.

3.3.7 Temperature Control

The temperature of the sample inside the NMR probe was controlled with a temperature unit (Eurotherm) supplied with Bruker spectrometers. This was used to vary the temperature of the NMR sample and thus for the study of the thermal *cis-trans* isomerisation process. For the photoisomerisation measurements the temperature was kept at 298 K. The percentage error in temperature as specified by this unit did not exceed ±0.05 % in all cases.

3.4 UV/Vis Absorption Spectroscopy

3.4.1 Spectrometer

UV/Vis absorption spectra were recorded using a Varian Cary 300 UV-visible spectrophotometer capable of measurements from 190-900 nm. Measurements were made using a matched pair of 10 mm pathlength fused silica cuvettes (Starna) regulated at 298 K through use of a peltier unit. The spectrometer was controlled from a PC with the Cary WinUV suite of software installed; spectra were obtained using the 'scan' command and single point measurements using the 'advanced read' command.

3.4.2 *Ex situ* laser Irradiation for UV/Vis Measurements

Where UV/Vis measurements of the photostationary state (PSS) of an azobenzene were required, the sample was irradiated using the xenon lamp excitation source of an Horiba-Jobin-Yvon Fluoromax fluorescence spectrometer. An initial spectrum was recorded in darkness prior to irradiation. To limit any possible solvent evaporation, and hence concentration change, a cap was used to seal the cuvette. After a suitable period of time had elapsed, the sample was transferred to the UV/Vis spectrometer, the compartment was closed, and the absorption spectrum was recorded. In many cases, single point measurements were conducted at λ_{irr} due to rapid *cis* isomer decay. Using thermal decay data derived from NMR experiments, it was possible to extrapolate a photostationary state molar absorption coefficient for the *cis* isomer from the acquired data (see Section 4.4.1.4.1). This was to correct for the time lapse between terminating the irradiation of the sample and taking a measurement, usually on the order of thirty seconds.

3.4.2.1 Measurements of the Thermal Rate *via* UV/Vis Absorption Spectroscopy

Stock solutions of the azobenzene in toluene and in DMSO (without added base) (1×10^{-4} M) were prepared and kept in the dark at room temperature. Approximately 4 ml of the stock solution was transferred promptly into a 1-cm quartz cuvette. To limit any possible solvent evaporation, and hence concentration changes, a cap was used to firmly seal the cuvette. The sample was transferred to the UV/Vis spectrometer, and the sample compartment was closed. It was assumed, according to previous studies,[40,41] that the *trans* isomer, due to its

higher stability, was the only isomer present in the solution in darkness before irradiation. The UV/Vis absorption spectrum was recorded in the range of 200-600 nm.

The *cis* isomer was obtained by transferring the sample into the Fluoromax spectrometer and exposing the sample to light of a specific wavelength for a suitable period of time (≈ 2hr), which was demonstrated to be long enough to reach the PSS. After irradiation the sample was transferred quickly from the Fluoromax spectrometer into the UV/Vis spectrometer. Following by closing the sample compartment, the absorption spectrum was recorded as a function of time to monitor the thermal isomerisation process, see Section 4.6.5.

3.5 Computation Method

Calculations were performed using an AMD opteron-based cluster, running the *Gaussian* 03 package[42] under Linux. Geometry optimisations were conducted by density functional theory (DFT) using Beck's three parameter exchange functional[13] and Lee-Yang-Parr correlation functional[16]. Calculations were performed at the 6-31G(d,p) basis set[17] unless otherwise specified in the text. Every bond length, bond angle and torsional angle for each structure was free of constraints and allowed to relax during the optimisation. The *trans* and *cis* structures presented later are the lowest energy local minima.

The potential energy curve (PEC) of the dihedral rotation pathway was constructed starting from either the *trans* or *cis* optimized geometry. The dihedral angle CN=NC was fixed at 0^0 or 180^0 depending on the starting geometry while optimizing the other structure parameters at the same time. The dihedral angle was incremented nineteen times by $\pm 10^0$. The energy of each optimized structure was obtained as a function of the dihedral angle. The transition state in all cases was the middle energy point at the top plateau region on the potential energy curve.

The PEC of the inversion pathway was constructed starting from the *trans* isomer, a smooth reaction pathway to the inversion transition state was obtained by stepwise increasing the N=NC bond angle while optimizing the other structure parameters at the same time, *i.e.* starting at bond angle of 110^0 and incrementing by $+10^0$ seven times until the transition state was reached (at $\approx 180^0$). For the *cis* isomer a smooth reaction pathway was obtained starting from the transition state, *i.e.* starting from $\approx 180^0$ optimized structure and incremented by $+10^0$ six times until 240^0 was reached. The energy of each optimized structure was obtained

as a function of the bond angle. The transition state in all cases was the maximum energy point on the potential energy curve.

Vibrational frequencies were computed on the optimized geometries. The nature of the stationary points for the studied molecules has been determined by mean of the number of imaginary frequencies, for the *cis* and *trans* structures, only real frequency values, and in the transition state structures only single imaginary frequency values were accepted.

Two potential energy curves were constructed for the inversion path of the studied asymmetric molecules depending on which N=N ring bond angle was inverted. The N=NC bond angle was designated as α-N=NC and β-N=NC, see Figure 5-1 for the definition of α and β in terms of the substituents.

Calculations in two solvents namely benzene and DMSO were performed employing the self consistent reaction field (SCRF) method based on the polarisable continuum model (PCM).[19,43] In solution, the optimized structures of the *cis*, *trans* and transition state obtained from the PEC in the gas phase were re-optimized in the desired solvent. Vibrational frequencies were computed on the re-optimized geometries in solution, the number of imaginary frequencies confirmed the nature of the stationary points for all geometries as mentioned before.

The thermodynamic functions (all corrected for the zero-point energy), *i.e.* E_0, enthalpy H (sum of the electronic and thermal enthalpy), Gibbs free energy G (sum of the electronic and thermal free energy) and entropy S, were calculated according to the following relations: $E = E_0 + E_{vib} + E_{rot} + E_{trans}$, $H = E + RT$, $G = H - TS$, as defined in the output of the frequency calculation. Using the corresponding calculated thermodynamic data for the *cis* and transition state, the activation parameters of the thermal *cis*-to-*trans* conversion process including E_a, $\Delta H^{\#}$, $\Delta S^{\#}$ and $\Delta G^{\#}$ were determined. Structural figures presented in this work were created using gOpenMol.

4 Experimental Study of the Kinetics of Photo- and Thermal Isomerisation of a Series of Azobenzenes

4.1 Introduction

From the time when Hartley [1937][1] published the first piece of work characterising the species resulting from the exposure of a solution of azobenzene to light, thus identifying for the first time the photochemical *trans*-to-*cis* isomerisation of azobenzene, the photoisomerisation of azobenzene has become one of the most well known and studied photochemical phenomena. It is well known now that azobenzene and a large number of its derivatives exist predominately in the *trans* form, thus the *trans* isomer is the thermodynamically favoured species and the isomerisation to the *cis* form is a photochemical process. The reverse isomerisation, *cis*-to-*trans,* is driven photochemically and thermally.

The investigation of both the photochemical processes (*trans*-to-*cis* and *cis*-to *trans*) and the thermal *cis*-to-*trans* isomerisation has been conducted extensively, experimentally, using UV/Vis absorption spectroscopy and, recently, using NMR spectroscopy with *in situ* laser irradiation, and of course computationally.

The pioneering use of NMR coupled with *in situ* laser irradiation in the study of photoisomerisation in azo compounds was a study of simple disperse monoazo molecules.[7,8] Through the observation and characterisation of the *cis* isomer and the monitoring of the thermal decay of the observed *cis* signals back to *trans*, the study proved that reversible *cis-trans* isomerisation was the exclusive photoinduced process occurring. However, the investigation of the kinetics of the photo- and thermal isomerisation was neglected and thus formed the subject of the present study. More complex azo dyes have also been studied using this technique[6], and the conclusions were similar to those that have been drawn for simple azo dyes. The *cis* isomer was observed as the exclusive product of irradiation by visible light without any additional photoinduced processes, thus the NMR spectra assignments were straightforward. Additionally, the proton peaks in both *trans* and *cis* isomers were often well resolved from one another, enabling the simple assignments of the spectrum. The kinetics of the photo- and thermal isomerisation of the more complex dyes have been investigated.[4,5] and the technique has proved to be effective in such studies. The

main observation was that large differences in the kinetic parameters resulted from minor structural changes to each dye. Following the success of these studies of complex azo dyes the present study of simpler dyes applying the same technique was undertaken with a view to gaining insight into the mechanism of the isomerisation process. Previously, complementary computational work on the structures of the *trans* and *cis* isomers was carried out in order to assist the explanation of the kinetic observations and to explain the differences in the chemical shift changes between *cis* and *trans* isomer protons in the NMR spectra.[4-8] However, the size of and complexity of the molecules prevented the use of computation for exploring the ground state potential energy curves and the transition states for the thermal isomerisation. In the present work, applying the computational calculations to smaller molecules allows not only calculation of the structural geometries of the *trans* and *cis* isomers but also permits exploration of the ground state potential energy curves, in the gas phase and in solution, and the geometries of the transition states involved in thermal isomerisation. Furthermore, frequency calculations for the *cis* isomer and the transition state allow prediction of the activation parameters of this isomerisation which can be compared with the corresponding experimental values. These comparisons allow judgment on the performance of such calculations. The results obtained experimentally and theoretically can be used in combination to investigate of the mechanism of thermal *cis*-t*o*-*trans* isomerisation.

Given the controversy regarding the photochemical isomerisation mechanism of azobenzene, (Section 2.7.1), in the same manner a great deal of debate has been conducted regarding thermal isomerisation of *cis* azobenzene, which follows first order kinetics. The mechanism of the thermal *cis*-to-*trans* isomerisation has been a controversial problem since two opposing mechanisms have been proposed, rotation about the N=N bond which proceeds *via* a dipolar transition state and an inversion mechanism involving flip-flop inversion of one of the nitrogen atoms which proceeds *via* an s*p*-hybridized linear transition state, as illustrated in Figure 4-1. Kinetic studies of the thermal *cis*-*trans* isomerisation of azobenzenes have been used to investigate the factors that affect the rate of such reactions and thus to predict the reaction mechanism. Studies have focused on the effect of; (i) substituents, (ii) solvent polarity, (iii) pressure (iv) volume and (v) pH of the solution. The early work of Schulte-Frohlinde [1958][44] was the first to suggest that azobenzenes isomerise thermally by rotation about the N=N bond. Talaty and Fargo [1967][45] suggested that, due to the lack of major solvent or substituents effects on the rate of isomerisation and the lower activation energies of several azobenzenes compared to that of stilbenes (which undergo exclusive rotation) the thermal isomerisation must be due to a mechanism other than rotation, *i.e.* inversion.

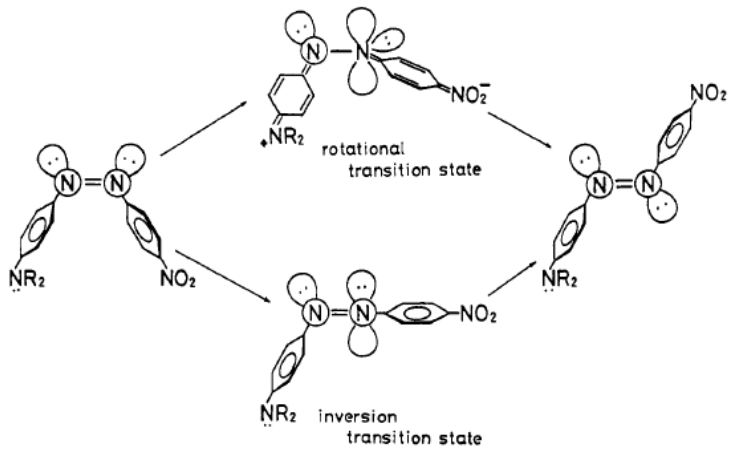

Figure 4-1 Schematic representation of rotational and inversion transition states. Reproduced from reference.[46]

The effect of substitution at the *ortho* position with respect to the azo linkage on the thermal rate and hence on the possible mechanism have been reported in several papers.[47-49] Gegiou *et al.* [1968][47] first studied the effect of *ortho* substitution. They found the thermal isomerisation rates of 2,4,6-trimethyl- and 2,2',4,4',6,6'-hexamethylazobenzene are very similar to the rate of azobenzene and concluded the inversion mechanism to be operative, and argued that a substituent in the *ortho* position to the azo group would hinder the rotation; the steric hindrance would be less severe in the linear transition state of the inversion mechanism than in the ground state. Nishimura *et al.* [1984][48,49] monitored the thermal isomerisation rate of 4-dimethylamino azobenzene (MY) and 4-nitroazobenzenes (NAB) [48].While the 2-methyl group (MMY) accelerated the rate, the 2'-methyl group did not have any significant effect. In the second study of 4-dimethylamino-4'-nitroazobenzene (DMNAB) derivatives[49], they found that 2-methyl- and 2'-chloro-DMNAB isomerise faster than DMNAB, and 2'-methyl- and 2-chloro-DMNAB isomerise slower than DMNAB. The results were very similar to MY derivatives, and thus they concluded that there are no fundamental differences in the kinetic substituent effect between MY and DMNAB. For both they postulated that the rate is controlled mainly by the resonance stabilization in the co-planar inversional transition state.

Wildes *et al.* [1970][50] suggested a rotational mechanism for the thermal isomerisation of some *para*-donor/*para*-acceptor azobenzenes by observing relaxation to equilibrium following flash photolysis. This was evident from the sizeable solvent effects on the rates

and activation energies of the thermal isomerisation of these dyes. In addition they showed much faster rates than those measured for azobenzene and its monosubstituted derivatives.

Sueyoshi *et al.* [1974][51] studied some substituted 4-dimethylaminoazobenzenes. They found that substitution effects on the isomerisation rates strongly support the view that the isomerisation proceeds *via* inversion at either one of the azo-nitrogen atoms. In addition they argued that the solvent effect reported by Wildes did not rule out the inversion mechanism, but rather supported it, so they suggested that the dipolar resonance contribution in the transition state is larger in the inversion mechanism than in the rotation mechanism.

Nishimura *et al.* [1976 and 1985][48,52] supported the inversion mechanism; they followed the thermal *cis*-to-*trans* isomerisation rate of various azobenzenes by means of spectrophotometer and flash photolysis techniques. They concluded this result from the observation that the rate for *para*-donor/*para*-acceptor substituted azobenzenes was distinctly accelerated, the activation energy decreasing, with the increase in the polarity of solvents.

Literature reports regarding correlation between the activation parameters of the thermal isomerisation with the possible mechanism are few.[53-56] Asano *et al.* [1981 and 1986][53,54] prepared an azobenzene-bridged crown ether and suggested that this molecule is the standard for the inversion mechanism. On the basis of $\Delta H^{\#}$-$\Delta S^{\#}$ compensation relationship which results in comparable values for $\Delta G^{\#}$ (see Section 2.10 for the discussion of $\Delta H^{\#}$-$\Delta S^{\#}$ compensation), and pressure effects, the azobenzenes could be distinguished as to whether they thermally isomerise by a rotational or inversional mechanism. They postulated that azobenzenes without push-pull substituents (*i.e. para*-electron donor/*para*- electron acceptor substituted azobenzenes) isomerise thermally *via* the inversion mechanism in disagreement with the previous conclusions. In the other study they postulated that the two reaction mechanisms in the *cis-trans* thermal isomerisation of push-pull azobenzenes are competing, and concluded this result from studying the thermal isomerisation of DMNAB in various solvents and different temperatures and pressures.[54] The temperature dependence of the activation volume was qualitatively different for different solvents. The Arrhenius plots were linear for ethanol and methanol but deviated upward at high temperatures for benzene and dioxane indicating that two mechanisms were operating in these solvents. Liu *et al.* [1992][56] correlated a small enthalpy of activation and larger negative entropy of activation with the occurrence of the inversional mechanism. This was evident from the results obtained from azobenzenes in assembled monolayer film.

Only a few systematic studies have been reported on the pH effect observed for the *cis-trans* isomerisation of azobenzenes[55,57-60]. Based on a study of solvent effects on the rate of the thermal isomerisation of 4-(diethylamino)-4'-nitroazobenzene (DENAB), Sanchez *et al.* [1983][55] suggested that the isomerisation reaction is accelerated in hydrogen-bonding donor (HBD) solvents relative to aprotic solvents of similar polarity. They attributed this to the hydrogen-bonding interaction between the solvent and the nitro group of the dye, this interaction is stronger with the transition state than with the *cis* isomer since the transition state is more dipolar than the *cis* isomer. Hence the observed acceleration in the thermal isomerisation is due to the lowering in $\Delta G^{\#}$ through stabilisation of the transition state. In a series of systematic studies Sanchez *et al.* [1993, 1995 and 1999][58-60] demonstrated, using time-resolved laser flash photolysis, the effect of pH of the medium on the thermal isomerisation rates for 4-[4-(Dimethylamino)phenylazo]benzenesulfonic acid sodium salt (MO) and 4-dimethylamino azobenzene (MY) and other molecules. The thermal rate was found to be catalysed by general acids and general bases, for example the observed rate constants for 4-(dimethylamino)-4'-methoxyazobenzene were decreased by a factor of 19 as the pH increased in solutions of NaOH of concentrations of 1.0×10^{-3} M and 1.0×10^{-1} M. In most of azo compounds there are several possible sites which could act as a base and abstract proton from the solution leading to the formation of the protonated azo compound, as shown in Figure 4-2.

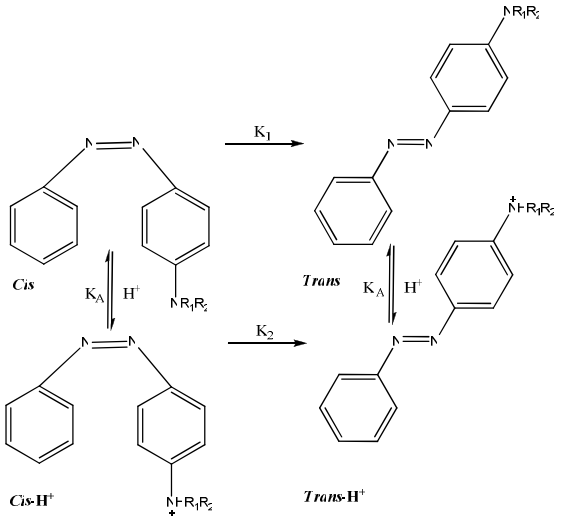

Figure 4-2 The proposed mechanism regarding the effect of pH on thermal *cis-trans* isomerisation.

The mechanism involving rotation was manifested by the fact that the rate of the thermal isomerisation is reduced by hydroxide ions. The protonated azo compounds isomerise so much faster than the unprotonated compound due to the occurrence of ammonium-azonium tautomerization, Figure 4-3.

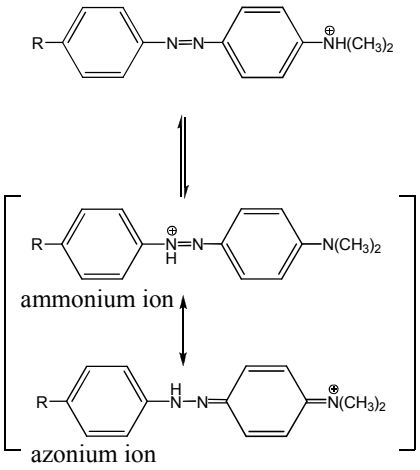

Figure 4-3 Ammonium/azonium tautomerisation of protonated azobenzenes.

The azonium tautomer easily isomerises *via* rotation since there is a decrease in the double bond character between the nitrogen atoms of the azo linkage, experiments have confirmed that $k_2 >> k_1$, where the values of k_2 are 108-1010 higher than those of k_1, where k_1 is the rate constant for the thermal isomerisation of unprotonated *cis* species and k_2 is the rate constant for the thermal isomerisation of the protonated *cis* species. Regarding the electron acceptor azobenzenes, there is no literatures available regarding the effect of pH on the thermal isomerisation of this type of azobenzenes molecule, and thus this point remains to be investigated.

Dubini-Paglia *et al.* [1992][61] studied the thermal *cis-trans* isomerisation of substituted 4-diethylaminoazobenzenes (DEAAB) kinetically as a function of temperature in various polymeric matrices, and found that even though solid systems reduce the substituents effects, the thermal isomerisation rates were dependent on the position of the substituents. This was evident from the fact that the kinetic coefficients of 4'-substituted dyes were found to be higher than those for 3'-substituted dyes by a factor of 30.

As can been seen from the literature cited above, little research has been carried out regarding the role that the activation parameters play in determining the mechanism, and

furthermore experimental studies of isomerisation may be difficult to interpret given that there are two competing mechanisms and the domination of one over the other depends on many factors including solvent properties and substituents.

This chapter reports the study of the kinetics of the photochemical and thermal isomerisation of a series of azobenzenes and they are; diphenyldiazene (azobenzene (AB)), 4-nitroazobenzene (NAB), *p*-phenylazoaniline (*p*-aminoazobenzene (AAB)), 4-(Dimethylamino)azobenzene (Methyl Yellow (MY)), 4-dimethylamino-2-methylazobenzene (*o*-Methyl-Methyl Yellow (MMY)), *p*-nitroazobenzene, 4-(4-Nitrophenylazo)aniline (Disperse Orange 3 (DO3)), 4-nitro-4'-dimethylaminoazobeneze (DMNAB), and N-ethyl-N-(2-hydroxyethyl)-4-(4-nitrophenylazo) (Disperse Red 1 (DR1)). The structures of these molecules are shown in Figure 4-4. The technique of NMR with *in situ* laser irradiation enables the time dependence of the concentration of *trans* and *cis* species to be accurately measured throughout the isomerisation process. The appropriate kinetic models can then be fitted to the experimental data to give the kinetic parameters of the photo- and thermal isomerisation. Studying the temperature-dependence of the thermal rates and applying the Arrhenius and Eyring equations, (see Section 2.8 and Section 2.9 for the details derivation of these equations), gives the activation parameters of the thermal isomerisation.

This chapter will begin by describing of the experimental procedures for both the NMR measurements and the kinetic studies, and an assessment of the reproducibility of the measurements. The investigation of the photoisomerisation kinetics will be then presented, including examination of the effect of molecular structure and solvent polarity. This is followed by an account of the study of the thermal *cis* to *trans* isomerisation, and discussion of the implications of the results regarding the mechanism of the thermal isomerisation. Sections 4.3.1, 4.4.2, 4.6.3, 4.6.4.1, and 4.6.4.2 of this chapter are based on material presented previously in the thesis of Tait / Gibson.[4,5]

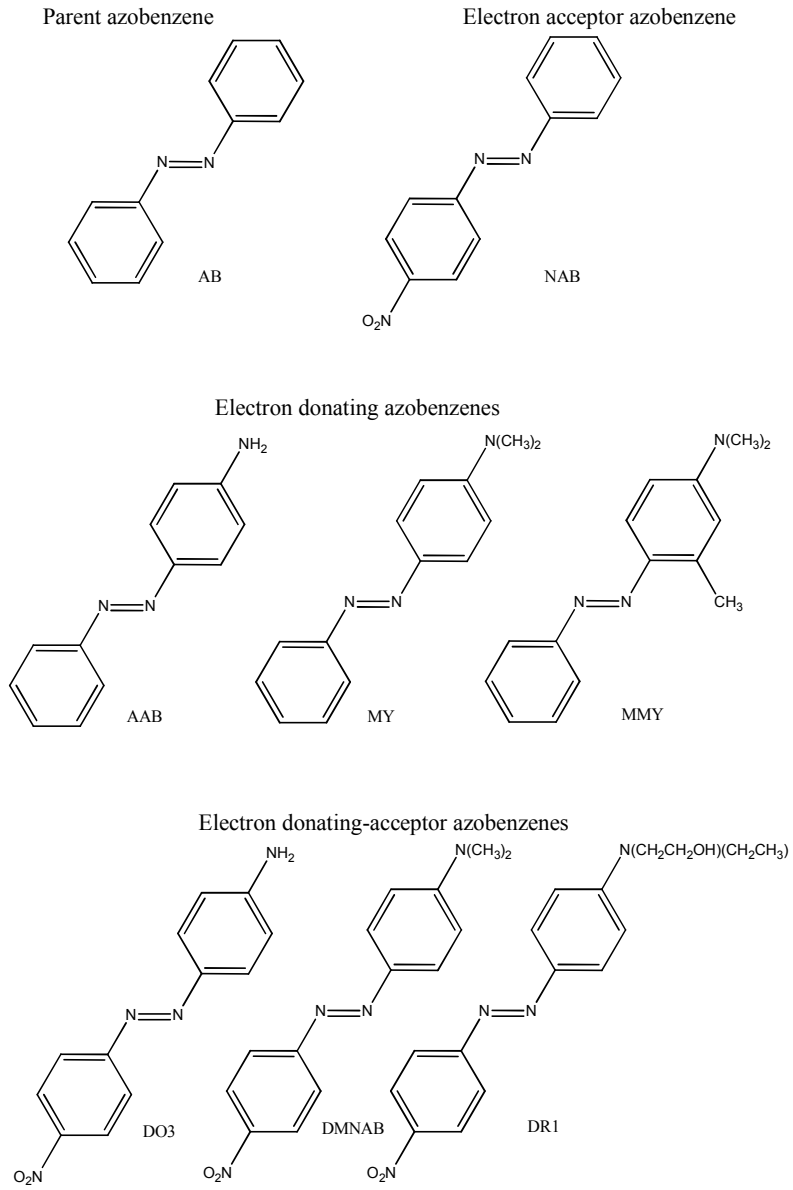

Figure 4-4 Structures of the *trans* isomers of the azobenzenes.

4.2 Experimental Conditions for NMR Spectroscopy

Formatted: Bullets and Numbering

4.2.1 Choice of Azobenzene Derivatives

This work focuses on the investigation the photo- and thermal isomerisation of simple disperse monoazo compounds, the investigation of the kinetics of both forward and reverse *trans-cis* photoisomerisation and of thermal *cis-to-trans* isomerisation.

The complementary computational calculations reported in Chapter 5 involved the investigation of the potential energy curves and the transition states of the thermal isomerisation process. In order for such calculations to be feasible, in terms of both time and cost of computing resources, simple disperse monoazo molecules were chosen for study. The effect of structural diversity on the thermal rate falls within the scope of this work. Therefore the molecules studied were chosen to include the parent compound, *i.e.* AB; azobenzenes of the type of aminoazobenzene, *i.e.* azobenzene substituted with an electron donating group; azobenzenes substituted with an electron acceptor group; and azobenzenes of the pseudostilbene type, *i.e.* substituted with an electron acceptor at the *para* position of one of the phenyl rings and an electron donating group at the other *para* position of the second phenyl ring. Due to the intramolecular charge transfer the later type of azobenzenes are also known as push-pull azobenzenes. Examples of aminoazobenzenes included *p*-aminoazobenzene (AAB), Methyl yellow (MY) and *o*-methyl Methyl Yellow (MMY), the examples of pseudostilbenes included Disperse Orange 3 (DO3), dimethyl-nitroazobenzene (DMNAB) and disperse Red 1 (DR1), and *p*-nitroazobenzene (NAB) was chosen as an example of *p*-electron acceptor azobenzene.

Formatted: Bullets and Numbering

4.2.2 Choice of Solvent

It is beneficial to study the effect of solvent on the thermal rate in order to investigate the mechanism of thermal isomerisation. The thermal isomerisation of simple disperse dyes is fast, in order of seconds to picoseconds.[62-65] As mentioned in Section 4.1, the thermal rate is enhanced significantly in proton-donating media. In the present work, it was impractical to perform the study with protic solvents, since the fast isomerisation will exceed the technique sensitivity limits, *i.e.* for fast decays it would be impractical to acquire sufficient kinetic data. Therefore, two aprotic (deuterated) solvents with different properties, benzene as a non-polar

solvent and DMSO as polar solvent, were chosen[i] for the NMR experiments. For UV/Vis studies, toluene was used as a less toxic alternative to benzene. Additionally a few experiments were carried out in cyclohexane and chloroform.

Using dry DMSO solvent was insufficient to prevent the existence of a certain amount of water in the samples (this is the origin of protons existence in DMSO solution which will be discussed in Section 4.2.3); therefore, the ^{1}H NMR spectra of the azobenzene derivatives contained significant water signals. Since the aromatic region of the NMR spectrum was the region of interest for these azobenzenes, the water peak was selectively suppressed. When using benzene as a solvent, the aromatic proton signal of the benzene ring overlaps with the signals of the aromatic protons of the molecule under investigation. However, the assignment of the other available signals was quite sufficient for the purpose of this study.

Formatted: Bullets and Numbering

4.2.3 pH of Samples in DMSO Solvent

The adjustment of the pH of the NMR samples was necessary to control the rate of the thermal isomerisation. It was found that the thermal rate markedly increased and the corresponding activation barrier decreased in the presence of a proton donor (HD) medium such as water in DMSO solutions. In order to investigate the effect of protonation of the azo molecules in DMSO solution the experiments were carried out without adding a base to these samples, hereafter such samples will be defined as "sample in protic DMSO". On the other hand, to eliminate protonation and study the effect of solvent polarity only on the thermal rates, prior to each experiment 5 µL aliquot of a 0.1 M aqueous solution of Na_2CO_3 was added to the 600 µL NMR sample, by this step the DMSO's solution was made basic and thus the protonation of azo molecules by water was prevented, hereafter such sample will be defined as "sample in basic DMSO".

Formatted: Bullets and Numbering

4.2.4 Selection of Irradiation Wavelength

Figure 4-5 and Figure 4-6 show the UV/Vis absorption spectra for the *trans* isomer of the studied azobenzenes in toluene and DMSO, respectively. As mentioned in Section 3.3.2, a limited number of visible wavelengths are available for use according to the available laser lines. It was necessary to optimise the concentration of the NMR samples to allow a spectrum of sufficient quality to be obtained, while at the same time enabling light to

[i] Dielectric constants are 2.2 and 47.2 for benzene and DMSO, respectively.

penetrate the sample, (see Section 3.3.3). To meet these criteria, an irradiation wavelength on the long-wavelength edge of the absorption spectrum was used.

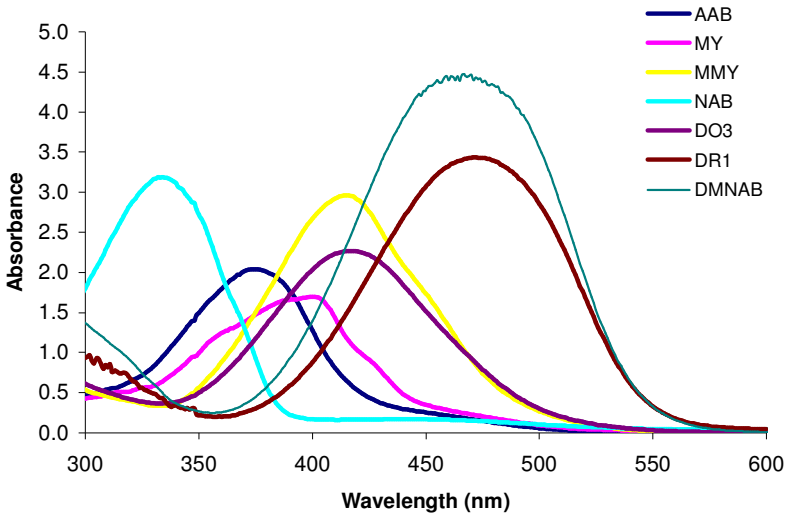

Figure 4-5 The UV/Vis absorption spectra for the *trans* isomers of the azobenzene derivatives ($1x10^{-4}$ M) in toluene.

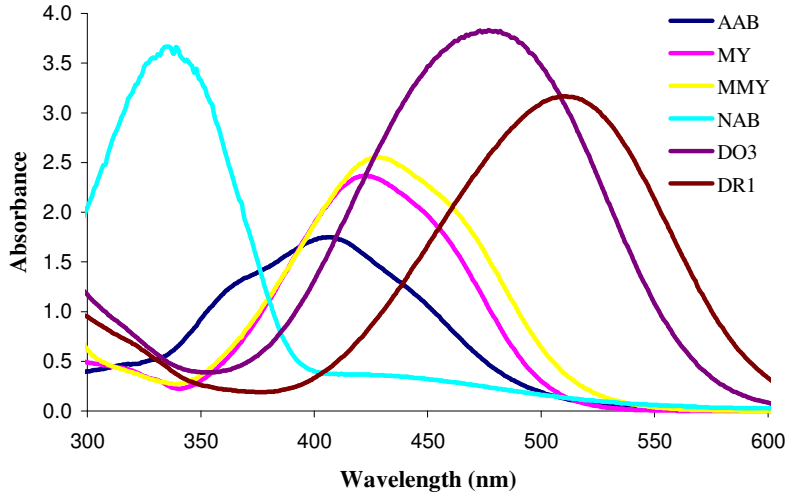

Figure 4-6 The UV/Vis absorption spectra for the *trans* isomers of the azobenzene derivatives ($1x10^{-4}$ M) in basic DMSO.

Table 4-1 summarises the chosen conditions for each azobenzene derivative in different solvents.

Table 4-1[ii] The irradiation wavelength, molar absorption coefficient of the *trans* isomer (at the irradiation wavelength) and NMR sample concentration for solutions in toluene (regular font), basic DMSO (bold font), protic DMSO (highlighted bold font), cyclohexane (italics font), and chloroform (bold and italics font) solution.

Molecule/structure	Irradiation wavelength, λ_{irr} / nm	Molar absorption coefficient, ε_{irr} / M^{-1} cm^{-1}	Concentration / mM
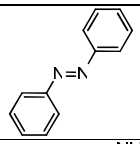 AB	**300**	**8204**	**0.18**
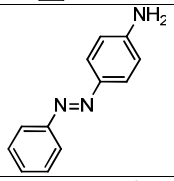 AAB	514	278	5.41
		1088	**1.38**
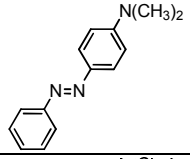 MY	514	561	2.68
		1126	**1.34**
		472	*3.19*
		790	***1.91***
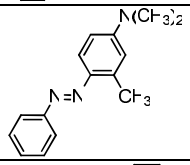 MMY	530	654	2.30
		1241	**1.21**
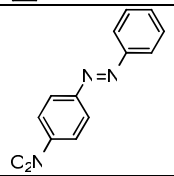 NAB	514	819	1.84
		1248	**1.21**
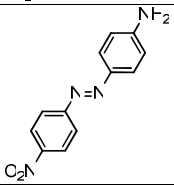 DO3	530	831	1.81
	568	119	12.6
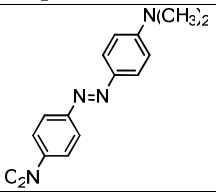 DMNAB	568	611	2.46

[ii] Table 4-1: continued overleaf

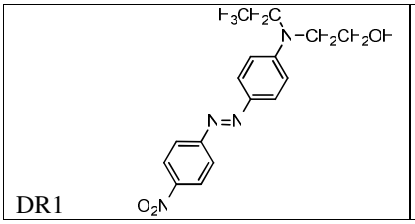 DR1	568	1163	1.29

Formatted: Bullets and Numbering

4.2.5 NMR Spectra Assignments Before and After Laser Irradiation

It is necessary to make the assignments of NMR spectra for the azobenzene investigated to confirm the identity of the molecule under study, and to prove that the *cis* isomer is the only photoproduct generated upon irradiation of the *trans* sample. The direct measurement of the signals belonging to the same proton in both the *trans* and *cis* isomers allows the composition of the photostationary state to be measured. An accurate determination of this value is not only useful as a measure of how much *cis* isomer is present, but is also very important for use in the isomerisation kinetics study. The general procedure will be demonstrated by using AAB as an example, Figure 4-7.

AAB has six sets of protons that are magnetically and chemically non-equivalent, labelled **a-f** for the *trans* form and **g-l** for the *cis* form, as illustrated in Figure 4-7 (a) and (b). Positions 2/6 *ortho* to the azo bond are equivalent giving a doublet signal of intensity two and protons at positions 3/5, which are equivalent giving a triplet of intensity two. A proton at position 4 gives a triplet of intensity one. Positions 8/12 *ortho* to azo bond are equivalent and protons 9/11 are equivalent both giving a doublet signal of intensity two. Protons of the amino group give a singlet signal of intensity two. The 500 MHz one-dimensional (1D) ^{1}H NMR spectra associated with AAB at a concentration of 1.38 mM are shown in Figure 4-7. Prior to irradiation, as shown in Figure 4-7 (a) the NMR spectrum consists of six sets of signals corresponding to the six sets of protons in the *trans* form. All signals in Figure 4-7 (a) were integrated to two protons which are equivalent, with the exception of the triplet signal **c** which were integrated to one proton equivalent, which was assigned to proton at position 4. The three doublet signals were assigned according to the shielding effect of the NH_2 group at position 10, protons at position 9/11 will resonate at the lowest frequency corresponding to signal **b**, followed by protons at position 8/12 corresponding to the signal **e**, followed by protons at position 2/6 corresponding to signal **f**. The second triplet signal **d** was assigned to protons at position 3/5. Finally, the singlet signal **a** was assigned to the protons of the amino group, its singlet nature indicating that the group is able to rotate freely on the NMR time-scale. The lack of any other significant signals in the 1D ^{1}H NMR spectrum of AAB

indicated that in the dark the molecule existed in only one isomeric form that was assigned to the *trans* configuration based on abundance.

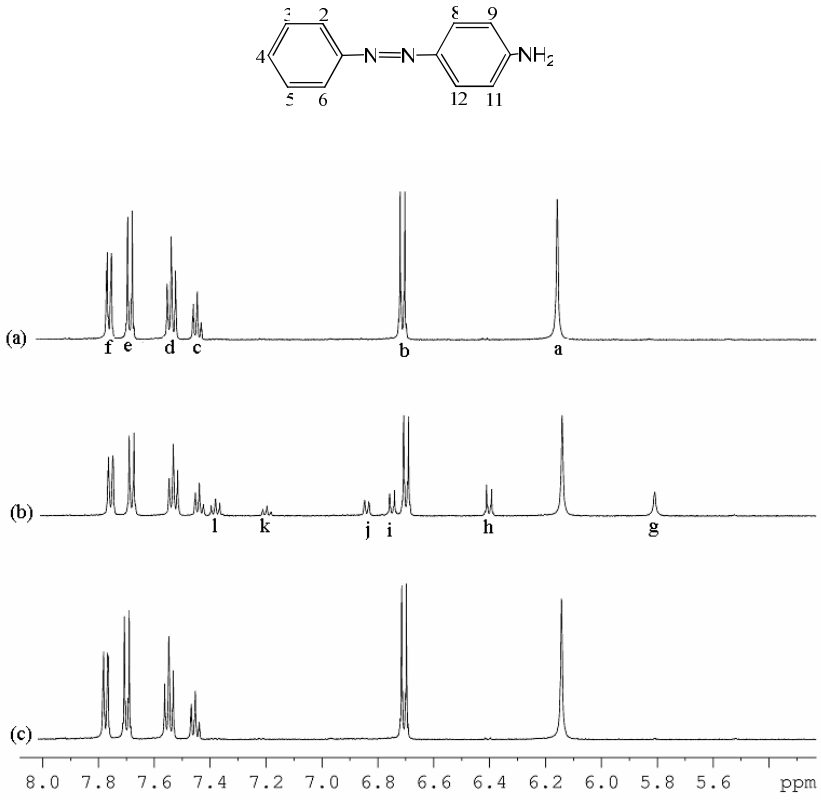

Figure 4-7 500 MHz 1D ^{1}H NMR spectra of AAB (1.38 mM) in d_6-DMSO (a) prior to irradiation, (b) at the 514 nm PSS, (c) after exposure of the PSS to darkness. TMS is the internal standard.

Irradiation of a 1.38 mM solution of AAB at 514 nm resulted in the appearance of a new set of signals as shown Figure 4-7 (b), which provides clear evidence of a photoinduced event. The disappearance of these new signals in darkness and restoration of the starting spectrum, Figure 4-7 (c), shows that the photoinduced event was thermally fully reversible, with no photodecomposition. These observations were interpreted as the occurrence of *trans-cis* isomerisation. According to the results obtained from the disperse dyes studied previously two pieces of information emerged; [7,8]

1. *Cis* isomer protons are consistently more shielded than their *trans* isomer counterparts.

2. Protons at position *ortho* to the azo linkage of the *trans* and *cis* isomers will resonate at significantly different positions, average $\Delta\delta$ ($=\delta_{cis}-\delta_{trans}$) = −1.24 and −1.07 ppm in benzene and cyclohexane, respectively.

The new set of signals labelled **g-l** in Figure 4-7 (b) consists of six signals and was assigned due to the *cis* isomer as follows; the two doublet signals **j** and **i** were close match the doublet signals corresponding to protons at positions 2/6 and 8/12 of the *trans* isomer, respectively, resulting in a change in a chemical shift of -0.94 ppm and of -0.93 ppm for protons 2/6 and protons 8/12, respectively, values that are similar in magnitude to the previous recorded average values. The doublet signal **h** was assigned to protons at position 9/11. The two triplets **l** and **k** were close matches to the triplets signals corresponding to the protons at positions 3/5 and 4 of the *trans* isomer. Thus signal **l** was assigned to protons 3/5 and signal at **k** was assigned to the proton at position 4. Finally, the singlet signal **g** was assigned to protons of the NH_2 group. A summary of the *trans* and *cis* proton resonance assignments of AAB and the corresponding $\Delta\delta$ values is provided in Table 4-2.

The NMR spectrum at the PSS for each azobenzene system was collected at 298 K and scanned by 32 to128 number of scan in order to obtain very clear signals, followed by accurate integration. The methods used for integration of signals were discussed in Section 2.2.2.1. Table 4-2 shows the composition of the photostationary state from the assignment NMR spectra method of AAB.

Deleted: p-aminoazobenzene

Trans signal	*Cis* signal	Proton assignment	$\Delta\delta$ / ppm
a	g	NH_2	-0.33
b	h	9/11	-0.30
c	k	4	-0.24
d	l	3/5	-0.15
e	i	8/12	-0.94
f	j	2/6	-0.93

Table 4-2 ^{1}H NMR assignments for the *trans* and *cis* isomers of AAB in d_6-DMSO, and the difference in chemical shift between *cis* and *trans* isomers, $\Delta\delta$. largest values of $\Delta\delta$ are highlighted.

Using the integrals of the *trans-cis* partner signals, the composition of the photostationary state at 514 nm was determined as 19 % *cis* and 81 % *trans* (Table 4-3). The values obtained are in good agreement with those from the kinetic data.

Position	Integral of signal		% *cis* at PSS
	Trans	*Cis*	
2/6	1.0000	0.1827	18.2
3/5	1.1488	0.21069	18.3
4	0.5193	0.11007	21.2
8/12	0.9791	0.18790	19.2
9/11	1.1931	0.21613	18.1
NH_2	1.2141	0.21594	17.8
Average % *cis* at PSS			19

Table 4-3 Photostationary state composition obtained using a number of the *cis-trans* signal pairs of AAB in d_6-DMSO at 298 K.

4.3 Experimental Procedures for Kinetic Measurements

Formatted: Bullets and Numbering

4.3.1 Obtaining Kinetic Data from NMR Spectra

A pseudo two-dimensional pulse programme was used to acquire the kinetic data presented in later sections. The F2 domain of the NMR spectrum was acquired as for a normal 1D spectrum using a presaturation pulse. The F1 domain was simply the time interval between successive 1D experiments. Changes in peak intensity as a function of time can be followed and the data extracted and fitted. Although this method is used primarily for t_1/t_2 relaxation experiments in NMR, this pulse programme is highly suitable for the kinetic experiments.[5]

Samples were prepared and allowed to stand in darkness overnight, the sample was kept in darkness until the optical fibre was attached to the NMR tube and the sample in the NMR probe, where an insignificant amount of light can reach it, ensuring that the *trans* isomer would be the only species present in the sample at the start of the experiment. However, this procedure in a few cases was not enough. Where there was a doubt that some of the *cis* isomer may be present in the sample, the temperature of the sample inside the NMR probe was increased to 323 or 333 K for an hour or two; then the sample was left to cool down to room temperature and the experiment started. An initial spectrum of this *trans* isomer was recorded and conditions for the pseudo 2D experiment optimised to bring about sufficient signal to noise in as short a time interval as possible. In monitoring the rise to the photostationary state, the first row of the data set, at t_0, was acquired in darkness. Upon completion of this scan, the laser shutter was opened allowing light to be delivered to the sample *via* the optical fibre, and the successive spectra of the sample undergoing irradiation

were recorded. Rows of the 2D data set were periodically extracted and compared until no further changes were observed, ensuring that the full photochemical process was recorded.

Following attainment of the photostationary state, the conditions were optimised and a high quality spectrum of the PSS recorded, prior to monitoring thermal decay of the *cis* isomer. The first row of the 2D spectrum was recorded under irradiation, at t_0, after which irradiation was terminated allowing the *cis* isomer to decay in darkness. Periodic monitoring of the decay was conducted until no further changes were observed, ensuring the full thermal decay process was recorded.

Each sample yielded two pseudo 2D data sets, one following the approach to the photostationary state, *i.e.* recording the rise of the *cis* isomer signals and the decay of the *trans* isomer signals, and the second following the thermal decay of the *cis* isomer to form 100% *trans*, *i.e.* recording the decay of the *cis* isomer and the rise of the *trans* isomer. Both data sets were processed in the same manner. The data were Fourier transformed in the F2 dimension only, F1 being the time dimension. The time interval is taken as the time that elapsed during the acquisition of each row. After the transformation of F2, the same phasing and baseline correction parameters were applied to each row of the data set. A 1D spectrum was extracted from the pseudo 2D file. *Trans* and *cis* signals were selected and the limits of integration for each peak defined. With these parameters defined, the Xwinnmr software was able to extract the integral for the same peak in all rows of the 2D spectrum, giving an output that was suitable for fitting by the appropriate mathematical function. The fitted functions and the fitting procedure are described in Section 4.4.

4.4 Processing the Kinetic Data

Formatted: Bullets and Numbering

4.4.1 The Kinetics of Isomerisation

The isomerisation of azobenzenes is represented as:

$$Trans \underset{k_{-1}(h\nu+\Delta)}{\overset{k_1(h\nu)}{\rightleftharpoons}} Cis$$ **Equation 4-1**

The interconversion of *trans* and *cis* isomers involves three processes: namely *trans*→*cis* photoisomerisation, *cis*→*trans* photoisomerisation and *cis*→*trans* thermal isomerisation. These are all first order kinetic processes. On irradiation the sample reaches the photostationary state, *i.e.* the equilibrium state between the *trans* and *cis* isomers, which can

be described by first order equilibrium kinetics. The time-dependence of the concentrations of *cis* and *trans* isomers are given by the Equation 4-2 and Equation 4-3:

$$\frac{[trans]_t - [trans]_{PSS}}{[trans]_0 - [trans]_{PSS}} = \exp^{\{-k_{PSS}t\}}$$ **Equation 4-2**

$$\frac{[cis]_t - [cis]_{PSS}}{[cis]_0 - [cis]_{PSS}} = \exp^{\{-k_{PSS}t\}}$$ **Equation 4-3**

where $[trans]_t$ is the concentration of the *trans* isomer at time t, $[trans]_{PSS}$ is the concentration of the *trans* isomer at the PSS, $[trans]_0$ is the initial concentration of the *trans* isomer, $[cis]_t$ is the concentration of the *cis* isomer at time t, $[cis]_{PSS}$ is the concentration of the *cis* isomer at the PSS, $[cis]_0$ is the initial concentration of the *cis* isomer and k_{PSS} is the rate constant for the approach to the PSS. Thus, k_{PSS} is the experimental parameter derived from fitting the data acquired from the pseudo 2D NMR spectra measured during irradiation of the sample, as described in Section 4.4.1.1. k_{PSS} is a sum of three separate rate constants as illustrated by the following equations. The deconstruction of this parameter into its components rate constants is discussed in Section 4.4.1.2.

$$k_{PSS} = k_1(h\nu) + k_{-1}(h\nu) + k_{-1}(\Delta)$$ **Equation 4-4**

Where $k_1(h\nu)$ is the rate constant for the photochemical isomerisation from *trans* to *cis*, $k_{-1}(h\nu)$ is the rate constants for the photochemical *cis* to *trans* isomerisation and $k_{-1}(\Delta)$ is the rate constant of the thermal *cis* to *trans* isomerisation.

When the irradiation is terminated, the photochemical process is ended and the *cis* isomer will thermally relax back to the *trans* form. The thermal relaxation of the *cis* isomer to the thermodynamically more stable *trans* form can be described by first order kinetics.[4,49,50,53,55,56,66,67] The time-dependence of the concentration of *cis* and *trans* isomers are given by the Equation 4-5 and Equation 4-6:

$$[cis]_t = [cis]_{PSS} \exp^{k_{-1}(\Delta)t}$$ **Equation 4-5**

$$[trans]_t = [trans]_{PSS} + [cis]_{PSS}\left(1 - \exp^{k_{-1}(\Delta)t}\right)$$ **Equation 4-6**

$k_{-1}(\Delta)$ is derived from the data acquired from the pseudo 2D NMR spectra recorded in darkness as the photostationary state reverts thermally to the *trans* isomer. The half-life, $t_{1/2}$ of the *cis* isomer is defined as:

$$t_{1/2} = \frac{\ln 2}{k_{-1}(\Delta)}$$ **Equation 4-7**

4.4.1.1 Fitting of Experimental Data

Formatted: Bullets and Numbering

The data were extracted from the pseudo 2D data sets for two separate data sets, one for the *trans* isomer integrals and one for the *cis* isomer integrals. Data were imported in Microsoft Excel. An iterative non-linear least square procedure was used to fit the data using the routine 'Solver' function. Data were fitted using integrated first order rate laws given in Equation 4-2, Equation 4-3, Equation 4-5, and Equation 4-6. The rate constants for the *trans* decay and *cis* rise in the approach to the PSS (Equation 4-2, and Equation 4-3, respectively) could be then compared to ensure that the data were in agreement. Similarly the rate constants of the *trans* rise and *cis* decay during the thermal reversal (Equation 4-5, and Equation 4-6, respectively) could be compared for the same reason. In all cases, the fitted functions well describe the experimental data, indicating the validity of the kinetic model.

Figure 4-8 and Figure 4-9 show typical experimental data and the corresponding fitted theoretical curves representing the change in concentration of the *trans* and *cis* isomers during the approach to the PSS and thermal reversal, respectively.

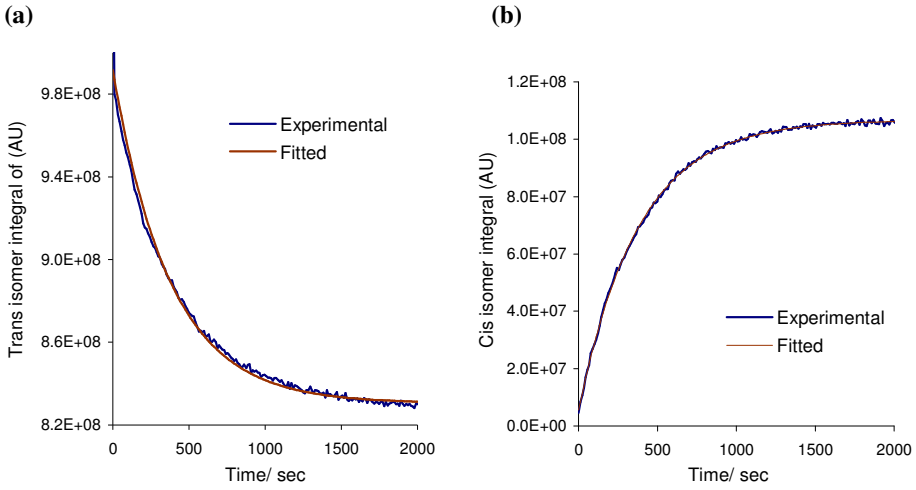

Figure 4-8 Time dependence of the concentration of (a) the *trans* isomer and (b) the *cis* isomer while approaching the PSS. The blue trace corresponds to the experimental data and the red trace corresponds to the fitted function.

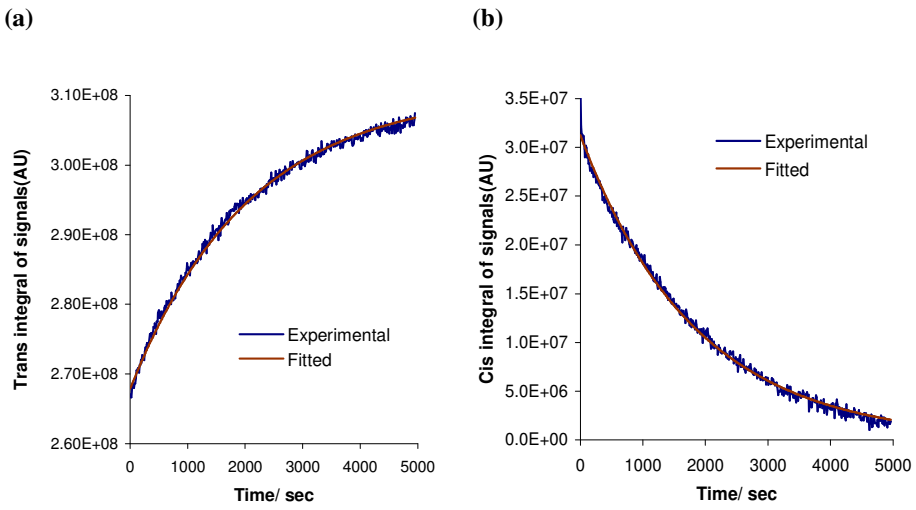

Figure 4-9 Time dependence of the concentration of (a) the *trans* isomer and (b) the *cis* isomer during darkness. The blue trace corresponds to the experimental data and the red trace corresponds to the fitted function.

Table 4-4 shows the fitted rate constants for AAB. It can be seen that the values obtained from fitting the time-dependence of the corresponding *trans* and *cis* signals are in good agreement. The rate constants reported in this chapter are the averages of the values obtained from the pairs of *trans* and *cis* data sets.

k_{PSS} / 10^{-4} s^{-1}		$k_{-1}(\Delta)$ / 10^{-4} s^{-1}	
Trans decay	*Cis* rise	*Trans* rise	*Cis* decay
26.33	24.12	0.950	1.006

Table 4-4 Rate constants obtained by fitting the experimental data for the approach to the PSS and thermal reversal for AAB at 298 K.

Formatted: Bullets and Numbering

4.4.1.2 Separating the Photochemical Rate Constant into its Components

Section 4.4.1 described the measurement of the total rate constant for the processes for attaining the photostationary state, k_{PSS}, and the rate constant of the thermal reversal, $k_{-1}(\Delta)$. We now consider how the component photochemical rates, $k_1(h\nu)$ and $k_{-1}(h\nu)$, can be extracted.

At the photostationary state an equilibrium state is attained, in which the *trans* and *cis* isomers exist in mixture of constant proportion defined by the equilibrium constant, K, as follows:

$$K = \frac{k_1}{k_{-1}(h\nu + \Delta)} = \frac{[cis]_{PSS}}{[trans]_{PSS}}$$ **Equation 4-8**

The composition of the PSS can be determined, as described in Section 4.4.1.3. Hence K can be obtained. The sum of the rate constants for both the thermal and photochemical *cis* to *trans* isomerisation, k_{-1}, is given by:

$$k_{-1}(h\nu + \Delta) = \frac{k_{PSS}}{K + 1}$$ **Equation 4-9**

The rate constant of the photochemical *cis* to *trans* isomerisation, k_{-1} (hν), is given by:

$$k_{-1}(h\nu) = k_{-1}(h\nu + \Delta) - k_{-1}(\Delta)$$ **Equation 4-10**

The rate constant of the photochemical *trans* to *cis* isomerisation, k_1 (hν), is given by:

$$k_1(h\nu) = k_{-1}(h\nu + \Delta)K$$ **Equation 4-11**

Thus, the rate constants for the three separate processes involved in this isomerisation, the composition of the PSS and the half life of the *cis* isomer can be obtained using the data acquired from the NMR spectra.

Continuing the analysis of AAB, the reported rate constants in Table 4-5 have been averaged to give two rate constants, from the NMR results presented in section 4.2.5, the fractional concentration of the *cis* isomer at the PSS was determined as being 19 %. This can be used to give an equilibrium constant, K, of 0.235. Table 4-5 shows the rate constants and half-life of the *cis* isomer. All data were processed in this manner to give the results presented in later sections.

k_{PSS} /10^{-4} s^{-1}	% *cis* at PSS	K	$k_{-1}(\Delta)$ / 10^{-4} s^{-1}	k_1 (hν) /10^{-4} s^{-1}	k_{-1} (hν) /10^{-4} s^{-1}	$t_{1/2}$ *cis* / s
25.23	19	0.235	0.978	4.79	19.46	7089

Table 4-5 Parameters used in separating k_{PSS} into component rate constants and the rate constants thus obtained for AAB at 298 K.

Formatted: Bullets and Numbering

4.4.1.3 Measurements of Photostationary State Composition

Under irradiation, a bulk azo sample will achieve a photostationary state, PSS, whose steady-state composition of *trans* and *cis* species is based upon the competition between photoisomerisation, in one or both directions and the thermal relaxation back into the *trans* form. Thus, the steady-state composition is unique to each system, depending upon the quantum yields of the photoisomerisation processes (Φ_{trans} and Φ_{cis}), and the thermal relaxation rate constant $k_{-1}(\Delta)$. The composition is affected by irradiation intensity, I, wavelength, λ_{irr}, temperature and the host matrix (be it solution, liquid crystal mixture, monolayer, polymer matrix, etc.).[2] The photostationary state composition was obtained using two methods:

1. From the kinetic data, using the fractional change in intensity of the *trans* isomer signal on reaching the PSS, as follows:

$$\%\ \text{cis at the PSS} = \frac{[trans]_0 - [trans]_{eq}}{[trans]_0} * 100 \qquad \textbf{Equation 4-12}$$

2. From the assignment of NMR spectra, by comparing the integrals for each pair of corresponding *cis* and *trans* signals. The errors associated with this procedure were minimized by averaging the fraction given by all available pairs of *cis-trans* signals; the application of this method for AAB is given in Section 4.2.5.

Formatted: Bullets and Numbering

4.4.1.4 Correction of Photochemical Rate Constants

The rate of the thermal reversal depends on the height of the potential energy barrier between the *cis* and *trans* isomers in the ground state and hence on the temperature at which the measurement is made. However, for the photochemical processes, the rates depend on two factors; the number of excited molecules and the quantum yield of isomerisation, Φ_{isom}, *i.e.* the fraction of the excited molecules that undergo isomerisation, which depends on the shape of the excited state and ground state potential energy surfaces.

The number of excited molecules depends on the number of photons available or in other words, the intensity of the irradiation, I. The number of excited molecules also depends on

the molar absorption coefficient of the molecule at the irradiation wavelength, ε. Thus, if two different azobenzenes have different molar absorption coefficients, then the rate of the processes will differ. For this reason it was necessary to determine the corrected photochemical rate constants, $k_1(h\nu)/\varepsilon_{trans}$ and $k_{-1}(h\nu)/\varepsilon_{cis}$, thus eliminating the influence of the varying molar absorption coefficients. The determination of the molar absorption coefficients of the *cis* isomer is described in the following section.

The resulting corrected photochemical rate constants, $k_1(h\nu)/\varepsilon_{trans}$ and $k_{-1}(h\nu)/\varepsilon_{cis}$, allow direct comparison of the quantum yield of photoisomerisation between different molecules and between both isomers of the same molecule, keeping in mind constancy of the intensity of irradiation thus at constant I:

$$\frac{k(h\nu)}{\varepsilon} \propto \phi_{iso} \qquad \textbf{Equation 4-13}$$

Formatted: Bullets and Numbering

4.4.1.4.1 Measurements of the Molar Absorption Coefficients of the *Cis* Isomer

It was impossible to measure the spectrum of the 100 % *cis* isomer, but the composition of the photostationary state for each molecule has been determined accurately by NMR spectroscopy. The procedure that was employed to measure the molar absorption coefficient of the *cis* isomer, *i.e.* ε_{cis}, was UV/Vis spectrometry of the samples at the PSS. To measure ε_{cis}, it is necessary first to determine the molar absorption coefficient of the sample at the PSS, ε_{PSS}. Since the spectrometer used to gather UV/Vis spectra did not allow *in situ* irradiation of the samples while the spectra were being collected, the cuvette containing the sample was irradiated *ex-situ* at the wavelength that was applied in the NMR experiment, λ_{irr}. After irradiation over a sufficient period of time to ensure the attainment of the PSS, the cuvette was immediately transferred to the UV/Vis spectrometer, and either a single wavelength absorption reading at the required wavelength, λ_{irr}, or a spectrum in the range of 200-600 nm was acquired depending on the longevity of the *cis* isomer, ε_{cis} using the following equation:

$$\varepsilon_{cis} = \frac{\varepsilon_{PSS} - (1-x)\varepsilon_{trans}}{x} \qquad \textbf{Equation 4-14}$$

Where x is the decimal fraction of *cis* isomer at the PSS. Applying Equation 4-14 to obtain the ε_{cis} is valid if the *cis* isomer is long-lived, since it can assumed that the samples could be transferred quickly enough between the irradiation source and the UV/Vis spectrometer to avoid thermal decay during the transportation process. But if the *cis* isomer is short-lived, this is the case of the *cis* isomers for MMY, DO3 and DR1 in benzene and NAB in DMSO ($t_{1/2}$ values of the *cis* isomers are 72, 216, 25 and 72 seconds, respectively), thermal decay

during the transportation process is unavoidable, thus applying the Equation 4-14 will produce incorrect values. Gibson used the thermal decay that has been determined from NMR experiments, and worked backwards from the molar absorption coefficient at time t seconds after the irradiation had been terminated, deriving the following equation to obtain ε_{cis} of the short-lived *cis* isomer.[5]

$$\varepsilon_{cis} = \frac{Abs_{PSS} - \varepsilon_{trans}\left([trans]_0 - [cis]_{PSS}\, e^{-k_{-1}(\Delta)t}\right)}{[cis]_{PSS}\, e^{-k_{-1}(\Delta)t}} \qquad \textbf{Equation 4-15}$$

Where Abs_{PSS} is the absorbance of the sample at the PSS at the wavelength under investigation, $[trans]_0$ is the initial concentration of the *trans* isomer before irradiation, $[cis]_{PSS}$ is the concentration of the *cis* isomer at the PSS, $k_{-1}(\Delta)$ is the thermal *cis*-to-*trans* isomerisation rate constant and the time is t at which the irradiation is terminated.

Where the thermal decay of the *cis* isomer was of sufficient length, a scan of wavelength was performed to examining the spectrum of the irradiated species rather than a single point. In all cases, as expected for these systems, a bleaching of the sample was apparent at the wavelength of maximum absorption, λ_{max}. This is expected since $\lambda_{max}(cis)$ is unlikely to be equal to $\lambda_{max}(trans)$, leading to the reduction of ε_{PSS} at λ_{max} as observed in the UV/Vis spectrum of MMY shown in Figure 4-10.

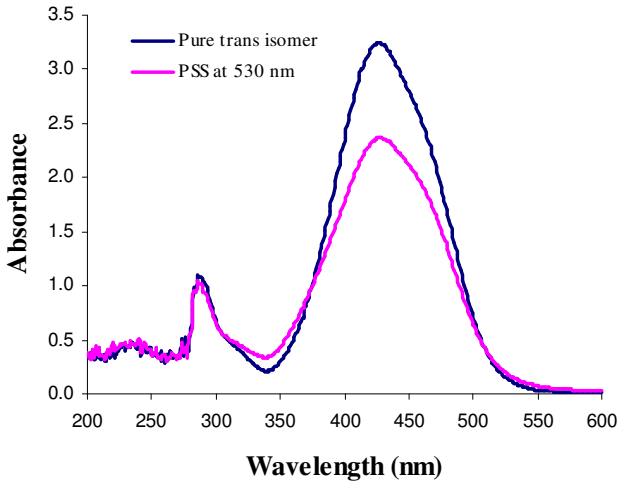

Figure 4-10 UV/Vis spectra of MMY in DMSO solution; pure *trans* form and PSS after irradiation at 530 nm. $t_{1/2}$ (*cis*) = 1.3 hr.

Table 4-6 Molar absorption coefficients for the *trans* and *cis* isomers in benzene (regular font) and DMSO (bold font). * Unobtainable. Highlighted font represents the molecules with large proportions of *cis* isomers at the PSS.

Molecule/structure	Molar absorption coefficient, ε_{trans} / $mol^{-1}lcm^{-1}$	Molar absorption coefficient, ε_{cis} / $mol^{-1}lcm^{-1}$
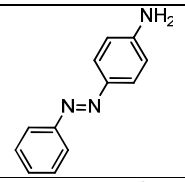 AAB	278	1395
	1088	**225**
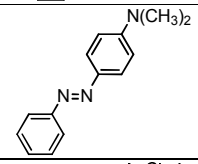 MY	561	355
	1126	**3102**
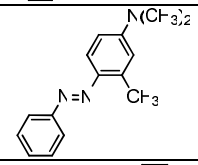 MMY	654	6356
	1241	**1855**
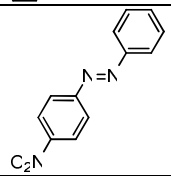 NAB	819	986
	1248	**8253**
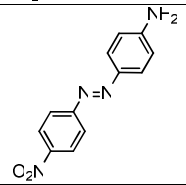 DO3	831	1353
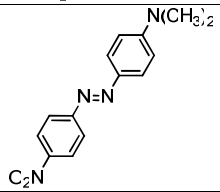 DMNAB	611	*
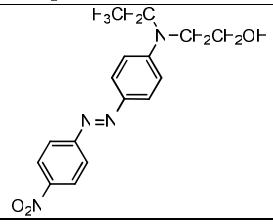 DR1	1163	*

The molar absorption coefficient of the *cis* isomer, ε_{cis}, have been obtained (experimental details for obtaining these values are in Section 3.4.2), and are presented together with the ε_{trans} value in Table 4-6. The molar absorption coefficient of the *cis* isomer for DR1 was not obtained because the *cis* isomer is considered in this study as extremely short-lived ($t_{1/2}$ = 25 seconds) and thus the *cis* would isomerise to the pure *trans* form during the transportation process.

In some molecules, there is insignificant difference between ε_{cis} and ε_{trans}. At the same time, it is clear that some of the molecules do exhibit a significant change in ε. The implication of the differing *trans* and *cis* molar absorption coefficients at λ_{irr} has been discussed previously in term of its effect on the photokinetic factor, F (see next paragraph for more detail about F), and consequently on the kinetic data.[5] Gibson concluded that in his work the effect on the time-dependent photokinetic factor due to the difference in the molar absorption coefficients of the *trans* and *cis* isomer can be neglected due to the relatively small percentage of *cis* isomer present in the irradiated sample. As shown below, the same conclusion can be drawn for the present work. The validity of neglecting the photokinetic factor is supported by the fact that the kinetic data are well described by simple first order kinetics.

Consider the simple case where species A photochemically converts to form species B.

$$A \xrightarrow{h\nu} B$$

The rate law of this photochemical reaction is reliant upon the quantum yield, the photon flux, the concentration of the photosensitive substrate and the photokinetic factor. The photokinetic factor, F, is used to correct the other terms when defining the rate and is by Equation 4-16, where Abs is the total absorbance of the solution.

$$F = \frac{1-10^{-Abs}}{Abs} \qquad \textbf{Equation 4-16}$$

If the absorbance of the solution changes over a period of time, *i.e.* $\varepsilon_A \neq \varepsilon_B$ at λ_{irr}, then F will be time dependent. Equation 4-17 may be used too described the rate of the reaction, assuming F remains constant. In this term, I_0 is the total intensity of light, $\phi_{A\rightarrow B}$ is the quantum yield for conversion of A to B, and ε_A is the molar absorption coefficient of species A.

$$\frac{-d[A]}{dt} = I_0 F \phi_{A \to B} \varepsilon_A [A]$$ **Equation 4-17**

In system where no difference is apparent in the molar absorption coefficients of the initial and final species, the *cis* and *trans* species in the case of this work, the photokinetic factor will not be a time –dependent and therefore a standard treatment of the kinetic data can be undertaken.[5]

The value of the photokinetic was calculated at t = 0 and PSS to determine if the difference in the molar absorption coefficients of the *cis* and *trans* isomers results in a significant change in F during the course of irradiation, using Equation 4-18 (the derivation of which is detailed in Gibson's thesis).[5]

$$F = \frac{1 - 10^{-((\varepsilon_{trans} - \varepsilon_{cis})[trans] + \varepsilon_{cis}[trans]_0)}}{((\varepsilon_{trans} - \varepsilon_{cis})[trans] + \varepsilon_{cis}[trans]_0)}$$ **Equation 4-18**

For AAB in benzene, the photokinetic factor changes from 2.230 at 100% *trans* to a PSS value of 2.180. Even in the most extreme case of change between ε_{trans} and ε_{cis} at λ_{irr}, seen in molecule NAB in DMSO, the photokinetic factor changes from 2.001 at 100% *trans* to a PSS value of 1.926. This small change in F can thus be assumed to have no significant impact on the kinetic treatment used for these azobenzenes. For MY and MMY in DMSO there are a significantly large percentages of the *cis* isomer in the PSS, 58% *cis* isomer at the PSS for both molecules, for MY the photokinetic factor changes significantly from 2.028 at 100% *trans* to a PSS value of 1.793. However, the kinetic data for this molecule were described well by the first-order model. For MMY, the photokinetic factor changes very little, from 2.003 at 100% *trans* to a PSS value of 1.927, due to the small difference between the molar absorption coefficients of the two isomers. Thus MY in DMSO is the only case that has significant change in the photokinetic factor due to the presence of large percentage of the *cis* isomer at the PSS combined with a significant difference between the molar absorption coefficients of the two isomers. However, since the kinetic data can be well fitted with the first-order model, the results will be tentatively included.

4.4.2 Reproducibility of the Data

This study involved a comparison between the kinetic parameters of the different azobenzenes. It was therefore important to determine how reproducible the experiments were. While every effort was made to ensure experimental parameters were kept constant,

the position of the fibre in the NMR sample tube was highlighted as the most likely cause of a significant systematic error. The experiments for the kinetic analysis were all carried out with the fibre positioned below the surface of the NMR sample, at the top edge of the detection volume (see Section 3.3.2). The error associated with the position of the fibre was estimated to be ±0.5 mm, this equates to variation in the transmission, at 2 mm inside the detection volume, of ± 9 %.[4]

To asses the reproducibility of the data, the isomerisation of one of the azobenzenes, at 298 K was carried out several times. Both the approach to the PSS and the thermal reversal were included in the study. Under constant absorption conditions, MY in cyclohexane requires a concentration of 3.19 mM at an irradiation wavelength of 514 nm. The error in the concentration of the NMR samples was regarded as negligible compared to that associated with the position of the fibre, so the same sample was used for each irradiation. At the end of the reverse process, the sample/fibre arrangement was removed from the NMR probe and the sample was detached from the fibre optic. The sample was then reattached to the fibre, the laser power at fibre output was checked and the experiment was repeated. Five sets of data were recorded. All integral data were extracted and analysed in an identical manner. The rate constants derived from the five runs are displayed in Table 4-7.

Run	k_{PSS} / 10^{-4} s^{-1} *Trans* decay	k_{PSS} / 10^{-4} s^{-1} *Cis* rise	$k_{-1}(\Delta)$ / 10^{-4} s^{-1} *Trans* rise	$k_{-1}(\Delta)$ / 10^{-4} s^{-1} *Cis* decay
1	26.7	26.3	4.8	5.5
2	28.2	25.8	5.4	5.7
3	34.2	26.8	5.3	5.7
4	32.2	22.8	5.3	5.9
5	22.8	35.1	5.0	5.7

Table 4-7 Rate constants of MY in cyclohexane derived from 5 irradiations of the approach to the PSS, k_{PSS}, and the thermal reversal, $k_{-1}(\Delta)$ at 298 K.

From the results presented in Table 4-7, it is clear that the irradiation experiments are reproducible, with only a small amount of spread in the data. The standard deviation was calculated separately for the approach to the PSS and the thermal reversal. Since the *trans* and *cis* data give estimates of the same parameters, and should be consistent, all ten estimates were included in the calculations. For the approach to the PSS, the standard deviation was calculated to be 4.37 x 10^{-4} s^{-1} or 16%. For the thermal reversal the standard deviation was calculated to be 3.27 x 10^{-5} s^{-1} or 6%. As expected the standard deviation for the approach to the PSS is greater than that of the thermal reversal, reflecting the additional

error due to the uncertainty in the fibre position. The error in measuring peak integrals for both isomers and relating them to equilibrium constant K was propagated into this error, the estimated error in K was estimated at 6%[5] leading to an overall 17% error in the photoisomerisation rate constants.

4.5 Activation Parameters of the Thermal *Cis-Trans* Isomerisation

In the derivation of Transition State Theory it is assumed that the reactants and transition state are in equilibrium. Statistical mechanics then is used to calculate the concentration of the transition state. This concentration is used, along with the rate at which the transition state proceeds to the product, to give a rate constant for the reaction. The ability to measure activation parameters gives us information about the manner in which the transformation to the transition state occurs, or in other words the kinds of structural changes that are occurring, the entropy changes, and the changes in solvation. The activation parameters are also the numerical values that give the relative energies of the reactants and transition state. Both the Arrhenius and Eyring Equations (Sections 2.8, and Section 2.9) were used to derive the activation parameters of the thermal *cis-trans* isomerisation of the studied azobenzenes. The Arrhenius equation is presented by Equation 4-19

$$\ln k_{-1}(\Delta) = \ln A - \frac{E_a}{RT}$$ **Equation 4-19**

Where $k_{-1}(\Delta)$ is the thermal rate constant, R is the universal gas constant with a value of 8.314 $JK^{-1}mol^{-1}$, T is the temperature in Kelvin, A is the steric factor and assumed to be constant over the temperature range studied and E_a is the activation energy. A straight line plot of lnk *vs.* 1/ T allows E_a to be calculated from the slope and A from the point of intercept with the y axis at x = 0.

Alternatively, the activation energy for a process can be studied using transition state theory. The rate constant is defined by Equation 4-20

$$\ln k = \ln \frac{k_B T}{h} + \ln K^{\#}$$ **Equation 4-20**

Where k_B is the Boltzmann constant, h is Plank's constant, T is the temperature in Kelvin, and $K^{\#}$ is the equilibrium constant between the transition state and the reactant. The equilibrium constant is related to the Gibbs free energy, $\Delta G^{\#}$, as presented by Equation 4-21:

$$\Delta G^{\#} = -RT \ln K^{\#}$$ **Equation 4-21**

This, in turn is related to the activation enthalpy and entropy, $\Delta H^{\#}$ and $\Delta S^{\#}$, as represented by Equation 4-22

$$\Delta G^{\#} = \Delta H^{\#} - T\Delta S^{\#}$$ **Equation 4-22**

According to the Equation 4-21 and Equation 4-22, Equation 4-20 could be written in the form called the Eyring equation, represented by Equation 4-23:

$$\ln\frac{k_{-1}(\Delta)}{T} = \frac{-\Delta H^{\#}}{RT} + \ln\frac{k_B}{h} + \frac{\Delta S^{\#}}{R}$$ **Equation 4-23**

A plot of $\ln(k_{-1}(\Delta) / T)$ *vs.* 1/ T allows $\Delta H^{\#}$ to be derived from the slope and $\Delta S^{\#}$ from the point of intercept with the y axis. From these two values the Gibbs free energy of activation could be calculated from the relation stated in Equation 4-22.

The pioneering experiments using NMR coupled with *in situ* laser irradiation in the investigation of the activation parameters of the thermal *cis*-t*o*-*trans* isomerisation were performed on a series of yellow azo dyes.[5] The excellent fit of the data to the Arrhenius and Eyring equations suggested that this method is ideal for determining thermal energy barriers.

4.5.1 Experimental Conditions

Thermal isomerisation in the azobenzenes was monitored at gradually elevated temperatures. The low temperature limit was the freezing point of DMSO, and the upper limit was determined by the rate of the *cis* isomer decay and whether this could be detected within the technique's sensitivity limit.

Fast isomerisation was studied at low temperatures, while slower processes were studied over a wider temperature range. The number of experiments performed was in the range 4-9, incremented by 2-10 K. The number of experiments performed was sufficient to obtain a good fit, with a sufficient amount of time allowed for the irradiated sample to relax to the new temperature between successive experiments. The applied temperatures were in the range 286-328 K, as summarised in Table 4-8.

Table 4-8 The applied temperatures in the measurements of the activation parameters of the thermal isomerisation of azobenzenes in benzene (regular font) and in basic DMSO (bold font) solutions.

Molecule/structure	Temperature / K
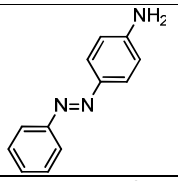 AAB	298,308,318,328
	298,301,305,310
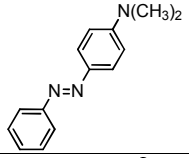 MY	288,298,308,318
	298,303,308,313
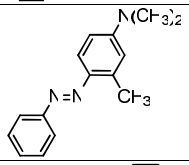 MMY	286,288,293,298
	298,308,318,328
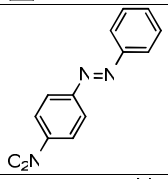 NAB	298,308,318,328
	293,298,303,308
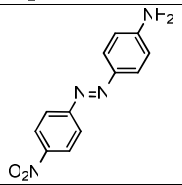 DO3	290,292,295,296,298, 303,305,310,312
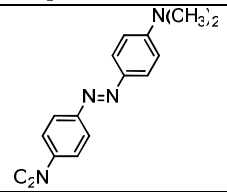 DMNAB	288,293,298,303
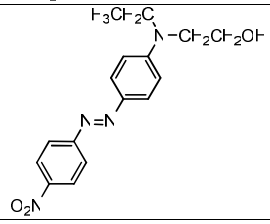 DR1	288,290,292,294,296,298

4.6 Results and Discussions

In this section the kinetic parameters obtained for the azobenzenes studied are presented and interpreted.

4.6.1 Photostationary State Composition

For the series of azobenzenes studied, at various irradiation wavelengths, the composition of the photostationary state ranged from 4-58 % *cis* isomer, as summarised in Table 4-9. Previously reported values obtained from the same experimental technique,[7] are also shown in Table 4.9. The general observation from this table is that there is a noticeable difference in the PSS composition for the eight azobenzenes. Values reported in the literature from UV/Vis measurements[28-30] are mainly for shorter irradiation wavelengths than those used here, but the following are in good agreement with the present results: DR1 > 31% *cis* at 450 nm in methylcyclohexane[68]; MY 68% *cis* at 460 nm in benzene.[25] A marked decrease in the proportion of the *cis* isomer at longer wavelength is observed, reflecting the increase in the relative absorption strength of the *cis* isomer at these wavelengths. At 568 nm in benzene, DO3 shows the least *cis* isomer (4% *cis*).The most *cis* isomer (58% *cis*) is found for MY and MMY at 514 and 530 nm in basic DMSO, respectively. For DO3, there is a marked difference in the PSS composition between irradiation at 530 nm (12% *cis*) and irradiation at longer wavelength at 568 nm (4% *cis*).

Molecule/structure	Percentage of the *cis* isomer at the PSS / %				
	300 /nm	457 /nm	514 /nm	530 /nm	568 /nm
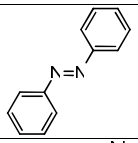 AB	*41*	25[a]	–	–	–
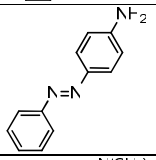 AAB	–	–	18	–	–
	–	–	**19**	–	–
	–	–	*28*	–	–
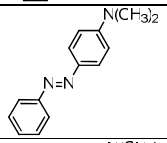 MY	–	66[a]	24	22[a]	–
	–	–	**58**	–	–
	–	–	*47*	–	–
	–	–	***15***	–	–
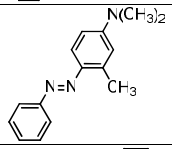 MMY	–	–	–	11	–
	–	–	–	**58**	–
	–	–	–	*13*	–
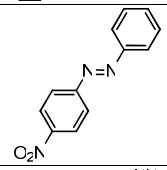 NAB	–	–	12	–	–
	–	–	**5**	–	–
	–	–	*21*	–	–
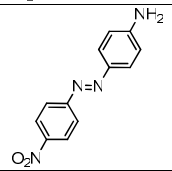 DO3	–	44[a]	–	12 18[a]	4
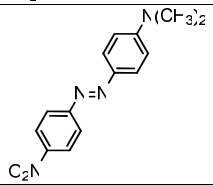 DMNAB	–	–	–	–	8
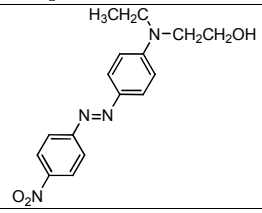 DR1	–	46[a]	–	–	10 12[a]

Table 4-9 the percentage of the *cis* isomer at the photostationary state in benzene (regular font), in basic DMSO (bold font), in protic DMSO (italics font), and in cyclohexane solutions (italics and bold font) at 298 K. [a]From reference[7] for 10 mM solution in benzene at 30 mW laser power.

At different wavelengths the ratio of absorption coefficients for the *cis* and *trans* isomers will differ, changing the ratio of isomers at the PSS. This means that the *cis* isomer of DO3 has a lower absorption coefficient at 530 nm than at 568 nm. Thus, upon irradiation at 568 nm, the possibility of switching from *cis* to *trans* is greater than at 530 nm.

There is a significant difference in the PSS composition for irradiation at a specific wavelength between solutions in different solvents, especially in the case of MMY. The percentages of *cis* are 11% in benzene and 58% in basic DMSO solution. MMY also shows the most significant difference in the PSS composition at a specific wavelength between DMSO solutions of different pH. The percentages of *cis* are 58% and 13% in basic and protic DMSO, respectively. This is consistent with the enhancement of *cis* to *trans* thermal isomerisation by protonation.

4.6.2 Rate Constants for Photo- and Thermal Isomerisation

Table 4-10 displays the rate constants for the photochemical *trans* to *cis* process, $k_1(h\nu)$, the photochemical *cis* to *trans* process, $k_{-1}(h\nu)$, and the thermal *cis* to *trans* process, $k_{-1}(\Delta)$, for all molecules in the series. Also displayed are the half lives of the *cis* isomers at the PSS obtained from $k_{-1}(\Delta)$.

Table 4-10[iii] The photochemical and thermal rate constants of *cis*↔*trans* isomerisation in benzene (regular font) and in DMSO (bold font) at 298 K. † *Via* UV/Vis absorption spectroscopy in toluene (regular font) and protic DMSO (bold font) solution. * Unobtainable. [a] standard deviation = 17%, [b] standard deviation = 6% for NMR data.

Molecule/ structure	[a]$k_1(h\nu)$ / 10^{-5} s^{-1}	[a]$k_1(h\nu)/\varepsilon^{irr}_{trans}$ / 10^{-7} s^{-1} M cm	[a]$k_{-1}(h\nu)$ / 10^{-5} s^{-1}	[a]$k_{-1}(h\nu)/\varepsilon_{cis}$ / 10^{-7} s^{-1} M cm	[b]$k_{-1}(\Delta)$ / 10^{-5} s^{-1}	[b]$t_{1/2}$ *Cis* /s
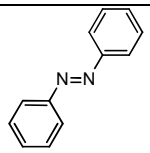 AB†	*	*	*	*	0.2	$4.3x10^5$
	*	*	*	*	**0.6**	**$1.2x10^5$**
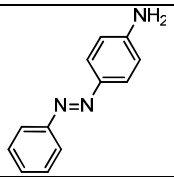	13	4.6	53	3.8	5.1	$1.4x10^5$
	48	**4.4**	**195**	**86.5**	**9.8**	**$7.1x10^3$**

[iii] Table 4-10: continued overleaf

AAB						
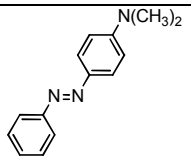 MY	73	13.1	223	62.8	9.8	$7.1x10^3$
	239	**21.2**	**169**	**5.4**	**3.9**	**$1.8x10^4$**
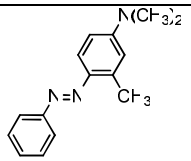 MMY	200	30.6	747	11.8	958.5	72
	359	**28.9**	**245**	**13.2**	**15.0**	**$4.6x10^3$**
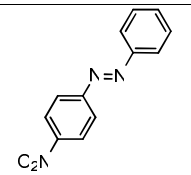 NAB	43	5.3	307	31.1	10.2	$6.8x10^3$
	235	**18.8**	**3496**	**42.4**	**959.1**	**72**
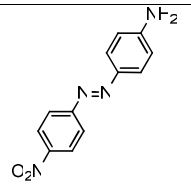 DO3	172	20.7	941	69.6	320.2	4
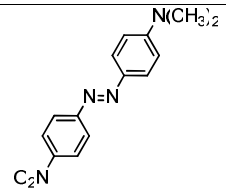 DMNAB	450	73.7	4026	*	1149.3	60
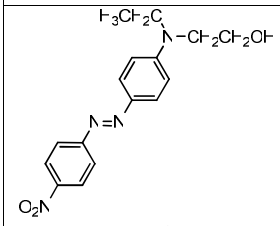 DR1	1260	108.3	8582	*	2757.4	25

For the photochemical rate constants the standard deviation is estimated to be 17% and for the thermal rate constants 6%, as discussed in Section 4.4.2. The parameters $k_1(h\nu)/\varepsilon_{trans}^{irr}$ and $k_{-1}(h\nu)/\varepsilon_{cis}$ for the *trans* and *cis* isomers of each molecule are included in Table 4-10. Quoting these parameters for $k_1(h\nu)$ and $k_{-1}(h\nu)$ eliminates the influence of varying molar absorption coefficients, and allow direct comparison of the quantum yield of photoisomerisation

between different molecules (where the same irradiation intensity has been used) and between both isomers of the same molecule, Section 4.4.1.4.

The standard deviation in ε is negligible in comparison to that of $k_1(h\nu)$ and $k_{-1}(h\nu)$. Therefore the standard deviation of 17% also applies to $k_1(h\nu)/\varepsilon^{irr}_{trans}$ and $k_{-1}(h\nu)/\varepsilon_{cis}$. The most significant observation to make concerning the values presented in Table 4-10 is the significant variation in the photo- and thermal rates with structural diversity and solvent polarity. A detailed discussion of the rate constants pertaining to the photo-and thermal isomerisation of these molecules will now follow, to explore the possible relationship between the kinetic behaviour and molecular structure on the one hand and on the other hand the solvent polarity.

4.6.3 Photochemical and Thermal Contribution to k_{-1}

On approach to the PSS, k_{-1} is composed of a thermal and a photochemical contribution, $k_{-1}(\Delta)$ and $k_{-1}(h\nu)$. Table 4-11 shows whether the thermal or photochemical route is dominant under the present experimental conditions. The implication of this is concerned with the dependence of the PSS composition on the intensity of irradiation. If k_1 and k_{-1} are both photochemically driven, the PSS will be independent of intensity. This is because k_1 and k_{-1} will both be equally affected by changes in intensity, leaving the PSS only dependent on the wavelength of irradiation. However, if k_{-1} contains a significant thermal contribution, the PSS will become dependent on the intensity since changes in $[k_{-1}(h\nu)+k_{-1}(\Delta)]$ with increasing intensity will differ from changes in $k_1(h\nu)$. In addition to this, if k_{-1} contains a significant thermal contribution, the PSS will also depend on temperature.

In Table 4-11, only MMY in benzene can be highlighted as having a greater thermal contribution than the photochemical: $k_{-1}(\Delta)$ is 959 x 10^{-5} s^{-1} whereas $k_{-1}(h\nu)$ is 747 x 10^{-5} s^{-1}. Therefore, for this molecule the PSS is dependent on the intensity of irradiation and temperature as well as the wavelength of irradiation. For all other molecules in the study k_{-1} is dominated by $k_{-1}(h\nu)$. The most extreme case of this is found for MY in DMSO where $k_{-1}(\Delta)$ is 3.9 x 10^{-5} s^{-1} and $k_{-1}(h\nu)$ is 169 x 10^{-5} s^{-1} a difference of a factor of 43, in the other cases it ranges from 3 to 30.

Molecule/ structure	$k_{-1}(h\nu)$ / 10^{-5} s^{-1}	$k_{-1}(\Delta)$ / 10^{-5} s^{-1}
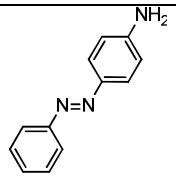 AAB	53	5
	195	**10**
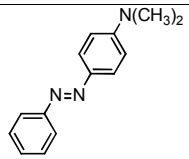 MY	223	10
	169	**4**
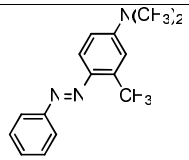 MMY	747	959
	245	**15**
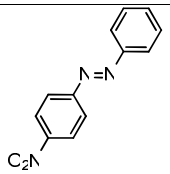 NAB	307	10
	3496	**959**
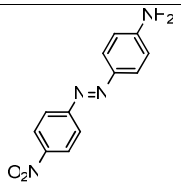 DO3	941	320
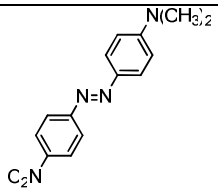 DMNAB	4026	1150
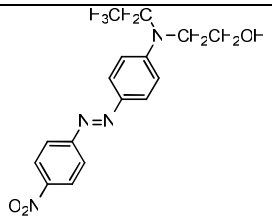 DR1	8582	2757

Table 4-11 The photo- and thermal rate constants of the *cis*-to-*trans* isomerisation, demonstrating their contribution to k_{-1} in benzene (regular font) and in basic DMSO (bold font). Highlighted font represents the case where the thermal contribution governs k_{-1}.

4.6.4 The Kinetics of Photoisomerisation

Formatted: Bullets and Numbering

4.6.4.1 Relating Photoisomerisation Rate Constants to the Quantum Yields

After correcting the photochemical rate constants with the molar absorption coefficients of the *trans* and *cis* isomers, cross-comparison of the two values k_1/ε_{trans} and $k_{-1}/\ \varepsilon_{cis}$ becomes applicable, since these are directly related to the quantum yields for photochemical *trans*-to-*cis* and *cis*-to-*trans* isomerisation, $\phi_{trans\rightarrow cis}$ and $\phi_{cis\rightarrow trans}$. Adopting the convention used by Gibson,[5] these values are expressed as relative quantum yields, $\phi^{rel}_{trans\rightarrow cis}$ and $\phi^{rel}_{cis\rightarrow trans}$, normalised to the to largest observed $k(h\upsilon)/\varepsilon$ value in this study, *i.e.* $k_1(h\upsilon)/\varepsilon_{trans}$ for Disperse Red 1 in benzene. From this point onwards, discussion of photochemical data will be in terms of these relative quantum yields, as listed in Table 4-12.

Comparison will be made between the molecules that were irradiated at the same wavelength and intensity. According to this the molecules will be grouped into three groups: group 1 (molecules irradiated at 514 nm, laser power of 3 mW) contains AAB, MY and NAB, group 2 (molecules irradiated at 530 nm, laser power of 30 mW) contains MMY and DO3, and group 3 (molecules irradiated at 568 nm, laser power of 20 mW) contains DMNAB and DR1.

Molecule/ structure	$k_1(h\nu)/\varepsilon_t^{irr}$ /10^{-7} s^{-1}Mcm	$\phi_{t\to c}^{rel}$	$k_{-1}(h\nu)/\varepsilon_c$ /10^{-7} s^{-1}Mcm	$\phi_{c\to t}^{rel}$	$\phi_{t\to c}^{rel}/\phi_{c\to t}^{rel}$
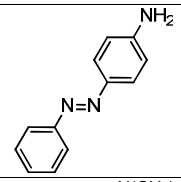 AAB	4.6	0.04	3.8	0.04	1.00
	4.4	**0.04**	**86.5**	**0.80**	**0.05**
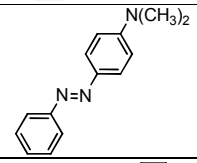 MY	13.1	0.12	62.8	0.58	0.21
	21.2	**0.20**	**5.4**	**0.05**	**3.89**
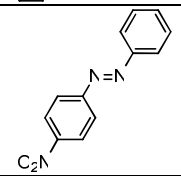 NAB	5.3	0.05	31.1	0.29	0.17
	18.8	**0.17**	**42.4**	**0.39**	**0.44**
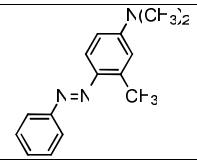 MMY	30.6	0.28	11.8	0.11	2.61
	28.9	**0.27**	**13.2**	**0.12**	**2.19**
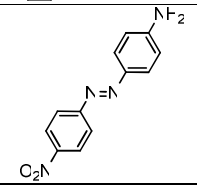 DO3	20.7	0.19	69.6	0.64	0.30
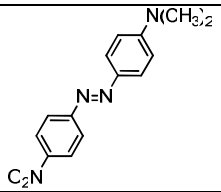 DMNAB	73.7	0.68	*	*	*
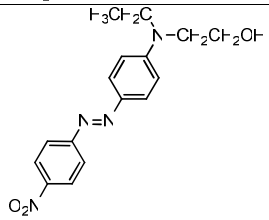 DR1	108.3	1.00	*	*	*

Table 4-12 Relative quantum yield values for the *cis* and *trans* isomers of each molecule in benzene (regular font) and in basic DMSO (bold font). Quantum yields are relative to that

for *trans* to *cis* isomerisation of DR1 $\varepsilon^{irr}_{trans}$ (highlighted).* Unobtainable. Grouped according to the irradiation intensity.

Formatted: Bullets and Numbering

4.6.4.2 Effect of Structural Change and Solvent on *Cis-Trans* Photoisomerisation

It is initially worth considering the relative quantum yields presented in Table 4-12. If photoisomerisation is the only decay channel for the excited state, and *trans-cis* and *cis-trans* isomerisation proceed *via* the same transition state (TS), then $\phi_{trans\rightarrow cis} + \phi_{cis\rightarrow trans} = 1$. Without a method of directly determining absolute quantum yields, only ϕ^{rel}_{isom} in each isomerisation direction is available. However, if $\phi_{trans\rightarrow cis} + \phi_{cis\rightarrow trans} = 1$, then an increase in $\phi^{rel}_{trans\rightarrow cis}$ must be accompanied by a decrease in $\phi^{rel}_{cis\rightarrow trans}$. In the case of this study, $\phi_{trans\rightarrow cis} + \phi_{cis\rightarrow trans}$ will equal a constant if the absolute quantum yields for photoisomerisation sums to unity. This is clearly not the case on varying structural diversity or solvent polarity, so *trans-cis* and *cis-trans* isomerisation must proceed *via* different transition states. Of course this assumption relies upon the assumption that no other decay routes are available to the excited molecules.

To interpret ϕ^{rel}_{isom} values requires a knowledge of the ground and excited state potential energy surfaces (PES). Given the complexity of the molecules studied, even calculation of the potential energy curves along a single reaction coordinate would be extremely time-consuming. Performing calculations to this extent and for excited state transition state structures of the molecules studied was outside the scope of this work.

It is clear from examining the relative quantum yields presented in Table 4-12 that structural diversity and solvent polarity lead to a large degree of variation in the values, ranging from 0.035 to 1.000. Therefore, the excited state reaction coordinate is influenced to a large degree by modifying the structure and by the polarity of solvent. In benzene the general observation is that 3 of the 5 molecules under comparison demonstrate $\phi^{rel}_{trans\rightarrow cis} < \phi^{rel}_{cis\rightarrow trans}$ with the exceptions of AAB and MMY, where the relative quantum yields have identical values or opposite trend, respectively. On the other hand, in DMSO the 4 molecules for which values are available demonstrate no general trend, *i.e.* the relative quantum yields for the *trans→cis* isomerisation are smaller than that of *cis→trans* isomerisation in two cases and larger in the other two cases. Although no information is available for the ground and excited state PES, it is possible to infer some conclusions from

these facts. At the instant a molecule undergoes irradiation the ground state (GS) structure is projected onto the excited state PES, and can be described as the Franck-Condon (FC) geometry for each isomer. After this, the molecular geometry will change until it reaches a transition state (local minimum) close to the FC geometry. The transition state accessed by excitation to the FC geometry, followed by relaxation, will hereafter be labelled *cis*-TS and *trans*-TS for the respective *cis* and *trans* isomers. To illustrate this principle, Figure 4-11 gives a simple representation of the reaction coordinate *vs.* energy for the expected species.

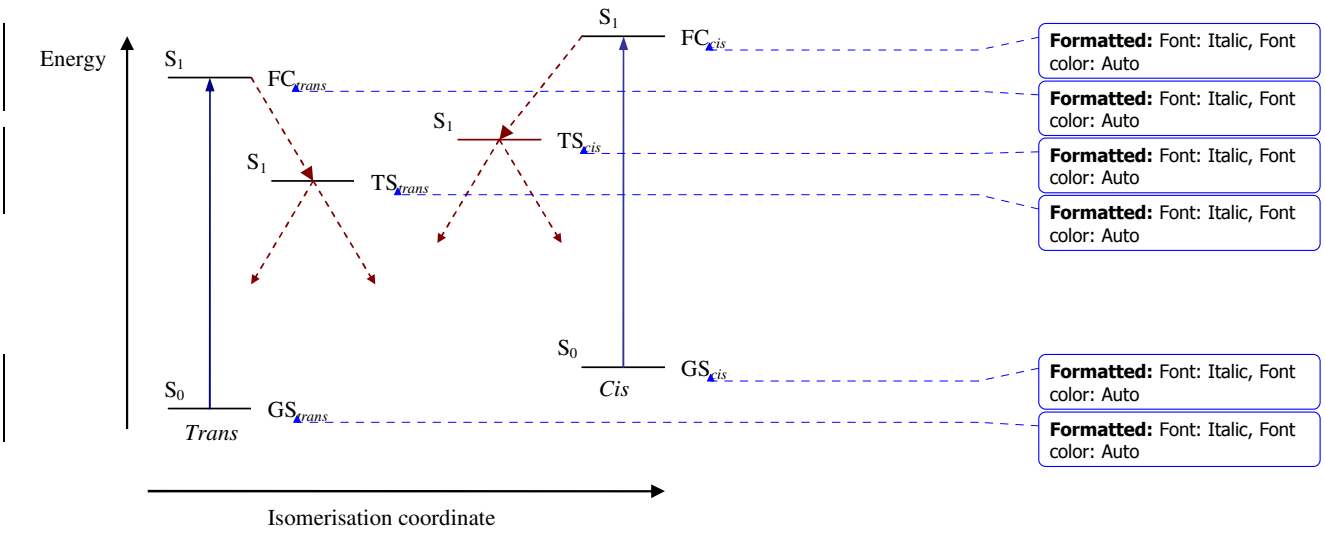

Figure 4-11 Simple representation of the isomerisation coordinate, where GS = Ground State, FC = Franck-Condon state, and TS = Transition State. Two separate excited state structures, TS_{trans} and TS_{cis}, are shown. Quoted from refrence.[5]

Figure 4-11 can be used to help understand other observations in ϕ_{isom}^{rel}. In benzene, azobenzene derivatives show an increase in both of the relative quantum yields when modified from electron donating azobenzenes into electron acceptor azobenzenes or when the ability of electron donating group is increased. This indicates that the geometry of both *trans*-TS and *cis*-TS is more similar to the Franck-Condon geometry for the respective isomer in the electron donating azobenzenes and in weaker *p*-electron donating azobenzenes.

The effects of solvent interaction on the electronic states of the azo molecules are evident from their UV/Vis absorption spectra. When the absorption spectra are measured in solvents of different polarity, it is found that the position and intensity of the absorption bands are modified by these solvents. These changes are due to physical intermolecular solute-solvent

interactions, which alter the energy difference between ground and exited states. More investigation of photochemical rates under the structural and solvent effects is undertaken in the sections that follow.

Deleted: [Gibson ref]

Formatted: Bullets and Numbering

4.6.4.2.1 Effect of *p*-Electron Donating Substituents

AAB and MY on one hand, and on the other hand DMNAB and DR1 are compared here to explore the effect of increasing the donating ability of the *p*-electron donating substituent. The data for these azobenzenes is presented in Table 4-13.

Molecule/ structure	$\phi^{rel}_{trans\rightarrow cis}$	$\phi^{rel}_{cis\rightarrow trans}$
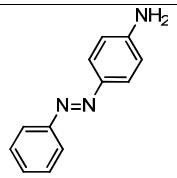 AAB	0.04	0.04
	0.04	**0.80**
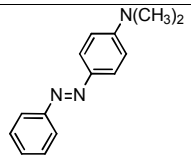 MY	0.12	0.58
	0.20	**0.05**
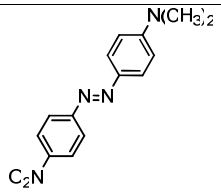 DMNAB	0.68	*
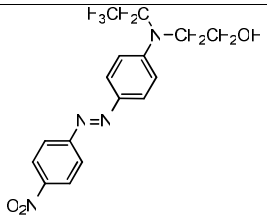 DR1	1.00	*

Table 4-13 Relative quantum yields for the photoisomers of AAB, MY, DMNAB, and DR1 in benzene (regular font) and basic DMSO (bold font).

In benzene, both pairs of molecules show increasing values of the relative quantum yields for *trans-cis* photoisomerisation, $\phi^{rel}_{trans\rightarrow cis}$, with increasing electron donating ability of the *p*-amino group. There is also an increase in the relative quantum yield for *cis-trans*

photoisomerisation, $\phi^{rel}_{cis\rightarrow trans}$, on going from AAB to MY. In DMSO, results are only available for AAB and MY and here an increase in $\phi^{rel}_{trans\rightarrow cis}$ is also seen with increasing electron donating power, but there is a decrease in $\phi^{rel}_{cis\rightarrow trans}$. Referring once more to Figure 4-11, in benzene *trans*-TS and *cis*-TS geometries of azobenzenes of weaker electron donating ability must resemble their respective Franck-Condon excited state geometries more than azobenzene with stronger electron donating ability. In other words, the possibility of switching from the *cis*-to-*trans* isomer and from *trans*-to-*cis* isomer in molecules with *p*-electron–donating group of stronger ability of donation, *i.e.* MY and DR1, is greater than the same type of molecules with weaker electron donating substituents, *i.e.* AAB and DMNAB. Thus, the TS structures in MY and DR1 will show greater differences from the FC geometries than AAB and DMNAB, allowing a greater number of isomerisation events to occur leading to the elevated ϕ^{rel}_{isom} values.

$\phi^{rel}_{trans\rightarrow cis}$ values for AAB are identical in benzene and DMSO solutions, whereas $\phi^{rel}_{cis\rightarrow trans}$ values increase in DMSO by a factor of approximately 20. For MY, $\phi^{rel}_{trans\rightarrow cis}$ is also relatively little affected by polar solvation, but $\phi^{rel}_{cis\rightarrow trans}$ decreases significantly, by a factor of 12, upon changing the solvent from benzene to DMSO. The simple interpretation is that the polarity of the solvent appears to change the structure of *cis* TS to a certain extent, moving it closer to or farther from the *cis* ground state. The nature of the *trans* TS is influenced to a lesser degree by the presence of the polar solvent. Examining the UV/Vis absorption spectra for the four molecules, Figure 4-12, indicates that a bathochromic shift is observed due to increase the electron donating ability of the electron-donating group, a clear indication that the excited state electronic structure of AAB differs from that of MY. In addition in DMSO a change in ε_{max} at λ_{max} was observed. A further indication that the polarity of the solvent influences the excited state electronic structure for the two molecules. For DMNAB and DR1, the UV/Vis absorption spectra of the two molecules indicate there is no shift in the position of the absorption band, but the change in ε_{max} at λ_{max} to smaller value for DR1 is observed.

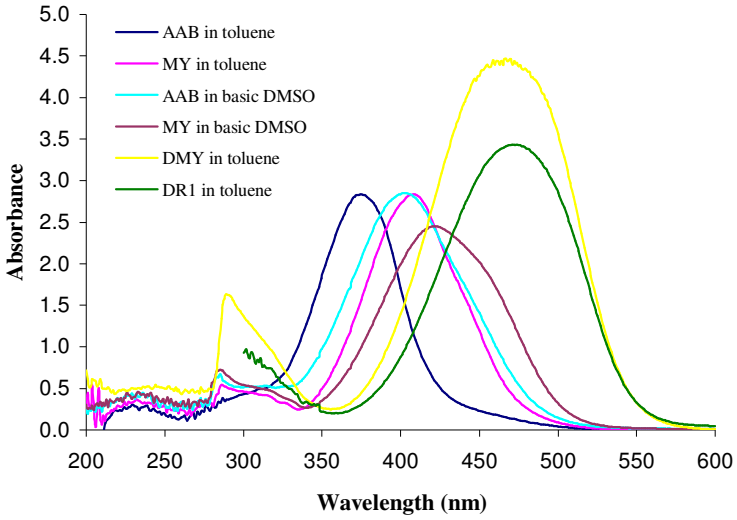

Figure 4-12 UV/Vis absorption spectrum of the *trans* isomers of 0.1 mM AAB, MY, DMNAB, and DR1 in toluene and basic DMSO.

Formatted: Bullets and Numbering

4.6.4.2.2 Comparison of Push/Pull Substituent Effects

Table 4-14 displays the photochemical rates of AAB and NAB; it demonstrates the effect of structural changes and solvent between azobenzenes substituted by *p*-donor (push) and *p*-acceptor (pull).

In benzene, comparison of *p*-electron donating azobenzene and *p*-electron acceptor azobenzene shows $\phi^{rel}_{trans\rightarrow cis}$ to be approximately 1.3x greater in the *p*-electron acceptor azobenzene, and $\phi^{rel}_{cis\rightarrow trans}$ 7.3x greater. Hence, the *trans*-TS and *cis*-TS structures are closer to their respective ground state starting geometries in *p*-electron donor than those with *p*-electron accepting azobenzenes. For the *p*-electron acceptor azobenzenes there is greater likelihood that the *cis*-TS will relax to *trans*-GS, and vice versa, hence giving a greater chance of isomerisation after photon absorption. In DMSO, the comparison shows the increase in $\phi^{rel}_{trans\rightarrow cis}$ is more pronounced and an approximate 4.3x increase in *p*-electron acceptor is observed. While $\phi^{rel}_{cis\rightarrow trans}$ is 2.1x smaller in *p*-electron acceptor molecules. Evidently the conversion from *p*-electron donating to *p*-electron acceptor group in this solvent is important for altering the photochemical properties of the azobenzene.

Deleted: conversion from p-electron donating to p-electron acceptor group are

Molecule/ structure	$\phi^{rel}_{trans \rightarrow cis}$	$\phi^{rel}_{cis \rightarrow trans}$
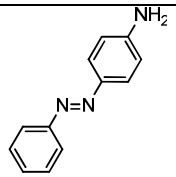 AAB	0.04	0.04
	0.04	**0.80**
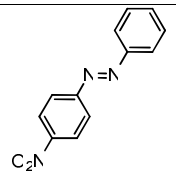 NAB	0.05	0.29
	0.17	**0.39**

Table 4-14 Rates of isomerisation for photoisomers of *p*-donor and *p*-accepter azobenzenes in benzene (regular font) and DMSO (bold font).

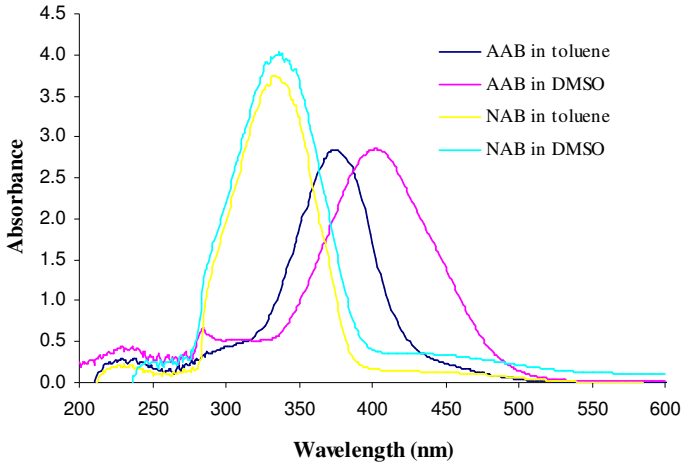

Figure 4-13 UV/Vis absorption spectrum of *trans* isomer of 0.1 mM AAB and NAB in toluene and DMSO solutions.

Examination the UV/Vis spectra of the two azobenzenes presented in Figure 4-13 shows two important points; a significant hypsochromic shift in the spectrum of *p*-acceptor azobenzene, a clear indication that the excited state electronic structure of the NAB differs from the AAB. A significant reduction in ε_{max} at λ_{max} and a significant variation in the molar absorption coefficients of the *trans* and *cis* isomer at λ_{irr}, with major deviation between the *trans* and *cis* isomers (refer to Table 4-12). A significant change in the observed kinetics is therefore not an unexpected observation.

4.6.5 The Kinetics of Thermal *Cis-Trans* Isomerisation

Formatted: Bullets and Numbering

Table 4-15[iv] displays the rate constants for the thermal *cis* to *trans* process, $k_{-1}(\Delta)$, for all molecules in the series, also displayed the half life of the *cis* isomer at the PSS obtained from $k_{-1}(\Delta)$. The standard deviation for the thermal rate constants is estimated to be 6%, as concluded in Section 4.4.2.

Molecule/ structure	$k_{-1}(\Delta)$ / 10^{-5} s^{-1}	$t_{1/2}$ *Cis* /s
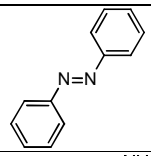 AB†	0.2	$4.3x10^5$
	0.6	**$1.2x10^5$**
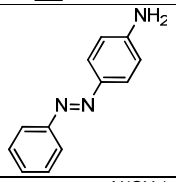 AAB	5.1	$1.4x10^4$
	9.8	**$7.1x10^3$**
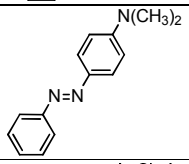 MY	9.8	$7.1x10^3$
	3.9	**$1.8x10^4$**
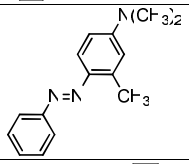 MMY	958.5	72
	15.0	**$4.6 x10^3$**
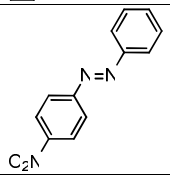 NAB	10.2	$6.8 x10^3$
	959.1	**72**
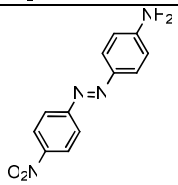 DO3	320.2	4
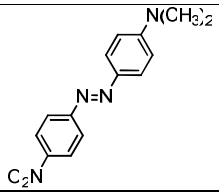 DMNAB	1150.0	60

[iv] Table 4-15: continued overleaf

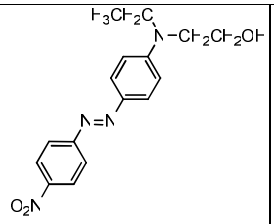 DR1	2757.4	25

Table 4-15 Rate constants of the *cis→trans* thermal isomerisation in benzene (regular font), and in DMSO (bold font) at 298 K. † *Via* UV/Vis absorption spectroscopy in toluene and protic DMSO solution. Standard deviation (NMR data) = 6%.

For AB, the kinetic data for the thermal *cis-trans* isomerisation in two solvents, namely toluene and protic DMSO, was obtained *via* UV/Vis absorption spectroscopy. Details of the experimental procedure are in Section 3.4.2.1. Figure 4-14 gives the UV/Vis absorption spectra in the dark and at the PSS at 300 nm for AB in toluene as an example.

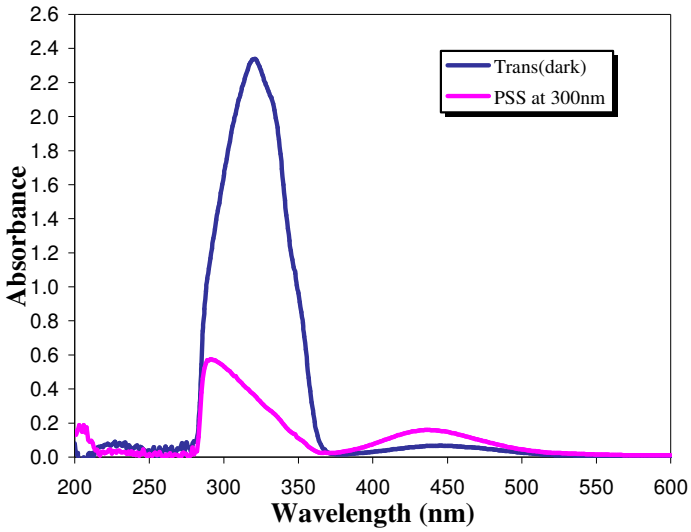

Figure 4-14 UV/Vis spectrum of AB in toluene before (*trans* isomer) and after (PSS) UV irradiation at 298 K.

The thermal *cis*-to-*trans* isomerisation was calculated by monitoring the absorption change near the absorption maximum of the *trans* isomer over a sufficient period of time. Figure 4-15. The process is first order, as shown by the linear plot of $\ln(A_\infty - A_t)$ versus time t, Figure 4-16, Where A_∞ at t = ∞ matches the absorbance of the sample before irradiation.

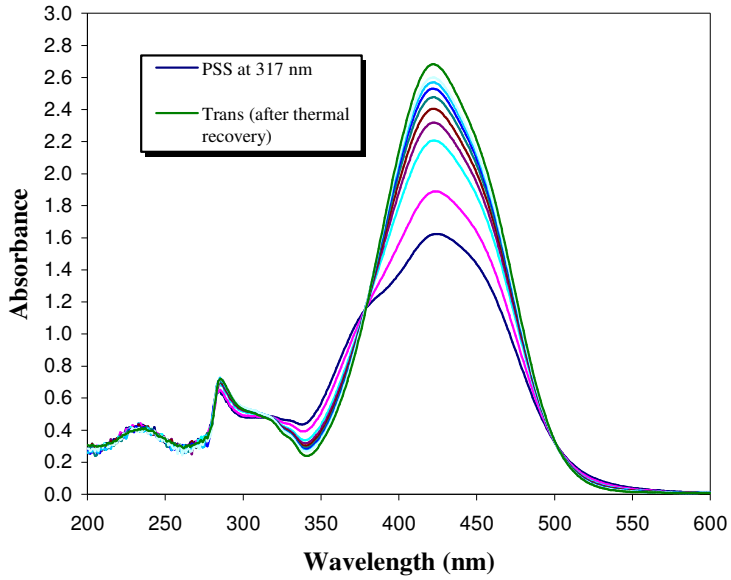

Figure 4-15 Spectra obtained as a function of time on irradiation of AB at 298 K in protic DMSO; for clarity selected spectra are presented.

The thermal rate constants, $k_{-1}(\Delta)$, of AB along with the corresponding values obtained *via* NMR spectroscopy are collected in Table 4-15.

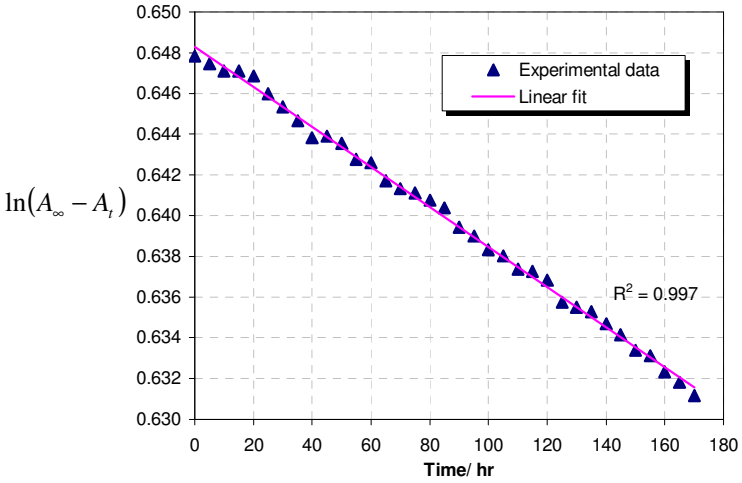

Figure 4-16 First-order kinetics of the *cis*-to-*trans* thermal relaxation of AB in toluene.

In contrast to the photochemical rates, kinetic data for the thermal *cis* isomer decay show more dependence upon molecular structure and solvent polarity. Some simple observation

can be made before an in depth analysis of structural diversity and solvent polarity effects is undertaken. Generally *para*-substitutions invariably accelerate the thermal rate, regardless of the nature of the substituent. For *para*-donor/*para*-Acceptor substituted (push-pull) azobenzenes, which have the potential for significant intramolecular charge-transfer through the presence of donor and acceptor groups in a conjugative relationship, the rate is much more rapid than for *para*-donor (push) or *para*-acceptor (pull) substituted azobenzenes. Furthermore, introduction of a methyl group *ortho* to the azo bond at the donating electron side in MMY increases the rate relative to the equivalent structure without such group (MY).

For the parent compound the thermal rate constants, $k_{-1}(\Delta)$, at 298K from the present work in two solvents, namely toluene and DMSO , and from literature in three solvents, namely hexane, chlorobenzene and *o*-dichlorobenzene at 293 K,[53] are summarised in Table 4-16. Table 4-16 shows that the solvent polarity plays a significant role in determining the thermal *cis* decay, since in general the rate becomes significantly faster as the solvent polarity increased.

Deleted: [Asano *et al.* 1981]

Solvent	Hexane[a]	Toluene	Chlorobenzene[a]	*o*-Dichlorobenzene[a]	DMSO
Dielectric constant	2.0	2.4	5.6	7.5	48
$k_{-1}(\Delta)/ 10^{-5}$ s^{-1}	0.3	0.2	1.8	10.3	11.3
$t_{1/2}$ / h	77	120	11	2	1.7

Table 4-16 Thermal rate constants of *cis-trans* isomerisation and half-lives of the *cis* isomers of AB. [a] from reference.[53]

For MY comparison between the present kinetic data and the available literature[67] at 298 K indicates that the thermal rate constant in benzene is greater by a factor of 3 than that from literature in cyclohexane. Again in more polar solvent the thermal *cis* decay increases (the dielectric constants of cyclohexane and benzene are 2.00 and 2.28, respectively). The magnitude of the increase in rate suggests that the polarisability of benzene also plays a role.

The thermal *cis* isomer decay of DO3 in benzene is in good agreement with literature[69] approximately identical values were obtained. The values of the thermal rate constants for DR1 in this work and literature[64] in solvents of similar properties, *i.e.* solvents of similar dielectric constant values are quite in good agreement. Where, this work gives $k_{-1}(\Delta) = 276 \times 10^{-4}$ s^{-1} in benzene, the literature[64] gives $k_{-1}(\Delta) = 350 \times 10^{-4}$ s^{-1} in toluene. For DMNAB, the thermal rate constants are 115×10^{-4} s^{-1} and 200×10^{-4} s^{-1} in benzene from the present study and refrence[50], respectively.

Formatted: Bullets and Numbering

Deleted: [Poprawa-Smoluch *et al.* 2006]

Deleted: in

Formatted: Not Highlight

Deleted: [Wildes *et al.* 1971]

4.6.5.1 Effect of Protonation on the Thermal Rates in DMSO Solutions

Sanchez *et al.*[58,59,70] used UV/Vis absorption spectroscopy and reported systematic studies of the acid catalysis observed for the *cis*-to-*trans* thermal isomerisation of a series of electron donating and electron donor-acceptor azobenzenes. They concluded that the protonated azo compounds isomerise thermally at much faster rate than the unprotonated compound, due to existence of azonium–ammonium tautomerisation in acidic or proton donor medium as described in Section 4.1. The present results are in total agreement with this observation, as can be seen from Table 4-17. In protic DMSO the thermal reversal is much more rapid than in basic DMSO solution. The increases were by a factor of 8, 10 and 143 for AAB, MY and MMY, respectively.

Molecule/ structure	$k_{-1}(\Delta)$ / 10^{-5} s^{-1}	$t_{1/2}$ *Cis* /s
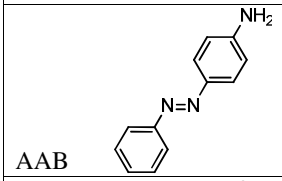 AAB	9.8	$7.1x10^3$
	77.4	**$9.0x10^2$**
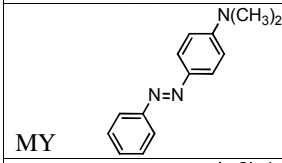 MY	3.9	$1.8x10^4$
	40.4	**$1.7x10^3$**
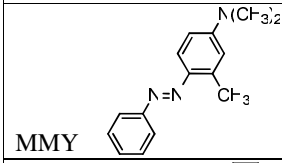 MMY	15.0	$4.6x10^3$
	2157.5	**32**
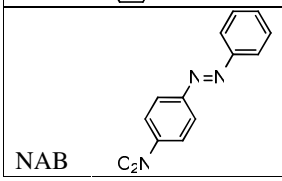 NAB	959.1	72
	10.2	**$6.4x10^3$**

Table 4-17 The thermal rate constants of *cis→trans* isomerisation in basic DMSO (regular font) and in protic DMSO (bold figures) at 298 K, demonstrating the effect of pH of DMSO solutions.

NAB shows exception from the last observation, where adding base to DMSO solution results in a significant increase and not decrease in the thermal rate by a factor of 88. To the best of the author's knowledge there are no previous results on the effect of protonation on the thermal rate of azobenzenes substituted with electron acceptor groups. The correlation

between faster thermal rates and hydrogen-bond donor (HBD) medium was recorded for push-pull azobenzene.[55] The present result suggests that in protonated NAB the proton does not reside on the azo group and, moreover, that protonation of the molecule inhibits isomerisation. The present work contains only one example of azobenzene substituted with an electron drawing group, thus it is unsuitable to generalize the result.

The kinetic measurements of the thermal isomerisation of DO3 and DR1 in DMSO were unobtainable. Applying the constant absorption condition for these two azobenzenes results in required concentrations of 0.42 and 0.12 mM at 568 nm, respectively. At these low concentrations, the signal to noise ratio was small, even with large number of scans. It was found to be impossible to detect any *cis* isomer and the obtained NMR spectra recorded after the laser irradiation consists only of pure *trans* isomer, even at low temperatures used to retard the *cis* conversion to the *trans* isomer. This suggests that the fraction of *cis* isomer at the PSS is less than 1%, as a result of rapid thermal isomerisation of these molecules in polar solvent.

4.6.5.2 Effects of Structural Changes and Solvent Polarity on the Rate of Thermal Isomerisation

Formatted: Bullets and Numbering

Detailed analysis of the thermal rates relating to each of the contrasting structures in each solvent is conducted in the following sections.

4.6.5.2.1 Comparison of *p*-Electron Donating Azobenzenes Kinetics

Formatted: Bullets and Numbering

The data for these azobenzenes along with that of the parent azobenzene are presented in Table 4-18. In comparison with the AB in benzene, an approximate 31 and 61-fold increase is observed in the thermal decay rate constant, $k_{-1}(\Delta)$, for AAB and MY, respectively. The change in $k_{-1}(\Delta)$ after structural modification of the parent molecule is distinct and must be attributed to a modification of the π electron structure of the molecule. The presence of the electron donating group at the *para* position is clearly instrumental in changing the ground state electronic structure of the molecule, shortening the *cis* isomer life-time. An approximately two-fold increase is observed in $k_{-1}(\Delta)$ following the conversion of the electron donating group (NH_2) in AAB to the group of stronger ability of donation ($N(CH_3)_2$) in MY. In DMSO solutions the opposite trend is observed, *i.e.* an approximate three-fold decrease in $k_{-1}(\Delta)$. The decrease in the thermal rate in DMSO solutions suggests that the polarity of the solvent plays a significant role in determining the rate of the thermal isomerisation.

Molecule/ structure	$k_{-1}(\Delta)$ / 10^{-5} s^{-1}	$t_{1/2}$ *Cis* / s
AB[a] 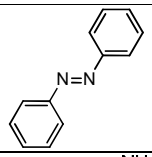	0.2	$4.3x10^5$
AAB 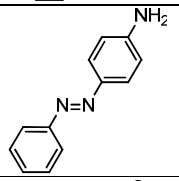	5.1	$1.4x10^4$
	9.8	**$7.1x10^3$**
MY 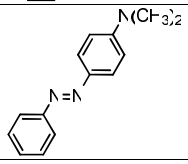	9.8	$7.1x10^3$
	3.9	**$1.8x10^4$**
DMNAB 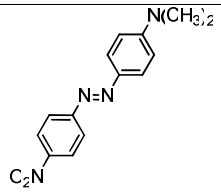	1149.3	60
DR1 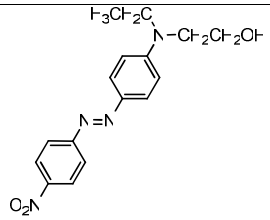	2757.4	25

Table 4-18 Rate constants and half-lives of thermal *cis-trans* isomerisation for the parent azobenzene and for *p*-electron donating azobenzenes in benzene (regular font) and in DMSO (bold font). [a] From reference.[71] DMSO solutions are basic.

Comparison between the DMNAB and DR1 in benzene, shows an approximate two-fold increase is observed in $k_{-1}(\Delta)$, following the modification of the electron donating group (NH_2) in DMNAB with ($N(CH_2CH_2OH)$ (CH_2CH_3)) in DR1, further evidence for effect of this structural modification on the thermal isomerisation rate.

4.6.5.2.2 Effect of *o*-Methyl Substituent on a *p*-Electron Donating Azobenzenes

Formatted: Bullets and Numbering

Data for these azobenzenes are presented in Table 4-19. In benzene a significant increase by a factor of 98 is seen in $k_{-1}(\Delta)$ when a methyl group is placed in the *o*-position at the electron donating side, namely for MMY compared to MY. This acceleration in the thermal

decay becomes less significant in polar solvent, where in DMSO the thermal rate increases only by a factor of four.

Molecule/ structure	$k_{-1}(\Delta)$ / 10^{-5} s^{-1}	$t_{1/2}$ *Cis* / s
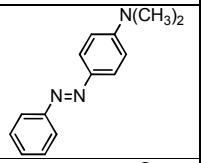 MY	9.8	$7.1x10^3$
	3.9	**$1.8x10^4$**
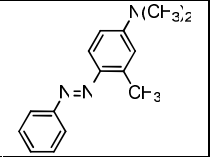 MMY	958.5	72
	15.0	**$4.6x10^3$**

Table 4-19 Rate constants and half-lives of thermal *cis-trans* isomerisation for MY and MMY in benzene (regular font) and in DMSO (bold font).

The observed acceleration in $k_{-1}(\Delta)$ due to this structural change is consistent with a previous observation.[48] However, the observed acceleration in cyclohexane at 308 and 313 K was by a factor of three, slightly less significant than the present observation in DMSO and much less than that in benzene. This indicates that effect of the interaction between the solvent and solute is determined not only by the solvent polarity but also whether it is aromatic or aliphatic.

Deleted: [ref Nishimura, yamanaka, imai 1976]

4.6.5.2.3 Comparison of Push/Pull Azobenzenes

Table 4-20 displays the thermal rates for two molecules of push (electron donating substituent) and pull (electron acceptor substituent) type, and three molecules of push-pull (electron donating and electron-acceptor substituents in 4 and 4' positions of the phenyl rings) type. For the mono-substituted molecules, the thermal rates increased significantly if the *p*-substitution is an electron acceptor group rather than an electron donating group, an approximate 2-fold increase in benzene. Moreover, the increase in the thermal rate becomes more significant in DMSO, where an approximate 98-fold increase is observed. The observed significant increase in $k_{-1}(\Delta)$ in DMSO solutions indicates the role that the solvent plays in determining the rate is important. For the push-pull molecules, a significant increase in the thermal rate, $k_{-1}(\Delta)$, with increasing the electron donating capability of amino group is observed in benzene with increasing the electron donating capability of amino group is observed, an approximate four- and nine-fold increase in $k_{-1}(\Delta)$ for DMNAB and DR1, respectively, compared to that of DO3.

Molecule/ structure	$k_{-1}(\Delta)$ / 10^{-5} s^{-1}	$t_{1/2}$ *Cis* / s
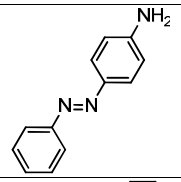 AAB	5.1	$1.4x10^4$
	9.8	**$7.1x10^3$**
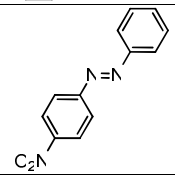 NAB	10.2	$6.8x10^3$
	959.1	**72**
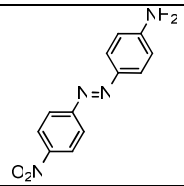 DO3	320.2	4
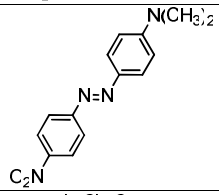 DMNAB	1149.3	60
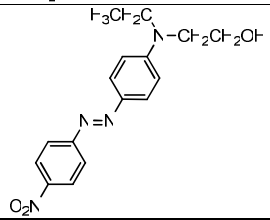 DR1	2757.4	25

Table 4-20 Rate constants and half-lives of thermal *cis-trans* isomerisation for push/pull azobenzenes in benzene (regular font) and in DMSO (bold font).

Formatted: Bullets and Numbering

4.6.5.2.4 Effect of the *p*-Nitro Substituent

Table 4-21 shows the thermal rates in benzene of AB and NAB on one hand, and MY and DMNAB on the other hand, to demonstrate the effect of addition of a nitro group. The thermal rate is significantly increase by a factor of 63 and 117, respectively, leading to an accelerated conversion of *cis* back to the more stable *trans* geometry. It is interesting that such a change in the molecule can introduce an enormous increase in the rate of thermal decay. Clearly this structural change is influential on the shape of the ground state potential energy surface.

Molecule/structure	$k_{-1}(\Delta)$ / 10^{-5} s^{-1}	$t_{1/2}$ *Cis* / s
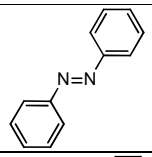 AB[a]	0.2	$4.3x10^5$
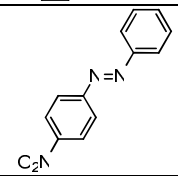 NAB	10.2	$6.8x10^3$
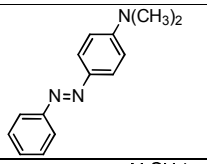 MY	9.8	$7.1x10^3$
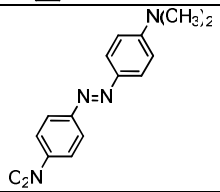 DMNAB	1149.3	60

Table 4-21 Rate constants and half-lives of thermal *cis-trans* isomerisation for AB, NAB, MY and DMNAB in benzene. [a] From reference.[71]

Formatted: Heading 3, No bullets or numbering

4.6.6 Temperature Dependence of the Thermal *Cis* Isomer Decay

In this section a detailed analysis and discussion of the temperature dependence of the thermal *cis* isomer decay is undertaken. The activation parameters for each molecule in two solvents, namely benzene and DMSO are summarised in Table 4-22. Table 4-22 displays the thermal rate constant, $k_{-1}(\Delta)$, the activation energies, E_a, activation enthalpy, $\Delta H^{\#}$, activation entropy, $\Delta S^{\#}$, and Gibbs free energy of activation, $\Delta G^{\#}$, for each molecule in the series.

Previous studies have reported the activation energies of thermal *cis-trans* isomerisation to range from 35 to over 100 kJ/mol.[50,53,67,72] The studies additionally display high sensitivity of these activation energies to the solvent environment. The available temperature-dependence of thermal *cis*-AB decay is in hexane.[71] To insure that the rate constant of AB in hexane is consistent with the present data in benzene, recalculation of the rate constants from Gibbs free energy of activation values applying Equation 4-24 is verified.

$$\Delta G^{\#} = RT\left(\frac{\ln k_B}{h} - \frac{\ln k_{-1}(\Delta)}{T}\right)$$ **Equation 4-24**

Table 4-22[v] The rate constants and activation parameters of the thermal isomerisation in benzene (regular font), in basic DMSO (bold font), and in hexane (italics font). [a]From reference[53], $k_{-1}(\Delta)$ is at 293 K, temperature range is 288-313 K.

Molecule/structure	k_{-1} (Δ), at 298 K / 10^{-5} s^{-1}	E_a / kJ mol^{-1}	$\Delta H^{\#}$ / kJ mol^{-1}	$\Delta S^{\#}$ / Jmol^{-1} k^{-1}	$\Delta G^{\#}$, at 298 K / kJ mol^{-1}
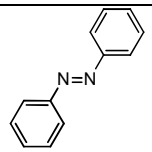 AB[a]	*0.3*	–	*88.7*	*-50.2*	*103.7*
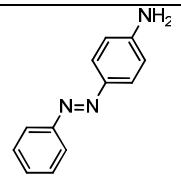 AAB	5.1	74.0	71.4	-88.1	97.7
	9.8	**114.8**	**112.28**	**54.4**	**96.1**
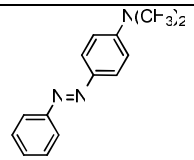 MY	9.8	58.1	55.5	-135.0	95.8
	3.9	**94.9**	**92.3**	**-19.7**	**98.2**
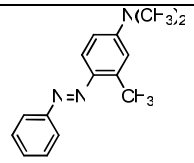 MMY	958.5	51.3	48.9	-119.6	84.5
	15.0	**82.6**	**80.0**	**-49.2**	**94.6**
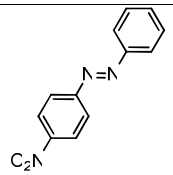 NAB	10.2	37.2	34.6	-205.5	95.9
	959.1	**91.7**	**89.2**	**17.7**	**84.0**
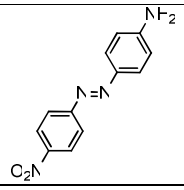	320.2	71.8	69.3	-60.7	87.4

[v] Table 4-22: continued overleaf

DO3					
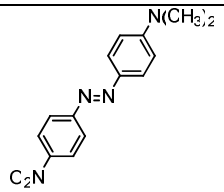 DMNAB	1149.3	64.6	62.1	-73.5	84.0
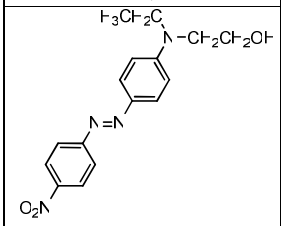 DR1	2757.4	40.5	38.0	-147.3	81.9

An examination of the available literature relating to the activation parameters of the *cis-trans* thermal isomerisation follows. For DMNAB and while the thermal rate constant values are in fairly in good agreement with that from reference[53] ($k_{-1}(\Delta)$ = 115 x 10^{-4} s^{-1} from the present data and 116 x 10^{-4} s^{-1} from that reference), In turn the activation parameters values including the enthalpy(related to the energy of activation) and entropy of activation(related to the Arrhenius pre-exponential factor), $\Delta H^{\#}$ and $\Delta S^{\#}$, respectively, are not in good agreement, where the discrepancies in these values are $\Delta\Delta H^{\#}$ =17 kJ/mol, $\Delta\Delta S^{\#}$ = -56 J/mol.K. The temperature range used in the pervious work is not given and it may be that a difference in the temperature range from the present study and that study is the reason for this disagreement. Due to the compensation between $\Delta H^{\#}$ and $\Delta S^{\#}$, the values of the Gibbs free energy of activation, $\Delta G^{\#}$, in the two studies are in quite good agreement.

The experimental data summarised in Table 4-22 shows that the values of the activation energy and the entropy of activation vary significantly from molecule to molecule and thus both of these parameters influence the inter-molecule variation of the rate constant. Similarly, both of these parameters influence the solvent-dependence of the rate constant, as discussed further in Section 4.6.6.4. The compensation between $\Delta H^{\#}$ and $\Delta S^{\#}$ and its application in determining the mechanism of the thermal isomerisation is discussed in Section 4.6.6.5.

Deleted: [Nishimura 1976].

4.6.6.1 Arrhenius Plots for DMSO Solutions

Formatted: Bullets and Numbering

All the Arrhenius plots in benzene are fitted very well by first order kinetics (R^2 is in the range 0.982-0.995) in the examined temperature range. On the other hand the Arrhenius plots in DMSO are subject to discussion. It was found that the Arrhenius plots in protic DMSO was not perfectly linear with relatively smaller correlations (R^2 is in the range 0.968-0.997), the reverse is true for experiments in basic DMSO (R^2 is in the range 0.999-1.000). The imperfect Arrhenius plots in protic solution suggests that more than one mechanism is operating. Figure 4-17 gives the Arrhenius plots in protic and basic DMSO solutions for AAB as an example.

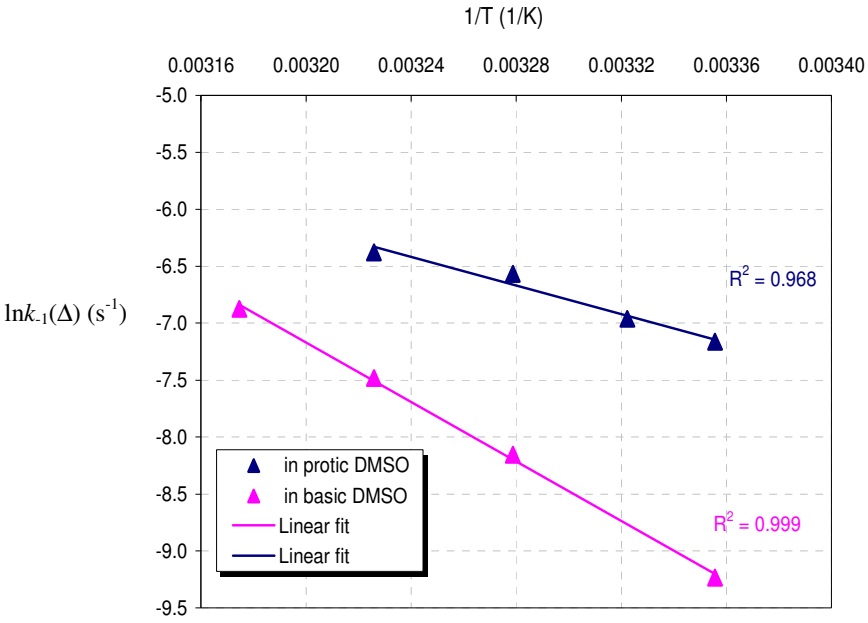

Figure 4-17 Arrhenius plots in protic and basic DMSO solutions of AAB.

In the case of NAB, as mentioned in Section 4.6.5.1, it was found that the thermal rate of NAB in basic DMSO was faster than in protic DMSO solution, contrary to the behaviour of all the other molecules The Arrhenius plots also have the opposite trend to the one observed for the other molecules, where a better linear plot was obtained now in the case of protic rather than basic solution, as shown in Figure 4-18.

To summarize in cases where the Arrhenius plots were perfectly linear, *i.e.* in benzene and basic DMSO solutions (NAB is exception), this indicates that there is no significant change in the reaction pathway over the temperature range examined.

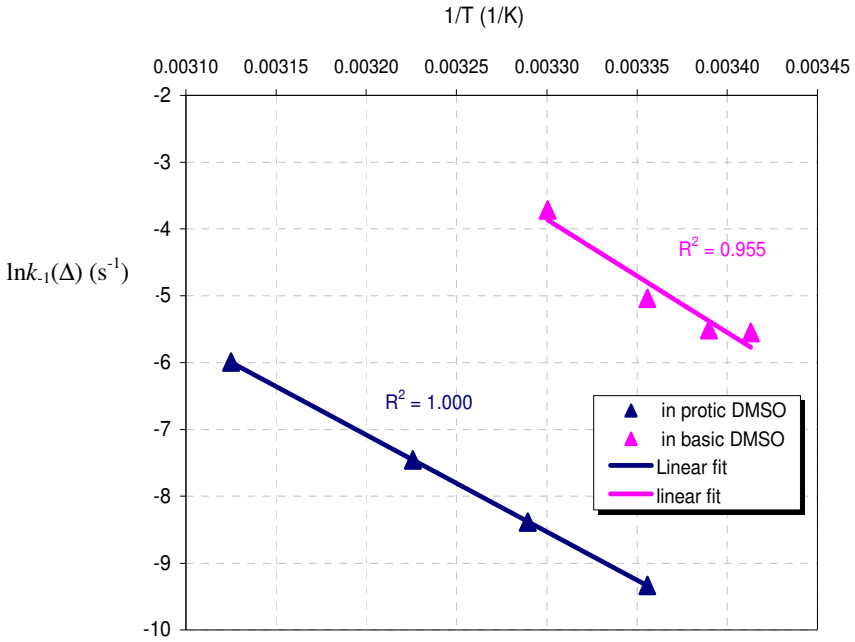

Figure 4-18 Arrhenius plots in protic and basic DMSO solutions of NAB.

4.6.6.2 Effect of Protonation on Thermal Activation Parameters in DMSO Solutions

The activation parameters in basic and protic DMSO solutions are displayed in Table 4-23. In general slower reactions correlate with larger activation barriers. In basic DMSO solutions, the thermal *cis-trans* isomerisation proceeds with high enthalpies of activation and small negative (or positive) entropies of activation, while in protic DMSO solutions, the reverse is true (NAB is exception). These differences reveal that the fundamental factors allowing for such isomerisation are not the same in the two media. Since the activation entropies in protic DMSO solution are more negative or less positive than the corresponding value in basic DMSO. The negative entropy of activation indicates a greater degree of ordering in the transition state than the initial state, since in protic DMSO a structured dynamic lattice of solvent-solvent hydrogen bonds may lead to increase in solvation during the activation process.

Molecule / structure	k_{-1} (Δ), at 298 K / 10^{-5} s^{-1}	E_a / kJ mol^{-1}	$\Delta H^{\#}$ / kJ mol^{-1}	$\Delta S^{\#}$ / $Jmol^{-1}$ k^{-1}	$\Delta G^{\#}$, at 298 K / kJ mol^{-1}
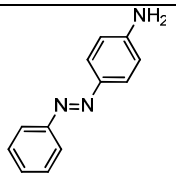 AAB	9.8	114.8	112.3	54.4	96.1
	77.4	**52.1**	**49.6**	**-137.8**	**90.7**
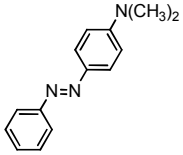 MY	3.9	94.9	92.3	-19.7	98.2
	40.4	**80.9**	**78.4**	**-46.5**	**92.2**
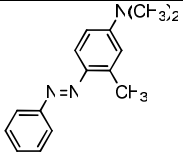 MMY	15.0	82.6	80.0	-49.2	94.6
	2157.5	**31.0**	**28.6**	**-180.4**	**82.3**
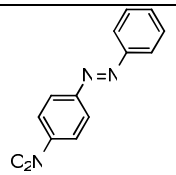 NAB	959.1	91.7	89.2	17.7	84.0
	10.2	**107.1**	**104.6**	**30.6**	**95.4**

Table 4-23 Activation parameters in basic DMSO (regular font) and protic DMSO (bold font) solutions.

Formatted: Bullets and Numbering

4.6.6.3 Correlation of Structural and Solvent Change with the Activation Parameters

The Arrhenius and Eyring plots of DO3 in benzene are given in Figure 4-19, from which the activation parameters were obtained. Table 4-22 gives the relevant data for the studied azobenzenes.

Comparison of the parent compound in hexane and azobenzene derivatives in benzene, Table 4-22, indicated that for all the azobenzene derivatives, regardless of the nature and position of substitutions the activation enthalpies values in benzene are less than that of AB in hexane. The activation enthalpy of AB in hexane is 88.70 kJ/mol, while the activation enthalpies of the azobenzene derivatives in benzene are in the range 34.65-69.23 kJ/mol. The activation entropy values in benzene for the azobenzene derivatives were more negative than

the value for AB, whereas for AB $\Delta S^{\#}$ = -50.21 J/mol.K and the activation entropies of the azobenzene derivatives are in the range -60.69 to -205.47 J/mol.K.

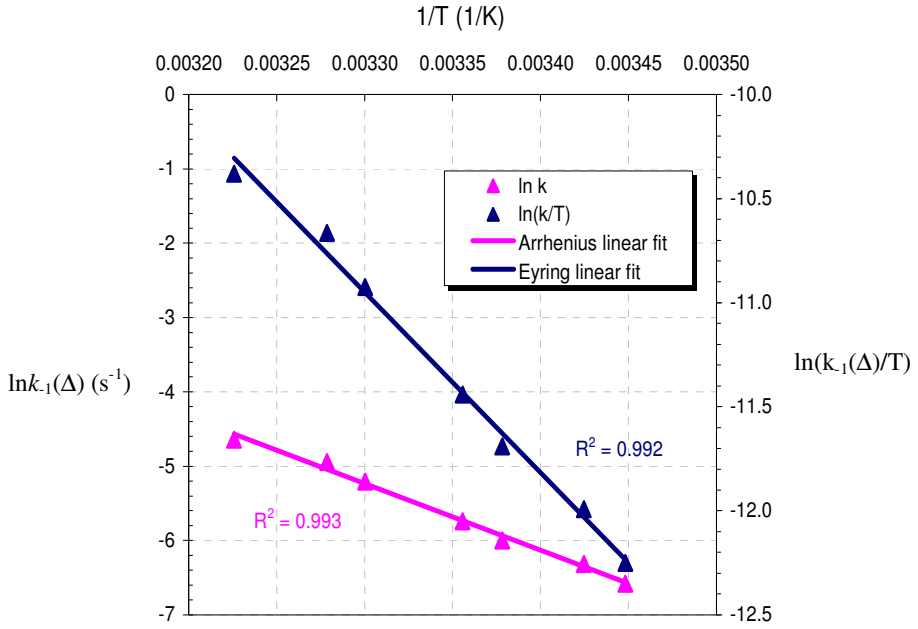

Figure 4-19 Graph showing the temperature dependence of the rate constant of DO3 in benzene.

The trend displayed by the activation parameters, $\Delta H^{\#}$ and $\Delta S^{\#}$, Table 4-22, show that the nature of the solvent plays an important role in determining whether the *cis-trans* isomerisation rate is controlled by the entropy or enthalpy term. In aprotic solvents (benzene and DMSO), $\Delta H^{\#}$ and $\Delta S^{\#}$ increase with increasing solvent polarity. The increase of $\Delta S^{\#}$ with increasing solvent polarity can be explained through an understanding of a model of the cybotactic region (the part of a solution in the vicinity of a solute molecule in which the ordering of the solvent molecules is modified by the presence of the solute molecule) around a *cis* isomer for the two cases: a relatively non-polar solvent, namely benzene, and a polar solvent, namely DMSO. In the benzene solution the solvent molecules in the cybotactic region of the azobenzene are relatively unstructured; as the *cis* molecule isomerise, however, the increase in dipole moment tends to organise the solvent molecule in the region. Thus the entropy of the system will be decreased overall and $\Delta S^{\#}$ decreases. Alternatively, in the DMSO medium the solvent molecules in the cybotactic region are already relatively structured. As the dissolved azobenzene reacts, the increased dipole moment of the transition state will not inflict as great an increase upon the structure of the solvent shell as in the

nonpolar case; hence $\Delta S^{\#}$ (DMSO) > $\Delta S^{\#}$ (benzene). This general effect has been observed in other chemical reactions that proceed through a dipolar transition state.[55,73,74]. In other words, the more negative values of the entropy of activation in benzene than in DMSO solutions, could be explained upon the reported statements that reactions generating electric charge exhibit negative entropies of activation. Negative entropy of activation implies that the transition state has much more charge separation than the ground state. The more polar transition state, the greater is the degree of ordering of solvent molecules relative to the ground state, leading to negative entropy of activation. In a less polar solvent, however, which has only a small or no dipole moment; the solvent molecules will be relatively un-orientated and consequently have higher entropy. Thus, a non-polar solvent will have a greater entropy loss as a result of increased solvation during the activation process. Consequently, reaction proceeding through a dipolar transition state should have larger negative entropy of activation in less polar solvent than in polar solvent.

The qualitative theory of solvent effects introduced by Hughes and Ingold in 1935 is expressed as a set of rules, see next paragraph, that take into account several factors including; (i) the change in charge magnitude and in charge distribution that occur between reactants and transition state, (ii) the dielectric characteristics of the solvents that enable them to solvate charged particles. Although the countless successful applications of this qualitative theory testify to its wide spread use, it does contain some limitations. The solvent effect discussed in the present work is under the scope of Hughes and Ingold rules, the results are found to obey in some cases these rules and show some limitations of these rules in other cases. Detailed analysis of the contribution of $\Delta H^{\#}$ and $\Delta S^{\#}$ in determining the thermal rates to each of the contrasting structures in each solvent is conducted in the following sections.

The effect of solvent was investigated by Hughes and Ingold. They used a simple qualitative solvation model considering only pure electrostatic interactions between ions or dipolar molecules and solvent molecules in initial and transition state. Depending on whether the reaction species are neutral, positively or negatively charged, the different reactions may be divided into different charge types. Based on certain reasonable assumptions as to the extent of solvation to be expected in the presence of electric charges: (i) Increase in magnitude of charge will increase solvation. (ii) Increase in dispersal of charge will decrease solvation. (iii) Destruction of charge will decrease solvation more than dispersal of charge.

The degree of variation in the thermal rates did not correlate as might be expected by the variation in the activations energies. It is expected that the trend of increasing rate constants for azobenzene derivatives would be paralleled with decreasing activation energies and vice versa. For example, in benzene, the thermal rate constant is 0.982 $x10^{-4}$ s^{-1} for MY and for DO3 is 32 $x10^{-4}$ s^{-1}, the thermal rate is smaller for MY by a factor of 33 compared to DO3, whereas the corresponding activation energies are 58 and 69 kJ/mole for MY and DO3, respectively, *i.e.* lower for MY by a factor of 1.2 compared to DO3. This can be explained by the significant role that the entropies of activation play in determining the thermal rates, since $\Delta\Delta S^{\#}$ = -74 J/mol.K for MY relative to DO3, resulting in a higher free energy of activation for MY.

In general, $\Delta H^{\#}-\Delta S^{\#}$ compensation is evident and results in values of Gibbs free energies of activation, $\Delta G^{\#}$, which lie in quite a narrow range, 82-98 kJ/mol. For example the significant difference in the activation enthalpies, $\Delta\Delta H^{\#}$ = 16 kJ/mol, for AAB and MY in benzene did not cause a significant difference in the corresponding Gibbs free energy of activation, $\Delta\Delta G^{\#}$= 2 kJ/mol, because of the compensating effect of the difference in the activation entropies, $\Delta\Delta S^{\#}$ = 47 J/mol.K ($T\Delta\Delta S^{\#}$ =14 kJ/mol)

4.6.6.4 Contribution of $\Delta H^{\#}$ and $\Delta S^{\#}$ in Determining the Thermal Rates

4.6.6.4.1 Comparison of *p*-Electron Donating Azobenzenes

Formatted: Bullets and Numbering

The data for these azobenzenes along with that of the parent azobenzene is presented in Table 4-24. In comparison with AB in hexane, an approximate 17 and 33 kJ/mol decrease is observed in $\Delta H^{\#}$ for AAB and MY, respectively, while $\Delta S^{\#}$ become more negative by approximately 38 and 85 J/mol.K for AAB and MY, respectively.

Comparing the two azobenzene derivatives in benzene, an approximate 16 kJ/mol decrease is observed in $\Delta H^{\#}$, following the change of the electron donating group (NH_2) in AAB to a stronger electron donor ($N(CH_3)_2$) in MY. In DMSO solutions a similar trend is observed, *i.e.* an approximate 20 kJ/mol decrease in $\Delta H^{\#}$. The entropy of activation, $\Delta S^{\#}$, becomes more negative by approximately 47 J/mol.K in benzene, where in DMSO it changes from a positive value for AAB to a negative value in MY, with $\Delta\Delta S^{\#}$=74 J/mol.K. In both solvents, this suggests a more polar transition state, relative to the ground state, for MY than AAB. As noted in Section 4.6.5.2.1, the structural modification from AAB to MY increases $k_{-1}(\Delta)$ in benzene, while in DMSO, the same structural modification leads to decrease in $k_{-1}(\Delta)$. This effect can be traced to the difference in $\Delta\Delta S^{\#}$ between the two solvents.

Molecule/ structure	$k_{-1}(\Delta)$, at 298 K / 10^{-5} s^{-1}	$\Delta H^{\#}$ / kJ mol^{-1}	$\Delta S^{\#}$ / J mol^{-1} K^{-1}
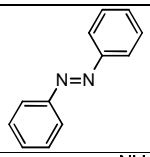 AB[a]	*0.3*	*88.7*	*-50.2*
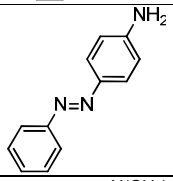 AAB	5.1	71.4	-88.1
	9.8	**112.3**	**54.4**
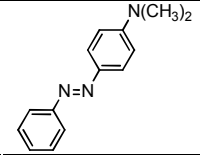 MY	9.8	55.5	-135.0
	3.9	**92.3**	**-19.7**

Table 4-24 Activation parameters of thermal *cis-trans* isomerisation in benzene (regular font), in DMSO (bold font), and in hexane (italics font). [a] From reference[45].

Formatted: Bullets and Numbering

Deleted: [31]

4.6.6.4.2 Effect of *o*-Methyl Substituent on *p*-Electron Donating Azobenzenes

Comparison of the activation parameters for MY and MMY, Table 4-25, is undertaken in the following paragraph.

Molecule/ structure	$k_{-1}(\Delta)$, at 298 K / 10^{-5} s^{-1}	$\Delta H^{\#}$ / kJ mol^{-1}	$\Delta S^{\#}$ / J mol^{-1} K^{-1}
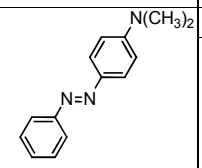 MY	9.8	55.5	-135.0
	3.9	**92.3**	**-19.7**
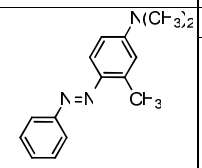 MMY	958.5	48.9	-119.6
	15.0	**80.0**	**-49.2**

Table 4-25 Activation parameters of thermal *cis-trans* isomerisation in benzene (regular font), and in DMSO (bold font).

In benzene indicates that introducing the o-methyl group results in a decrease of the enthalpy of activation, and $\Delta\Delta H^{\#}$ = 7 kJ/mol, whereas the entropy of activation increases (become less

negative), $\Delta\Delta S^{\#}$ = 15 J/mol.K. Thus the large increase in $k_{-1}(\Delta)$ for MMY relative to MY arises from a decrease in $\Delta H^{\#}$ combined with an increase in $\Delta S^{\#}$ to give a decrease in $\Delta G^{\#}$ of 11 kJ/mol. In DMSO the trend of change in the $\Delta H^{\#}$ is the same but greater, $\Delta\Delta H^{\#}$ = 12 kJ/mol, whereas the change in $\Delta S^{\#}$ is opposite, since it become more negative in MMY compared to that of MY, and $\Delta\Delta S^{\#}$ = -30 J/mol.K.

Formatted: Bullets and Numbering

4.6.6.4.3 Comparison of Push/Pull Azobenzenes

Comparing the activation parameters in the two solvents for AAB and NAB as push and pull azobenzenes, respectively, Table 4-26, shows that in benzene NAB has a smaller activation enthalpy and more negative entropy of activation by a significant amount, since $\Delta\Delta H^{\#}$ = -37 kJ/mol, and $\Delta\Delta S^{\#}$ = -117 J/mol.K. In DMSO the same trend of variation is observed for the two activation parameters, and $\Delta\Delta H^{\#}$ = -23 kJ/mol and $\Delta\Delta S^{\#}$ = -37 J/mol.K. This implies that, in both solvents, NAB has a more polar transition state, relative to the ground state, than AAB.

For NAB , the large increase in rate constant on going from benzene to DMSO correlates with a large increase in the entropy of activation, with $\Delta\Delta S^{\#}$ = + 223 J/mol.K, which overrides the increase in $\Delta H^{\#}$.

For the push-pull azobenzenes (in benzene), $\Delta H^{\#}$ decreases and $\Delta S^{\#}$ becomes more negative as the electron donating ability of the push substituent is increased upon going from DO3 to DMNAB to DR1. Again, this points to increasing polarity of the transition state along the series.

Molecule/ structure	$k_{-1}(\Delta)$, at 298 K / 10^{-5} s^{-1}	$\Delta H^{\#}$ / kJ mol^{-1}	$\Delta S^{\#}$ / J mol^{-1} K^{-1}
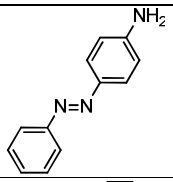 AAB	5.1	71.4	-88.1
	9.8	**112.3**	**54.4**
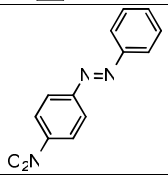 NAB	10.2	34.6	-205.5
	959.1	**89.2**	**17.7**
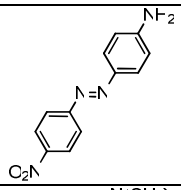 DO3	320.2	69.3	-60.7
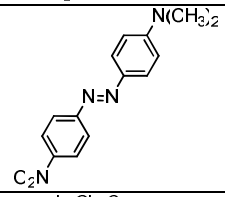 DMNAB	1149.3	62.1	-73.5
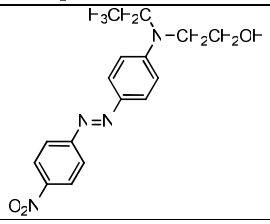 DR1	2757.4	38.0	-147.3

Table 4-26 Activation parameters of thermal *cis-trans* isomerisation for push/pull azobenzenes in benzene (regular font) and in DMSO (bold font).

Formatted: Bullets and Numbering

4.6.6.5 Predicting the Mechanism of Thermal Isomerisation from $\Delta H^{\#}$ and $\Delta S^{\#}$

Formatted: Font: Not Italic

Asano *et al.* [1981][53] synthesised an azobenzene-bridged crown ether in which the thermal *cis*-to-*trans* isomerisation *via* the rotational mechanism is highly unlinkely due to steric hindrance. They confirmed that the thermal isomerisation of this compound proceeds *via* the inversion mechanism and proposed it as a standard. For a series of azobenzenes in various solvents, they established a compensation relationship between $\Delta H^{\#}$ and $\Delta S^{\#}$, such that a plot of $\Delta H^{\#}$ versus $\Delta S^{\#}$ is linear. The points for the synthesised inversion standard were found to be co-linear with the other azobenzene and the authors concluded that the isomerisation of

these azobenzenes occurs *via* a single mechanism which is the inversion mechanism. On the other hand, for DMNAB, as a push-pull substituted azobenzene, the plot of $\Delta H^{\#}$ and $\Delta S^{\#}$ was not collinear with the standard, and they inferred the involvement of the rotational mechanism. The magnitude of the deviation from collinearly was proposed to be a measure of the contribution of the rotational mechanism, lets us label this as 'Asano model'.

The present results have been combined with those for the inversion standard of Asano and DMNAB from reference [53] to compose isokinetic plots for $\Delta H^{\#}$ and $\Delta S^{\#}$ in order to predict the isomerisation mechanism. The comparison was made as follows; $\Delta H^{\#}$ was plotted versus $\Delta S^{\#}$ for each studied molecule in each solvent, the points that are collinear with those of the inversional standard points of Asano were considered to demonstrate an inversion mechanism and the points that deviate from the Asano inversional standard points and are collinear with DMNAB points were considered to demonstrate a rotational mechanism or at least a predominant contribution from rotation. Table 4-27 gives the activation parameters that have been plotted, including those of Asano for the standard and DMNAB.

Deleted: *l*

Deleted: .

Molecule/structure	Solvent	$\Delta H^{\#}$ / kJ mol^{-1}	$\Delta S^{\#}$ / J mol^{-1} K^{-1}
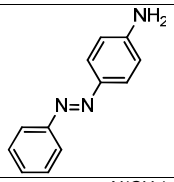 AAB	Benzene	71.4	-88.1
	DMSO	112.3	54.4
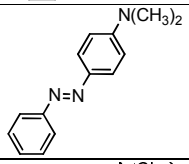 MY	Cyclohexane	31.5	-201.9
	Benzene	62.8	-135.0
	DMSO	92.3	-19.7
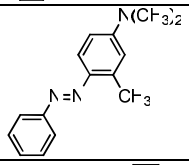 MMY	Benzene	48.9	-119.6
	DMSO	80.0	-49.2
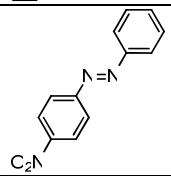 NAB	Benzene	34.6	-205.5
	DMSO	89.2	17.7
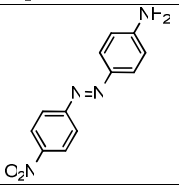 DO3	Benzene	69.3	-60.7
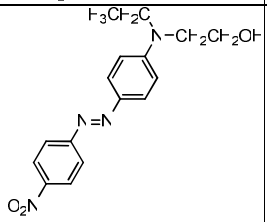 DR1	Benzene	38.0	-147.3
Azobenzene-bridged crown ether [a]	Benzene	76.2	-94.6
	Methanol	64.9	-133.5
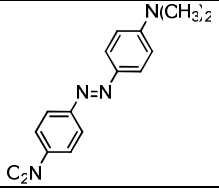 DMNAB	Benzene	62.1	-73.5
	Benzene[a]	44.8	-129.3
	Hexane[a]	62.8	-79.5
	Dioxane[a]	63.6	-66.1
	Benzene:dioxane[a] (1:1 v/v)	60.7	-75.8

Table 4-27 The activation parameters for the *cis*-to-*trans* thermal isomerisation of the studied molecules in various solvents that are plotted in Figure 4-20. [a] from reference[53].

Figure 4-20 gives the $\Delta H^{\#}$ -$\Delta S^{\#}$ compensation plot for the studied molecules along with the values of the standard and DMNAB in various solvents. Points were correlated with each other in several attempts to search for lines with maximum correlation coefficient.

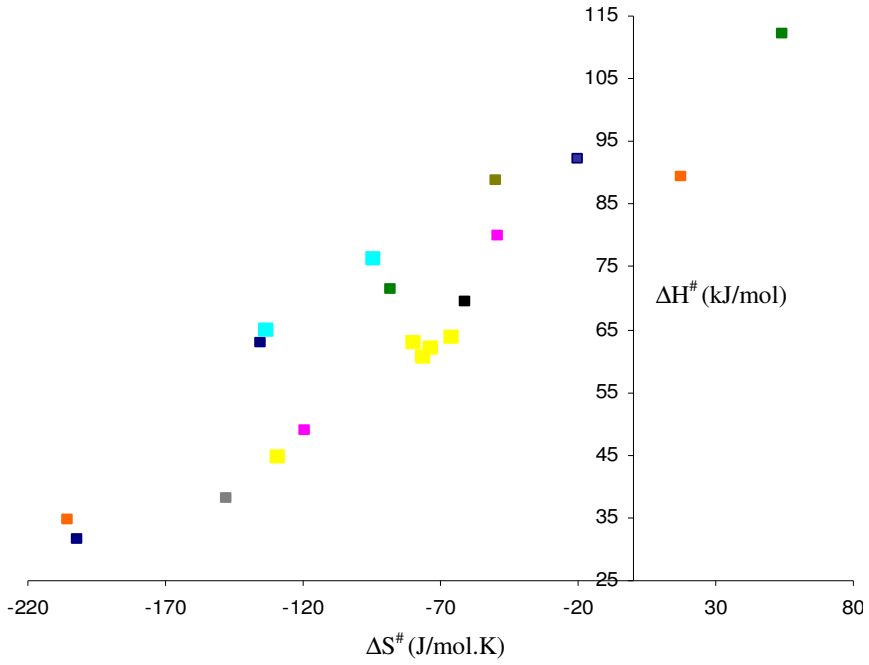

Figure 4-20 $\Delta H^{\#}$-$\Delta S^{\#}$ compensation relationship; ■ AB ■ AAB, ■ MY, ■ MMY, ■ NAB, ■ DO3, ■ DR1, ■ Inversional standard and ■ DMNAB.

Two straight lines were obtained with good correlation coefficients. The first line contains the points for DMNAB and collinear with these points are those for DO3, DR1, and MMY in benzene and NAB in DMSO. This suggests a rotational mechanism in these cases. The straight line is expressed by Equation 4-25 with correlative coefficient, R^2=0.989.

$$\Delta H^{\#}(kJ/mol) = 0.308\Delta S^{\#}(J/mol.K) + 85.11$$ **Equation 4-25**

The second straight line includes the standard points collinear with those of AB, AAB, MY, NAB in benzene and MMY in DMSO. This implies an inversional mechanism in these cases. The straight line is expressed by Equation 4-26 with correlative coefficient, R^2=0.966.

$$\Delta H^{\#}(kJ/mol) = 0.302\Delta S^{\#}(J/mol.K) + 99.38$$ **Equation 4-26**

In conclusion, the inferences from this treatment of the results are:

i. The rotation and inversion mechanisms appear to be distinguishable on the basis of a $\Delta H^{\#}$-$\Delta S^{\#}$ compensation relationship aided with a standard azobenzene derivative for the inversion mechanism.

ii. The thermal *cis*-to-*trans* isomerisation of push-pull substituted azobenzenes occurs *via* the rotational pathway.

iii. Azobenzenes with *p*-substitution of electron-donating group isomerises thermally *via* the inversional pathway, unaffected by the solvent polarity.

iv. The introduction of a donating group into the *ortho*- position for azobenzene with an electron-donating group introduces a solvent effect on the isomerisation pathway.

v. Azobenzene with *p*-NO_2 electron-drawing group isomerises thermally *via* a rotational pathway in DMSO and *via* an inversional pathway in benzene.

4.7 Conclusions

The results presented in this chapter have further demonstrated the application of NMR with *in situ* laser irradiation to investigate the kinetics of the photochemical and thermal isomerisation rates of simple mono disperse dyes. Combining data from UV/Vis absorption and NMR spectroscopes enabled the molar absorption coefficients of the short-lived *cis* isomers to be obtained. It was found that the presence of a small amount of *cis* isomer at the photostationary state results in a very limited influence on the absorption coefficient of the irradiated sample. The negligible effect of the time-dependent photokinetic factor was confirmed, by fitting the data to a first order kinetic model.

In all cases, for the dyes studied in benzene and DMSO in this work, the photochemical contribution to the *cis*↔*trans* isomerisation is greater than the thermal contribution. The excited state kinetics represented in this work by relative quantum yields of photoisomerisation, $\Phi^{rel}_{trans\rightarrow cis}$ and $\Phi^{rel}_{cis\rightarrow trans}$, assisted the previous conclusion by D. I. Gibson[5] that the photoisomerisation of the *cis* and *trans* isomers proceed *via* different transition states on the excited state potential energy surface. Also this photoisomerisation processes showed a high degree of variation with molecular structure and solvent polarity. In addition to some simple information about the structure of the transition state relative to the corresponding ground state was derived. UV/Vis absorption spectra for each molecule in different solvents were assisted the information about the structure of the transition state.

Formatted: Not Highlight

Formatted: Not Highlight

A structural variation was seen to have a profound effect on the rate of thermal *cis* isomer decay, in agreement with previous observations in the literature. Azobenzene derivatives have much faster decay rate than the parent compound regardless of the nature and position of substituent/s. Push-pull azobenzenes have much faster rates than push or pull azobenzene. The influence of substitution *ortho* to the azo bond was consistent with observations from many other research groups. The introduction of a methyl group at the *ortho* position on the donating side of a *p*-electron donating azobenzene has a prominent influence on the thermal *cis* isomer decay, a significant acceleration of the decay process leading to faster reversion to the *trans* isomer. The kinetics of the thermal reversal of push-pull azobenzenes are greatly affected by nature of the electron donating substituent. Modifying of the electron donating group with groups of higher ability of donation markedly increases the thermal decay rate.

Solvent polarity was also to play an important role in determining the thermal decay of the *cis* isomer. The limited data available precludes general conclusions, but pronounced differences in rates were seen for MMY and NAB in DMSO and benzene. For the former the rate was almost a factor 100 greater in benzene and for the latter almost 100 times less in benzene. For *p*-electron donating azobenzenes the effect of protonation on lowering the activation thermal barrier and consequently accelerating the thermal decay rate was demonstrated, in agreement with previous studies. However, anomalous behaviour was found for nitroazobenzene, for which protonation resulted in a decrease in the thermal rate and a corresponding increase in the activation barrier.

The technique of NMR with *in situ* laser has been extended to determine the energy barrier to the thermal isomerisation for the studied azobenzene derivatives. Rate constants obtained through monitoring *cis* isomer decay after *in situ* irradiation over a range of temperatures in benzene and DMSO solutions demonstrated a very good fits to the Arrhenius and Eyring equations, allowing activation parameters to be derived. The energy barriers are in good agreement with reports from studies conducted on the same or similar azo dyes using spectroscopic techniques. In almost all cases highly linear Arrhenius plots indicated that only one mechanism was operating in the examined temperature range. However, imperfect linearity of these plots for samples in protic DMSO indicated a competition between the two proposed mechanisms, namely rotation and inversion mechanism.

The experimental data show that the values of the activation enthalpy (energy) and the entropy of activation vary significantly from molecule to molecule and that both of these parameters influence the inter-molecule variation of the rate constant. Similarly, both of

Deleted: activation vary

these parameters influence the solvent-dependence of the rate constant. For all four molecules studied in both benzene and DMSO, the activation enthalpy is lower in benzene and the activation entropy is correspondingly more negative. These observations are consistent with a transition state that has more charge separation than the ground state.

The role that $\Delta H^{\#}$ and $\Delta S^{\#}$ play in determining the rate of the thermal isomerisation has been discussed. The study shows clearly some examples where the entropy of activation governs the Gibbs free energy of activation, and thus records a limitation of the Hughes and Ingold rules.

The compensation relationship between $\Delta H^{\#}$ and $\Delta S^{\#}$ was used to predict whether thermal isomerisation occurs by the rotation or inversion mechanism. This led to the following postulates; the thermal *cis*-to-*trans* isomerisation of push-pull substituted azobenzenes occurs *via* the rotational pathway. Azobenzenes with *p*-substitution of electron donating groups isomerise thermally *via* an inversional pathway. The introduction of a donating group into the *ortho*- position for an azobenzene with a *p*-electron donating group introduces a solvent effect on the isomerisation pathway. Nitroazobenzene isomerises thermally *via* a rotational pathway in polar solvent and *via* an inversional pathway in non-polar solvent.

5 DFT Calculations of the Kinetics of Thermal Isomerisation of a Series of Azobenzenes

5.1 Introduction

Density functional theory (DFT) is being widely used for the computation of molecular geometry and vibrational frequencies[75-81] due to the development of numerous density functional forms and their efficiency, which leads to the computation of highly accurate fundamental vibrational frequencies, in addition to the modest computational expenses as compared to other sophisticated approaches such as the second-order Møller-Plesset (MP2) perturbation method. In particular, for polyatomic molecules (typically normal modes exceeding 50), the DFT methods lead to the prediction of very accurate molecular geometry and vibrational frequencies as compared to the conventional *ab initio* restricted Hartree-Fock (RHF) and MP2 calculations. Computed frequencies using MP2 (compared to RHF) are found to be relatively close to the experimental results, due to inclusion of electron correlations;[82] however, computationally it is very demanding (in terms of CPU time and disk storage) in comparison to the density functional methods, as a result of which their usefulness is restricted to rather small systems. The DFT methods thus provide a promising cost-effective approach for calculating the vibrational modes of large polyatomic molecules. In this Chapter we employ density functional theory (DFT); the main objectives for carrying out the present investigation are 4-fold:

i. An accurate theoretical method is necessary to predict the structures of the *cis* and *trans* isomers and the transition state, to explore the reaction coordinate of the thermal isomerisation of *cis*-to-*trans* form of these molecules.
ii. Carrying out the frequency calculations is necessary to compute the kinetic and thermodynamic parameters, and to the best of the author's knowledge these data are not available in the literature.
iii. A critical comparison of the experimentally obtained parameters (NMR spectroscopy) with the theoretically (DFT) parameters is absolutely essential in order to test the accuracy of the theory.
iv. The prediction of the thermal isomerisation mechanism is aided experimentally and computationally.

Kikuchi *et al.* [1999][83] used *ab initio* restricted Hartree-Fock (RHF) and restricted open shell Hartree-Fock (ROHF) methods, including solvent effects based on the generalised Born (GB) formula, to examine the solvent effect on the inversion and rotation mechanisms of the thermal *cis*-to-*trans* isomerisation of DMNAB. It was found that the inversion through the phenyl ring substituted by the electron acceptor group (pull-group inversion) path was more favourable than the inversion through the phenyl ring substituted by the electron donating group (push-group inversion) in the gas phase and in solution. They concluded that searching for the rotation transition state gave the pull-group inversion transition state even in polar solvent. Wang and Wang [2007][84] used the MP2 and DFT calculations to study the thermal isomerisation of AB and AAB. They found that the relative stability of *trans* to *cis* isomer is not obviously affected by the $-NH_2$ substitution. For the thermal isomerisation of AB, DFT/B3LYP calculation showed that the energy barrier to overcome *via* the inversion pathway is lower than that *via* rotation. For AAB, the thermal isomerisation through inversion and rotation pathways were found to possess identical molecular structures at the highest energy points on the PECs and the energy barriers to be overcome through inversion and rotation pathways were the same: no explanation was given for this observation. Since it is physically unrealistic to pass through identical transition states from two different pathways, and since the transition state obtained was characterised by the features of the inversion transition state (a linear one) this strongly suggests that during the search for the rotation transition state a passage to the inversion pathway was found.

The literature that is available to the present author does not include any calculations of the activation parameters, such as the entropy of activation, $\Delta S^{\#}$, and the Gibbs free energy of activation, $\Delta G^{\#}$, for the thermal isomerisation of azobenzenes systems. The *ab initio* calculations of the activation parameters of systems other than azobenzenes are as follows. Nori-Shargh and Ghanizadeh [2003][85] studied the conformational properties of a bridged biphenylene system. Using *ab initio* molecular orbital and DFT methods they determined from the relative energy differences between different conformations the lowest energy conformation. They calculated the activation parameters for each conformation. The entropies of activation were relatively small, thus the enthalpies of activation and Gibbs free energies of activation were close to the relative energies values. No comparison with experimental values was provided. Gholami and Azadyar [2004][86] carried out DFT calculations at RHF, MP2 and B3LYP levels of theory, using the 6-31G(d) basis set to study the structural and kinetic aspects of a retro-cheletropic ene reaction for some molecules and their deuterated derivatives in the gas phase. Through the isotope effect the mechanism of

the reaction was investigated, they found a good agreement between the calculated activation parameters and the experimental values, since the theoretical energy barrier was 35.99 kcal/mol compared to experimental value 44.2 kcal/mol, the theoretical activation entropy was -2.13 cal/mol K compared to experimental value of 2.0 cal/mol.K.

Because of the fundamental importance of double bond isomerisation in chemistry, the mechanism of the thermal isomerisation of azobenzenes deserves special attention. In order to get reliable information about the mechanism, in the present work the inversion and rotation pathways are calculated in a consistent way at a moderate *ab initio* DFT (B3LYP/6-31G(d,p)) level of theory/ basis set. A consistent treatment of the linear transition state of the inversion pathway, on one hand, and the rotation transition state, on the other hand is a delicate problem, which has to be treated with special care.

This chapter will begin by presenting a detailed description of the DFT calculations carried out for AAB as an example; the procedures that were applied for this molecule were applied to all other molecules. Detailed investigation of the two mechanisms of the thermal isomerisation *via* construction of the potential energy curves will be then presented. This involved the scanning of CN=NC dihedral angle and CN=N bond angle of the azo linkage. This is followed by a detailed thermodynamic study of the thermal *cis*-to-*trans* isomerisation and comparison with experimental data, and attempts will be made to rationalise the mechanism of the thermal isomerisation in the context of the theoretical and experimental findings. The final section is concerned the study of the effect of protonation on the isomerisation rate and activation barrier in. The *trans* structures of the studied azobenzenes are represented in Figure 5-1.

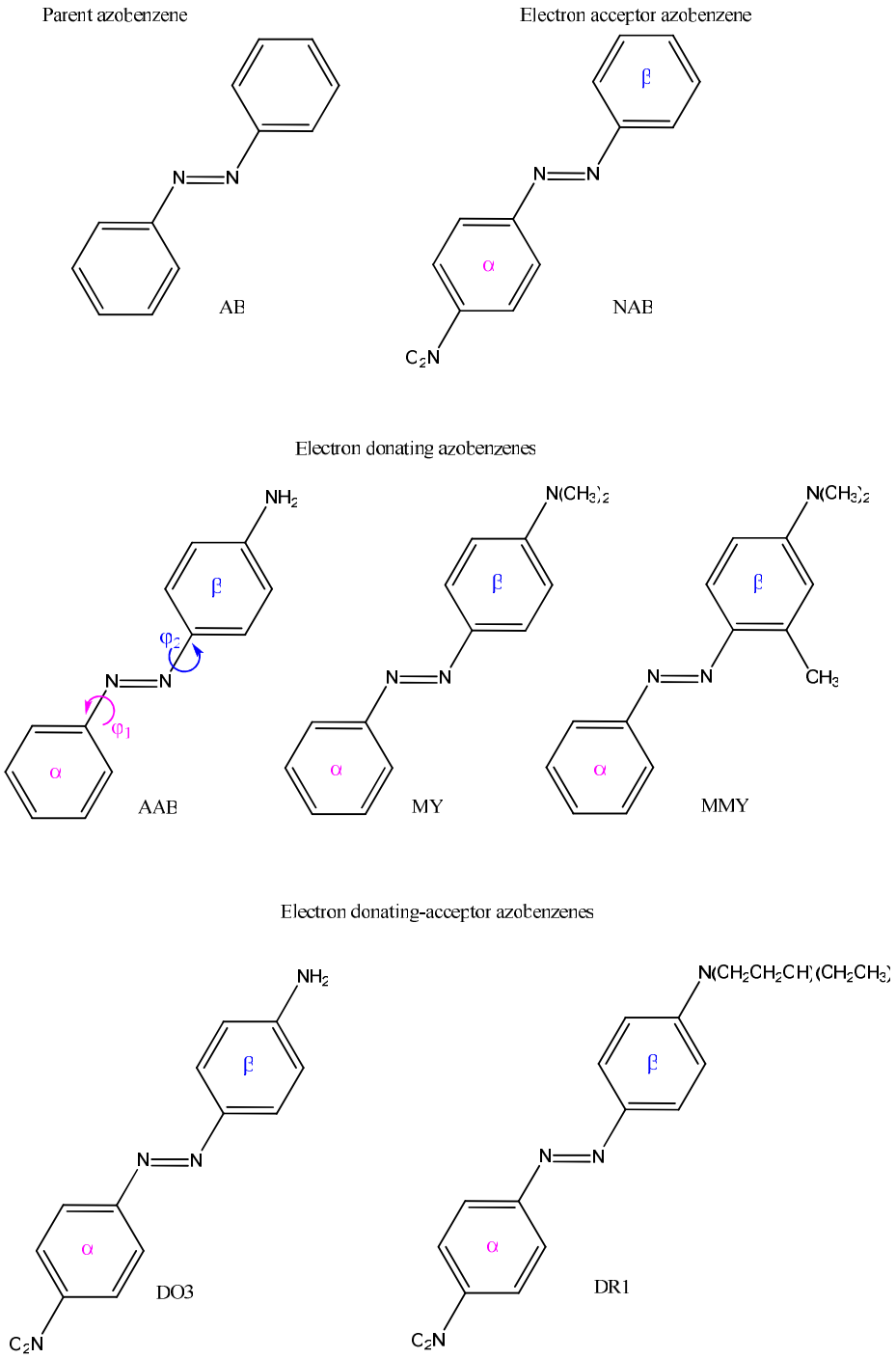

Figure 5-1 Structures of the *trans* isomers of the azobenzenes. α and β symbols identify the phenyl rings with respect to the inversion mechanism. φ_1 and φ_2 are the torsional angles related with α and β phenyl rings.

5.2 Structural Notation

Throughout this chapter, the rotation pathway which involves scanning the dihedral angle C-N=N-C of the azo- linkage, while optimizing the other structure parameters (refer to Section 3.5) will be denoted as dihedral rotation (dihedral rot). The inversion pathway which involves scanning one of C-N=N angles of the azo- linkage, while optimizing the other structure parameters (refer to Section 3.5) is designated as α-inversion or β-inversion, the corresponding angle as α-CN=N and β-N=NC, the corresponding phenyl rings as α-phenyl ring and β-phenyl ring, and the corresponding transition state (TS) as α-TS and β-TS, all depicted in Figure 5-1. All DFT/B3LYP calculations were performed using the 6-31G(d,p) basis set unless otherwise stated.

5.3 Results and Discussion

In this section the results of DFT calculations on the azobenzenes, depicted in Figure 5-1, the obtained data is analysed and interpreted.

5.3.1 Geometries of Gas Phase *Cis* and *Trans* Isomers

Figure 5-2[vi] presented the gas phase minimum energy structures of the *trans* and *cis* isomers for the studied azobenzenes. The obtained geometries of these isomers have the general features of such isomers with flat and bent geometries for the *trans* and *cis* isomers, respectively. More detail discussion is carried out in the following sections.

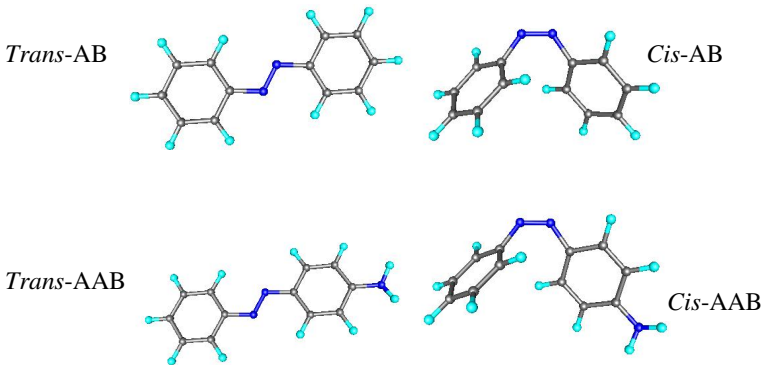

[vi] Figure 5-2: continued overleaf

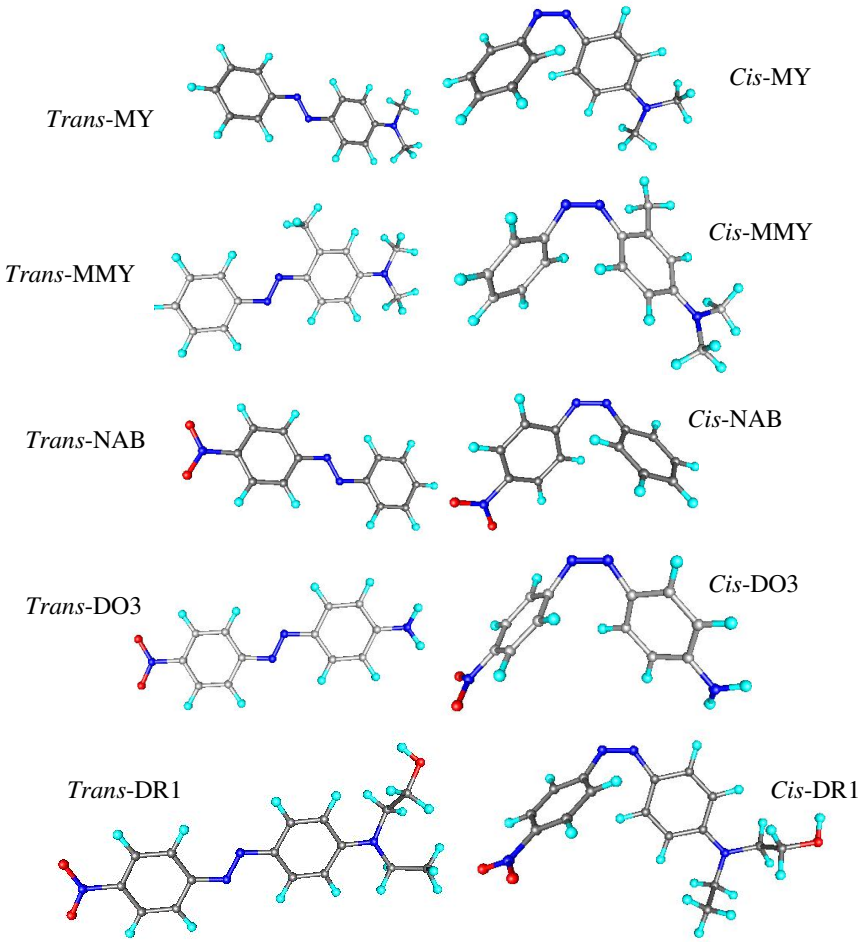

Figure 5-2 The calculated minimum energy structures of the *trans* and *cis* isomers of azobenzenes in the gas phase.

5.3.1.1 Comparison with Literature

In this section, the optimised geometric parameters obtained will be compared with the available literature and experimental values.

5.3.1.1.1 Azobenzene

In comparison with the work that has been reported in the literature on *trans*-AB, only a little work has been carried out on the corresponding *cis* form. In fact the present study has no more to say about the computational results concerning the *trans*-AB; however, to discuss the computational results for the *cis* isomer it is useful first to confirm on the correctness of

the computational values for the *trans* isomer by comparing it with the available literature and with experiments. After that a detailed comparison will be carried out between the new computational results for the *cis* isomer with the available literature and at the same time comparison with experiments will carried out too.

The DFT-B3LYP/6-31G and 6-31G (d, p) results for the *trans* geometries of AB are given in Table 5-1 along with the available literature and experimental data. Figure 5-3 depicts AB with the atomic numbering.

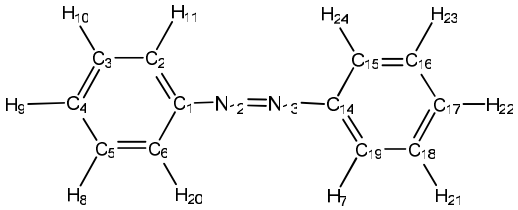

Figure 5-3 AB is depicted with atomic numbering.

In Table 5-1, we compare the gas phase theoretical geometric parameters of *trans*-AB with the experimental ones from the X-ray diffraction (XRD) and Gas Electron Diffraction (GED). It turns out that the optimised parameters obtained in the present work are in total agreement with those in literature from calculations performed at the same basis sets.

Table 5-1 Optimised and experimental geometries of *trans*-AB. Distances are in angstroms,

	N=N	**C–N**	**C–C**	**C–H**	**C–N =N**	**C–C–N**	**C–C–C**	**C–C–H**	**C–C –N=N**
XRD[a]	1.247	1.433	–	–	113.3	123.0	–	–	–
GED[b]	1.268	1.427	1.396	1.088	114.5	123.0	–	–	27.9
6-31G	1.278	1.424	1.402	1.084	115.7	124.3 115.4	119.9	119.9	0.0 180.0
6-31G[c]	1.278	1.424	1.402	1.084	115.7	124.3 115.4	119.9	119.9	–
6-31+ G(d)[d]	1.258	1.420	–	–	115.3	124.7 115.3	–	–	0.0 180.0
6-31 G(d,p)	1.261	1.419	1.282	1.086	114.80	124.7 115.3	119.987	119.990	0.0 180.0
6-31 G(d,p)[d]	1.261	1.419	–	–	114.8	124.8 115.3	–	–	0.0 180.0
6-311 G(d,p)[e]	1.253	1.418	–	–	115.1	124.6 115.5	–	–	0.0 180.0

angles are in degrees. [a] From reference[87]. [b] From reference[88]. [c] From reference[75]. [d] From reference[89].[e] From reference[90].

As the XRD results include solid-state effects, and the Gas Electron Diffraction (GED) measurements are performed at relatively high temperature, an immediate comparison with theory is difficult. However, the N=N distance, which is of major concern because the diazo bond qualifies to be the chromophoric unit, is generally overestimated with respect to XRD results, while, it is over/underestimated with respect to GED results. It is interesting to note that 6-311G(d,p) overestimates N=N bond distance from XRD by only 0.006 Å, but the 6-31G(d,p) underestimates this bond distance by only 0.007 Å. The C-C and C-H bond distances are available only from the GED, 6-31G overestimates the C-C bond distance by only 0.006 Å, while the C-H bond distance are over/underestimated by the same extent and by 0.002 Å. The best basis set for estimation of the C-N bond distance in comparison with XRD and GED is 6-31G. The C-N=N and C-C-N bond angles are generally overestimated, the best estimation for C-N=N bond angles is from 6-31G (d, p) by 0.003^0 and for C-C-N is from is 6-31G by 1.3^0. Overall, we find that the optimised bond lengths and bond angles calculated from 6-31G gives the best structural parameters followed by the 6-31G(d,p) basis set.

The DFT-B3LYP/6-31G and 6-31G(d,p) results for the *cis* geometries of AB are given in Table 5-2 in comparison with the available literature and experimental data. The only available experimental results are from XRD experiments for the solid state,[87] there is no available literature for experiments using the GED method. Distortion of the phenyl ring of the *cis*-AB is significant to avoid the steric hindrance of the phenyl rings. XRD shows that the dihedral angle at the N=N is 8^0, and the phenyl ring is rotated by about 53^0 about the C-N bond relative to a planar N=N-C arrangement, whereas theoretically calculated values for these are -11^0 and 47^0, respectively from B3LYP/6-31G and for 6-31G(d,p) are10^0 and 50^0, respectively, and BP86/TZVP are 11^0 and 48^0, respectively. Thus, the optimised structural parameters obtained from these levels of theories are in reasonable agreement to the observed XRD values. The calculated N=N bond distance is underestimated by 0.005 Å from B3LYP/6-31G(d,p) and overestimated by 0.002 Å from BP86/TZVP compared to the XRD data, whereas, C-N is underestimated by average of 0.011 Å from the two levels of theory. Average C-C bond length is under/overestimated by 0.319 Å, and always overestimated by 0.02 Å from BP86/TZVP.

	B3LYP		BP86 [b]	XRD [a]
	6-31G	6-31G(d,p)	TZVP	
Bond length / Å				
N_{12}–N_{13}	1.266	1.248	1.255	1.253
C_1–N_{12}	1.446	1.439	1.437	1.449
C_1–C_2	1.404	1.400	1.406	1.410
C_1–C_6	1.407	1.402	1.405	1.385
C_5–C_6	1.397	1.394	1.395	1.377
C_4–C_5	1.401	–	1.400	1.389
C_6–H_{20}	1.084	1.084	1.090	–
C_5–H_8	1.085	1.086	1.092	–
Bond angle / ^{0}				
C_1–N_{12}–N_{13}	125.1	124.0	124.1	121.9
C_2–C_1–N_{12}	116.0	116.2	116.4	117.3
C_6–C_1–N_{12}	123.4	123.2	122.9	122.5
C_2–C_3–C_4	120.1	120.2	120.1	121.7
C_3–C_4–C_5	119.8	119.8	119.8	119.0
H_{20}–C_6–C_1	120.2	119.9	119.9	–
H_{11}–C_2–C_1	118.7	118.9	118.7	–
Torsional angle / ^{0}				
C_1–N_{12}–N_{13}–C_{14} (dihedral)	-10.8	9.8	11.4	8.0
N_{12}–N_{13}–C_{14}–C_{19}	-46.7	50.4	48.4	53.3

Table 5-2 Optimised and experimental geometries of *cis*-AB. [a] From reference[87]. [b] From reference[91].

5.3.1.1.2 Methyl Yellow

Figure 5-4 depicts the MY structure with the atomic numbering. The experimental and optimised geometric parameters (bond lengths, bond angles and dihedral angles) of *trans*-MY by DFT (B3LYP) with 6-31G, 6-31G(d,p) and 6-311G(d,p)[92] basis sets are listed in Table 5-3.

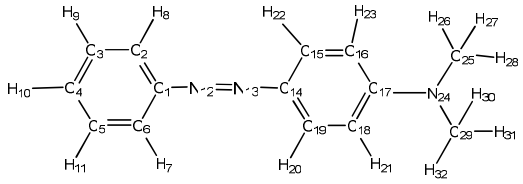

Figure 5-4 MY is depicted along with the atomic numbering.

	XRD [a]	6-31G	6-31G(d,p)	6-311G(d,p) [b]
Bond length / Å				
N=N	1.261(0)	1.284	1.266	1.258
C–N(azo) un-substituted side	1.412(2)	1.424	1.418	1.417
N–C (azo) donating side	1.417(1)	1.410	1.404	1.403
C_1–C_2	1.383(2)	–	1.4062	1.4036

C_1–C_6	1.391(1)	–	1.4017	1.3991
Bond angle / ^{0}				
C–N=N un-substituted side	113.9(7)	115.5	114.544	115.0
N=N–C donating side	115.4(0)	116.3	115.320	115.7
N_{12}–C_1–C_2	124.2(2)	–	124.910	124.79
N_{13}–C_{14}–C_{15}	117.8(7)	–	116.273	116.47
N_{13}–C_{14}–C_{19}	125.1(4)	–	–	125.28
Torsional angle / ^{0}				
C_1–C_2–N_{12}–N_{13}	0.3(5)	–	0.007	0.011
C_6–C_2–N_{12}–N_{13}	178.6(1)	–	-179.994	179.99
N_{12}–N_{13}–C_{14}–C_{15}	-175.9(8)	–	179.999	179.99
N_{12}–N_{12}–C_{14}–C_{19}	5.5(1)	–	0.001	-0.025
C–N=N–C (dihedral)	-178.2(5)	180.0	-180.0	-180.0

Table 5-3 Optimised and experimental geometries of *trans*-MY. [a] From references[93,94]. [b] From reference[92].

From this table, the general observation is that the optimised geometric parameters obtained by different basis sets are similar and in good agreement with the experimental values. Taking into consideration the time consumed in performing calculations with larger basis set, *i.e.* 6-311G(d,p) and the fairly good agreement with the experimental values obtained from relatively simple basis set, *i.e.* 6-31G, this point is crucial when the available computational resources are scarce.

5.3.1.2 Effect of Substitution/s

The effect of substitution/s on the optimised geometrical parameters of the *trans* and *cis* isomer of the studied azobenzenes, and comparison with the parent compound will be conducted in the following sections.

5.3.1.2.1 Structures of *Trans* Isomers

During complete optimisation, AB adopted the C_{2h} point group, and NAB adopted the C_s point group with only a plane of symmetry, whereas, due to the presence of the amino group in AAB, dimethyl group in MY, dimethyl group and methyl group in MMY, amino group in DO3 and $N(CH_2CH_3)(CH_2CH_2OH)$ group in DR1, these adopted the C_1 point group containing no symmetry element. The optimised parameters of the azo linkage computed using B3LYP with the 6-31G(d,p) basis set is presented in Table 5-4. To the best of the author's knowledge, this is the first report on the molecular structural parameters of these important classes of molecules, *viz.* MMY and DR1. Literature calculations of the geometrical parameters of the *trans* forms of the other molecules were available.[75,76,83,90,92,95,96] It was proved in the literature and in Section 5.3.1.1.1 that the

calculated bond lengths, *viz.* N=N, α-C-N and β-N-C, and bond angles, *viz.* α-C-N=N, β-N=N-C and C-N=N-C dihedral, from B3LYP in the case of AB and MY are comparable to the experimental values. This gives additional confidence that the B3LYP calculation predicts optimised structural parameters in good agreement with the experiment. The knowledge of the differences between the experimental and theoretical calculated optimised structures is essential when experimental structural parameters are not available and one has to rely completely on the calculated parameters. Thus, with the information that B3LYP is capable of predicting reliable optimised structures, this section presents a comparative study of the N=N, α-C-N and β-N-C bond lengths as well as α-C-N=N and β-N=N-C bond angles and C-N=N-C dihedral angle in these molecules.

Table 5-4[vii] Optimized geometrical parameters of the *trans* isomer of the studied azobenzenes in the gas phase.

	AB	AAB	MY	MMY	NAB	DO3	DR1
Bond length / Å							
N=N	1.261	1.265	1.266	1.266	1.261	1.268	1.269
C–N(azo) un-substituted side	1.419	1.418	1.418	1.418	1.415	–	–
C–N(azo) donating side	–	1.407	1.404	1.404	–	1.399	1.397
C–N(azo) acceptor side	–	–	–	–	1.419	1.415	1.414
C(ph)–C(ph)	1.282	1.399	1.400	1.400	1.397	1.401	1.400
C(ph)–H	1.086	1.086	1.085	1.085	1.084	1.085	1.083
C(ph)–N(H)	–	1.386	–	–	–	1.378	–
N–H	–	1.010	–	–	–	1.009	–
C(ph)–N(NO)	–	–	–	–	1.471	1.467	1.467
N–O	–	–	–	–	1.231	1.232	1.232
C(ph) –N(Me)	–	–	1.379	1.379	–	–	–
C–H(Me)	–	–	1.096	1.096	–	–	–
C(Me)–N	–	–	1.453	1.453	–	–	–
C(ph) –N (Et-EtOH)	–	–	–	–	–	–	1.386
Bond angle / ^{0}							
C(ph) –N=N un-substituted	114.802	114.602	114.544	114.54	115.10	–	–
C(ph) –N=N donating side	–	115.270	115.320	115.32	–	115.57	115.52
C(ph) –N=N acceptor side	–	–	–	–	114.29	114.10	114.09
C(ph)–C(ph)–N un-substituted	120.053	120.173	120.206	120.21	119.97	–	–

[vii] Table 5-4: continued overleaf

side							
C(ph)–C(ph)–N donating side	–	120.618	120.850	120.85	–	120.20	120.93
C(ph)–C(ph)–N acceptor side	–	–	–	–	119.97	120.14	120.16
C(ph)–C(ph) –C(ph)	119.99	120.16	119.96	119.96	120.01	120.15	119.79
C(ph)–C(ph)–H	119.990	119.838	119.748	119.81	120.13	119.96	119.80
C–C–N(H)	–	120.640	–	–	–	120.593	–
C–N–H	–	116.572	–	–	–	117.779	–
C–C–N(NO)	–	–	–	–	118.90	119.01	119.02
C–N–O	–	–	–	–	117.68	117.78	117.79
C–C–N(Me)	–	–	121.209	121.21	–	–	–
C–N–C(Me)	–	–	120.193	120.19	–	–	–
N–C–H(Me)	–	–	110.993	110.99	–	–	–
C–C– N(Et-EtOH)	–	–	–	–	–	–	121.53
Torsional angle / ^{0}							
C(ph)–C(ph) –N=N	180.01	-179.95	-179.99	-179.99	-179.99	-179.76	-179.41
C(ph)–C(ph) –N–H	–	-160.55	–	–	179.983	162.775	–
C(ph)–C(ph) –N–O	–	–	–	–	–	-179.98	-179.92
C–N=N–C (dihedral)	180.00	-179.95	-180.00	-180.0	-180.00	-179.93	-179.83

From Table 5-4, it is found that, upon substitution of the parent *trans*-AB molecule by an electron donor (NH_2 group in AAB, N,N-dimethylamino group in MY and two donating groups, *i.e.* N,N-dimethylamino group, and *o*-methyl group in MMY) , electron acceptor (nitro group in NAB), and electron donor-acceptor (NH_2 and NO_2 groups in DO3, $N(CH_2CH_2OH)(CH_2CH_3)$ and NO_2 groups in DR1), the N=N bond distance increases from 1.261 to 1.265, 1.266, 1.266, 1.268 and 1.269 Å, for the parent azobenzene, electron donating and electron donating-acceptor azobenzenes, respectively. On the other hand the N=N bond distance is identical for the parent azobenzene and electron acceptor azobenzene. The N=N bond distance changed due to the electronic effect of substitution, where the electron donating group elongates the N=N distance, the electron acceptor group has no effect on this bond and the electron donating-acceptor groups elongate the same bond to greater extent than the electron donating group.

Similarly, the C(ph)–C(ph) bond distance increases gradually upon going from the parent molecule to the substituted molecules. Interestingly, a reverse trend is observed for the C–N(azo) bond distance in all cases, it decreases by the average of 0.001 Å in the un-

substituted side, by the average of 0. 014 Å in the electron donating side and by 0.013 Å in the electron acceptor side as compared to the parent compound. The C(ph)–H bond lengths are almost the same in AB and all its substituted analogues, and the value for this bond length is 1.085 Å.

In DO3, there is a shortening in C(ph)–N(H) and N–H bond lengths by 0.008 and 0.001 A^0, respectively, as compared to AAB. Similarly, in DO3 relative to NAB, the C(ph)–N(NO) bond distance decreases by 0.004 Å, and the N–O bond length undergoes an increase of 0.001 Å. The observed contraction in the C–N(azo) in the donating and accepting sides of DO3, as compared to AAB and NAB, indicates a greater conjugation and π-electron delocalisation in electron donating-accepting azobenzenes as compared to electron donating and electron-accepting azobenzenes. The C–C–N(H) and C–N–H bond angles are subject to an increase by 0.017^0 and 1.082^0, respectively, as compared to that in AAB. Similarly, as compared to that in NAB, the C–C–N(NO) and C–N–O bond angles increase by 0.108 and 0.1^0, respectively, in DO3.

In comparison between MY and MMY, the C(ph) –N(Me), C–H(Me) and C(Me)–N bond lengths are found to be very similar, thus the effect of introducing the *o*-methyl group on these bond lengths is negligible. The negligible effect of the introducing this group is also applied to the C–C–N(Me), C–N–C(Me) and N–C–H(Me) bond angles.

Comparing DO3 and DR1 with NAB, the C(ph)–N(NO) bond length is decreased by 0.004 and 0.004 Å, respectively, while N–O bond length is increased by the same extent for DO3 and for DR1 by 0.001 Å, compared to that in NAB. The C–C–N(NO) and C–N–O bond angles are increased significantly, by 0.108^0 and 0.1^0 for DO3, and 0.12^0 and 0.109^0 for DR1, respectively, as compared to that in NAB.

5.3.1.2.2 Structures of *Cis* Isomers

The optimised parameters of the *cis* forms of AB, AAB, MY, MMY, NAB, DO3 and DR1 are presented in Table 5-5. To the best of the author's knowledge, this is the first report on the molecular structural parameters of the *cis* conformations of these important classes of molecules, *viz.* MY, MMY, NAB, DO3 and DR1. Literature calculations of the geometrical parameters of the *cis* forms of the other molecules were available.[76,83,91,95]

Table 5-5[viii] Optimized geometrical parameters of the *cis* isomers of the studied azobenzenes in the gas phase.

	AB	AAB	MY	MMY	NAB	DO3	DR1
Bond length / Å							
N=N	1.249	1.254	1.255	1.255	1.248	1.254	1.255
C–N(azo) un-substituted side	1.436	1.434	1.433	1.434	1.433	–	–
C–N(azo) donating side	–	1.427	1.424	1.422	–	1.419	1.415
C–N(azo) acceptor side	–	–	–	–	1.431	1.423	1.421
C(ph)–C(ph)	1.397	1.399	1.400	1.401	1.397	1.399	1.400
C(ph)–H	1.086	1.086	1.085	1.085	1.084	1.085	1.083
C(ph)–N(H)		1.387	–	–	–	1.379	–
N–H		1.010	–	–	–	1.009	–
C(ph)–N(NO)	–	–	–	–	1.468	1.464	1.463
N–O	–	–	–	–	1.232	1.233	1.233
C(ph) –N(Me)	–	–	1.382	1.383	–	–	–
C–H(Me)	–	–	1.096	1.096	–	–	–
C(Me)–N	–	–	1.454	1.453	–	–	–
C(ph) –N(Et-EtOH)	–	–	–	–	–	–	1.381
Bond angle / ^{0}							
C(ph) –N=N un-substituted side	124.036	124.346	124.398	124.195	123.787	–	–
C(ph) –N=N donating side	–	125.013	125.153	125.204	–	124.957	125.101
C(ph) –N=N acceptor side	–	–	–	–	124.576	125.436	125.497
C(ph) –C(ph) –N un-substituted side	119.711	119.751	119.776	119.803	119.726	–	–
C(ph)–C(ph)–N donating side		120.539	120.787	120.195	–	120.616	121.038
C(ph)–C(ph)–N acceptor side	–	–	–	–	119.518	119.638	119.678
C(ph)–C(ph) –C(ph)	119.991	119.880	119.926	119.826	120.016	119.976	119.775
C(ph)–C(ph)–H	119.999	119.816	119.721	119.699	120.125	119.907	119.741
C–C–N(H)	–	120.740	–	–	–	120.757	–
C–N–H	–	116.440	–	–	–	117.522	–
C–C–N(NO)	–	–			119.035	119.143	119.164
C–N–O	–	–			117.688	117.788	117.806
C–C–N(Me)	–	–	121.359	121.322	–	–	–
C–N–C(Me)	–	–	119.881	119.847	–	–	–

[viii] Table 5-5: continued overleaf

N–C–H(Me)	–	–	110.988	110.999	–	–	–
C–C–N(Et-EtOH)	–	–	–	–	–	–	121.639
Torsional angle / ^{0}							
C(ph)–C(ph)–N=N un-substituted side	50.420	57.443	57.384	-53.845	-45.374	–	–
C(ph)–C(ph)–N=N donating side	–	35.632	34.327	-39.322	–	30.407	28.005
C(ph)–C(ph)–N=N acceptor side	–	–	–	–	-56.270	60.333	61.022
C–N=N–C (dihedral)	9.782	10.423	10.563	-11.743	-10.246	11.502	11.841

From Table 5-5, it is found that, during complete optimisation, all *cis* isomers show the completely twisted conformation for the C(ph)–C(ph)–N=N torsional angles because of the repulsive interactions between the hydrogen atoms of the phenyl rings. The electron donating substitution/s show more obvious influence on the C(ph)–C(ph)–N=N torsional angle as compared to that in the parent molecule. The change in C(ph)–C(ph)–N=N torsional angle on the un-substituted side is by 7.02^0, 6.96^0 and 3.43^0, whereas the change on the electron donating side is by 14.8^0, 16.1^0 and 11.1^0 for AAB, MY and MMY, respectively. On the other hand, the electron acceptor substitution shows similar influence on the un-substituted and the electron accepting sides as compared to AB, since the change in C(ph)–C(ph)–N=N dihedral angle on the un-substituted side is by 5.05^0 and on the electron acceptor side is by 5.85^0. For the electron donating-acceptor azobenzenes the influence is much more obvious, the change is by 22.42^0 on the electron donating side and by 10.60^0 on the electron acceptor side. The change in the C–N=N–C dihedral angles are in the following order:

DR1 > MMY > DO3 > MY > AAB > NAB > AB

DR1 and MMY with the largest substituent in the first molecule and with an additional substitution at the *ortho* position for the second molecule present the largest C–N=N–C dihedral angles, where NAB as an electron acceptor azobenzene shows the smallest C–N=N–C dihedral angle after the parent molecule.

Upon substitution of the parent *cis*-AB molecule by an electron donor in AAB, MY, and MMY, electron acceptor in NAB, and electron donor-acceptor DO3, and DR1, the N=N bond distance increases from 1.249 Å to 1.254, 1.255, 1.255, 1.254 and 1.255 A^0, for the

parent azobenzene, electron donating and electron donating-acceptor azobenzenes, respectively. On the other hand the N=N bond distance decreases from 1.249 Å to 1.248 Å, for the parent azobenzene and electron acceptor azobenzene, respectively. The N=N bond distance changed due to the electronic effect of substitution, where the electron donating group elongates the N=N distance, the electron acceptor group shortens this bond and the electron donating-acceptor groups elongate the same bond with similar extent as the electron donating group.

Similarly, the C(ph)−C(ph) bond distance remains the same in NAB as compared to AB, but increases in the other molecules by 0.002, 0.003, 0.004, 0.002 and 0.003 Å, for AAB, MY, MMY, DO3 and DR1, respectively. Interestingly, a reverse trend is observed for the C−N(azo) bond distance in all cases, it decreases by the average of 0.003 Å in the un-substituted side, by the average of 0.013 Å in the electron donating side, and by 0.011 Å in the electron acceptor side as compared to the parent compound. The shortening is significant for DO3 and DR1; 0.013 and 0.017 Å for DO3 and by 0.015 and 0.021 Å for DR1 in the electron donating and accepting sides, respectively. The C(ph)−H bond lengths are almost the same in AB and all its substituted analogues, and the value for this bond length is 1.085 Å.

The calculated C(ph) −N=N bond angle is a measure of the distance separating the two phenyl rings. In all molecules the two phenyl rings were not facing each other due to the electronic repulsion between the hydrogen atoms in one hand, and the substituent atoms on the other hand. The C(ph) −N=N bond angles in the un-substituted side increase for electron donating azobenzenes by 0.310^0, 0.362^0 and 0.159^0 for AAB, MY and MMY, respectively, and decreases for electron acceptor azobenzene by 0.249^0 . It increases by a significant amount for the electron donating azobenzenes in the electron donating side; the increase is by 0.977^0, 1.117^0 and 1.168^0 for AAB, MY and MMY, respectively, and by insignificant amount for electron acceptor azobenzene, 0.54^0. The electron donating-acceptor azobenzenes in turn show a significant increase in the C(ph) −N=N bond angles on both sides, the change is 0.921^0 and 1.4^0 for DO3, where for DR1 the increase is the maximum, 1.065^0 and 1.461^0 on the electron donating and electron accepting sides, respectively. This indicates that larger substitution lead to larger repulsive interaction and the two phenyl rings are more separated from each other corresponding to larger C(ph) −N=N bond angles.

In DO3, there is a shortening in C(ph)−N(H) and N−H bond lengths by 0.008 Å and 0.001 Å, respectively, as compared to AAB. Similarly, in DO3 relative to NAB, the C(ph)−N(NO)

bond distance decreases by 0.004 A^0, and the N–O bond length undergoes an increase of 0.001 Å. The observed contraction in the C–N(azo) bond in the donating and accepting sides of DO3, as compared to AAB and NAB, indicates a greater conjugation and π-electron delocalisation in electron donating-accepting azobenzenes as compared to electron donating and electron-accepting azobenzenes. The C–C–N(H) and C–N–H bond angles show an increase of 0.017^0 and 1.082^0, respectively, as compared to that in AAB. Similarly, as compared to that in NAB, the C–C–N(NO) and C–N–O bond angles increase by 0.108^0 and 0.1^0, respectively, in DO3.

Comparing MY and MMY, the C(ph) –N(Me), C–H(Me) and C(Me)–N bond lengths are found to be very similar, thus the effect of introducing the *o*-methyl group on these bond lengths is negligible. Whereas the C–C–N(Me), C–N–C(Me) and N–C–H(Me) bond angles are different, the first two bond angles are increased for MMY by 0.037^0 and 0.034^0, respectively, while the third decreases by 0.011^0 for MMY, as compared to that in MY.

Comparing DO3 and DR1 with NAB, the C(ph)–N(NO) bond length is decreased by 0.004 Å and 0.005 Å, respectively, while N–O bond length is increased by the same extent for DO3 and DR1 by 0.001 A^0 compared to that in NAB. The C–C–N(NO) and C–N–O bond angles are increased significantly, by 0.108^0 and 0.1^0 for DO3, and 0.129^0 and 0.118^0 for DR1, respectively as compared to that in NAB.

5.3.1.3 Relative Energies of *Cis* and *Trans* Isomers

The importance of the number and type of functions used to describe the electrons in determining the accuracy of a calculation in the system being studied is discussed in Section 2.4.2. The *trans* and *cis* geometries at B3LYP/6-31G and 6-31G(d,p) basis set were obtained, Table 5-6. The effect of basis sets on the relative stability of *trans* and *cis* isomer is obvious the larger basis set generally results in slightly smaller relative stability between the *trans* and *cis* isomer. The difference in the relative energies between the two different basis sets are in the range of 0.05-3.06 kJ/mol, where MY shows the smallest difference and NAB shows the largest one.

Molecule/ structure	6-31G		6-31G(d,p)	
	E_0	$\Delta E_0^{\dagger}$	E_0	$\Delta E_0^{\dagger}$
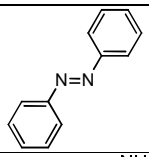 AB	**-572.417727** *-572.392932*	65.10	**-572.586831** *-572.562486*	63.92
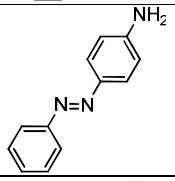 AAB	**-627.744165** *-627.718234*	68.08	**-627.931721** *-627.906689*	65.72
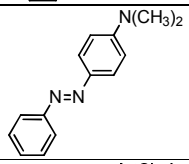 MY	**-706.275845** *-706.250055*	67.71	**-706.490785** *-706.465013*	67.66
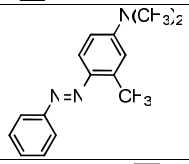 MMY	**-745.556314** *-745.531234*	65.85	**-745.783299** *-745.759083*	63.58
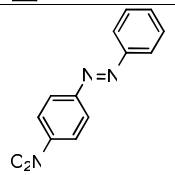 NAB	**-776.834582** *-776.810214*	63.98	**-745.759083** *-777.083469*	60.92
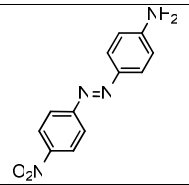 DO3	**-832.163558** *-832.137714*	67.85	**-832.4303740** *-832.405874*	64.32
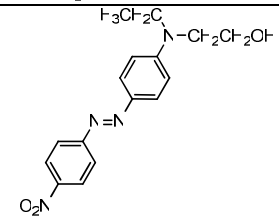 DR1	***** *	*	**-1064.7452290** *-1065.7452290*	69.13

Table 5-6 *Trans-cis* energies differences (in kJ/mol) and their dependence on the basis set for azobenzenes in the gas phase. E_0 is the sum of electronic and zero point energy. Energy values in hartree of *trans* (bold font) and *cis* (italics font). † Relative to *trans* isomer. * Not calculated.

The obtained values were in good agreement with the available literature,[38,64,84,89] Table 5-7. All molecules have comparable values of energy difference between the *cis* and *trans* isomer

in the range 58-68 kJ/mol, the electronic contribution of substituents has no significant effect on the relative stability of the two isomers. In comparison to the parent compound, some molecules show smaller difference between the energies of the two isomers, whereas some molecules show larger difference. In general DR1 and NAB have the lowest energy difference, E_{cis}-E_{trans}= 58 and 61 kJ/mol, respectively, compared to 64 kJ/mole for AB. For the other molecules, MMY has energy difference comparable with AB. While the rest of molecules have energy differences larger than AB, ranging from 65−68 kJ/mol.

Table 5-7[ix] Calculated energies (in kJ/mol) of *trans* (bold font) and *cis* (italics font) geometries of azobenzenes in gas phase. ZPE is the zero point energy. E_{el} is the electronic energy. E_0 is the sum of electronic and zero point energy. † Relative to the *trans* isomer. [a] From reference[89], at 6-31+G(d). [b] From reference[84] , at 6-31G(d). [c] From reference[38] at 6-31G(d). [d]From reference[64] at 6-31G(d).

Molecule/structure	ZPE	E_{el}	E_0	ΔE_0 †
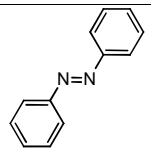 AB	**0.1909700**	**-572.7778010**	**-572.5868310** **-572.78430**[a]	63.92 66.24[a]
	0.190424	*-572.752910*	*-572.562486* *-572.75907*[a]	
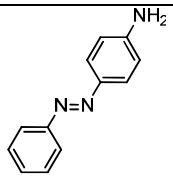 AAB	**0.207552**	**-628.139273**	**-627.931721**	65.72
	0.207067	*-628.113756*	*-627.906689*	
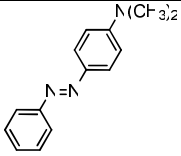 MY	**0.263973**	**-706.754758**	**-706.490785**	67.66
	0.2634890	*-706.728502*	*-706.465013*	
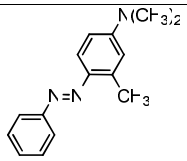 MMY	**0.291560**	**-746.074859**	**-745.783299**	63.58
	0.291139	*-746.050222*	*-745.759083*	
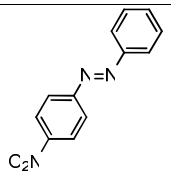 NAB	**0.193442**	**-777.276911**	**-777.083469**	60.92
	0.193021	*-777.253287*	*-777.060266*	

[ix] Table 5-7: continued overleaf

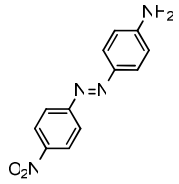 DO3	**0.210043**	**-832.430374**	**-832.4303740**	64.32 68.00[b] 65.27[c]
	0.209658	*-832.615532*	*-832.405874*	
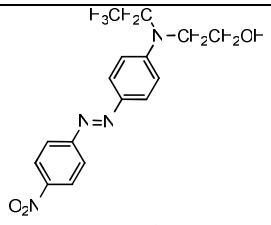 DR1	**0.3285880**	**-1065.0738170**	**-1064.7452290**	69.13 65.31[d]
	0.328588	*-1065.073817*	*-1065.7452290*	

5.3.1.4 Dipole Moments of Gas phase *Cis* and *Trans* Isomers

The dipole moments of the *cis* and *trans* isomers in the gas phase are displayed in Table 5-8. For most molecules the dipole moment of the *cis* isomer is greater than that of the *trans* isomer, this may due to the unequal sharing of electrons in the bent structure of the *cis* isomer. However, for NAB, DO3 and DR1 the dipole moment of the *trans* isomer is greater than that of the *cis* isomer, the apparent difference between these molecules and other molecules is the presence of the NO_2 at the *para* position.

Table 5-8[x] DFT dipole moments magnitudes and directions for the optimised geometries of *cis* and *trans* in the gas phase.

Molecule /structure	μ_{Cis} / debye	μ_{Trans} / debye
AB	3.19 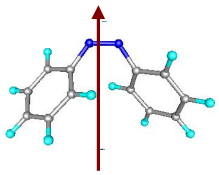	0.00
AAB	6.37 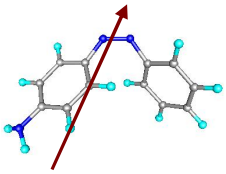	3.75 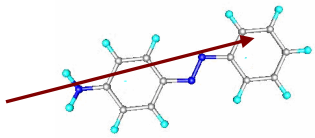
MY	5.99 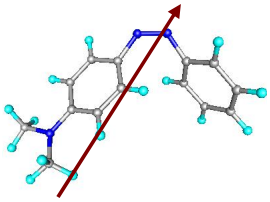	4.16 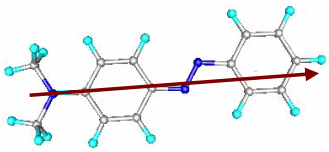
MMY	5.45 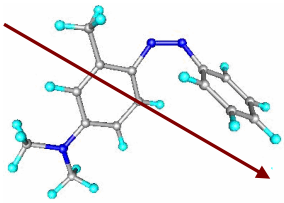	4.00 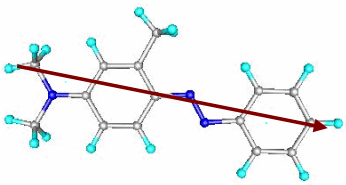
NAB	4.21 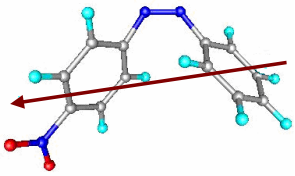	5.92 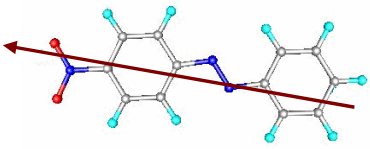

[x] Table 5-8: continued overleaf

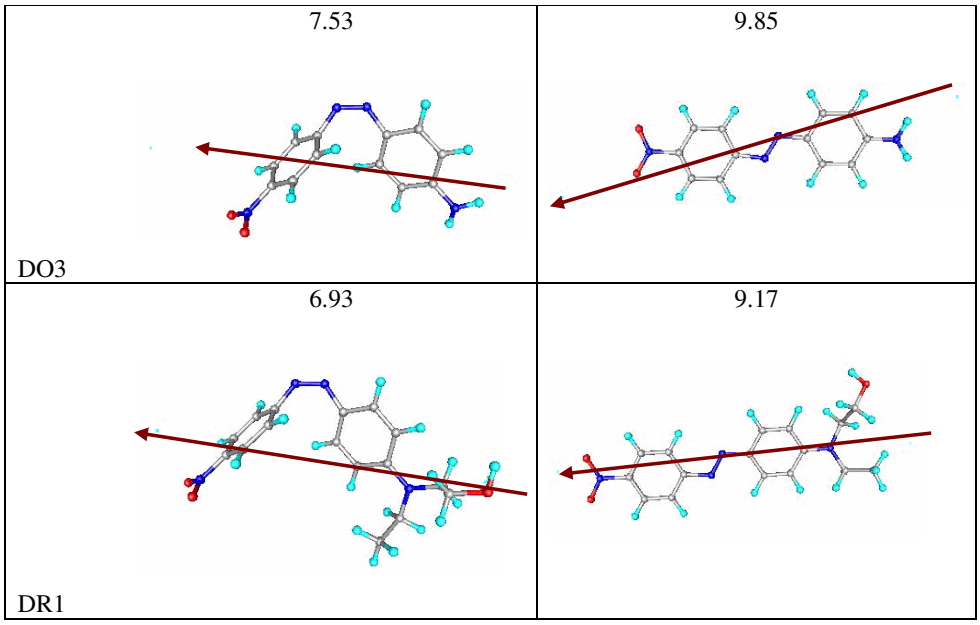

5.3.2 Geometries of Solvated *Cis* and *Trans* isomers

5.3.2.1 Relative Energies of *Cis* and *Trans*

Examination of the effect of basis sets on the relative stability of the *trans* and *cis* isomer in solution is performed at the same basis sets as tested in the gas phase, *i.e.* 6-31G and 6-31G(d,p). Table 5-9 displays the total energies of the *trans* and *cis* isomer, E_0, and energy differences between the two isomers, ΔE_0, at B3LYP/6-31G and B3LYP/6-31G(d,p) level of theory/basis set for AAB as an example.

	6-31G		6-31G(d,p)	
	E_0	ΔE_0	E_0	ΔE_0
Trans	-627.766143	55.90	-627.952475	58.08
Cis	-627.744853		-627.930354	

Table 5-9 The total energies of the *trans* and *cis* isomer (in hartree) for AAB in DMSO and their dependence on the basis set. ΔE_0 values in kJ/mol.

The difference between the energies of the two isomers in the gas phase is significantly larger than that in DMSO. In the gas phase, the energy difference between the *cis* and *trans* isomer was larger at smaller basis than at larger basis set, ΔE_0 = 68.08 and 65.72 kJ/mol at 6-31G and 6-31G(d,p), respectively. Oppositely, in DMSO ΔE_0 = 55.90 and 58.08 kJ/mol at 6-31G and 6-31G(d,p), respectively.

Table 5-10[xi] shows the energy and *cis-trans* energy difference of stable conformers for the azobenzenes studied at 6-31G(d,p) basis set. The energy differences between the *cis-trans* pairs of different molecules in the gas phase and in solution were in the range 57-68 kJ /mol, from gas phase to solution and from benzene to DMSO the differences in energy decrease, indicating a correlation between the polarity of the solvent and the relative stabilization of the *cis-trans* pair, the polar solvent in this study leads to more stabilisation of the *cis* isomer.

Molecule/structure	*Cis-Trans* energy difference ($\Delta E^0_{cis-trans} = E^0_{cis} - E^0_{trans}$) / kJ mol^{-1}		
	ε = 1.0	ε = 2.2	ε = 46.7
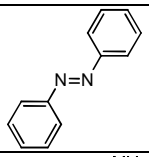 AB	63.92	58.31	53.90
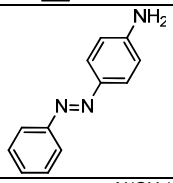 AAB	65.72	62.27	58.08
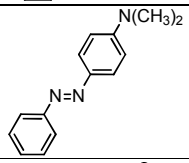 MY	67.66	61.90	57.60
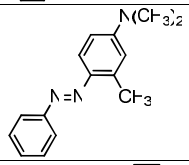 MMY	63.58	60.90	56.00
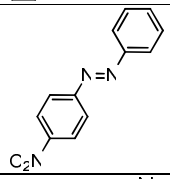 NAB	60.92	57.16	52.19
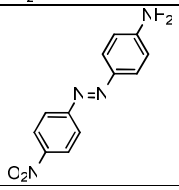 DO3	64.32	61.00	*

[xi] Table 5-10: continued overleaf

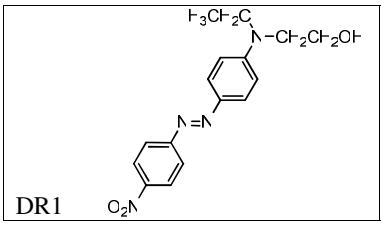 DR1	69.13 65.31[a]	* 64.06[a]	*

Table 5-10 *Trans-cis* energy differences in gas phase, ε = 1.0 and solution; benzene, ε = 2.2, and DMSO, ε = 46.7). [a] From reference[64] at 6-31G(d). *Not calculated.

5.3.2.2 Effect of Solvent

Briquet *et al.* [2006][90] reported using the Møller-Plesset approach (MP2) and time-dependent DFT (TDDFT) for the first time to determine the ground state geometry of the *trans*-AB in solution, and concluded that the planarity of the molecule increased with the polarity of the solvent. The planarity of *trans*-AB has been proved as detailed in Section 5.3.1.2.1. Otherwise, the present study is the first reported of the ground state geometries of *trans* and *cis* forms of the studied molecules in solution.

For the sake of brevity, only the optimised parameters belonging to the azo linkage are considered. The optimised parameters of the azo linkage of the *trans* and *cis* isomers, in the gas phase and two solvents, namely benzene and DMSO, for AAB as a representative example are summarised in Table 5-11. From Table 5-11, the impact of the solvent is significant for the bond lengths and bond angles of the azo linkage compared to those in the gas phase, their respective variations being limited to 0.003 Å and 0.9^0. The changes in these parameters from the gas phase into the solution are more significant upon changing the solvent. The general effect of more polar solvent is elongation of the azo linkage bond lengths and increase of the azo linkage bond angles: however, there are some exceptions. The N=N bond distance increased in DMSO solvent by 0.003 Å and 0.005 Å for the *trans*, and *cis* isomer, respectively, while the effect on the C−N(azo) bond lengths depends on the position of this bond. In the un-substituted side, the bond distance of this bond is the same for the *trans* isomer and increases by 0.001 Å in the *cis* isomer. On the other hand, on the electron donating side the trend is different, for the *trans* isomer and *cis* isomer the C−N(azo) bond length decreases by 0.003 Å and 0.006 Å, respectively. The bond angles of the azo linkage change with DMSO in similar manner as the bond lengths, since C(ph)−N=N bond angles on the un-substituted side increase by 0.141^0 for *trans*, oppositely for the *cis* isomer it decreases by 0.009^0. The C(ph) −N=N bond angles on the electron donating side increase in DMSO in all cases by 0.375^0 and 0.689^0 for the *trans* and *cis* isomer,

respectively. The effect of solvent on the C-N=N-C dihedral angles is generally to increase as the solvent polarity is increased by 0.032^0 and 0.124^0 for the *trans* and *cis* isomer, respectively, *viz* to DMSO than to benzene.

	Trans	*Cis*
Bond length / Å		
N=N	1.265 **1.267** *1.270*	1.254 **1.256** *1.261*
C–N(azo) un-substituted side	1.418 **1.418** *1.418*	1.434 **1.434** *1.435*
C–N(azo) donating side	1.407 **1.404** *1.401*	1.427 **1.423** *1.417*
Bond angle / ^{0}		
C(ph) –N=N un-substituted side	114.602 **114.626** *114.767*	124.346 **124.254** *124.245*
C(ph) –N=N donating side	115.270 **115.552** *115.927*	125.013 **125.272** *125.961*
CN=NC dihedral	-179.950 **179.916** *179.948*	10.423 **10.624** *10.748*

Table 5-11 Optimised parameters of the azo linkage of AAB for the *trans* and *cis* isomers in gas phase (regular font), benzene (bold font), and DMSO (italics font).

5.3.2.3 Dipole Moments of Solvated *Cis* and *Trans* Isomers

The dipole moments of the *cis* and *trans* isomers in the gas phase and in solution are displayed in Table 5-12. Dipole moments directions for AAB are shown in Figure 5-5. In general, for both isomers, the dipole moments are increase gradually from the gas phase to solution and from benzene to DMSO. As mentioned in Section 5.3.2.2, the solvent plays a significant role in determining the relative stability of the *trans* and *cis* isomer.

Molecule/structure	μ_{Cis}	μ_{Trans}
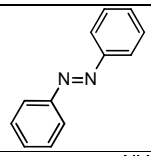 AB	3.19	0.00
	4.35	**0.00**
	5.25	*0.01*
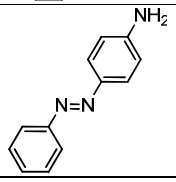 AAB	6.37	3.75
	6.44	**4.00**
	8.34	*5.31*
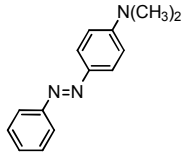 MY	5.99	4.16
	6.97	**4.81**
	9.61	*5.68*
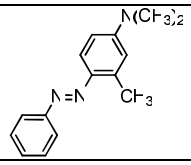 MMY	5.45	4.00
	6.37	**4.66**
	7.81	*5.56*
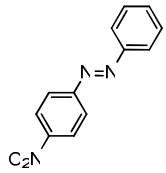 NAB	4.21	5.92
	5.86	**6.79**
	6.61	*7.77*
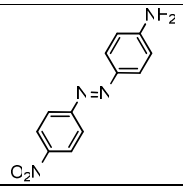 DO3	7.53	9.85
	10.80	**13.77**
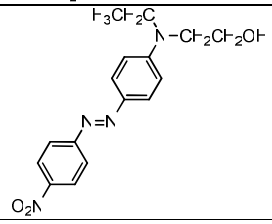 DR1	6.93	9.17
	8.20	*

Table 5-12 DFT dipole moments in debye for the optimised geometries of *cis* and *trans* in gas phase (regular font), in benzene (bold font), and in DMSO (italics font). *Not calculated.

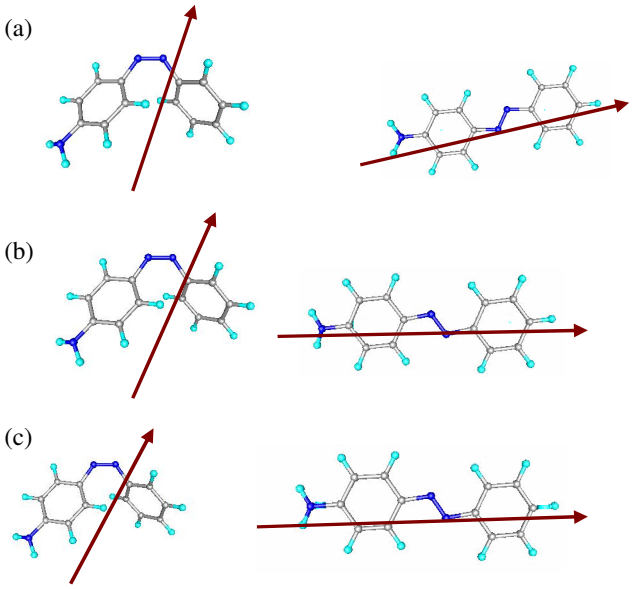

Figure 5-5 Dipole moments directions of *cis* and *trans* isomers of AAB in gas phase and solution. (a) gas phase, (b) benzene phase, and (c) DMSO phase.

5.3.3 Potential Energy Curves for Thermal *Cis-Trans* Isomerisation

5.3.3.1 Case Study; *p*-aminoazobenzene

5.3.3.1.1 Methodology

5.3.3.1.1.1 Gas Phase

First, we optimised the *trans*-AAB geometry (or starting with *cis* geometry in some molecules) with standard thresholds for optimisation; vibrational analysis was followed to ensure the nature of the stationary point; the geometry was confirmed to be the minimum energy geometry of the *trans*/*cis* form by the absence of any imaginary frequencies.

After geometry optimisations of the *trans*/*cis* isomer, the potential energy curves of the dihedral rotation and inversion pathways were constructed by scanning the appropriate angles while all the other geometrical parameters were fully optimised without any symmetry restrictions. The geometry of the *cis*/*trans* isomer was extracted from such curves, and re-optimised without any symmetry restriction and confirmed to be the minimum energy geometry by the aid of the frequency calculations, *i.e.* by the absence of any imaginary frequencies. The transition state geometry was determined from the intermediate energy point (see below) in the potential energy curve of the dihedral rotation pathway and the maximum energy point in the potential energy curve of the inversion pathway; these

geometries were confirmed to correspond to the transition states by frequency calculations, where only one imaginary frequency for each geometry was obtained.

5.3.3.1.1.2 Solution Phase

For assessing the solvent effects, the well-known Polarisable Continuum Model (PCM)[90] was selected. In PCM, the system is divided into a solute part lying inside a cavity, and a solvent part represented as a structureless material, characterised by its dielectric constant, radius, density, molecular volume, etc. Because of the lack of solvent structure, the model is not appropriate for solvents that have important specific interactions like hydrogen bonds since the solvents used in this study are aprotic solvent such shortcomings of the model should not be important. It has the advantage of allowing the geometry and dipole moment of the solute to be adjusted to reflect the interaction with the medium. Also, it is particularly simple to implement and it is a computationally efficient method for the prediction of general structural and stability trends in polar solvent media such as DMSO. The PEC for the dihedral rotation pathway of AAB was constructed in the gas phase and in solutions, namely in benzene and DMSO; such plots are represented in Figure 5-6.

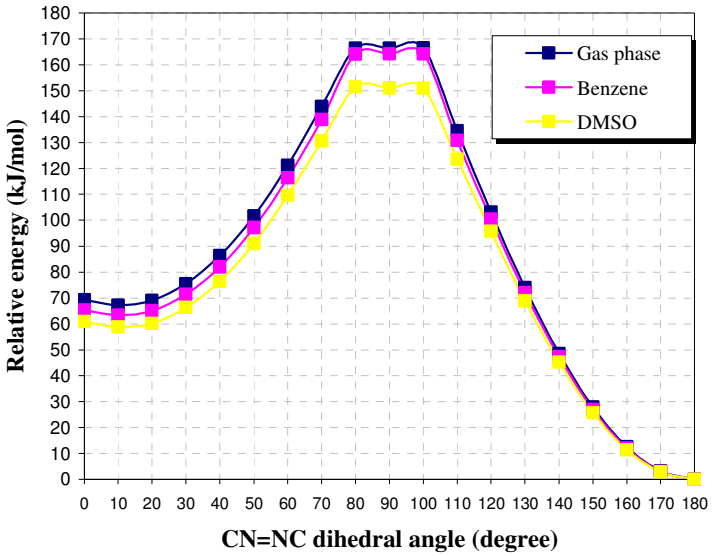

Figure 5-6 DFT-calculated energy profiles of the PECs of the dihedral rotation pathway.

From Figure 5-6, it is clear that the PECs in the gas phase, in benzene and DMSO have the same form, *i.e.* the *trans*, *cis* and transition state geometries have similar CN=NC dihedral

angles. The *trans* has the dihedral angle CN=NC ≈180^0, *cis* CN=NC ≈10^0 and the transition state CN=NC ≈ 90^0. Accordingly, for all the other molecules only the PECs in the gas phase were constructed, the gas phase structures of the *cis, trans* and transition state were determined and assumed to also represent the structures of these species in the two solvents. This procedure is considered appropriate for the following two reasons:

i. The optimized geometries obtained in the gas phase were re-optimized in the solvated state.
ii. Vibrational frequencies were computed for the re-optimized geometries in solution, the number of imaginary frequencies confirmed the nature of the stationary points for all geometries, in which real frequencies for the *cis* and *trans* isomers and one imaginary frequency for the transition state were accepted.

The title geometries where re-optimised in the desired solvent, *viz.* benzene and DMSO by fixing the CN=NC dihedral angle (for the dihedral rotation transition state) at 90^0 while all the other parameters were fully optimised without any symmetry constrains, or by fixing one of the CN=N angle (for the inversion transition state) at 180^0 and also all the other parameters were fully optimised without any symmetry constrains. From the frequency calculations it was possible to draw the kinetics and activation parameters for the thermal *cis*-to-*trans* isomerisation considering the following reaction.

$$Cis \xrightarrow{K^{\#}} [\text{Transition State}]^{\#} \xrightarrow{k_{-1(\Delta)}} Trans$$

5.3.3.1.2 Dihedral Rotation and Inversion Potential Energy Curves in the Gas Phase

The potential energy of the molecule was plotted as a function of rotation of the dihedral angle C-N=N-C (azo linkage group connected to the two phenyl rings) across a 180^0 range to produce the dihedral rotation potential energy curve. While, for the inversion pathway, such a curve was obtained by scanning one of N=N-C bond angles (azo linkage group connected to one of the phenyl rings). In the dihedral rotation pathway, in all cases, the scanning angle was initialised at 0^0 (or 180^0) and incremented by 10 degrees until reaching a 180^0 (or 0^0) dihedral angle while all the other parameters were fully optimized. In the inversion pathway, there are two possible pathways, depending on which ring inverts, and the two alternative PECs were constructed. In all cases, starting from the *trans* geometry the bond angle was fixed at 100^0 and incremented by +10 degrees until reaching the 240^0 bond angle, while all the other parameters were fully optimized. We assign the two inversion pathways as α- and

β-inversion, as illustrated in Figure 5-1. Figure 5-7 illustrated the PECs of the dihedral rotation and the two inversion pathways for AAB.

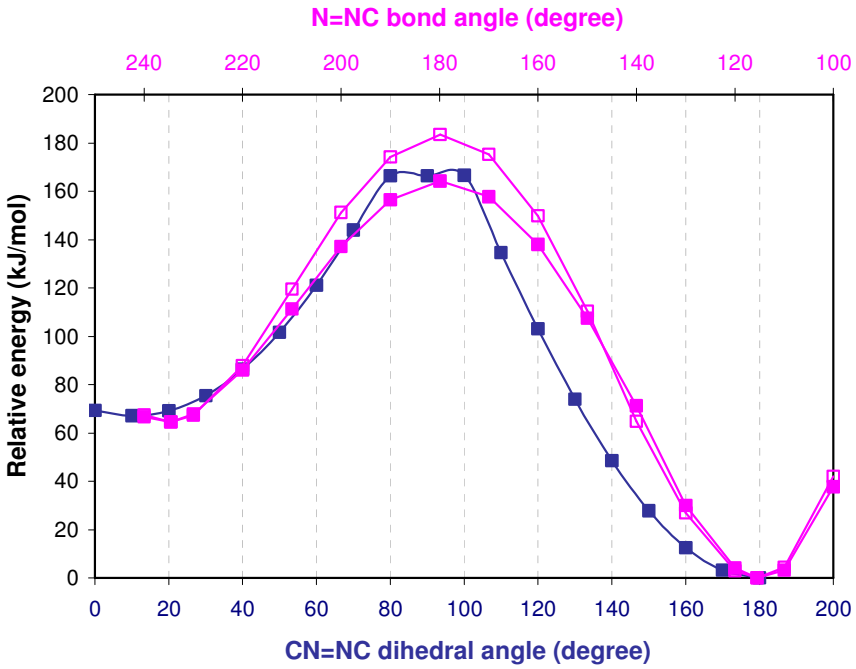

Figure 5-7 DFT-calculated energy profiles of the PECs of the dihedral rotation and inversion pathways of AAB: PEC of -■-: dihedral rotation pathway, -■-: α-inversion pathway, -□-: β-inversion pathway.

The features of the PECs may be summarised as follows:

i. The PEC produced *via* the dihedral rotation pathway has a plateau region at the top of the curve instead of the expected maximum, as illustrated in Figure 5-7 ; this is the case for all molecules expect the parent compound, *i.e.* azobenzene. The PEC was constructed by varying the torsional angle NC=CN by 10 degree each time up to 19 times, the plateau spans 3 to 5 angles around 90^0. Generally the plateau region extends over a wider range for larger molecules (expect for MMY). It was found that the shape of the curve did not change with higher basis sets, see Section 5.3.3.1.2.1. The transition state geometry of the dihedral rotation pathway was taken to be that corresponding to the dip at the centre of the plateau region, in all cases at a 90^0 torsional angle (the nature of this transition state is discussed below). The frequency

calculations confirmed that the obtained geometry was corresponded to the transition state through one imaginary frequency.

ii. The PECs *via* both of the alternative α- and β-inversion pathway, showed clear maxima in all cases, thus the determination of the transition states geometries for the two inversion pathways was straightforward, as illustrated in Figure 5-7. Also the frequency calculations confirmed that the obtained geometries corresponded to the transition states through one imaginary frequency.

iii. In all cases except the parent molecule, the transition states geometries obtained *via* dihedral rotation and α-inversion pathways have essentially identical structures, *i.e.* they are linear transition states with the same ring inverted in each case. Table 5-13 gives the important geometrical parameters of the transition states obtained *via* the dihedral rotation and α-inversion pathway for AAB, discussion of this point in more detail is carried out in Section 5.3.5.

	Dihedral rotation	α-inversion
Bond length / Å		
N=N	1.230	1.230
α-C-N	1.332	1.332
β-N-C	1.435	1.435
Bond angle / ^{0}		
α-C-N=N	179.997	179.900
β-N=N-C	117.640	117.611
Torsional angle/ ^{0}		
α-C-C-N=N	89.7236	-89.9294
β-N=N-C-C	-0.0974	-0.4251
C-N=N-C (dihedral)	90.00	179.63

Table 5-13 Key parameters of the transition state geometries of AAB obtained *via* the dihedral rotation and α-inversion pathways, demonstrating the equivalence of the two geometries.

5.3.3.1.2.1 Effect of Basis Sets

Although, there were no dramatic differences in the structures of the potential energy surfaces obtained at different basis sets, some minor differences could be seen. Two examples of the effect of basis sets on the structure of the potential energy surface are discussed in this section.

Figure 5-8 presents the PECs for the dihedral rotation pathway of AB at two basis sets, *viz.* 6-31G and 6-31G(d,p). 6-31G(d,p) is rich in polarisable functions relative to the other basis set 6-31G. The lack of polarisation functions results in weak ability in optimisation to the minimum energy geometries at some points. This is seen clearly in the geometry at CN=NC

dihedral angle equals to 70^0 since it was not optimised properly, and to a lesser extent for the geometries at dihedral angles equal 0^0, 10^0, 20^0, and 30^0. Alternatively optimisation at dihedral angle equals 80^0, seems to occur to give a lower minimum energy compared to the optimisation of the same angle at higher basis set, 6-31G(d,p).

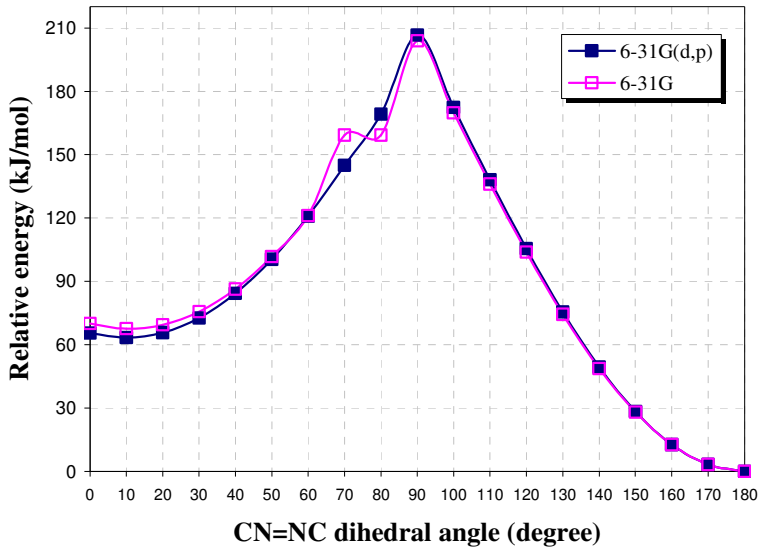

Figure 5-8 DFT–calculated energy profile of the PECs for the dihedral rotation pathway of AB in the gas phase, obtained using two basis sets at the B3LYP level of theory.

Similarly, the potential energy curves at four basis sets were constructed for AAB and represented in Figure 5-9. The effect of basis sets appeared clearly at CN=NC dihedral angles ranges from 70^0-110^0. On one hand, the basis sets produce similar forms of the curve, *i.e.* the expected maximum that defines the geometry of the transition state did not appear for any basis set. On the other hand, there are some dissimilar features of the curves.

(a)

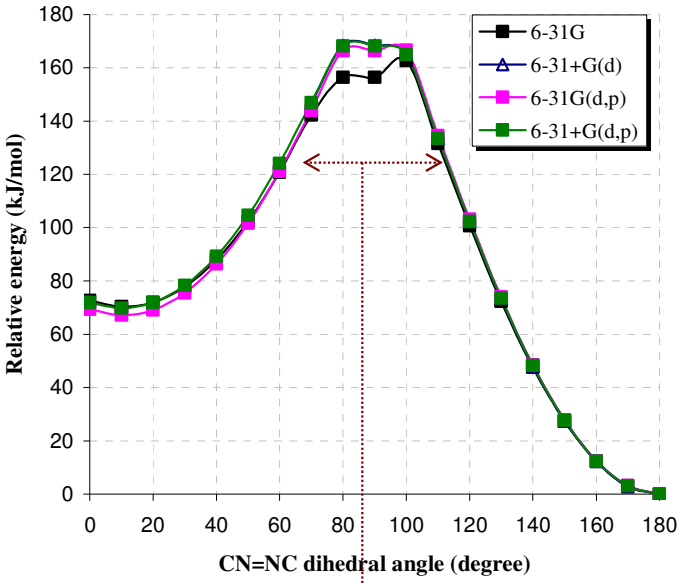

(b)

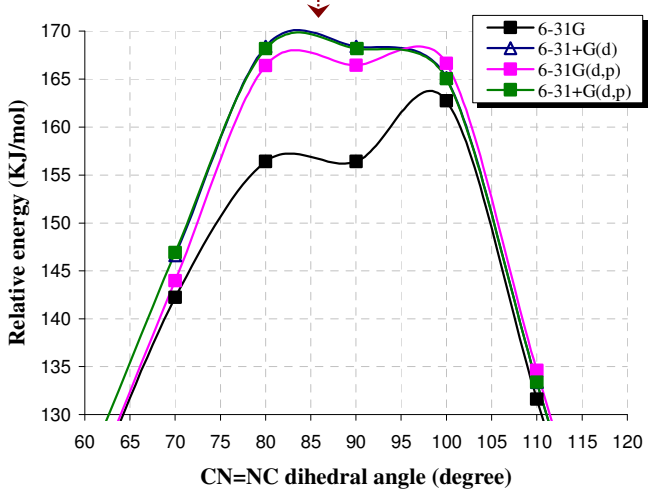

Figure 5-9 Energy profile of the PECs of the dihedral rotation pathway at four basis sets. (a) CN=NC dihedral angles ranges 0-180^0; (b) CN=NC dihedral angles ranges 60-120^0, to illustrate the basis sets effects at this region of the curves.

5.3.4 Inversion Pathways for Asymmetric Azobenzenes

For asymmetric azobenzenes the inversion can occur through two different pathways, depending on which ring will invert. Figure 5-10 gives the two PECs of the α- and β-inversion routes for MY as an example.

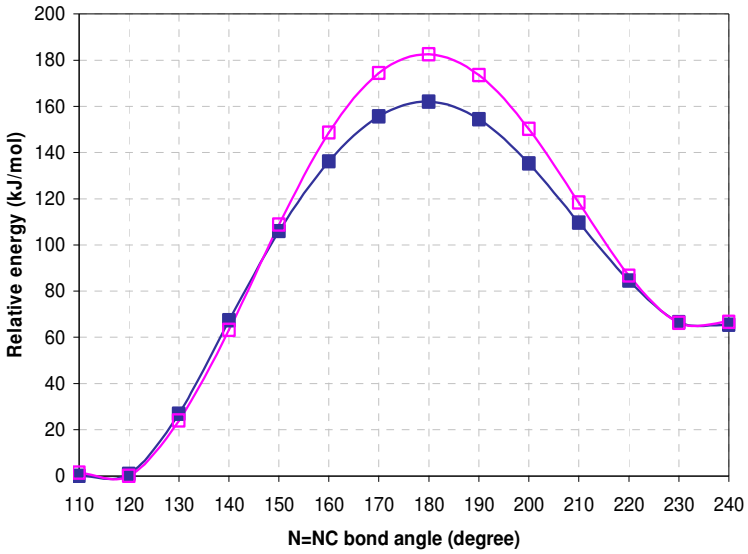

Figure 5-10 Energy profile of the PECs of MY for -■-: α-inversion and -□-: β-inversion pathways.

Figure 5-11 gives the structures of α- and β-TS structures. As can be seen from Figure 5-11, α-inversion for electron donating azobenzenes is through the unsubstituted phenyl ring, for electron acceptor azobenzene and push/pull azobenzenes it is through the phenyl ring that is substituted by the electron acceptor group. The converse is true for β-inversion route, thus the phenyl ring that is substituted with electron donating group is inverted for electron donating azobenzenes and push-pull azobenzenes, while the unsubstituted phenyl ring is inverted for the electron acceptor azobenzene. All of these geometries have linear structures in which one phenyl ring is at right angles to the other ring.

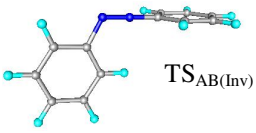

$TS_{AB(Inv)}$

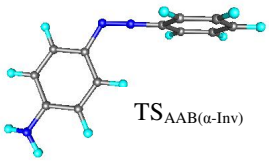

$TS_{AAB(\alpha\text{-}Inv)}$

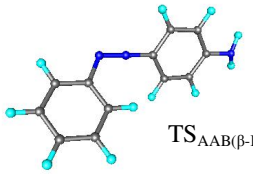

$TS_{AAB(\beta\text{-}Inv)}$

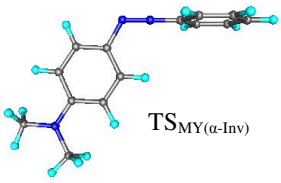

$TS_{MY(\alpha\text{-}Inv)}$

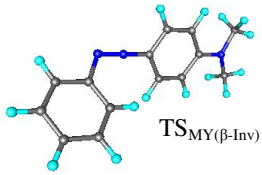

$TS_{MY(\beta\text{-}Inv)}$

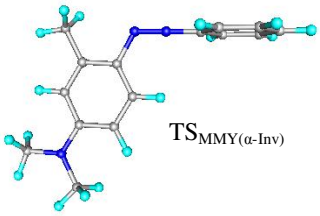

$TS_{MMY(\alpha\text{-}Inv)}$

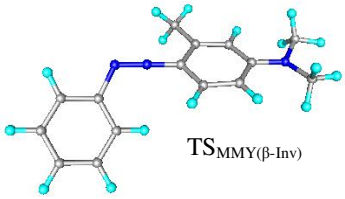

$TS_{MMY(\beta\text{-}Inv)}$

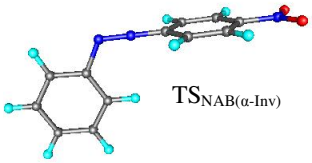

$TS_{NAB(\alpha\text{-}Inv)}$

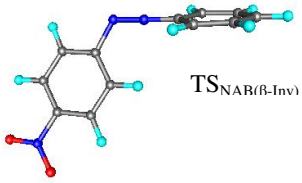

$TS_{NAB(\beta\text{-}Inv)}$

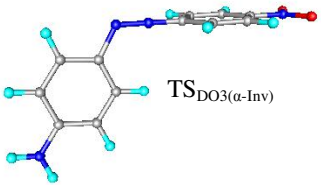

$TS_{DO3(\alpha\text{-}Inv)}$

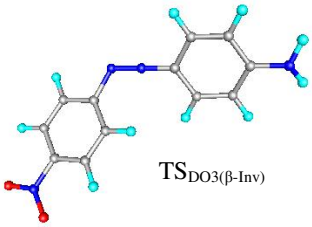

$TS_{DO3(\beta\text{-}Inv)}$

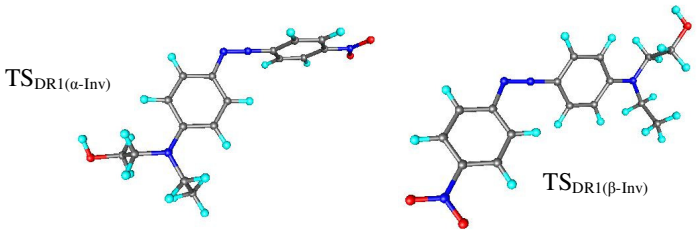

Figure 5-11 The calculated minimum energy structures of the transition states of azobenzenes in the gas phase. TS (α-inv); transition state of inversion through α-phenyl ring, TS (β-inv); transition state of inversion through β -phenyl ring.

Table 5-14[xii] gives the activation energies and the energy difference of the two inversion pathways of the thermal isomerisation in the gas phase.

Molecule/structure	α-inversion $(E_a = E_{\alpha-TS} - E_{cis})$ / kJmol^{-1}	β-inversion $(E_a = E_{\beta-TS} - E_{cis})$ / kJmol^{-1}	Energy difference ΔE_a / kJmol^{-1}
AB 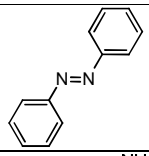	103.71	–	–
AAB 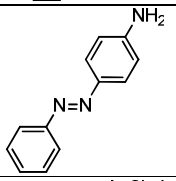	94.4 (-415.67)	113.68 (-462.84)	19.28
MY 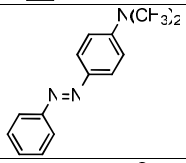	91.57 (-412.47)	111.8 (-464.81)	20.23
MMY 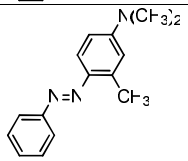	94.86 (-408.46)	109.90 (-449.61)	15.04
NAB 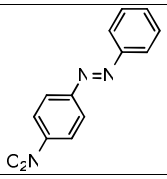	76.62 (-355.47)	107.95 (-433.72)	31.33

[xii] Table 5-14: continued overleaf

DO3 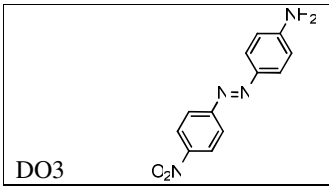	69.49 (-341.22)	116.73 (-474.71)	47.24

Table 5-14 Activation energies in kJ/mol and energy difference for the two inversion pathways of the thermal isomerisation in the gas phase. Values in parentheses are the imaginary frequencies of the transition state geometries in cm^{-1}.

The general observation is that the thermal barrier of inversion for the parent compound is higher than that of the substituted azobenzenes, regardless the nature/position of substituent/s. The closest values to AB are AAB and MMY, where the difference between the energy barriers is less than 10 kJ/mol, and the greatest difference is for DO3 approximately 34 kJ/mol. In all cases, the results indicate that inversion through the α-TS is preferred with respect to the β-TS.

The activation energies of the α- inversion, *i.e.* the more favourable pathway, for the electron donating azobenzenes derivatives are higher than that for electron withdrawing azobenzene and those for the push-pull azobenzenes, where the values for the first mentioned molecules are in the range 92-95 kJ/mol, and for the other molecules it is in the range 69-77 kJ /mol. On the other hand, the activation energies of β-inversion, *i.e.* the less favourable route are comparable for all molecules, and in the range 108-117 kJ/mol.

For azobenzenes substituted by an electron donating group, the α-β energy differences are comparable and decrease with increasing the size of the donating group (comparing AAB and MY) and with introduction of a donating group at the *ortho*- position to the azo bond (comparing MY and MMY). NAB (electron drawing group) and DO3 (push-pull group) show larger difference in the activation energies between the two inversion pathways, the energy difference range is 31-47 kJ/mol. MMY shows the smallest difference ΔE_a=15 kJ/mol, while DO3 shows the largest difference ΔE_a=47 kJ/mol. More detailed dissection is conducted in the following section.

5.3.4.1 Steric Effects and Inversion Centre

For asymmetric azobenzenes, if the substituent at the *para* position is an electron acceptor group, the repulsive force among paired electrons on the nitrogen atom attached to that ring will be lowered, resulting in the increase in the s-character in the C-N bond and the increase in the bond angle of the other phenyl ring. This should cause the inversion on that nitrogen

atom more easily than the other nitrogen. With substitution, as an electron donating, the reverse effect is expected.[97] This theoretical point of view has been supported by the present computational data, which can be summarized as follows: The two inversion routes show that for NAB the inversion of the phenyl ring substituted with nitro group (α-N) has lower energy than of the unsubstituted phenyl ring (β-N), E_a(α-inv) =77 and E_a (β -inv) =108 kJ/mol. Whereas for AAB, MY and MMY the inversion of the unsubstituted phenyl ring (α-N) has lower energy than of the inversion of the phenyl ring substituted with the amine group (β-N), for AAB E_a=94 and 114 kJ/mol for α-inversion and β-inversion, respectively. In the case of push-pull azobenzenes the more favourable inversion centre is α-phenyl ring, supporting the previous observation, the electron acceptor substituted side is more favourable to invert than the electron donating side.

The larger absolute value of the imaginary frequency of the β-inversion transition state with respect to α-inversion transition state should be taken into consideration for its possible consequences in the tunnelling correction at the level of the transition state theory.[98]

5.3.5 α-Inversion *vs.* Dihedral Rotation Mechanism

DFT calculations have been carried out to investigate the competition between the inversional and dihedral rotational mechanisms. It was possible to conclude the more favourable path of inversion by comparing the activation energies of the two inversion pathways, Section 5.3.4. Comparison between the more favourable inversion route, *i.e.* α-inversion and dihedral rotation route was made and discussed in the following paragraph.

A conclusion upon the preferred mechanism for the thermal isomerisation for AB could be drawn just by looking to the PECs for the two pathways, Figure 5-12. From Figure 5-12 it is clear that the thermal *cis*-to-*trans* isomerisation occurred preferably through in plane inversion of one of the phenyl ring. The difference in the activation energy between the dihedral rotation and inversion routes is 32 kJ/mol at 6-31G(d,p) level/basis set, somewhat less than with the value of 46 kJ/mol obtained at different basis set 6-31+G(d),[84] however, both results indicate the predominance of the inversion route for AB.

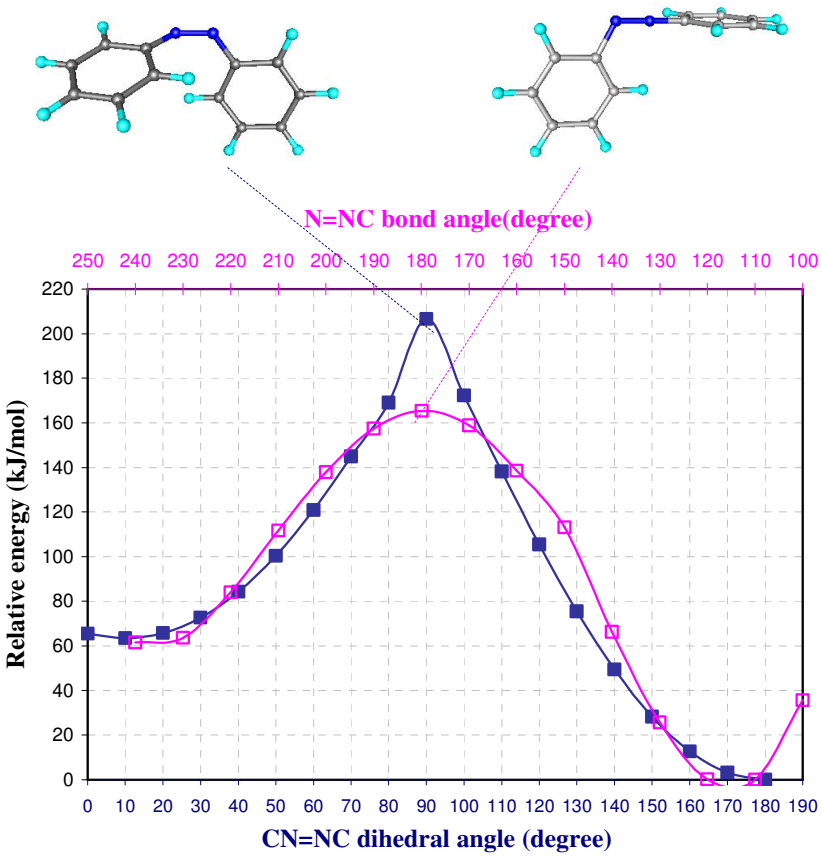

Figure 5-12 Energy profiles of the PECs of AB for -■- dihedral rotation and -□-inversion pathways. Above are shown the corresponding transition states.

For the substituted azobenzenes, as shown in the Table 5-15, the activation energies for the dihedral rotation and α-inversion pathways are essentially the same since both pathways access the same transition state structure, as will now be discussed.

Molecule/structure	Dihedral rotation $E_a = E^0_{TS/\text{dihedral rot}} - E^0_{cis/\text{dihedral rot}}$ /kJmol^{-1}	α-inversion $E_a = E^0_{TS/\alpha-inv} - E^0_{cis/\alpha-inv}$ /kJmol^{-1}
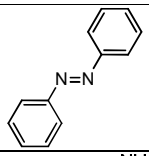 AB	135.55(-10.02) 146.44[a]	103.71 100.42[a]
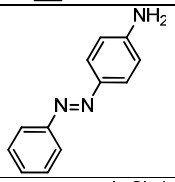 AAB	94.12 (-415.28)	94.42 (-415.67)
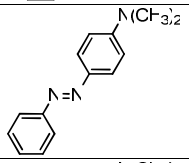 MY	91.52 (-412.55)	91.57 (-412.47)
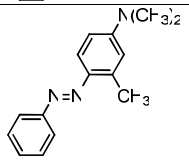 MMY	94.84 (-408.47)	94.86 (-408.46)
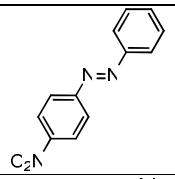 NAB	76.65 (-355.34)	76.62 (-355.47)
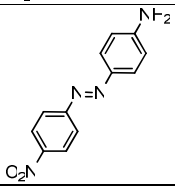 DO3	69.54 (-340.57)	69.49 (-341.21)

Table 5-15 Activation energies (kJ/mol) of the thermal isomerisation *via* rotation and inversion pathways in the gas phase. Values in parentheses are the imaginary frequencies of the transition state geometries in cm^{-1}. [a] From reference[84] at 6-31+G(d). [b] From reference[64] at 6-31G(d).

From close inspection of the molecular structures of $TS_{AAB/\text{dihedral rot}}$ and $TS_{AAB/\alpha\text{-inv}}$ it is clear that they are exceedingly similar. The N=N bond length, CN bond length, α-CNN angle and one of NNCC dihedral angle (Φ_1) of $TS_{AAB/\text{dihedral rot}}$ are almost the same as those of $TS_{AAB/\alpha\text{-inv}}$, Φ_1 and Φ_2 were defined in Figure 5-1. The β-CNN angle (a parameter optimised during the rotation PEC scanning) of $TS_{AAB/\text{dihedral rot}}$ is 179.7^0, which is very close to the corresponding value (179.9^0, a value obtained from the α-inversion PEC scanning) of

$TS_{AAB/\alpha\text{-inv}}$. The planes of the phenyl rings are perpendicular to each other in both structures. Only the CN=NC and N=NCC (Φ_2) dihedral angles of $TS_{AAB/\alpha\text{-inv}}$, which are directly related to the β-CNN, differ from those of $TS_{AAB/\text{dihedral rot}}$. As the β-CNN angle is approximately 180^0 at the transition and the three atoms almost align in a line, the tiny variation of the linear conformation will cause drastic change in the dihedral angles. Therefore, even though the CNNC and NNCC (Φ_2) dihedral angles appear to be different at the transition states structures. The molecular structures of $TS_{AAB/\text{dihedral rot}}$ and $TS_{AAB/\alpha\text{-inv}}$ are identical. Wang and Wang [2007][84] assumed that due to the existence of these identical molecular structures for the transition states on the PECs along the inversion and dihedral rotation pathways, the two mechanisms (α-inversion and dihedral rotation) operate simultaneously for this molecule. But the postulated competition between these two mechanisms can not be concluded from the formation of geometrically identical transition states, since it is physically inapplicable to obtain identical transition states from two different pathways.

Inspection of the potential energy curves for the α-inversion and dihedral rotation mechanism for AAB, Figure 5-13, reveals that the restriction that was made to obtain pure rotation pathway potential energy surface was not sufficient, and in the CN=NC dihedral angle range from 80-100^0 the passage to the inversion transition state is not prevented. This explains the insignificant difference in activation energies between the two pathways. We believe that the obtained transition state is formed due to the transformation, that occurs in this range, from the rotation pathway to inversion one. Further discussion of this point is undertaken in the section that follows.

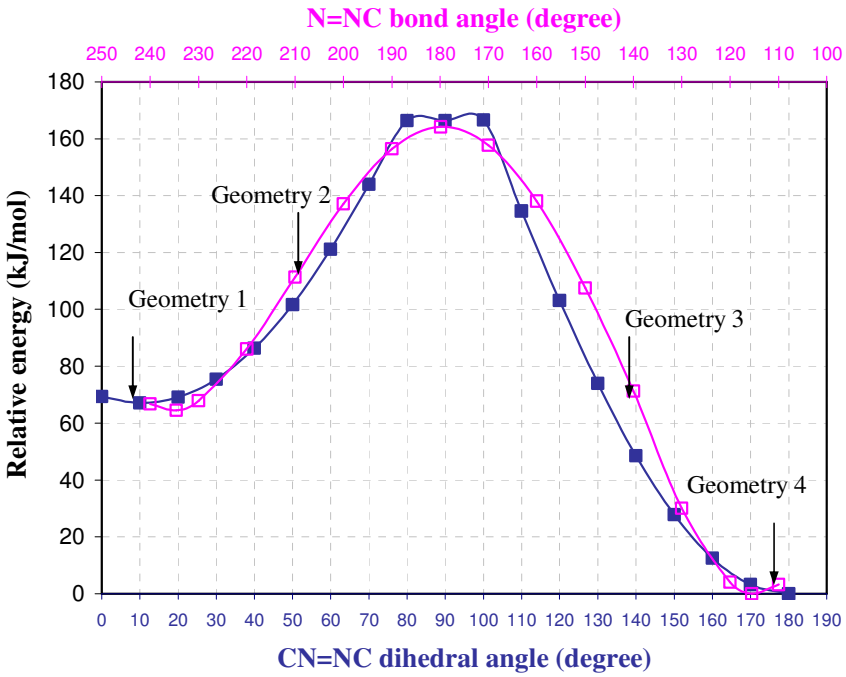

Figure 5-13 Energy profile of the PECs of AAB for -■-: dihedral rotation and -□-: α-inversion pathways.

Table 5-16 displays some structural parameters of geometries corresponding to the dihedral rotation and α-inversion routes. Geometry 1 shows that at this point the bond lengths and angles are very similar regardless of the route of isomerisation. Geometry 2 which is closer to the transition state demonstrates a significant change in the bond lengths, *i.e.* N=N, C_1-N_{12}, and C_{14}-C_{15} are decreased by 0.03 Å, 0.03 Å and 0.01 Å, respectively, while N_{13}-C_{14} bond length is increased by 0.03 A^0, for inversion compared to dihedral rotation route. The bond angles of N_{12}-N_{13}-C_{14}, and N_{13}-C_{14}-C_{15} are decreased significantly by 2.6^0 and 11.0^0, respectively, while C_2-C_1-N_{12}, C_{16}-C_{17}-N_{24}, and C_{17}-N_{24}-H_{25} are increased by 1.1^0, 0.2^0, and 0.3^0, respectively, for inversion compared to dihedral rotation route. The dihedral angles show a significant change, where, N_{12}-N_{13}-C_{14}-C_{15} dihedral angle changes from 14^0 to (-179^0) for inversion compared to dihedral rotation route, respectively. This contraction in the bond lengths/angles that occurs at the electron donating side indicates more contribution of the lone pair of electrons of this group in the electron distribution of the system.

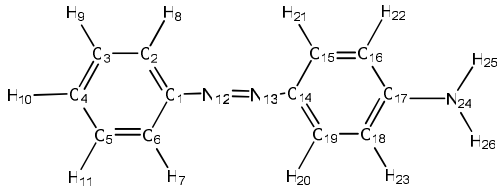

Figure 5-14 AAB molecule is depicted with atomic numbering.

Table 5-16[xiii] Structural parameters of geometries corresponding to dihedral rotation (regular font) and α-inversion (bold font) routes. Atomic numbering is depicted in Figure 5-14.

	Geometry 1		Geometry 2		TS		Geometry 3		Geometry 4	
C_1-N_{12}-N_{13}-C_{14} dihedral	9.5	**9.5**	50.0	**1.9**	90.0	**174.0**	140.0	**180.0**	-180	**-180**
C_1-N_{12}-N_{13}	110.0	**120.0**	124.3	**150.0**	179.5	**180.0**	115.7	**114.8**	114.6	**110.0**
Bond length / Å										
N=N	1.27	**1.27**	1.27	**1.24**	1.23	**1. 23**	1.28	**1.25**	1.26	**1.27**
C1-N12	1.47	**1.47**	1.41	**1.38**	1.33	**1.33**	1.40	**1.38**	1.42	**1.43**
N_{13}-C_{14}	1.42	**1.42**	1.41	**1.44**	1.44	**1.44**	1.40	**1.41**	1.41	**1.40**
C_1-C_2	1.40	**1.40**	1.41	**1.41**	1.42	**1.42**	1.41	**1.41**	1.41	**1.41**
C_{14}-C_{15}	1.41	**1.41**	1.41	**1.40**	1.40	**1.40**	1.41	**1.41**	1.41	**1.41**
Bond angle / ^{0}										
N_{12}-N_{13}-C_{14}	130.0	**130.0**	123.6	**121.0**	117.6	**117.6**	140.0	**180.0**	115.3	**115.5**
C_1-C_2-N_{12}	118.7	**118.7**	28.6	**29.7**	120.6	**120.7**	123.8	**124.7**	124.9	**125.5**
N_{13}-C_{14}-C_{15}	113.6	**113.6**	125.5	**114.5**	125.0	**125.0**	124.6	**125.5**	125.2	**125.3**
C_{16}-C_{17}-N_{24}	120.9	**120.9**	120.6	**120.8**	120.3	**120.3**	120.5	**120.5**	120.4	**120.5**
C_{17}-N_{24}-H_{25}	116.2	**116.2**	116.7	**117.0**	117.3	**117.3**	116.9	**121.0**	116.6	**121.1**
Torsional										

[xiii] Table 5-16: continued overleaf

angle / ^{0}										
C_1-C_2-N_{12}-N_{13}	-124	**-124**	-157	**126**	0	**-90**	-14	**-0.02**	0.06	**0.00**
N_{12}-N_{13}-C_{14}-C_{15}	-150	**-150**	14.3	**-179**	-0.1	**-0.4**	-8.9	**0.0**	-0.1	**0.0**
C_{16}-C_{17}-N_{24}-H_{25}	-159	**-159**	-161	**-161**	-162	**-162**	-160	**-180**	-161	**180**

In Geometry 4, the bond lengths/angles show little variations between the two routes. Since, N=N, and C_1-N_{12} are increased by 0.01 Å, and 0.01 Å, respectively, N_{13}-C_{14} bond length is decreased by 0.01 A^0, while, C_1-C_2, and C_{14}-C_{15} remain the same for inversion compared to dihedral rotation route. The bond angles are increased for the inversion routes compared to the dihedral rotation route; this appears more significantly in C_2-C_1-N_{12} and C_{17}-N_{24}-H_{25} bond angles, where the differences are 0.6^0 and 4.5^0, respectively. The dihedral angles show also insignificant change between the two routes. Comparison between Geometry 1 and 4 in the two routs indicates that at the start of the curve at the both sides the two geometries show little variation. Geometry 3 which is closer to the transition state from the *trans* isomer side show a significant variation in some bond lengths/angles as follows: the bond lengths of N=N, and C_1-N_{12} are decreased by 0.03 Å, and 0.02 Å, respectively, while N_{13}-C_{14} bond length is increased by 0.01 Å for inversion compared to dihedral rotation route. The bond angles of N_{12}-N_{13}-C_{14}, and N_{13}-C_{14}-C_{15} are decreased significantly by 2.6^0 and 11.0^0, respectively, for inversion compared to dihedral rotation route, while C_1-C_2 and C_{14}-C_{15} bond lengths remain the same. For the bond angles of N_{12}-N_{13}-C_{14}, C_1-C_2-N_{12}, N_{13}-C_{14}-C_{15}, and C_{17}-N_{24}-H_{25} the increases are significant by 30^0, 0.9^0, 0.9^0, and 4.1^0, respectively. The C_{16}-C_{17}-N_{24} bond angle remains the same. The dihedral angles for this geometry show a significant change, *i.e.* C_1-C_2-N_{12}-N_{13}, N_{12}-N_{13}-C_{14}-C_{15}, and C_{16}-C_{17}-N_{24}-H_{25} dihedral angle differences are 14^0, 9^0, and 20^0, respectively. The contraction in the bond lengths/angles that occurs at the electron donating side is less compared to that in geometry 2; this indicates that the contribution of the lone pair of electrons of this group in the electron distribution of the system is smaller in this flat geometry compared to that in the bent geometry.

5.3.6 Pure Rotation *vs.* Dihedral Rotation Mechanism

Kikuchi *et al.* [1999][83] applied *ab initio* RHF and ROHF methods to examine the inversion and rotation mechanisms of the thermal *cis*-to-*trans* isomerisation of the DMNAB molecule, including the role that the solvent plays in determining the mechanism. They found that the searching for the rotation TS of this molecule gave the TS for the pull group inversion path

(= α-inversion pathway), as has been observed in the present work. This was explained by the two reaction mechanisms mixing with each other so that they cannot be considered separately, because the azo nitrogen atoms can change their hybridization from sp^2 to sp^1, and the transition state for the rotation path coincides with that of the inversion path when the N=NC bond angle is 180^0. Poprawa-Smoluch *et al.* [2006][64] found a similar flat region for the potential energy surface of the dihedral rotation pathway of DR1 at TDDFT/B3LYP/6-31G(d) level of theory/basis set.[64] Cattaneo *et al.* [1999][31] Also found a flat region in the inversion PEC of AB and was attributed to the arbitrariness of the rotation pathway; in particular, the synchronism of the out-of-plane torsion of the phenyl groups with the N-inversion.

This led us to attribute the appearance of the flat region in the rotation PECs to the same phenomenon, *i.e.* the arbitrariness of the inversion pathway for azobenzene derivatives. The flat region may be attributed to the fact that in the search of the potential energy surface of the rotation pathway up to a CN=NC dihedral angle of 100^0-130^0 depending on the molecule under investigation, a smooth path is followed, in which minor changes of other geometrical parameters occur following the imposed change in the dihedral angle. Then suddenly the nitrogen inversion coordinate enters into play (on the electron donating side/ electron withdrawing side), and the structure optimizes to the inversion transition state by an increase of the CN=N bond angle to 180^0. In this geometry the CN=NC dihedral angle is no longer defined.

For azobenzene, the pure rotation coordinate can be followed without passage to the inversion transition state. Figure 5-15 shows the potential energy surfaces and the transition states of AB and AAB and indicates the appearance of the plateau region in the case of AAB and a curve with a maximum in the case of AB. The different transition state structures are also shown, the AB transition state has non linear configuration while AAB the transition state has a linear configuration.

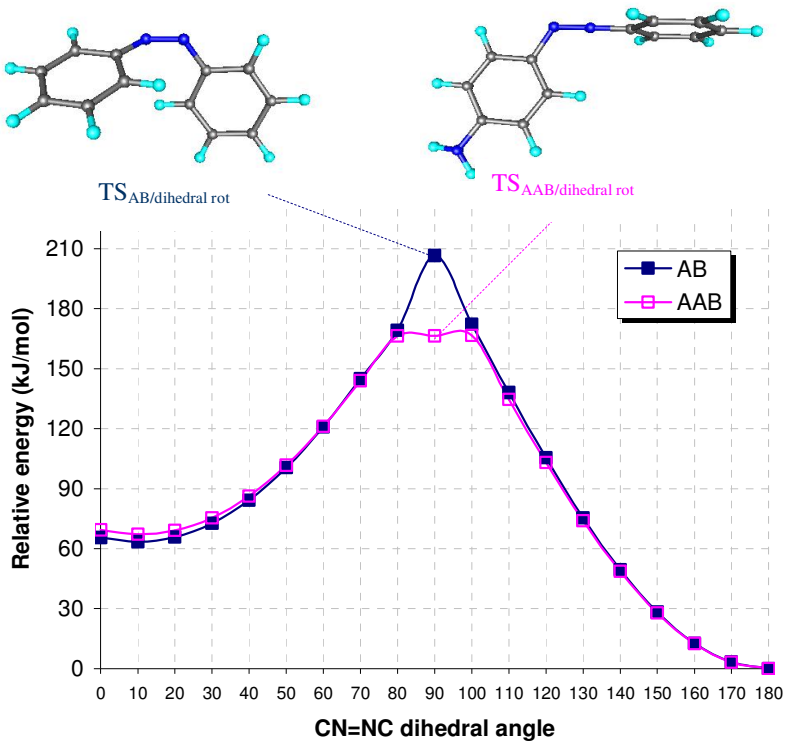

Figure 5-15 Energy profile of the PEC of the dihedral rotation pathway for AB and AAB. The corresponding transition states are shown, note the linearity of TS-AAB and non linearity of TS-AB.

This work searched for a transition state of the pure rotation pathway, *i.e.* a PEC for a rotation mechanism with out any passage to the inversion pathway. This was investigated for AAB and DO3. For AAB, obtaining the pure rotation pathway was performed by constraining the α-CN=N bond angle to value of 115.5^0 and β-N=NC bond angle to the value of 116.3^0, *i.e.* the values of these angles in the *trans* form. Under such circumstances, the passage to the inversion pathway as well as the occurrence of the linear CN=N is prevented. The obtained transition state has two important features:

1. It is 38.5 kJ/mol higher in energy than the dihedral rotation transition state.
2. It has non linear geometry.

Frequency calculations were performed on the obtained transition state in addition to the isomer geometries to verify the nature of the stationary points. Figure 5-16 shows the

potential energy curves for the dihedral rotation and the postulated pure rotation pathway, and the corresponding transition states.

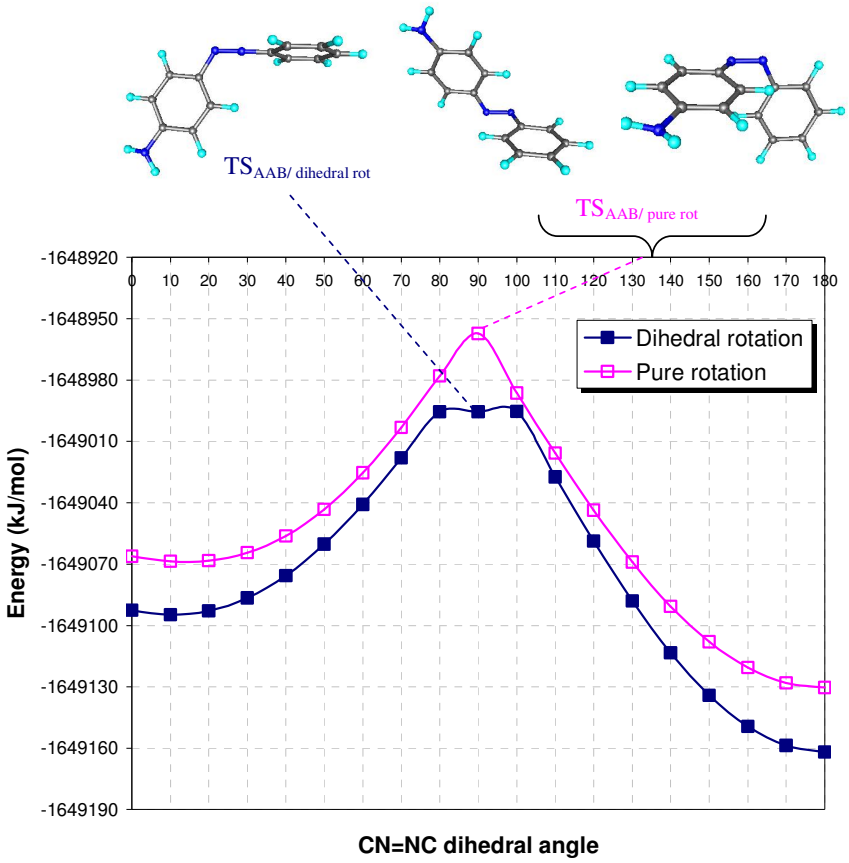

Figure 5-16 Energy profile of the PECs of the dihedral rotation and the postulated pure rotation of AAB in the gas phase. Above are shown the transition states structures. Two views of the transition state of the pure rotation pathway are shown, to illustrate the relative orientation of the phenyl rings.

Table 5-17 displays the key coordinates, *i.e.* the bonds lengths and angles of the azo linkage, activation energies and imaginary frequencies of the transition states for the two rotation pathways. Examining the changes that occur upon the two rotation pathways indicates that the N=N bond distance is greater for pure rotation than in the dihedral rotation pathway, since the rotation mechanism involves a weakening of the double bond between the nitrogens of the azo linkage.

	Dihedral rotation	Pure rotation
N=N / Å	1.230	1.329
CN=N unsubstituted side / ^{0}	179.486	115.500
N=NC donating side / ^{0}	117.640	116.300
CN=NC / ^{0}	90.002	90.000
$^\dagger E_a \left(= E_{TS} - E_{cis}\right) / kJmol^{-1}$	99.29	137.79
Imaginary frequency /cm^{-1}	-415.276	-23.015

Table 5-17 The key coordinates, activation energies and imaginary frequencies of the transition states of the dihedral rotation and postulated pure rotation for AAB. †Without including of the zero point vibrational corrections.

As can be seen from Figure 5-16, the energy values for the optimised geometries that correspond to the pure rotation route are generally larger than those corresponding to the dihedral rotation route. More constraints were applied in the optimisation of the pure rotation path geometries, or in other words, these geometries were forced more to follow a specific route, and this leads to elevation in their energies. A small change in the α- and β-N=NC bond angles causes a significant difference in the energies between structures at the same CN=NC dihedral angle. Table 5-18 displays some structural parameters of geometries at the C-N=N-C dihedral angles = 10^0, 90^0, and 180^0, from which the following observations are concluded: Geometry at C-N=N-C dihedral angle = 10^0 shows that most of the bond lengths are elongated under constrains of the pure rotation mechanism, by an average of 0.02 Å. The bond angles become significantly smaller in pure rotation mechanism, *i.e.* C_1-C_2-N_{12}, N_{13}-C_{14}-C_{15}, and C_{17}-N_{24}-H_{25} bond angles become smaller by 0.8^0, 8.8^0, and 0.8^0, respectively. The torsional angles in turn show significant differences between the two routes.

The transition state geometries in the two routes show significant differences in bond lengths/angles. The bond length of N=N, C_1-C_2 and C_{14}-C_{15} become longer by 1.0 Å, 0.1 Å, and 0.3 A^0 in the pure rotation, while, C_1-N_{12} and N_{13}-C_{14} become shorter by 0.6 A^0 and 0.9 Å. Most bond angles examined become smaller in the pure rotation, *i.e.* C_1-C_2-N_{12}, N_{13}-C_{14}-C_{15}, and C_{16}-C_{17}-N_{24} by 2.7^0, 7.4^0, and 0.1^0. The exception is C_{17}-N_{24}-H_{25} which becomes larger by 1.2^0. The same conclusion could be drawn for Geometry 2 at C-N=N-C dihedral angle of 180^0, *i.e.* a significant difference in the bond lengths/angles is observed.

It appears that in the pure rotation route there is a stronger contribution of the lone pair of electrons of the amine group into the π electron of the system. To conclude, the significant difference in the energies of the geometries at the same torsional angle in the two routes can be explained in terms of the significant variation in the bond lengths/angles.

	Geometry 1		TS		Geometry 2	
Bond length / Å						
N=N	1.25	**1.27**	1.23	**1.33**	1.27	**1.26**
C_1-N_{12}	1.43	**1.45**	1.42	**1.36**	1.42	**1.42**
N_{13}-C_{14}	1.43	**1.45**	1.44	**1.35**	1.41	**1.40**
C_1-C_2	1.40	**1.40**	1.42	**1.43**	1.41	**1.40**
C_{14}-C_{15}	1.41	**1.40**	1.40	**1.43**	1.41	**1.40**
Bond angle / ^{0}						
N_{12}-N_{13}-C_{14}	125.1	**116.3**	117.6	**116.3**	115.2	**116.3**
C_1-C_2-N_{12}	121.8	**121.0**	120.6	**117.9**	124.9	**115.6**
N_{13}-C_{14}-C_{15}	126.3	**117.5**	125.0	**117.6**	125.2	**116.1**
C_{16}-C_{17}-N_{24}	120.7	**120.9**	120.3	**120.2**	120.4	**120.8**
C_{17}-N_{24}-H_{25}	116.3	**115.5**	117.3	**118.5**	116.6	**116.6**
Torsional angle / ^{0}						
C_1-C_2-N_{12}-N_{13}	58	**-126**	-0.1	**176**	0.1	**180**
N_{12}-N_{13}-C_{14}-C_{15}	36	**-130**	-0.1	**176**	-0.1	**180**
C_{16}-C_{17}-N_{24}-H_{25}	-160	**-158**	-162	**-166**	-161	**-160**
C_1-N_{12}-N_{13}-C_{14} (dihedral)	10	**10**	90	**90**	180	**180**

Table 5-18 Structural parameters of geometries corresponding to dihedral (regular font) and pure rotation (bold font) routes. Atomic numbering of AAB is depicted in Figure 5-14.

Another effort was made to obtain the potential energy curve for the pure rotation this time for one of push-pull azobenzene molecules, DO3. Obtaining the pure rotation pathway was performed by constraining the α-CN=N bond angle to value of 127.0^0 and β-N=NC bond angle to the value of 126.0^0, *i.e.* the values of these angles in the *cis* form. Under such

circumstances, the passage to the inversion pathway as well as the occurrence of the linear CN=N is prevented. The obtained transition state has two important features:

1) It is 38.9 kJ/mol higher in energy than the previous dihedral rotation transition state.
2) It has non linear geometry.

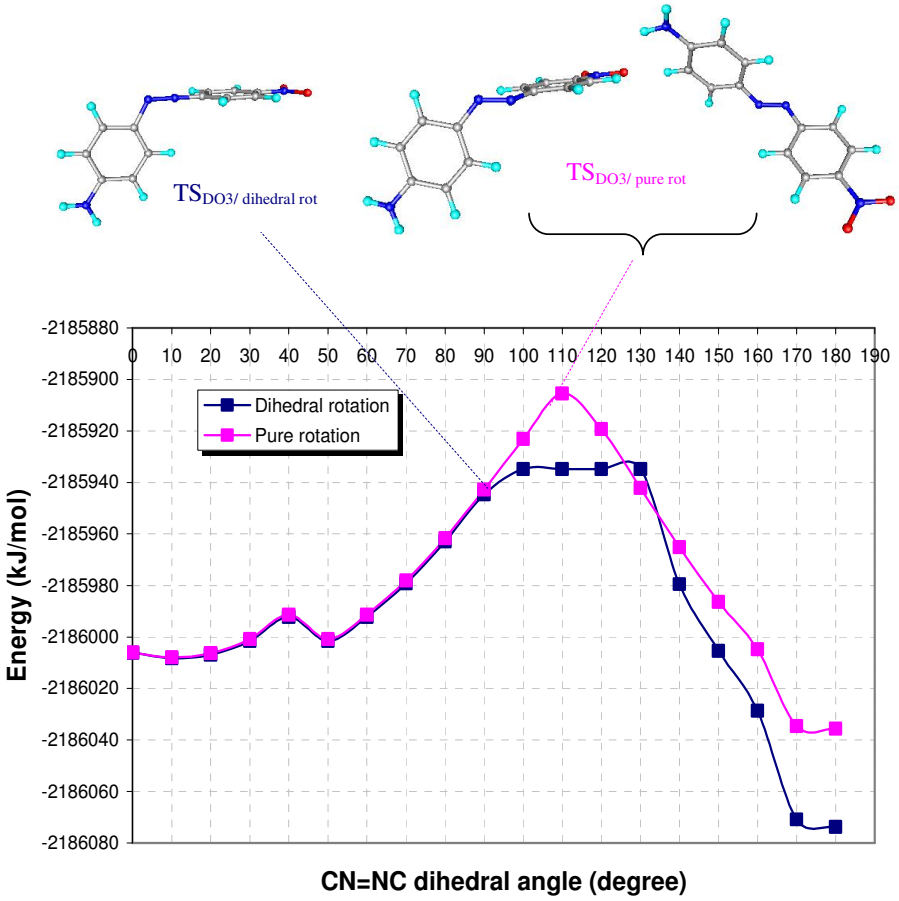

Figure 5-17 Energy profile of the PECs of the dihedral rotation and postulated pure rotation of DO3 in the gas phase. Above are shown the transition states, two views of the transition state of the pure rotation pathway are shown, to illustrate the relative orientation of the phenyl rings.

Table 5-19 displayed the key coordinates, *i.e.* the bonds lengths and angles of the azo linkage, activation energies and imaginary frequencies of the transition states for the two rotation pathways. Examining the change that occur upon the two rotation pathways indicates that the N=N bond distance is longer for pure rotation than in the dihedral rotation pathway, as observed for AAB above.

	Dihedral rotation	Pure rotation
N=N / Å	1.2409	1.2697
N=NC donating side / ^{0}	119.6	126.0
CN=N acceptor side / ^{0}	179.7	127.0
CN=NC / ^{0}	90.1	110.0
$^{\dagger} E_a \left(= E_{TS} - E_{cis}\right) / kJmol^{-1}$	63.60	102.47
Imaginary frequency /cm^{-1}	-340.57	-296.28

Table 5-19 The key coordinates, activation energies and imaginary frequencies of the transition states of the rotation and postulated pure rotation for DO3. †Without including of the zero point vibrational corrections.

5.3.6.1 α-Inversion *vs.* Pure Rotation Mechanism

Comparing the energy barrier of the pure rotation and α-inversion pathways confirms the inversion route for the thermal isomerisation of AAB to be more favourable than the rotational route, see Figure 5-18. E_a values (without the zero point vibrational corrections) are 137.79 kJ/mole and 97.47 kJ/mole for the pure rotation and α-inversion pathways, respectively, thus the difference in energy between the energy barriers for the two mechanisms is 40.3 kJ/mol, comparable with that of AB, for AB ΔE_a (E_a (dihedral rotation) - E_a (inversion)) = 39.3 kJ/mol (without the zero point vibrational corrections).

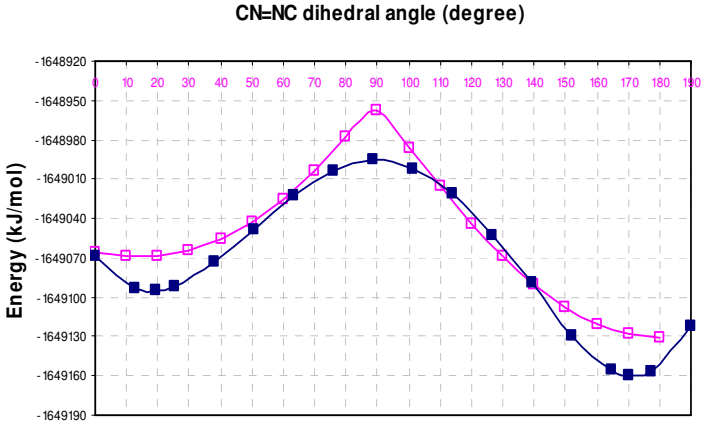

Figure 5-18 Energy profile of the PECs for -□-: pure rotation and -■-: α-inversion pathways of AAB.

5.3.7 Geometries of Gas Phase Transition States

Transition state structures of the studied azobenzenes obtained in the gas phase are presented in Figure 5-2. Figure 5-2 presents the minimum energy transition state geometry for each

molecule obtained by comparing the energy barriers from the dihedral rotation, α-inversion and β-inversion PECs, refer to Table 5-14 and Table 5-15. From Figure 5-2, it is clear that the structures of the transition states all correspond to the α-inversion/dihedral rotation pathway; no structure corresponds to the β-inversion pathway.

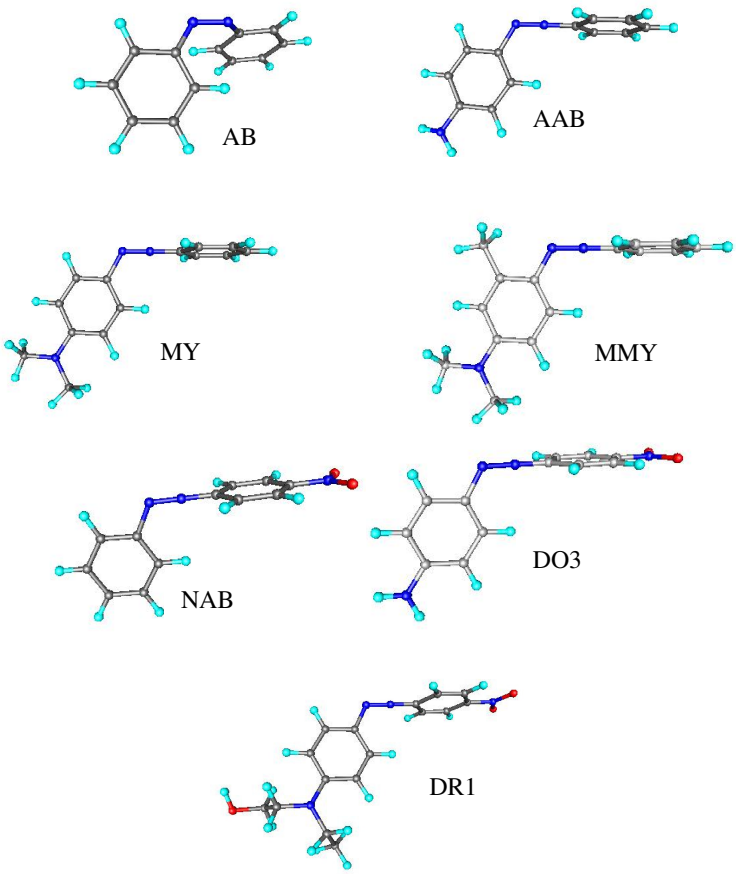

Figure 5-19 The calculated minimum energy structures of the transition state of azobenzenes in the gas phase.

The optimised parameters, *i.e.* bond lengths and bond angles, of the transition states of AB, AAB, MY, MMY, NAB, DO3 and DR1 computed using B3LYP with 6-31G(d,p) basis set are presented in Table 5-20. To the best of author's knowledge, this is the first report on the molecular structural parameters of the transition states of AAB, MY, MMY, NAB and DR1. Such information for the other molecules was included in litrature.[83,98] For the sake of brevity, only the average optimised parameters are presented.

	AB	AAB	MY	MMY	NAB	DO3	DR1
Bond length / Å							
N=N	1.297	1.230	1.231	1.232	1.223	1.228	1.230
C–N(azo) un-substituted side	1.357	1.332	1.331	1.330	1.444	–	–
C–N(azo) donating side	–	1.435	1.432	1.429	–	1.421	1.418
C–N(azo) acceptor side	–	–	–	–	1.321	1.317	1.316
C(ph)–C(ph)	1.404	1.401	1.403	1.404	1.400	1.402	1.404
C(ph)–H	1.085	1.086	1.085	1.085	1.084	1.085	1.084
C(ph)–N(H)	–	1.381	–	–	–	1.372	–
N–H	–	1.009	–	–	–	1.008	–
C(ph)–N(NO)	–	–	–	–	1.444	1.441	1.440
N–O	–	–	–	–	1.238	1.239	1.239
C(ph) –N(Me)	–	–	1.376	1.376	–	–	–
C–H(Me)	–	–	1.095	1.095	–	–	–
C(Me)–N	–	–	1.454	1.454	–	–	–
Bond angle / ^{0}							
C(ph) –N=N un-substituted side	120.556	179.997	179.842	179.960	117.767	–	–
C(ph) –N=N donating side	–	117.640	117.685	118.079	–	118.489	118.544
C(ph) –N=N acceptor side	–	–	–	–	179.942	179.679	179.532
C(ph) –C(ph)–N un-substituted side	120.319	120.683	120.731	120.772	119.459	–	–
C(ph)–C(ph)–N donating side	–	120.198	120.429	120.053	–	120.176	120.525
C(ph)–C(ph)–N acceptor side	–	–	–	–	120.412	120.616	120.652
C(ph)–C(ph) –C(ph)	119.992	120.177	120.000	120.166	119.922	120.282	120.074
C(ph)–C(ph)–H	119.905	119.834	119.777	119.616	120.031	119.851	119.689
C–C–N(H)	–	120.559	–	–	–	120.547	–
C–N–H	–	117.268	–	–	–	118.891	–
C–C–N(NO)	–	–	–	–	119.768	119.840	119.853
C–N–O	–	–	–	–	118.060	118.161	118.178
C–C–N(Me)	–	–	120.681	121.111	–	–	–
C–N–C(Me)	–	–	120.236	120.261	–	–	–
N–C–H(Me)	–	–	110.953	110.955	–	–	–
C-N=N-C (dihedral)	90.00	90.00	90.10	90.00	89.99	90.00	90.00

Table 5-20 Optimized geometrical parameters of the transition states of the studied azobenzenes in the gas phase.

From the table, it is found upon substitution of the parent AB molecule by an electron donor, the N=N bond distance increases from 1.297 A^0 to 1.230 A^0, 1.231 A^0 and 1.232 A^0, for the

parent azobenzene and electron donating azobenzenes, respectively. On the other hand the N=N bond distance decreases from 1.297 Å to 1.223 Å, 1.228 Å and 1.230 Å, for the parent azobenzene and electron acceptor azobenzenes and electron donating-accepting azobenzenes, respectively. Of particular importance for the prediction of the thermal isomerisation mechanism is the length of the N=N double bond, since the rotation mechanism involved out of plane rotation about the N=N bond, weaker bond lead to easier rotation and the reverse is true. Thus the longer bond lengths seen for electron acceptor and electron donating-acceptor azobenzenes compared to the parent compound and to electron donating azobenzenes suggests weaker bond and thus increases the possibility of rotation mechanism for such type of molecules. On the other hand, the shorter bond lengths that were observed for electron donating azobenzenes compared to the parent compound and to the electron acceptor and electron donating-accepting azobenzenes suggests stronger bond and thus decreases the possibility of rotation mechanism for such type of molecules. The order of change the N=N double bond character is:

DR1 > DO3 > NAB > AB > AAB > MY > MMY

5.3.7.1 Effect of Solvent

In general, the transition state geometry in the solution shows insignificant differences from that in the gas phase. For the sake of brevity, the reported optimised parameters are those belonging to the azo linkage only. The optimised parameters of the azo linkage of the transition state in the gas phase and two solvents, namely benzene and DMSO for AAB as a representative example are summarised in Table 5-11. From Table 5-11, the impact of the solvent is small for the bond lengths and bond angles of the azo linkage compared to that in the gas phase. The changes in these parameters from the gas phase into the solution are more significant upon changing the solvent to DMSO than to benzene. The general effect of more polar solvent, *i.e.* DMSO to benzene, is elongation of the azo linkage bond lengths and increase of the azo linkage bond angles, however there are some exceptions. The N=N bond distance increased in DMSO solvent by 0.004 Å, while the effect on the C–N(azo) bond lengths is different with respect to the position of this bond. On the un-substituted side the bond distance of this bond decreases by 0.002 Å. On the other hand, in the electron donating side the trend is different the C–N(azo) bond length decreases 0.009 A^0. The bond angles of the azo linkage change with DMSO in similar manner as the bond lengths, since C(ph) –N=N bond angles on the un-substituted side increase by 0.196^0. The C(ph) –N=N bond angles on the electron donating side increases by 0.607^0 in DMSO.

	TS
Bond length / Å	
N=N	1.230 **1.232** *1.236*
C–N(azo) un-substituted side	1.332 **1.331** *1.329*
C–N(azo) donating side	1.435 **1.429** *1.420*
Bond angle / ^{0}	
C(ph) –N=N un-substituted side	179.997 **180.627** *180.823*
C(ph) –N=N donating side	117.640 **118.060** *118.667*
CN=NC (dihedral)	90.00 **90.00** *90.00*

Table 5-21 Optimised parameters of the azo linkage for transition state of AAB in gas phase (regular font), benzene (bold font), and DMSO (italics font).

5.3.8 Dipole Moments of Transition States

Dipole moments of the transition states of the studied azobenzenes in the gas phase and in solution are displayed in Table 5-22. The dipole moments of the transition states increase from gas phase to solution and from benzene to DMSO. Table 5-22 also displays the dipole moments corresponding to the *cis* geometries. In all molecules except the parent molecule the dipole moment of the *cis* isomer is smaller than that of the transition state, this means that the transition state is more polar than the corresponding *cis* isomer; this is applied to the geometries in the gas phase as well in solution. Also Table 5-22 displays the dipole moment of the transition state of the pure rotation pathway for AAB and DO3, the dipole moment for this geometry has a slightly larger value than the one corresponding to the dihedral rotation (= α-inversion), more obvious for DO3.

Molecule/structure	μ_{Cis}	μ_{TS}
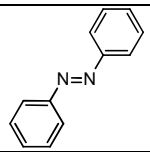 AB	3.43	2.49
	4.35	**2.94**
	5.25	*3.71*
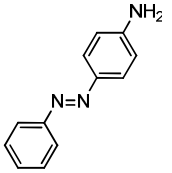 AAB	6.37	6.21 6.54†
	6.44	**7.50**
	8.34	*9.53*
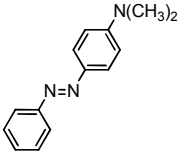 MY	6.86	7.49
	6.97	**8.36**
	9.61	*12.95*
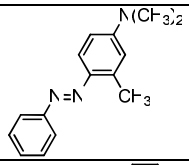 MMY	5.45	7.31
	6.37	**8.21**
	7.81	*9.67*
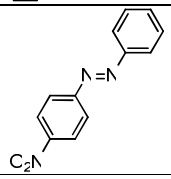 NAB	5.13	10.84
	5.86	**13.11**
	6.61	*16.54*
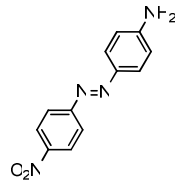 DO3	7.53	14.90 15.61†
	10.80	**18.38**
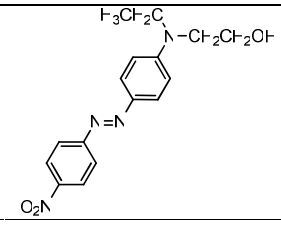 DR1	6.93	13.10
	8.20	**15.96**

Table 5-22 DFT dipole moments in debye for the optimised geometries of the *cis* and the transition state in gas phase (regular font), benzene (bold font), and DMSO (italics font). † *Via* pure rotation pathway.

Figure 5-20 presents the directions of the dipole moments of the *cis* isomers, and their corresponding transition states of AAB in the gas phase and in solution. In general there is only a small change in the direction from *cis* to transition state; this applies the gas phase and solution phase. In addition, there is insignificant change in the directions of the dipole moments between the gas phase and solution phase.

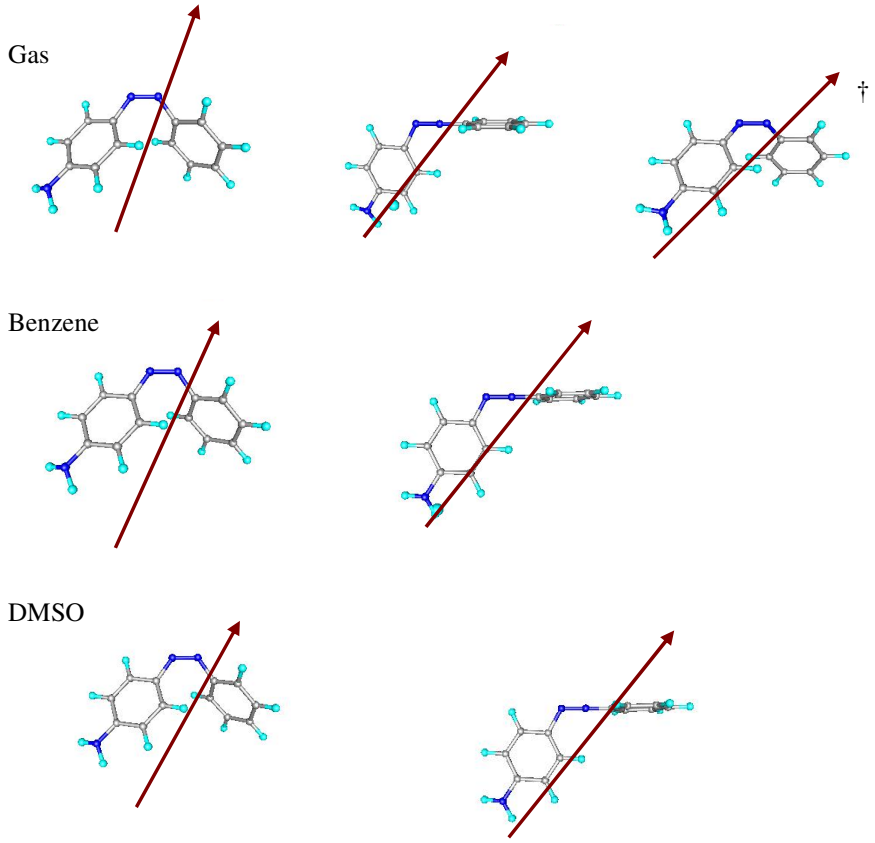

Figure 5-20 Dipole moments directions of *cis* isomers and the corresponding transition states of AAB in gas phase and solution. † *Via* pure rotation pathway.

5.3.9 Activation Parameters of Thermal *Cis-Trans* Isomerisation

The basic equations used to calculate activation parameters in *Gaussian 03* are based on those used in standard texts. Since the vibrational partition function depends on the frequencies, the investigation of such parameters should be carried out on a structure that has

either a minimum (*cis* or *trans* structures) or a saddle point (TS structure) as discussed in Section 3.5.

Gaussian 03 gives the thermodynamic parameters all corrected to zero point energy, ε_{ZPE}. It gives the internal thermal energy which includes the translational, rotational, vibrational and electronic energy of the molecule, E_{tot}, as illustrated by Equation 5-1.

$$E_{tot} = E_t + E_r + E_v + E_e \qquad \textbf{Equation 5-1}$$

And then it calculates the enthalpy of the molecule corrected to the zero point energy, H_{corr} given by Equation 5-2.

$$H_{corr} = E_{tot} + K_B T \qquad \textbf{Equation 5-2}$$

Then it calculates the total entropy of the molecule, S_{tot}, given by Equation 5-3.

$$S_{tot} = S_t + S_r + S_v + S_e \qquad \textbf{Equation 5-3}$$

Corrected Gibbs free energy, G_{corr}, is calculated by knowing the enthalpy and entropy of the system according to Equation 5-4.

$$G_{corr} = H_{corr} - TS_{tot} \qquad \textbf{Equation 5-4}$$

The values of these thermodynamic parameters were taken after including to them the total electronic energy of the system, $\varepsilon_{0,}$ (all at 1.0 atmosphere and 298.15K).

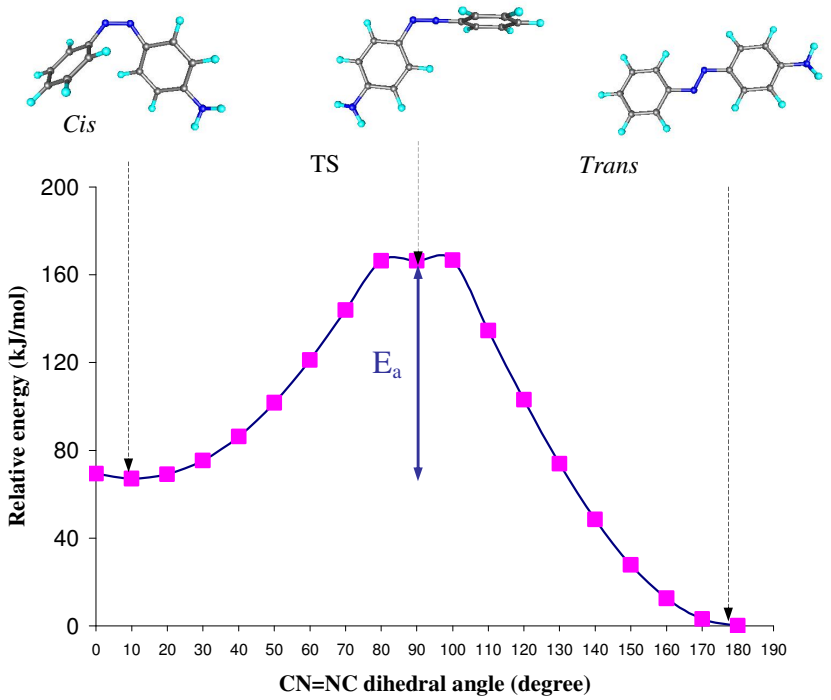

Figure 5-21 DFT-calculated energy profile of the PEC of the dihedral rotation pathway of AAB in the gas phase. On the top, the corresponding optimized geometries are shown from left to right for the torsional angles of 10^0, 90^0 and 180^0, for the *cis*, transition state and *trans*, respectively.

The rate of the thermal *cis*-to-*trans* isomerisation was computed using the thermodynamic output from *Gaussian*, by applying the transition state theory equations for calculating reaction rates as detailed in Section 2.9.

The activation energy of the thermal *cis*-to-*trans* isomerisation calculation is illustrated in Figure 5-21. As illustrated the activation energy, E_a, was calculated from the energy difference between the total energy corrected to zero point energy (sum of electronic and thermal energies) of the transition state and the *cis* isomer. The thermodynamic parameters including $\Delta H^{\#}$, $\Delta G^{\#}$ and $\Delta S^{\#}$ all corrected to the zero point energy were obtained at 298.15 K, from the difference between H, G and S values, respectively, of the transition state and the *cis* geometry obtained from the frequency calculations output.

5.3.9.1 Activation Parameters in the Gas Phase and their Dependence on the Basis Sets

In contrast to the relative energy stability of the isomers, the calculated activation barriers show dramatic basis set effects, Table 5-23. Unexpectedly, the basis set lacking any polarisation functions, 6-31G, show significant lower activation energies than the basis set relatively rich in polarisation functions, 6-31G(d,p). The difference in the activation energies, ΔE_a, obtained by the two basis sets are in range 9.7-16.8 kJ/mol, where MY shows the smaller difference and DO3 shows the largest difference.

Table 5-23 Activation energies (kJ/mol) and their dependence on the basis set for azobenzenes in the gas phase. [i]The imaginary frequencies in cm^{-1}. E_0 values (in hartree) for *cis* (regular font) and transition state (bold font).

Molecule/ structure	6-31G		6-31G(d,p)	
	E_0	ΔE_0 (= E_a)	E_0	ΔE_0 (= E_a)
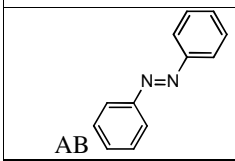 AB	-572.392932	120.82	-572.5624860	135.55
	-572.3469130		**-572.5108570**	
	-95.69[i]		**-10.02[i]**	
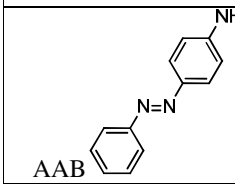 AAB	-627.718234	81.81	-627.906689	94.12
	-627.6870750		**-627.8708420**	
	-370.57[i]		**-415.28[i]**	
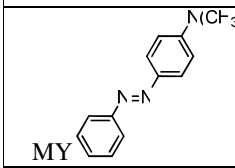 MY	-706.2500550	81.81	-706.4650130	91.52
	-706.218894		**-706.4301560**	
	-369.51[i]		**-412.55[i]**	
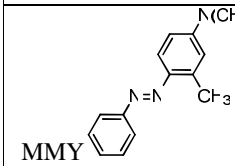 MMY	-745.531234	83.12	-745.7590830	94.84
	-745.4995750		**-745.7229620**	
	-364.61[i]		**-408.47[i]**	
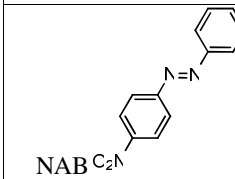 NAB	-776.8102140	60.00	-777.0602660	76.65
	-776.7873620		**-777.0310720**	
	-308.09[i]		**-355.34[i]**	
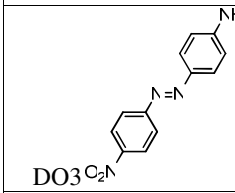 DO3	-832.1377140	52.73	-832.4058740	69.54
	-832.1176320		**-832.3793890**	
	-295.69[i]		**-340.57[i]**	
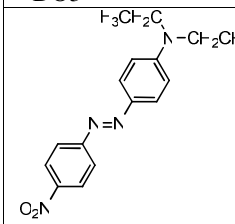 DR1	-1064.396105	54.78	-1064.745229	69.11
	-1064.375242		**-1064.718899**	
	-295.80[i]		**-338.39[i]**	

No general correlation could be made between the difference in the *cis-trans* relative stability and the *cis*-to-*trans* activation barrier, *i.e.*

ΔE_0 DR1 >MY > AAB > DO3 > AB > MMY >NAB

(= E_0(*trans*)-E_0(*cis*))

E_a AB >MMY > AAB > MY > DO3 > DR1 > NAB

The exception is NAB, since it shows the smallest difference in *cis-trans* relative energy and the smallest value for the activation barrier of *cis*-to-*trans* isomerisation.

5.3.9.2 Activation Parameters in Solution and their Dependence on the Basis Sets

The thermal isomerisation of AAB in DMSO solvent has been investigated at the same level of theory but at different basis sets as an example. The obtained activation parameters and the thermal rates were compared with the experimental data that recorded in Chapter 4.

The basis sets that are used are 6-31G, 6-31+G(d), 6-31G(d,p) and 6-31+G(d,p), the first one is simple basis set, lacking any contribution from diffusion and polarisation functions. The second basis set has both a contribution of a diffuse and a polarisable function. The third basis set has a contribution from polarisable functions but lacks diffuse functions. The fourth basis set is similar to the second basis set but richer in polarisation functions.

Table 5-24 summarised the computed activation energies at different basis sets at B3LYP level of theory. From Table 5-24 the following conclusions could be drawn; the lowest activation energy is obtained *via* 6-31G, E_a = 90 kJ/mol, followed by 6-31+G(d), E_a = 91, the other basis sets gives very similar values , E_a = 98 kJ/mol. The last two basis sets differ from each other in that one contained a diffuse function while the other did not, and they are similar to each other in their contents of the polarisation function, both of them contain the *f* and *p* functions. From this observation it is clear that the diffuse functions have insignificant effect on this type of calculations. This is expected, since the diffuse functions play significant role for systems carrying high negative charges, systems in this study do not have species with high electronic charge in the TS. Other comparison could be made between 6-31+G(d) and 6-31+(d,p), these two basis sets similar in their contents of diffuse function and dissimilar in their contents of polarisation functions. The addition of a *p* function lead to significant difference in the calculated activation energies, the obtained activation energy by the basis set contained the *p* polarisable function is larger than the activation energy obtained by the basis lack to that function by 6.5 kJ/mol. The addition of the *p* polarisation function allows orbitals to change shape with this added function by higher angular momentum than

required for ground state description for each atom in a better way than due to d polarisation function.

The percentage of error associated with the computed activation energies were obtained by comparing the computed values with the experimental activation energy value, the percentage of error of the activation energy for each basis set is represented in Table 5-24. It is clear that the smallest percentage of error were associated with the values obtained *via* 6-31G(d,p) and 6-31+G(d,p), and equals 15 %. The percentage of errors in the other basis sets are 22 and 20 % for 6-31G and 6-31+G(d) basis sets, respectively. Thus the best calculated E_a is obtained from 6-31G(d,p), whereas the 6-31+G(d,p) also produced a good activation energy value but in more time. This last point is crucial when the available computational resources are scarce.

	6-31G	6-31+G(d)	6-31G(d,p)	6-31+G(d,p)
E_0 (*cis*)	-627.744853	-627.910397	-627.930354	-627.959008
E_0 (TS)	-627.709767 -370.5694[i]	-627.875581 -430.1475[i]	-627.893131 -415.3311[i]	-627.921711 -425.1744[i]
ΔE_0 (= E_a)	89.9	91.41	97.73	97.92
Error / %	22	20	15	15

Table 5-24 The total energies of the *cis* and the transition state (in hartree), and the activation energies of the thermal isomerisation (in kJ/mol) for AAB in DMSO and their dependence on the basis sets. [i] The imaginary frequency in cm^{-1}. Experimental activation energy: E_a=114.82 kJ/mol.

Examining the computed activation parameters at the same level of theory/basis sets, Table 5-25, indicates that the activation entropy values in all basis sets are significantly different from the experimental value.

	6-31G	6-31+G(d)	6-31G(d,p)	6-31+G(d,p)
$\Delta H^{\#}$	89.99	91.51	98.12	98.31
$\Delta S^{\#}$	13.53	3.19	10.76	13.23
$\Delta G^{\#}$	85.97	90.56	94.92	94.37
$k_{-1}(\Delta) / 10^{-5}$	551	86	17	21

Table 5-25 kinetic and activation parameters of the thermal isomerisation for AAB at 298 K in DMSO and their dependence on the basis sets ($\Delta H^{\#}$ and $\Delta G^{\#}$ in kJ/mol, $\Delta S^{\#}$ in J/mol K and k in s^{-1}). Experimental results (Chapter 4): $\Delta H^{\#}$ =112.28 kJ/mol, $\Delta S^{\#}$ = 54.37 J/mol K, $\Delta G^{\#}$ =96.07 kJ/mol and $k_{-1}(\Delta)$ =10 x10^{-5} s^{-1}.

The calculations of the activation entropies at different basis sets are random and no general trend could be concluded. The computation of activation entropy include obtaining all the vibrational modes (translational, rotational, vibrational and electronic), slight differences in

the calculations of these vibrational modes from one basis set to another can cause significant difference in the value of the total activation entropy, this is one possible explanation for the last observation. The least difference between the computed and experimental values of the activation entropy is found at 6-31G and 6-31+G(d,p), $\Delta\Delta S^{\#}$ ($\Delta S\#$ (exp) -$\Delta S^{\#}$ (theo)) = 41 J/mol K. These two basis sets that are quite different from each other 6-31G is quite simple where 6-31+G(d,p) is not. On the other hand, the largest difference is found at 6-31+G(d), $\Delta\Delta S^{\#}$ = 51 J/mol K. The difference at 6-31G(d,p) is intermediate equals 44 J/mol K. The Gibbs free energy of activation is better estimated at 6-31G(d,p) and 6-31+G(d,p), the associated percentage of errors are 1 and 2%, respectively. In the other basis sets the corresponding percentage of errors are 11 and 6% at 6-31G and 6-31+(G), respectively. The variation in predicted barriers has a large effect on the predicted rate of isomerisation; lowering the barrier from 98 kJ/mol at 6-31G(d,p) level to 90 kJ/mol at 6-31G level leads to a 32-fold increase in the predicted rate at 298 K.

5.3.9.3 DFT Activation Parameters

Table 5-26 shows the theoretical kinetic and activation parameters of the thermal isomerisation in the gas phase and in solution.

To the best of the author's knowledge no extensive work has been published previously in this area of research. The available literature to compare with is from Poprawa-Smoluch *et al.* [2006];[64] they studied the thermal isomerisation of *cis*-DR1. The calculated activation barrier in the gas phase equals 72.9 kJ/mol at 6-31G(d) level/basis set in partially good agreement with the present value 66.9 kJ/mol at 6-31G(d,p) considering the effect of varying the basis set.

	Molecule/structure	E_a / kJ mol^{-1}	$\Delta H^{\#}$ / kJmol^{-1}	$\Delta S^{\#}$ /J mol^{-1} K^{-1}	$\Delta G^{\#}$ / kJ mol^{-1}
AB	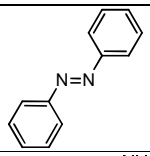	135.55	134.21	-0.014	138.51
		140.02	**138.56**	**-0.017**	**143.69**
AAB	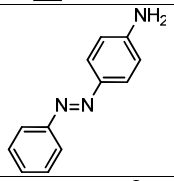	94.12	94.27	7.22	92.12
		95.40	**95.66**	**7.86**	**93.31**
		97.73	*98.12*	*10.76*	*94.92*
MY	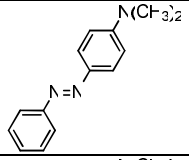	91.52	91.80	9.40	88.96
		95.79	**95.86**	**4.04**	**94.76**
		98.92	*98.98*	*3.33*	*97.99*
MMY	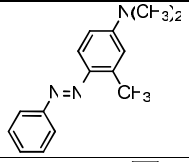	94.84	95.56	17.96	90.18
		96.20	**96.75**	**15.34**	**92.18**
		98.73	*99.25*	*18.23*	*93.82*
NAB	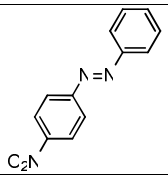	76.65	76.41	0.22	76.31
		73.24	**72.91**	**-0.69**	**73.12**
		68.61	*68.19*	*-3.19*	*69.14*
DO3	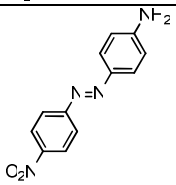	69.54	69.51	1.61	69.00
		64.36	**64.56**	**9.11**	**61.85**
DR1	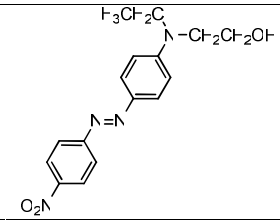	69.13	69.09	7.17	66.93
		66.21	**63.67**	**-29.33**	**72.40**

Table 5-26 The theoretical activation parameters of the *cis-trans* thermal isomerisation in the gas phase (regular font), benzene (bold font), and DMSO (italics font).

Table 5-26 shows that in the gas phase, the theoretical activation energies are very comparable for electron donating azobenzenes, and in the range 92-95 kJ/mol. Where for push-pull azobenzenes the values are comparable, and have a significant difference from

those for electron donating azobenzene, and in the range 69-70 kJ/mol. Where for electron acceptor azobenzene the activation energy has an intermediate between these two extremes, and equals 77 kJ/mol. Thus the computational method distinguishes between the three types of molecules. Consequently, this predicts that the *cis* isomers of push-pull azobenzenes are decaying thermally at faster rates followed by that of electron acceptor azobenzenes followed by that of electron donating azobenzenes. The estimated entropies of activation for the electron donating azobenzenes are relatively larger than those of push-pull azobenzenes. For electron donating azobenzenes the activation entropies increase with the increasing ability of donation or with introduction of methyl group in the *ortho* position with respect to the azo linkage at the donating side, and it is in the range 7-18 J/mol K. For push-pull azobenzenes the activation entropies are in the range 2-7 J/mol K. Alternatively for the electron acceptor azobenzene the entropy of activation is close to zero. Comparing the Gibbs free energy of activation indicates that the compensation between $\Delta H^{\#}$ and $\Delta S^{\#}$ gives comparable values for this parameter. For the electron donating azobenzenes it is in the range 89-92 kJ/mol, for the push-pull azobenzenes in the range 67-69 kJ/mol and for electron acceptor azobenzenes the value is intermediate between the two extremes and equals 76 kJ/mol.

DFT calculations predict an increase in the activation barrier upon going from the gas phase to benzene to DMSO for electron donating azobenzenes, and reverse trend for electron accepting azobenzenes and push-pull azo benzenes. The average change in the activation barrier is 3.1 kJ/mol, the maximum difference is found for DO3, ΔE_a (E_a (in gas phase)- E_a (in benzene)) = 5.2 kJ/mol, and the minimum difference is for AAB, ΔE_a (E_a (benzene)- E_a (in gas phase)) = 1.3 kJ/mol, later this will be compared to the trends of the activation barriers changes observed experimentally. The computed activation parameters in solution are discussed in the following two paragraphs.

The available literature to compare with is also Poprawa-Smoluch *et al.* [2006],[64] the activation barrier of the thermal reversal of *cis*-DR1 in toluene at 6-31G(d) is 68.7 kJ/mole, which does not vary significantly from the present value in benzene, which is 66.21 kJ/mole, taking into account the effect of different basis set and solvent. The Gibbs free energy of activation did not vary significantly for each molecule in solution, indicating that the compensation between $\Delta H^{\#}$ and $\Delta S^{\#}$ parameters is not affected significantly by the solvent. The activation energies changed from benzene to DMSO solvent but the changes are insignificant indicate that the computational method (PCM) did not predict very accurately the effect of solvent on the thermal decay barrier, (see the detailed comparison between the

experimental data reported in Chapter 4 with the present theoretical data in the following section). This indicates that not all the interactions between the solute and solvent are taken into account by the applied computational method. The trend of activation energy change from benzene to DMSO is not constant, the applied method predicts that the thermal barrier increases as the solvent become more polar for electron donating azobenzene, and has the opposite trend for electron acceptor azobenzenes.

The change in activation entropy due to solvent effect is insignificant in most cases, and the changes were by a factor in the range of 1.2-1.4 J/mol.K. The case where the change is significant is for NAB, and the change is by 4.6 J/mol.K. The entropies of activation are small and positive in most cases, expect in case of NAB and DR1 where negative entropy of activation is predicted. NAB has a very small negative activation entropy, close to zero, in benzene, $\Delta S^{\#}$ = -0.69 J/mol K, and DR1 in benzene has relatively large negative entropies of activation, $\Delta S^{\#}$ = -29.33 J/mol K.

In general in all molecules in the gas phase and in solution $\Delta H^{\#}$ values are very similar to $\Delta G^{\#}$ values; this indicates that the role of $\Delta S^{\#}$ in determining the $\Delta G^{\#}$ is predicted to be insignificant.

5.3.9.3.1 Comparison with Experiments

Table 5-27 shows comparison between the theoretical and experimental activation parameters of the thermal isomerisation.

In general the DFT-predicted values of the activation energy and Gibbs energy of activation in DMSO are in reasonably good agreement with the experimental values, while the values in benzene tend to be in less good agreement, this is more pronounced in the case of Gibbs free energy of activation. The DFT calculations are unsuccessful at predicting the entropy of activation, where in all cases there is a large discrepancy between the theoretical and experimental values.

	Molecule/structure	Solvent	E_a / kJ mol^{-1}	$\Delta S^{\#}$ /J mol^{-1} K^{-1}	$\Delta G^{\#}$ / kJ mol^{-1}
AAB	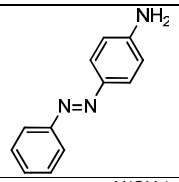	Benzene	95.40	7.86	93.31
			74.02	**-88.05**	**97.66**
		DMSO	97.73	10.76	94.92
			114.82	**54.37**	**96.07**
MY	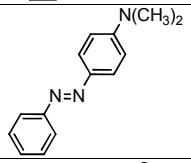	Benzene	95.79	4.04	94.66
			58.09	**-135.03**	**103.00**
		DMSO	98.92	3.33	97.99
			94.92	**-19.67**	**98.18**
MMY	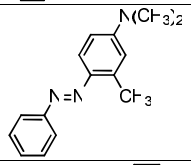	Benzene	96.20	15.34	92.18
			51.32	**-119.64**	**84.53**
		DMSO	98.73	18.23	93.82
			82.59	**-49.18**	**94.64**
NAB	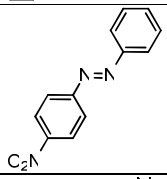	Benzene	73.24	-0.69	73.12
			37.20	**-205.47**	**95.87**
		DMSO	68.61	-3.19	69.14
			91.71	**17.66**	**83.97**
DO3	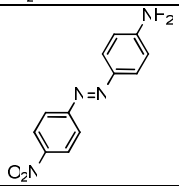	Benzene	64.36	-9.11	61.85
			71.82	**-60.69**	**87.41**
DR1	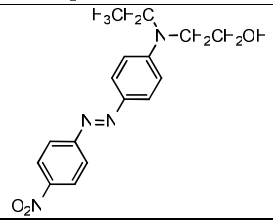	Benzene	66.21	-29.33	72.40
			40.48	**-147.30**	**81.94**

Table 5-27 Theoretical (regular font) and experimental (bold font) activation parameters of the *cis-trans* thermal isomerisation. Experimental data in DMSO were obtained from basic solutions.

The theoretical activation parameters are over/underestimated. In benzene the activation energies are overestimated in most cases, 5 out of 6, where in DMSO there is equality between the overestimation and underestimation values, 2 of each. Table 5-28 shows the percentage of errors associated with the computed activation parameters using the experimental activation parameters.

Molecule/structure	Error in E_a / %	Error in $\Delta S^{\#}$ / %	Error in $\Delta G^{\#}$ / %
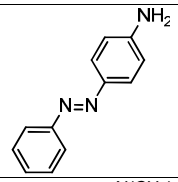 AAB	29	109	4
	15	**80**	**1**
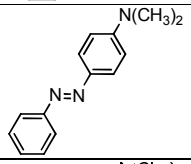 MY	65	103	8
	4	**117**	**0**
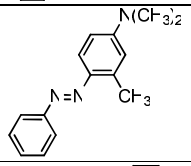 MMY	87	113	9
	20	**137**	**1**
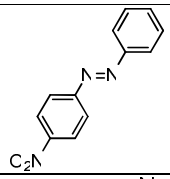 NAB	97	100	24
	25	**118**	**18**
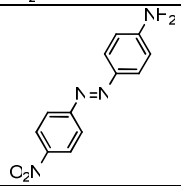 DO3	10	85	29
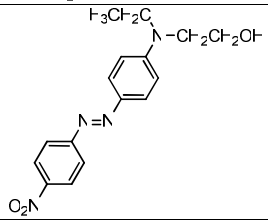 DR1	64	80	12

Table 5-28 Percentages of errors in the theoretical activation parameters in benzene (regular font) and in DMSO (bold font) solutions.

From this table, it is obvious that MY has the lowest percentage of error in the computed activation energy, followed by AAB, and followed by MMY and last by NAB in DMSO. The percentages of error are 4, 15, 20 and 25%, respectively. In benzene the better agreement between the theoretical and experimental activation energy was shown in DO3 and AAB, the percentages of error are 10 and 29%, respectively. In all other cases and due to large percentage of error, in the range 61-97%, it is inapplicable in these cases to consider any agreement between the two values. On the other hand, the agreement in the values of

Gibbs free energies of activation is generally very good and in some cases excellent; for example, in the case of MY in DMSO the values are almost identical. For AAB, MY and MMY in benzene and DMSO there is very good agreement, the percentage of error lie in the range 1-9%. For NAB in benzene and DMSO and DO3 and DR1 in benzene, there is good agreement with the percentages of error in the range of 12-29%. The percentages of error in the entropies of activation are quite large and lie in the range 80-137%; leading to an unambiguous conclusion that DFT calculations are unable to reproduce the experimental entropies of activation. The theoretical activation entropies are more positive (or less negative) compared to the experimental values, the exception is AAB in DMSO where the theoretical activation entropy equals 10.76 J/mol K and the experimental value equals 54.37 J/mol K.

The results where there are poor agreement between the experimental and theoretical activation parameters, led us to reconsider the method used to determine the theoretical activation parameters. As mentioned before the optimised structures of the *cis* isomers and transition states were obtained from following the potential energy curve in the gas phase, the corresponding geometries in solution were taken from these geometries and re-optimised again in the specific solvent and the frequency calculations were carried out on these geometries, to obtain the activation parameters. Thus the potential energy curves in solution were not constructed, let us call this method as method 1. The other way to obtain the activation parameters in solution would be to construct the potential energy curve in solution, obtaining the geometries of the *cis* isomer and the transition state from it and then applying the frequency calculations to obtain the activation parameters, let us called this method 2. The question that arises is whether it is worthwhile to perform this time and money consuming processes to obtain the potential energy curves in solution? In other words, will be there any improvement in the results, *i.e.* will the ability of DFT calculations to reproduce the experimental activation parameters be improved? To answer this question the constructed potential energy curves for AAB in the gas phase and in benzene and DMSO, Figure 5-6, were used to calculate the activation energies in these three cases, then the percentages of error associated with method 1 and method 2 were compared and are represented in Table 5-29.

	Method 1		Method 2	
	E_a /kJ mol-1	Error in E_a / %	E_a /kJ mol-1	Error in E_a / %
Benzene	95.40	29	97.57	32
DMSO	97.73	15	88.45	23

Table 5-29 The activation energies of AAB and the associated percentages of error of method 1 and 2. Details of method 1 and 2 to obtain the activation energy are within this section.

From Table 5-29 it is clear that applying method 2 to obtain the activation energies did not improve the situation but in fact make it worse, where in benzene the percentage of error from method 1 and method 2 are 29 and 32 %, respectively and in DMSO are 15 and 23 %, respectively.

Table 5-30 gives a correlation between the percentages of errors in the predicted values of Gibbs free energy of activation and the fraction of change in the dipole moments of the *cis* and transition state. The cases in which there are a good agreement between the experimental and theoretical values of the Gibbs free energy of activation show also a small change in the dipole moment magnitude between the *cis* and transition state, *i.e.* for electron donating azobenzenes. On the other hand, the cases those show less good agreement between the experimental and predicted values show also a large change in the dipole moments values between the *cis* and transition state, *i.e.* for electron acceptor azobenzenes and push-pull azobenzenes.

The prediction of the activation entropies involves the frequency calculations. Houck and Pollack [2003][99] in their experimental study of a second-order reaction gave a theoretical explanation for the positive change in entropy and attributed it to the formation of low frequency vibrational levels, the weak ability of DFT calculations in predicting such parameter may be attributed tentatively to the same reason.

Molecule/structure	Error in $\Delta G^{\#}$ / %	μ_{TS}/μ_{cis}
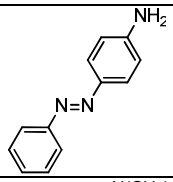 AAB	4	1.2
	1	**1.1**
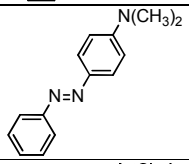 MY	8	1.2
	0	**1.4**
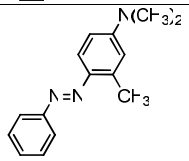 MMY	9	1.3
	1	**1.2**
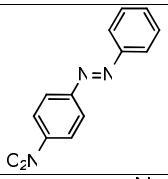 NAB	24	2.2
	18	**2.5**
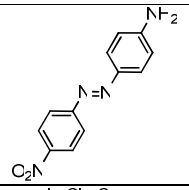 DO3	29	1.7
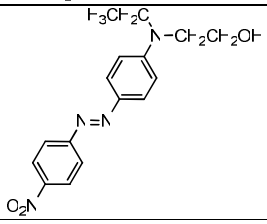 DR1	12	2.0

Table 5-30 Percentages of errors in the predicted values of Gibbs free energy of activation and the fractions of the dipole moments of *cis* and transition state in benzene (regular font), and in DMSO (bold font).

5.3.9.3.2 DFT Rate Constants

Table 5-31 displayed the theoretical and experimental rate constants in benzene and DMSO.

Molecule/structure	$k_{-1}(\Delta)$ / 10^{-5} s^{-1}
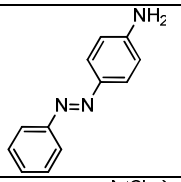 AAB	27.2 (5.1) **16.7** **(9.8)**
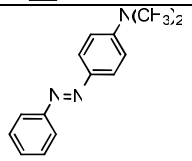 MY	16.3 (9.8) **4.2** **(3.9)**
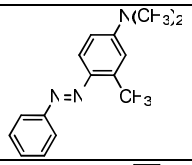 MMY	53.9 (958.5) **27.5** **(15.0)**
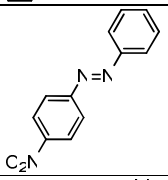 NAB	82896.3 (10.2) **397683.9** **(959.1)**
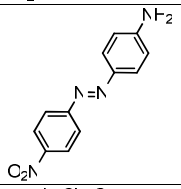 DO3	9705798.3 (320.2)
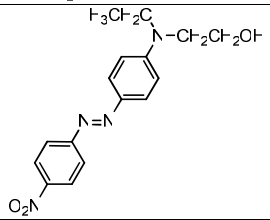 DR1	45161.9 (2757.4)

Table 5-31 The theoretical and experimental (in parentheses) rate constants of thermal *cis→trans* isomerisation in benzene (regular font) and DMSO (bold font) at 298 K.

The ability of DFT calculations to predict the thermal rate constant is determined by its ability in predicting the Gibbs free energy of activation. Thus cases were there is large discrepancy in $\Delta G^{\#}$ with the experimental value will be accompanied by a large discrepancy

in $k_{-1}(\Delta)$ value. The large discrepancies between the theoretical and experimental thermal rate constants are more pronounced in case of benzene than in DMSO. In benzene, in most cases the theoretical rates are much faster than the experimental ones; the exception is MMY since the theoretical rate is smaller than the experimental one by a factor of 18. The discrepancies in these values for AAB and DR1 are not so significant, by a factor of 5 and 16. On one hand MY shows the least discrepancy, where the difference between the theoretical and experimental values is just by a factor of 2.

Table 5-31 shows that in most cases the ability of DFT calculations in predicting the rate constants in DMSO is better than in benzene, but the theoretical thermal rate is much more rapid than the experimental one, by a factor of 2, 1.5 and 580 for AAB, MMY and NAB, respectively.

It was evident from the experimental data that there is a significant contribution of the entropy of activation to the value of Gibbs free energy of activation, but this is not reproduced in the computed values, the computed values of E_a alone do not accurately predict the relative values of the rate constants, *i.e.* the relative rates cannot be reliably predicted just by calculating the potential energy curve.

5.3.10 Effects of Protonation in DMSO Solutions

Experimentally, the *cis-trans* isomerisation is enhanced in aprotic medium and inhibited in a basic one [58,59,69,97,100]. Theoretically, *ab initio* calculations on protonated molecules showed that the activation energies of protonated compounds were lower than the neutral counterparts[101]. The present experimental data support this observation, since the rates of the thermal isomerisation are decreased and the activation energies are increased in basic DMSO solutions. Complementary DFT calculations carried out for the protonated compounds showed much lower activation energies compared to the corresponding neutral compounds. The effect of protonation on the activation in addition to its effect on the corresponding thermal rates is conducted in the following two sections.

5.3.10.1 Effect of Protonation on the Activation Barriers

An investigation of the detailed mechanism of the *cis-trans* conversion of azo compounds in a protic environment and the role of protonation of the azo bond has been carried out previously,[101] that work found that protonation of one of the nitrogens at the N=N bond leads

to a considerable reduction of the activation barrier (21-84 kJ/mol). The experimental data presented in Chapter 4, Section 4.6.5.1 and Section 4.6.6.2, for azobenzenes substituted with electron donating groups clearly indicated the effect of protonation on the thermal barrier and the thermal rate. A significant reduction of the thermal barrier was evident (14-63 kJ/mol). In order to study the effect of protonation on the activation energies of the thermal isomerisation computationally, the thermal isomerisation of neutral and protonated forms of AAB in the gas phase and in DMSO has been investigated with *ab initio* approach using the B3LYP/6-31G level of theory/basis set.

The protonated forms for the *trans* geometry was constructed, *i.e.* the azonium tautomer, the species that are formed due to the presence of protons in the medium, refer to Figure 4-2 and Figure 4-3. Starting from the azonium tautomer geometry of the *trans* isomer, the potential energy curve of the α-inversion pathway was constructed passing to the protonated transition state and ending at the protonated geometry of the *cis* isomer. Performing the frequency calculations allows the confirmation of the nature of the stationary points and gives the total energy for each geometry corrected to the vibrational zero point energy.

The potential energy curve *via* the α-inversion route was applied in the same fashion as for the construction of the potential energy curve for the neutral or un-protonated molecule, *i.e.* scanning the α-CN=N bond angle in the range 110^0-240^0. Figure 5-22 gives the PECs *via* the inversion pathway for the neutral and protonated of AAB in the gas phase.

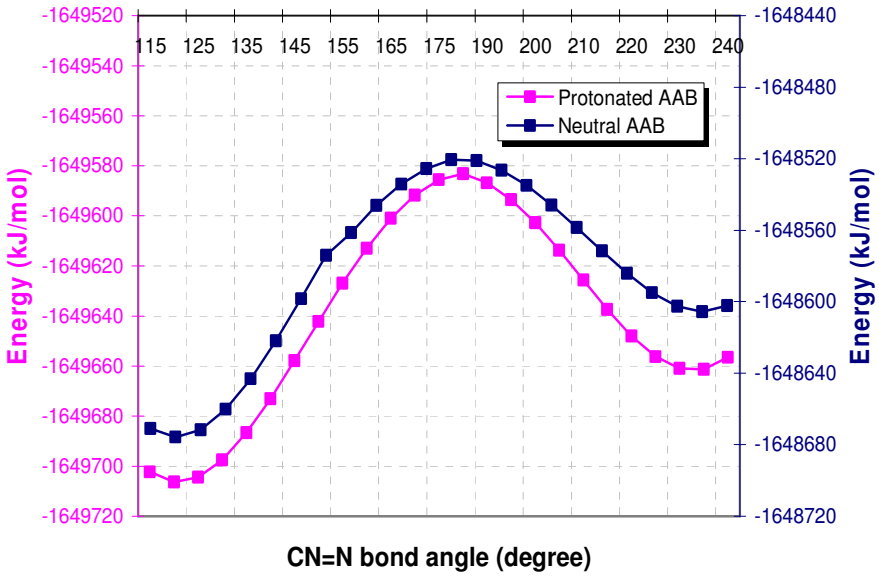

Figure 5-22 DFT-calculated energy profile of PECs *via* the α-inversion route for AAB; neutral and protonated forms in the gas phase at the 6-31G basis set.

The difference in energy between the two isomers and the two isomers and their transition state were obtained. As performed in case of neutral molecule, the optimised geometries in the gas phase were reoptimised in DMSO applying SCRF/PCM model. The obtained values were compared with the corresponding values of the un-protonated species. The computed thermal barrier in DMSO will be compared with the experimental one.

Table 5-32 shows the DFT data of the key coordinates, *i.e.*, NN bond lengths, α-/β-CN=N valence angles and the magnitude of the imaginary frequencies obtained for the transition states of the neutral and protonated forms of AAB.

	Gas phase				DMSO	
	Neutral form		Protonated form		Neutral form	Protonated form
	AB[a]	AAB	AB[a]	AAB	AAB	
N=N	1.200	1.2438	1.206	1.2483	1.2500	1.247
α-CN=N	180.00	–	178.88	177.0	–	177.0
β-N=NC	117.36	118.4523	127.17	129.0561	119.5768	127.1786
Imaginary frequency /cm^{-1}	-501	-371	-468	-361	-379	-376

Table 5-32 Transition state geometries for the isomerisation of the neutral and protonated forms of AAB (α-inversion pathway) at 6-31G basis set. [a] From reference[101], Inversion mechanism at LCAO MO SCF 6-31G(d).

Indeed, the activation barrier parameters presented in Table 5-33 display a considerable dependence on the pH of the medium. For AB, all protonated compounds have activation energies lower than their neutral counterparts by 38 kJ/mol for the E_{TS}-E_{trans} barrier, by 21 kJ/mol for E_{cis}-E_{trans}, and by 17 kJ/mol for the E_{TS}-E_{cis} barrier from reference. [101] This is in agreement with the observed result from the present work, where the activation barrier is lowered due to protonation of AAB molecule by 8 kJ/mol for E_{TS}-E_{cis}, by 33 kJ/mol for the E_{TS}-E_{trans} barrier, by 22 kJ/mol for E_{cis}-E_{trans},

The observed lowering in the activation barrier for protonated AAB molecule is in agreement with the experimental observation in DMSO solution. Table 5-33 gives the obtained experimental and theoretical activation energies. The theoretical results are consistent with the experimental results but differ in the magnitude of the lowering in the activation barrier due to protonation, since in the experimental case the decrease in the activation barrier between E_{TS}-E_{cis} is 63 kJ/mol, higher than the theoretically predicted value, where the decrease is 10 kJ/mol. For the present author, it was not found possible to construct the potential energy curve for the protonated AAB molecule *via* dihedral rotation, since the frequency calculations on the obtained transition state showed no imaginary frequency, no explanation for this can be given. But Sokalski *et al.* [101] mentioned that the ability to construct such a curve for a protonated diazene molecule using CASSCF model required the use of a much more costly multideterminant CASSCF approach due to the multideterminant character of the transition state for the rotation mechanism. However, the reduction in the activation barrier by the rotational route may be greater than that observed due to the inversional route, since the effect of protonation observed experimentally results in a greater decrease in the barrier and has been taken to imply the rotation mechanism for protonated molecule. Thus the disagreement in the degree of reduction in these barriers

between the experimental and computational data might be less if the rotational route was applied for the protonated molecule opens this point to interpretation.

Table 5-33 The theoretical and experimental (in parentheses) activation energies (in kJ /mol) of the neutral and protonated forms at 6-31G basis set. Energy values in the gas phase (regular font) and in DMSO (bold font). * Unobtainable. [a]From reference [101] Inversion mechanism at LCAO MO SCF 6-31G(d). [†]Without the zero point vibrational corrections for the energy of the *trans* isomer.

Molecule/structure	Neutral form			Protonated form		
	E_{TS}-E_{cis}	E_{TS}-E_{trans}	E_{cis}-E_{trans}	E_{TS}-E_{cis}	E_{TS}-E_{trans}	E_{cis}-E_{trans}
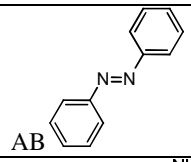 AB	120.82 105.94[a]	185.92 169.54[a]	65.10 63.60[a]	89.16[a]	131.34[a]	42.17[a]
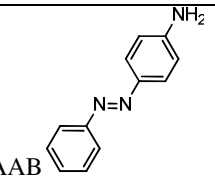 AAB	81.81	149.89	68.08	73.89	116.69[†]	45.79[†]
	92.12 (114.82)	**148.02**	**55.90**	**82.48 (52.15)**	*	*

5.3.10.2 Effect of Protonation on the Thermal Rates

Table 5-34 displays the theoretical and experimental entropies of activation, the activation energies, and the rate constants for the *cis*-to-*trans* thermal isomerisation in DMSO at 298 K.

The theoretical thermal rate constants of the neutral and protonated forms of AAB in DMSO were obtained from the computed activation parameters are 3.5×10^{-5} s^{-1} and 3.7×10^{-2} s^{-1} for the neutral and protonated forms, respectively. The computed thermal rate constants for protonation results in faster rate of isomerisation but the predicted enhancement of the thermal isomerisation is a huge 1066-fold increase. In contrast the observed experimental enhancement in the thermal isomerisation is 8-fold increase. The theoretical rate constant for the neutral form is underestimated by a factor of 3, whereas for the protonated form it is overestimated by a factor of 48. Thus it appears more feasible to simulate accurately the parameters for the neutral molecules than for the protonated one with the DFT approach. Although, the theoretical enhancement in the rate constants is so great, the predicted decrease in the activation energy is underestimated, this could be explained in terms of the predicted values of the entropy of activation for the neutral and protonated forms, as can be seen from Table 5-34 that the predicted values of the entropy of activation are underestimated for neutral form and overestimated for the protonated form.

	$\Delta S^{\#}$ /Jmol^{-1} K	E_a /kJ mol^{-1}	k / 10^{-5} s^{-1}
Neutral form	-21.06 (54.37)	92.12 (114.82)	3.5 (9.8)
Protonated form	4.54 (-137.80)	82.48 (52.15)	3734.3 (77.4)

Table 5-34 The theoretical and experimental (values in parentheses) rate constants of thermal *cis→trans* isomerisation of AAB in DMSO at 298 K. The theoretical values are at 6-31G basis set.

5.4 Conclusions

The results presented in this chapter provide an extensive computational study of the thermal *cis*-to-*trans* isomerisation of simple mono disperse dyes. Combined with the experimental results in Chapter 4 they allow judgement of the ability of DFT calculations to predict the activation parameters of the thermal isomerisation, and provide insight into the possible mechanism of isomerisation.

DFT calculations of the optimised geometries of *trans*-AB calculated at two basis sets justify the reliability of the computational calculations of the equilibrium structures of the *trans* and *cis* isomer of the studied molecules, by their excellent agreement with the available literature and experimental data. A comparison with the available literature for the other molecules also showed good agreement. The effect of substituents on the optimised geometries of the *trans* and *cis* isomer and on the corresponding transition state in the gas phase was assessed, The *trans* isomer is planar for AB and NAB, and non planar for AAB, MY, MMY, DO3 and DR1 in the gas phase and in solution (with respect to substituents). All *cis* isomers show a twisted conformation because of the repulsive interactions between the hydrogen atoms of the phenyl rings. The effect of solvent on the optimised geometries in solution was also assessed; the impact of solvent is insignificant for the bond lengths and bond angles of the azo linkage compared to that in the gas phase, their respective variations being limited to 0.003 Å and 0.9^0. The changes in these parameters from the gas phase into the solution are more significant upon changing the solvent to DMSO than to benzene. The general effect of more polar solvent, *i.e.* DMSO to benzene, is elongation of the azo linkage bond lengths and increase of the azo linkage bond angles.

There is an effect of varying the basis sets, *viz.* 6-31G and 6-31G(d,p) on the relative stability of the *trans* and *cis* isomer, the larger basis set results in a larger difference between the two isomers. The difference between the two basis sets is in the range 0.05-3.06 kJ/mol.

This study indicated that a potential energy curve for isomerisation by pure rotation about the azo bond could be obtained by DFT-B3LYP calculations by merely constraining the C-N=N-C dihedral angle. The optimised geometries in which the C-N=N-C dihedral angle is in the range 60-120 degrees were converted to a linear (inversion) transition state, which was confirmed to be the characteristic geometry of the transition state for the inversion pathway. To obtain a potential energy curve corresponding to uncontaminated rotation the constraints should increase to include restriction of the C-N=N bond angle to prevent the passage to the inversion transition state. This study successfully obtained a pure rotation potential energy curve for AAB and DO3; the transition state for the pure rotation path way is higher in energy by 40 kJ/mol than the one corresponding to the inversion pathway.

DFT calculations were used successfully to obtain the potential curves for the two alternative pathways of the inversion mechanism for the azobenzenes, and, by comparing the corresponding activation energies, to determine the geometry of the transition state for the favourable pathway. The unsubstituted phenyl ring is the one that inverts more favourably for electron donating substituted azobenzenes, while the electron acceptor substituted ring is the one that inverts more favourably for the electron acceptor and electron donating-acceptor azobenzenes. The difference in energy between the two inversions pathways is in the range 19.3-47.2 kJ/mol. For all of the molecules studied, the DFT calculations predict a linear (inversion) transition state. However, two alternative routes from the *cis* isomer to the transition state were found, dihedral rotation or α-inversion about the azo bond, both leading to the same linear transition state, with the same activation energy. It is evident that passage to the transition state involves rotation and inversion and, therefore, the notion of two discrete mechanisms, one occurring exclusively by rotation and one exclusively inversion, is an oversimplification. For selected molecules, the activation energy for the formation of a pure rotational transition state has been calculated (by constraining the inversion coordinate) and found to be substantially higher than that of the linear (inversion) transition state.

The experimental and theoretical results predict faster isomerisation and lower activation barriers on protonation of electron donating azobenzenes. On the basis of a linear transition state, the decrease in activation energy predicted by DFT calculations is significantly smaller than that observed experimentally. This may suggest that isomerisation of the protonated molecule occurs *via* a rotational transition state, as a result of weakening of the N=N bond by protonation. However, this could not be confirmed theoretically.

DFT calculations of the activation parameters of the thermal isomerisation in two solvents, namely benzene and DMSO were performed. The activation energies are in the range 70-95 kJ/mol, the activation entropies are in the range (-0.7)-(18.2) J/mol.K and the Gibbs free energies of activation are in the range 61.9-98.0 kJ/mol. Direct comparisons with experimental results reported in Chapter 4 was conducted, the DFT-predicted values of the activation energy and Gibbs energy of activation in DMSO are in good agreement with the experimental values, while the values in benzene tend to be in less good agreement. The DFT calculations are unsuccessful at predicting the entropy of activation, where in all cases there is a large discrepancy between the theoretical and experimental values. This in turn means that the values of the rate constant cannot be predicted correctly from the DFT-calculated activation parameters.

6 Conclusions

The work presented in this thesis was concerned with experimental and computational studies of *cis-trans* isomerisation of simple azo molecules. NMR spectroscopy coupled with *in situ* laser irradiation has been used to reveal important information about the structural and solvent effects on the kinetics of the photo- and thermal isomerisation, and the activation parameters of thermal *cis* isomer decay. The thermal *cis* isomer decay was also studied *via* DFT calculations. A summary of conclusions is presented below.

One of the major advantages of the employed spectroscopic technique is the *in situ* irradiation while the NMR spectrum is acquired; this allows the short-lived *cis* isomer to be detected and analysed. The shortest half life that was measured for a *cis* isomer in this study was for DR1, with a half-life time of 15 seconds. The *cis* isomers of the push-pull azobenzenes in DMSO were too short lived for their half-lives to be measured by the NMR technique. Consistent with previous observations[4-8] it was found that the *cis* isomer signal is always more shielded than the relevant *trans* signal, and the largest difference in the chemical shifts of the *cis* and *trans* forms is observed for those protons in the *ortho*-positions to the azo linkage.

NMR coupled with *in situ* irradiation has proved to be an effective method to investigate the rates of photo- and thermal isomerisation. This is afforded by the high spectral resolution, and the ability to record and process data efficiently using a pseudo 2D acquisition. By careful control of the experimental conditions it has been possible to compare the experimental kinetic data obtained for different molecules in two different solvents.

The kinetic data obtained for each azobenzene consisted of rate constants for the reversible photoisomerisation, and the rate constant for thermal *cis* isomer decay. In all cases, the photochemical contribution to the *cis-trans* isomerisation is greater than the thermal contribution. The measured photoisomerisation rate constants yield values for the relative quantum yields of *trans-cis* and *cis-trans* photoisomerisation, $\phi^{rel}_{trans\rightarrow cis}$ and $\phi^{rel}_{cis\rightarrow trans}$. In most cases, $\phi^{rel}_{cis\rightarrow trans}$ was greater than or equal to $\phi^{rel}_{trans\rightarrow cis}$. The values of ϕ^{rel}_{isom} show a high degree of variation with the structural variation in the molecules and with solvent polarity, but no obvious correlation was found between these two factors and ϕ^{rel}_{isom}. However, it is apparent from the relative quantum yields that photoisomerisation of the *cis* and *trans* isomers

proceeds *via* different transition states on the excited state potential energy surface. In addition, from comparing the relative quantum yields some information was obtained about the structure of the transition state relative to the corresponding ground state.

A number of thermal kinetic effects have been identified for different azobenzene derivatives. The rate of thermal isomerisation for the parent molecule is much slower than that of the substituted azobenzenes regardless of the nature or position of the substituents. Push-pull azobenzenes have much faster rates than *p*-donor and *p*-acceptor molecules. Examination of the kinetics of the thermal reversal of push-pull azobenzenes shows it is greatly affected by nature of the electron-donating substituent. Modifying the electron-donating group to give a higher ability of donation has been shown to markedly increase the thermal decay. The influence of substitution *ortho* to the azo bond is in good agreement with observations in the literatures. The introduction of a methyl group at the *ortho* position on the donating side of a *p*-electron donating azobenzene, (*i.e.* in MMY) results in a significant acceleration of the decay process leading to faster reversion to the *trans* isomer.

The activation parameters of thermal *cis* isomer decay were determined using NMR. The *in situ* technique allows the kinetics to be monitored at elevated temperatures for these systems since detection is possible immediately after terminating the irradiation. The measured activation parameters correlate well with previously reported values for azo molecules. The values of the activation energy and the entropy of activation vary significantly from molecule to molecule and thus both of these parameters influence the inter-molecule variation of the rate constant. Similarly, both of these parameters influence the solvent-dependence of the rate constant. The study shows clearly some examples where the entropy of activation governs the Gibbs free energy of activation, and thus records a limitation of the Hughes and Ingold rules.

Ab initio (DFT) calculations have proved effective in predicting the structures of the photoisomers, and exploring the ground state potential energy curves (PECs) of the dihedral rotation and inversion pathways. In combination with *ab initio* (DFT) calculations, the thermal *cis* decay mechanism was investigated. The more favourable phenyl ring for inversion was concluded from the DFT calculations. DFT calculations showed that the spontaneous passage to the α-inversion transition state, (*i.e.* inversion through the unsubstituted phenyl ring for electron donating azobenzenes and the phenyl ring substituted by the nitro group for electron acceptor and push-pull azobenzenes) while scanning the CN=NC dihedral angle indicates that the inversion through the α-phenyl ring has lower

activation energy compared to that of the dihedral rotation pathway. Thus for all cases except the parent molecule α-inversion is the predominant mechanism. This was confirmed by comparing the activation barriers between the α-inversion pathway and the proposed pure rotation pathway.

The DFT-predicted values of the activation energy and Gibbs energy of activation in DMSO are in good agreement with the experimental values; while the values of the same parameters in benzene tended to be in less good agreement. The DFT calculations are unsuccessful at predicting the entropy of activation, where in all cases there is a large discrepancy between the theoretical and experimental values. This in turn means that the values of the rate constant cannot be predicted accurately from the DFT-calculated activation parameters.

The mechanism of the thermal isomerisation was distinguished between rotation and inversion on the basis of a $\Delta H^{\#}$-$\Delta S^{\#}$ isokinetic relationship aided with a standard azobenzene derivative for the inversion mechanism as reported by Asano Model.[53] However, the physical significance of linear entropy-enthalpy correlation has been questioned in the literature.[102-104] Although, there appears a correlation between the predications of Asano *et al.*[53,54] and the polarity of the transition state (TS) predicted by DFT calculations. In general, the Asano model predicts rotation for cases with a large change in dipole moment between *cis* and TS, and inversion where there is a smaller change in dipole moment. Thus the model may indicate the nature of the TS. However, a large change in dipole moment does not necessarily indicate a rotation mechanism, since, as the DFT calculations show, a linear TS can have a large dipole moment. The reliability of the predictions of DFT regarding the nature of the TS should also be considered. For the push-pull azobenzenes, where there is a large change in dipole moment between *cis* and TS, the DFT-predicted free energies of activation are not in good agreement with the experimental values. Thus the prediction of linear TS for these systems (in solution) may not be reliable.

Overall, both theory and experiment indicate a linear (inversion) transition state for the electron donor azobenzenes and both experiment and theory support a large change in dipole moment on formation of the TS for push-pull azobenzenes, but the nature of the TS for the latter cannot be concluded.

To sum, this study provided evidence supporting the previous studies, that NMR spectroscopic monitoring of samples undergoing *in situ* irradiation is a particularly effective tool for observing and structurally characterising azo *cis* isomer species, following the

kinetics of photoisomerisation, and investigating the activation parameters of thermal *cis* isomer decay. The research also confirmed the efficacy of the DFT calculations in predicting the structures of the *cis*, and *trans* isomers, and illustrated their efficiency in exploring the reaction coordinate of the thermal isomerisation of simple azo dyes molecules.

The research presented in this thesis seems to have raised more questions that it has answered. There are several lines of research arising from this work which could be pursued.

1. It would be interesting to investigate more azo molecules of electron acceptor type, to assess the obtained conclusions regarding the effect of protonation on the thermal isomerisation rate and barrier.
2. The DFT calculations did not predict accurately the effect of the solvent on energy (enthalpy) of activation, E_a ($\Delta H^{\#}$), and the entropy of activation, $\Delta S^{\#}$. The experimental findings on the effect of solvent can be interpreted in terms of reorientation of solvent molecules. The PCM model does not deal with solvent at a molecular level; this is most likely why the calculations do not reproduce the experimental observations. This could be tested by using of a non-polar, non-polarisable solvent, or by applying another solvation model (explicit model).
3. The prediction of Gibbs free energy of activation, $\Delta G^{\#}$, is generally in good agreement between the computed and experimental values; this indicates the good calculations of the frequency of vibrational modes. But it would be useful to obtain the normal vibrational modes experimentally by Infra Red (IR) spectroscopy, especially in the cases of disagreement, in order to determine the vibrational modes that could not be predicted computationally.

Bibliography

(1) Hartley, G. S. *Nature (London, United Kingdom)* **1937**, *140*, 281.
(2) Yager, K. G.; Barrett, C. J. *Journal of Photochemistry and Photobiology A: Chemistry* **2006**, *182*, 250-261.
(3) Irie, M. *Chem. Rev.* **2000**, *100*, 1683-1684.
(4) Tait, K. M., University of Edinburgh, 2005.
(5) Gibson, D. I., University of Edinburgh, 2007.
(6) Tait, K. M.; Parkinson, J. A.; Gibson, D. I.; Richardson, P. R.; Ebenezer, W. J.; Hutchings, M. G.; Jones, A. C. *Photochemical & Photobiological Sciences* **2007**, *6*, 1010-1018.
(7) Tait, K. M.; Parkinson, J. A.; Bates, S. P.; Ebenezer, W. J.; Jones, A. C. *Journal of Photochemistry and Photobiology A: Chemistry* **2003**, *154*, 179-188.
(8) Tait, K. M.; Parkinson, J. A.; Jones, A. C.; Ebenezer, W. J.; Bates, S. P. *Chemical Physics Letters* **2003**, *374*, 372-380.
(9) Cramer, C. J. *The Essentials of Computational Chemistry*, 2002.
(10) Pople, J. A.; Santry, D. P.; Segal, G. A. *The Journal of Chemical Physics* **1965**, *43*, S129-S135.
(11) Hohenberg, P.; Kohn, W. *Phys. Rev.* **1964**, *136(3B)*, B864-B871.
(12) Kohn, W.; Sham, L. J. *Phys. Rev.* **1965**, *140(4A)*, A1133-A1138.
(13) Becke, A. D. *Phys. Rev. A* **1988**, *38*, 3098.
(14) Perdew, J. P.; Wang, Y. *Phys. Rev. B* **1992**, *45*, 13244-13249.
(15) Becke, A. D. *J. Chem. Phys.* **1993**, *98*, 5648.
(16) Lee, C.; Yang, W.; Parr, R. G. *Physical Review B* **1988**, *37*, 785.
(17) Hariharan, P. C.; Pople, J. A. *Theoretical Chemistry Accounts: Theory, Computation, and Modeling (Theoretica Chimica Acta)* **1973**, *28*, 213-222.
(18) Jacopo Tomasi, R. C. B. M. *International Journal of Quantum Chemistry* **1999**, *75*, 783-803.
(19) Mierts, S.; Scrocco, E.; Tomasi, J. *Chemical Physics* **1981**, *55*, 117-129.
(20) Tomasi, J.; Mennucci, B.; Cancès, E. *Journal of Molecular Structure: THEOCHEM* **1999**, *464*, 211-226.
(21) Hutton, R. F.; Steel, C. *J. Am. Chem. Soc.* **1964**, *86*, 745-746.
(22) Rau, H. *Azo Compounds; In Photochromism - Molecules and Systems*; eds. Elsevier, 1990.
(23) Griffiths, J. *Chemical Society Reviews* **1972**, *1(4)*, 481-493.
(24) Birnbaum, P. P.; Linford, J. H.; Style, D. W. G. *Trans. Faraday Soc.* **1953**, *49*, 735-744.
(25) Brode, W. R.; Gould, J. H.; Wyman, G. M. *J. Am. Chem. Soc.* **1952**, *74*, 4641-4646.
(26) Knoll, H. *CRC Handbook of Organic Photochemistry and Photobiology*, 2004.
(27) Bortolus, P.; Monti, S. *J. Phys. Chem.* **1987**, *91*, 5046.
(28) Rau, H.; Lddecke, E. *J. Am. Chem. Soc.* **1982**, *104*, 1616.
(29) Fujino, T.; Tahara, T. *The Journal of Physical Chemistry A* **2000**, *104*, 4203-4210.
(30) Monti, S.; Orlandi, G.; Palmieri, P. *Chem. Phys.* **1982**, *71*, 87.
(31) Cattaneo, P.; Persico, M. *Phys. Chem. Chem. Phys.* **1999**, *1*, 4739-4743.
(32) Lednev, I. K.; Ye, T. Q.; Abbott, L. C.; Hester, R. E.; Moore, J. N. *J. Phys. Chem. A* **1998**, *102*, 9161.
(33) Lednev, I. K.; Ye, T. Q.; Hester, R. E.; Moore, J. N. *J. Phys. Chem.* **1996**, *100*, 13338.

(34) Lednev, I. K.; Ye, T. Q.; Matousek, P.; Towrie, M.; Foggi, P.; Neuwahl, F. V. R.; Umapathy, S.; Hester, R. E.; Moore, J. N. *Chemical Physics Letters* **1998**, *290*, 68-74.
(35) Fujino, T.; Arzhantsev, S. Y.; Tahara, T. *Bulletin of the Chemical Society of Japan* **2002**, *75*, 1031-1040.
(36) Fujino, T.; Arzhantsev, S. Y.; Tahara, T. *J. Phys. Chem. A* **2001**, *105*, 8123.
(37) Wei-Guang Diau, E. *The Journal of Physical Chemistry A* **2004**, *108*, 950-956.
(38) Crecca, C. R.; Roitberg, A. E. *The Journal of Physical Chemistry A* **2006**, *110*, 8188-8203.
(39) Wang, L.; Wang, X. *Journal of Molecular Structure: THEOCHEM* **2007**, *847*, 1-9.
(40) Kobayashi, S.; Yokoyama, H.; Kamei, H. *Chemical Physics Letters* **1987**, *138*, 333-338.
(41) Sekkat, Z.; Wood, J.; Knoll, W. *The Journal of Physical Chemistry* **1995**, *99*, 17226-17234.
(42) Frisch, M. J. T., G. W.; Schlegel, H. B.; Scuseria, G. E.; Robb, M. A.; Cheeseman, J. R.; Montgomery, J. A., Jr.; Vreven, T.; Kudin, K. N.; Burant, J. C.; Millam, J. M.; Iyengar, S. S.; Tomasi, J.; Barone, V.; Mennucci, B.; Cossi, M.; Scalmani, G.; Rega, N.; Petersson, G. A.; Nakatsuji, H.; Hada, M.; Ehara, M.; Toyota, K.; Fukuda, R.; Hasegawa, J.; Ishida, M.; Nakajima, T.; Honda, Y.; Kitao, O.; Nakai, H.; Klene, M.; Li, X.; Knox, J. E.; Hratchian, H. P.; Cross, J. B.; Bakken, V.; Adamo, C.; Jaramillo, J.; Gomperts, R.; Stratmann, R. E.; Yazyev, O.; Austin, A. J.; Cammi, R.; Pomelli, C.; Ochterski, J. W.; Ayala, P. Y.; Morokuma, K.; Voth, G. A.; Salvador, P.; Dannenberg, J. J.; Zakrzewski, V. G.; Dapprich, S.; Daniels, A. D.; Strain, M. C.; Farkas, O.; Malick, D. K.; Rabuck, A. D.; Raghavachari, K.; Foresman, J. B.; Ortiz, J. V.; Cui, Q.; Baboul, A. G.; Clifford, S.; Cioslowski, J.; Stefanov, B. B.; Liu, G.; Liashenko, A.; Piskorz, P.; Komaromi, I.; Martin, R. L.; Fox, D. J.; Keith, T.; Al-Laham, M. A.; Peng, C. Y.; Nanayakkara, A.; Challacombe, M.; Gill, P. M. W.; Johnson, B.; Chen, W.; Wong, M. W.; Gonzalez, C.; Pople, J. A. Gaussian 03, revision C.02; Gaussian, Inc.: Wallingford, CT, 2004. Wallingford, CT, 2004.
(43) Cossi, M.; Scalmani, G.; Rega, N.; Barone, V. *The Journal of Chemical Physics* **2002**, *117*, 43-54.
(44) Dietrich, S.-F. *Justus Liebigs Annalen der Chemie* **1958**, *615*, 114-123.
(45) Talaty, E. R.; Fargo, J. C. *Chemical Communications* **1967**, *933*, 65-66.
(46) Asano, T.; Okada, T.; Shinkai, S.; Shigematsu, K.; Kusano, Y.; Manabe, O. *J. Am. Chem. Soc.* **1981**, *103*, 5161.
(47) Gegiou, D.; Muszkat, A.; Fischer *J. Am. Chem. Soc.* **1968**, *90*, 3907.
(48) Nishimura, N.; Sueyoshi, T.; Yamanaka, H.; Imai, E.; Yamamoto, S.; Hasegawa, S. *Bull. Chem. Soc. Jpn* **1976**, *49*, 1381-1387.
(49) Nishimura, N.; Kosako, S.; Sueishi, Y. *Bull. Chem. Soc. Jpn* **1984**, *57*, 1617-1625.
(50) Wildes, P. D.; Pacifici, J. G.; Gether Irick, J.; Whitten, D. G. *Journal of the American Chemical Society* **1971**, *93:8*, 2004-2008.
(51) Sueyoshi, T.; Nishimura, N.; Yamamoto, S.; Hasegawa, S. *Chemistry Letters* **1974**, 1131-1134.
(52) Nishimura, N.; Tanaka, S.; Sueishi, Y. *J. Chem. Soc., Chem. Commun.* **1985**, *026*, 903-904.
(53) Asano, T.; Okada, T.; Shinkai, S.; Shigematsu, K.; Kusano, Y.; Manabe, O. *J. Am. Chem. Soc.* **1981**, *103*, 5161-5165.
(54) Asano, T.; Okada, T. *J. Org. Chem* **1986**, *51*, 4454-4458.
(55) Schanze, K. S.; Mattox, T. F.; Whitten, D. G. *J.Org. Chem* **1983**, *48*, 2808-2813.
(56) Liu, Z. F.; Morigaki, K.; Enomoto, T.; Hashimoto, K.; Fujishima, A. *J. Phys. Chem.* **1992**, *96*, 1875-1880.
(57) Hartley, G. S. *J. Chem. Soc.* **1938**, 633-642.
(58) Sanchez, A. M.; dr Rossi, R. H. *J.Org. Chem* **1993**, *58*, 2094.

(59) Sanchez, A. M.; Rossi, R. H. *J. Org. Chem.* **1995**, *60*, 2974-2976.
(60) Sanchez, A. M.; Barra, M.; de Rossi, R. H. *J. Org. Chem.* **1999**, *64*, 1604-1609.
(61) Dubini-Paglia, E.; Beltrame, P. L.; Osti, R. *Dyes and Pigments* **1992**, *18*, 287-295.
(62) Nicolae, H.; Dominique, A.; Joël, B.; Alain, S.; Georges, S. *Macromolecular Chemistry and Physics* **2007**, *208*, 2600-2610.
(63) Keita, B.; Hajime, O.; Eri, I.; Sumitaka, I.; Kyoko, N.; Toshinori, U.; Koji, I.; Masahiko, I.; Hideo, D. T.; Tsutomu, A. *Chemistry - A European Journal* **2006**, *12*, 5328-5333.
(64) Poprawa-Smoluch, M.; Baggerman, J.; Zhang, H.; Maas, H. P. A.; DeCola, L.; Brouwer, A. M. *J. Phys. Chem. A* **2006**, *110*, 11926-11937.
(65) De Maria, P.; Fontana, A.; Gasbarri, C.; Siani, G.; Zanirato, P. *ARKIVOC* **2009**, *viii*, 16-29.
(66) Ball, P.; Nicholls, C. H. *Dyes and Pigments* **1985**, *6*, 13-25.
(67) Nishimura, N.; Sueyoshi, T.; Yamanaka, H.; Yamamoto, S.; Hasegawa, S. *Bulletin of the Chemical Society of Japan* **1976**, *49(5)*, 1381-1387.
(68) King, N. R.; Whale, E. A.; Davis, F. J.; Gilbert, A.; Mitchell, G. R. *J. Mater. Chem.* **1997**, *7(4)*, 625-630.
(69) Wildes, P. D.; Pacific, J. G.; Irick, G.; Jr.; Whitten, D. G. *J. Am. Chem. Soc.* **1971**, 93-98.
(70) Sanchez, A. M.; Barra, M.; de Rossi, R. H. *J. Org. Chem.* **1999**, *64*, 1604-1609.
(71) De Maria, P.; Fontana, A.; Gasbarri, C.; Siani, G.; Zanirato, P. *ARKIVOC* **2008**, *viii*, 16-29.
(72) Matczyszyn, K.; Bartkowiak, W.; Leszczynki, J. *Journal of Molecular Structure* **2001**, *565-566*, 53-57.
(73) Reichardt, C. *Angew. Chem., Int. Ed. Engl.* **1965**, *4*, 29-40.
(74) Ralph, G. P. *The Journal of Chemical Physics* **1952**, *20*, 1478-1480.
(75) Biswas, N.; Umapathy, S. *The Journal of Physical Chemistry A* **2000**, *104*, 2734-2745.
(76) Biswas, N.; Umapathy, S. *The Journal of Physical Chemistry A* **1997**, *101*, 5555-5566.
(77) Stepanian, S. G.; Reva, I. D.; Radchenko, E. D.; Adamowicz, L. *J. Phys. Chem. A* **1999**, *103*, 4404.
(78) Wheeler, D. E.; Rodriguez, J. H.; McCusker, J. K. *J. Phys. Chem. A* **1999**, *103*, 4101.
(79) Pan, D.; Phillips, D. L. *J. Phys. Chem. A* **1999**, *103*, 4737.
(80) Stephens, P. J.; Devlin, F. J.; Chablowski, C. F.; Frisch, M. J. *J. Phys. Chem.* **1994**, *98*, 11623.
(81) Walden, S. E.; Wheeler, R. A. *J. Phys. Chem.* **1996**, *100*, 1530.
(82) Hout, R. F.; Jr; Hehre, W. J. *J. Comput. Chem.* **1982**, *3*, 234.
(83) Kikuchi, O.; Azuki, M.; Inadomi, Y.; Morihashi, K. *Journal of Molecular Structure: THEOCHEM* **1999**, *468*, 95-104.
(84) Wang, L.; Wang, X. *Journal of Molecular Structure: THEOCHEM* **2007**, *806*, 179-186.
(85) Nori-Shargh, D.; Ghanizadeh, F.-R. *Journal of Molecular Structure: THEOCHEM* **2003**, *637*, 115-128.
(86) Gholami, M. R.; Izadyar, M. *Journal of Molecular Structure: THEOCHEM* **2004**, *672*, 61-66.
(87) Mostad, A.; Romming, C. *Acta Chem. Scand* **1971**, *25*, 3561.
(88) Traetteberg, M.; Hillmo, I.; Hagen, K. *Journal of Molecular Structure* **1977**, *39*, 231-239.
(89) Kurita, N.; Tanaka, S.; Itoh, S. *J. Phys. Chem. A* **2000**, *104*, 8114-8120.
(90) Briquet, L.; Vercauteren, D. P.; Perpète, E. A.; Jacquemin, D. *Chemical Physics Letters* **2006**, *417*, 190-195.

(91) Fliegl, H.; Kohn, A.; Hattig, C.; Ahlrichs, R. *J. Am. Chem. Soc.* **2003**, *125*, 9821-9827.
(92) Yang, W.; You, X.; Zhang, Y.; Zhang, D. *Dyes and Pigments* **2006**, *68*, 27-31.
(93) Allen, F.-H. *J. Crystallogr Spectrosc Res* **1991**, *22*, 151.
(94) Whitaker, A. *Journal of Chemical Crystallography* **1992**, *22*, 151-155.
(95) Chen, P. C.; Chieh, Y. C. *Journal of Molecular Structure: THEOCHEM* **2003**, *624*, 191-200.
(96) Kurita, N.; Ikegami, T.; Ishikawa, Y. *Chemical Physics Letters* **2002**, *360*, 349-354.
(97) Nishimura, N.; Sueyoshi, T.; Yamanaka, H.; Imai, E. *Bull.Chem. Soc.of Japan* **1976**, *49*, 1381-1387.
(98) Angeli, C.; Cimiraglia, R.; Hofmann, H.-J. *Chemical Physics Letters* **1996**, *259*, 276-282.
(99) Houck, W. J.; Pollack, R. M. *J. Am. Chem. Soc.* **2003**, *125*, 10206-10212.
(100) Andersson, J.-A.; Petterson, R.; Tegner, L. *Journal of Photochemistry* **1982**, *20*, 17-32.
(101) Sokalski, W. A.; Gora, R. W.; Bartkowiak, W.; Kobylinski, P.; Sworakowski, J.; Chyla, A.; Leszczynski, J. *J. Chem. Phys.* **2001**, *114*, 5504-5508.
(102) Sharp, K. *Protein Science* **2001**, *10*, 661-667.
(103) Cooper, A.; Johnson, C. M.; Lakey, J. H.; Nöllmann, M. *Biophysical Chemistry* **2001**, *93*, 215-230.
(104) Cornish-Bowden, A. *Journal of Biosciences* **2002**, *27*, 121-126.

Appendices

Appendix A: ^{1}H NMR Spectra and Assignments

This appendix contains the proton assignments and chemical shifts for the azobenzenes and their photoisomers described within the thesis. (NMR spectra assignments of the other molecules could be found in the thesis of K. M. Tait).[6]

AAB Spectral Assignment

The ^{1}H NMR spectra of AAB (mM) in d_{12}-benzene (a) prior to irradiation and (b) during irradiation at the 514-nm PSS. Spectra recorded at 298 K. ^{1}H NMR assignments for the *trans* and *cis* isomers are given in the table, along with chemical shifts and Δδ values.

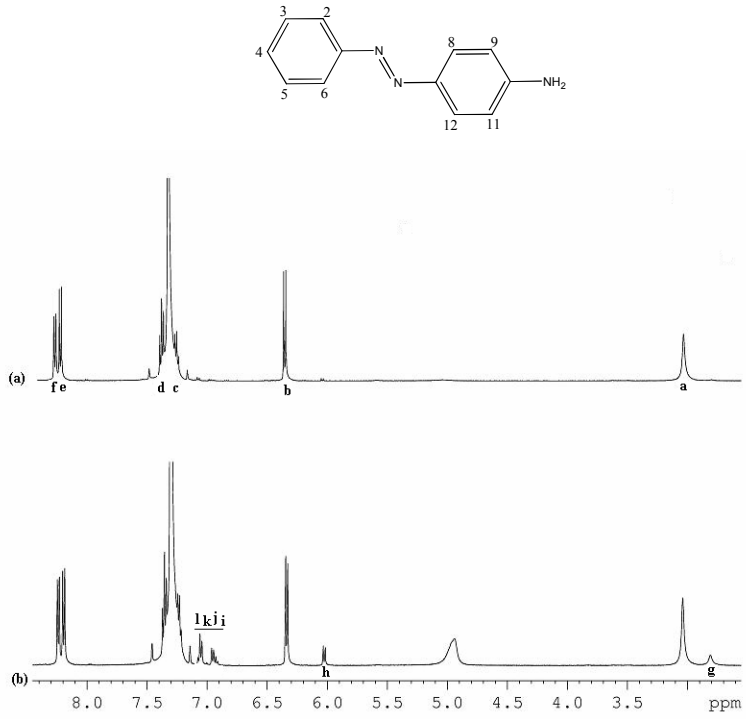

Trans signal	*Trans* chemical shift δt / ppm	*Cis* signal	*Cis* chemical shift δc / ppm	Proton assignment	Δδ / ppm
a	3.0403	g	2.8048	NH_2	-0.24
b	6.3285	h	6.0170	9/11	-0.31
c	7.2319	k	*	4	*
d	7.3556	l	*	3/5	*
e	8.1866	i	*	8/12	*
f	8.2480	j	*	2/6	*

MY Spectral Assignment

The ^{1}H NMR spectra of MY (mM) in d_6-DMSO (a) prior to irradiation and (b) during irradiation at the 514-nm PSS. Spectra recorded at 298 K. ^{1}H NMR assignments for the *trans* and *cis* isomers are given in the table, along with chemical shifts and Δδ values.

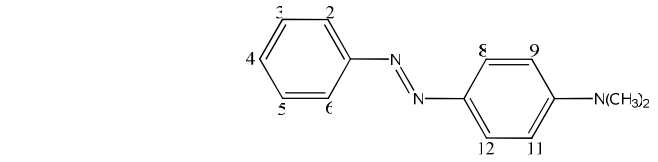

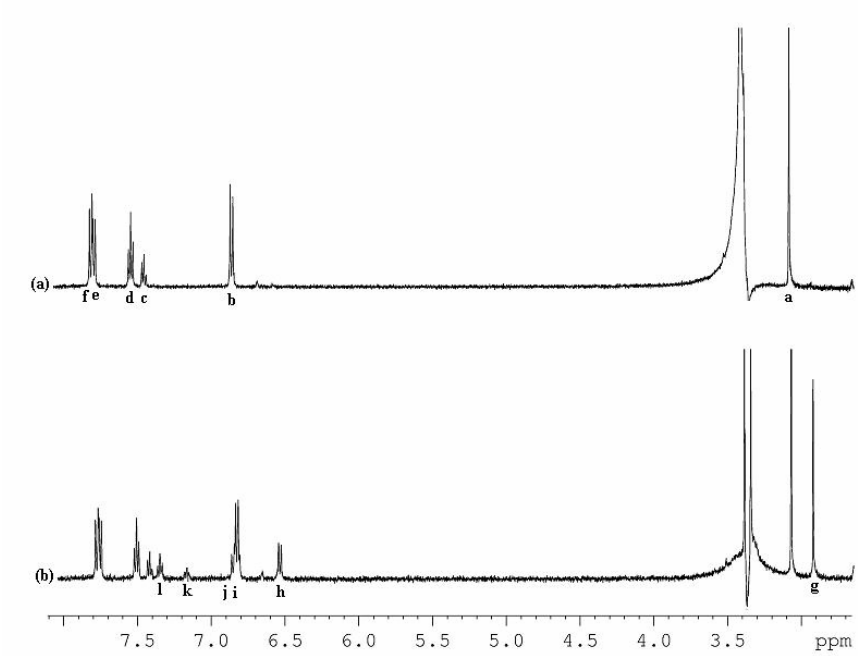

Trans signal	*Trans* chemical shift δ_{trans} / ppm	*Cis* signal	*Cis* chemical shift δ_{cis} / ppm	Proton assignment	Δδ / ppm
a	3.1029	g	2.9512	$(CH_3)_2$	-0.15
b	6.8898	h	6.5763	9/11	-0.31
c	7.4704	k	7.2143	4	-0.26
d	7.5619	l	7.4019	3/5	-0.16
e	7.8013	i	6.8870	8/12	-0.91
f	7.8272	j	6.8990	2/6	-0.93

MMY Spectral Assignment

The ^{1}H NMR spectra of MMY (mM) in d_{12}-benzene (a) prior to irradiation and (b) during irradiation at the 530-nm PSS. Spectra recorded at 298 K. ^{1}H NMR assignments for the *trans* and *cis* isomers are given in the table, along with chemical shifts and Δδ values.

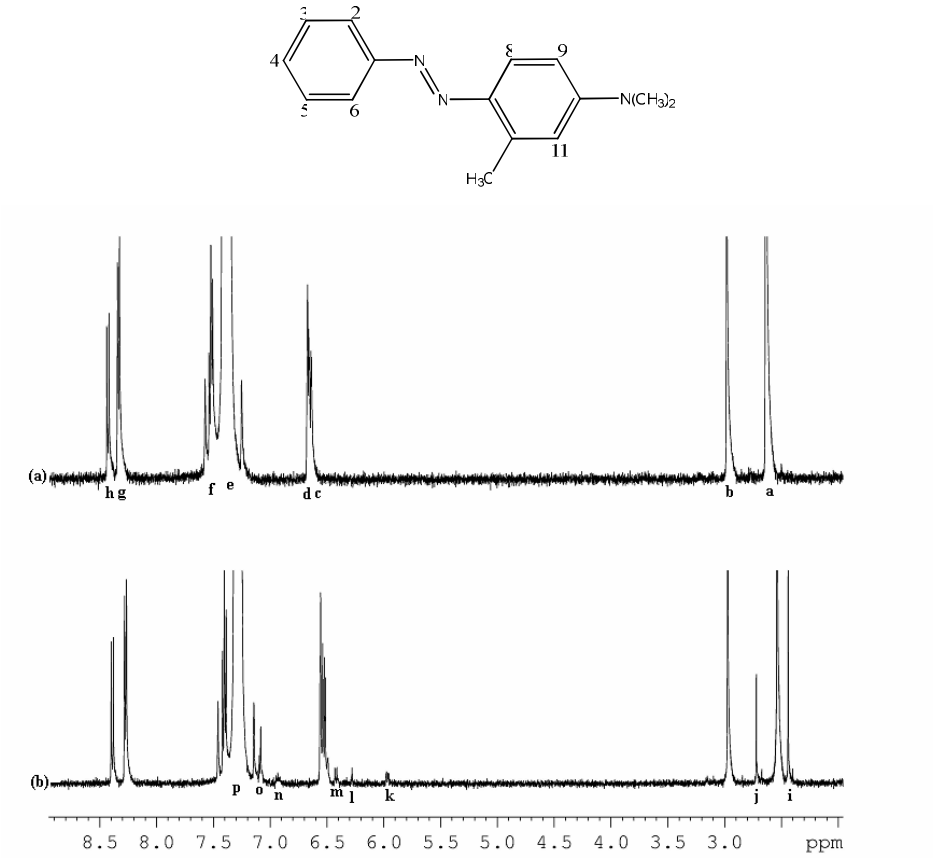

Trans signal	*Trans* chemical shift δ_{trans} / ppm	*Cis* signal	*Cis* chemical shift δ_{cis} / ppm	Proton assignment	Δδ / ppm
a	2.5398	i	2.4326	$(CH_3)_2$	-0.11
b	2.9734	j	2.7072	CH_3	-0.27
c	6.5246	m	6.4210	9	-0.10
d	6.5569	k	5.9643	11	-0.59
e	*	o	7.0839	4	*
f	7.4020	p	*	3/5	*
g	8.2803	n	6.9304	8	-1.35
h	8.3977	l	6.2805	2/6	-2.12

The ^{1}H NMR spectra of MMY (mM) in d_6-DMSO (a) prior to irradiation and (b) during irradiation at the 530-nm PSS. Spectra recorded at 298 K. ^{1}H NMR assignments for the *trans* and *cis* isomers are given in the table, along with chemical shifts and Δδ values.

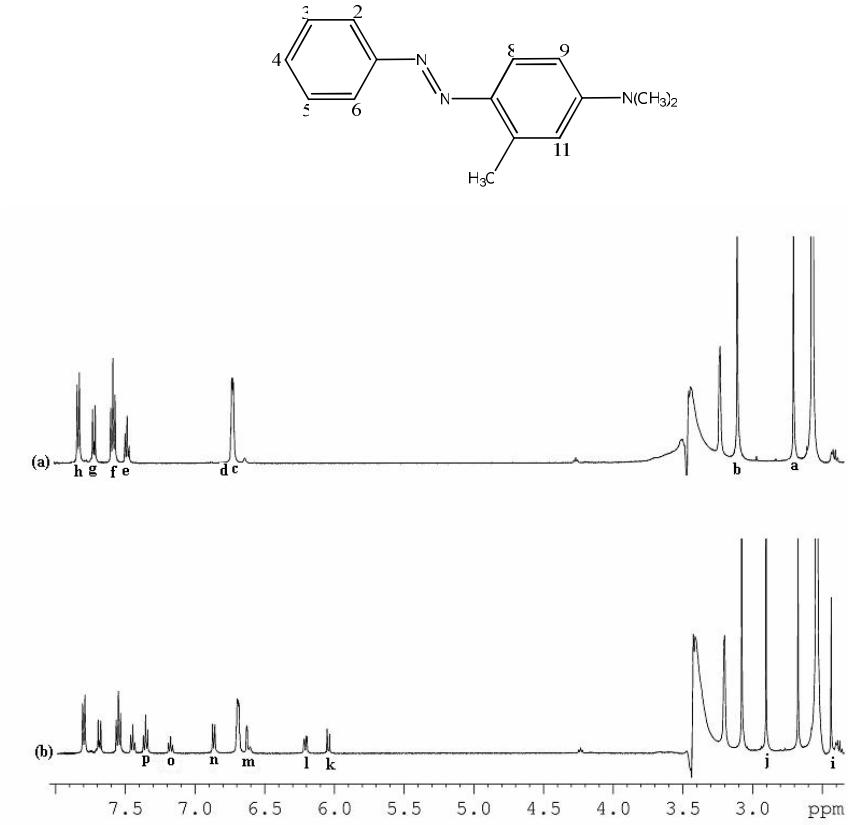

Trans signal	*Trans* chemical shift δ_{trans} / ppm	*Cis* signal	*Cis* chemical shift δ_{cis} / ppm	Proton assignment	Δδ / ppm
a	2.6758	i	2.1210	CH_3	-0.55
b	3.0807	j	2.9060	$(CH_3)_2$	-0.17
c	6.6974	m	6.6207	9	-0.08
d	6.6928	l	6.2056	11	-0.49
e	7.4500	o	7.1763	4	-0.27
f	7.5480	p	7.3585	3/5	-0.19
g	7.6783	n	6.8611	8	-0.82
h	7.7921	k	6.0373	2/6	-1.75

NAB Spectral Assignment

The ^{1}H NMR spectra of NAB (mM) in d_{12}-benzene (a) prior to irradiation and (b) during irradiation at the 514-nm PSS. Spectra recorded at 298 K. ^{1}H NMR assignments for the *trans* and *cis* isomers are given in the table, along with chemical shifts and Δδ values.

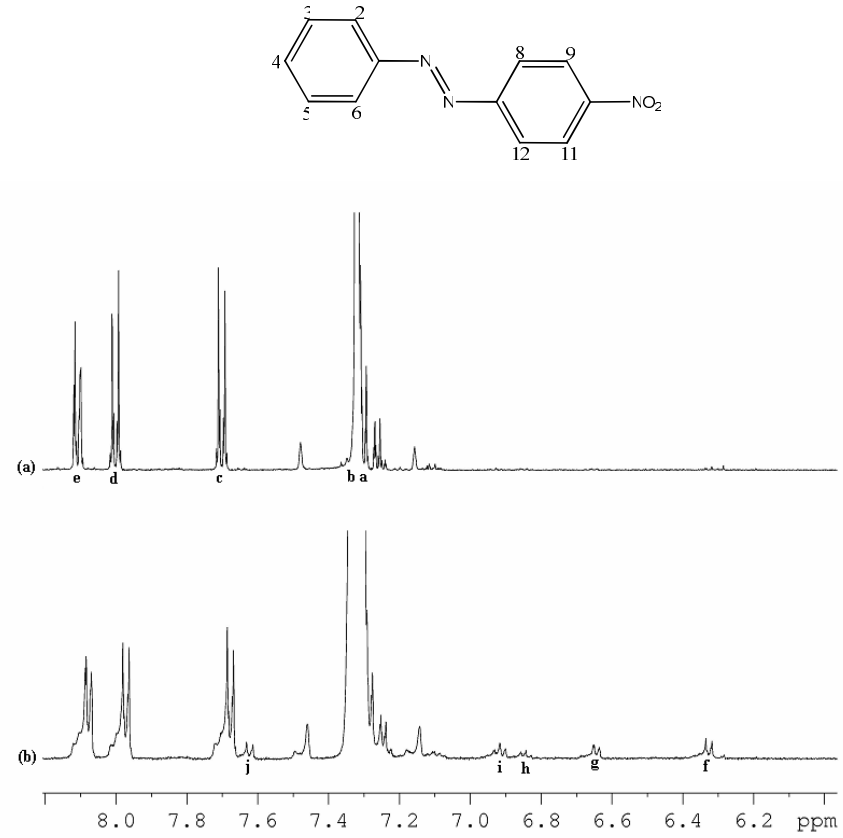

Trans signal	*Trans* chemical shift δ_{trans} / ppm	*Cis* signal	*Cis* chemical shift δ_{cis} / ppm	Proton assignment	Δδ / ppm
a	*	h	6.8425	4	*
b	*	i	6.9167	3/5	*
c	7.6735	g	6.6354	2/6	-0.05
d	7.9685	f	6.3184	8/12	-1.65
e	8.0702	j	7.6194	9/11	-1.43

DMNAB Spectral Assignment

The 1H NMR spectra of DMNAB (mM) in d_{12}-benzene (a) prior to irradiation and (b) during irradiation at the 568-nm PSS. Spectra recorded at 298 K. 1H NMR assignments for the *trans* and *cis* isomers are given in the table, along with chemical shifts and Δδ values.

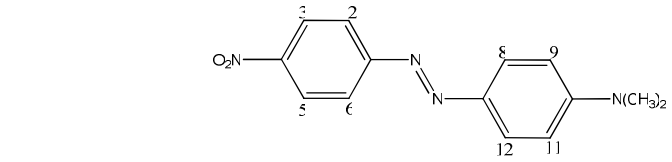

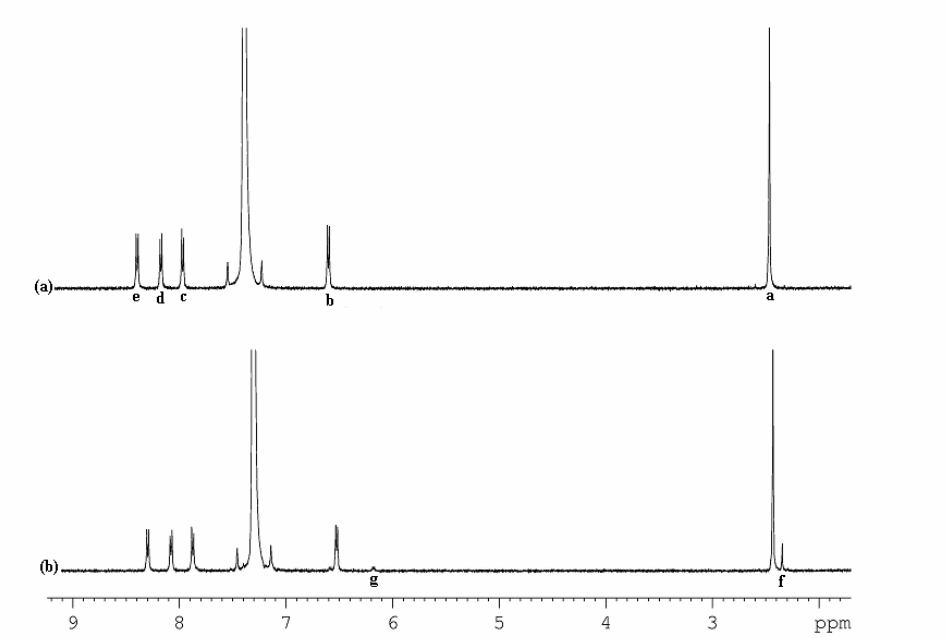

Trans signal	*Trans* chemical shift δ_{trans} / ppm	*Cis* signal	*Cis* chemical shift δ_{cis} / ppm	Proton assignment	Δδ / ppm
a	2.4337	f	2.3458	$(CH_3)_2$	-0.09
b	6.5173	g	6.1819	9/11	-0.34
c	7.8815	*	*	8/12	*
d	8.0721	*	*	2/6	*
e	8.3075	*	*	3/5	*

Appendix B: Cartesian Coordinates of DFT Optimised Geometries

This appendix contains the Cartesian coordinate's matrices for the calculated structures in the gas phase presented within Chapter 5 of this thesis.

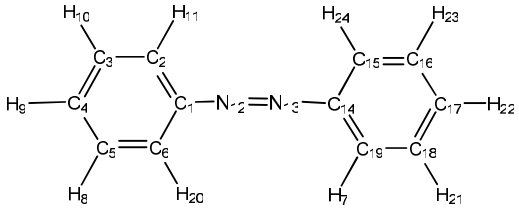

1. Cartesian coordinates for *trans*-AB optimised at the B3LYP/6-31G(d,p) level of theory

Atom Number	Atom	X Coordinate	Y Coordinate	Z Coordinate
1	C	1.768024	0.184519	-0.000092
2	C	2.633404	1.286297	0.000022
3	C	4.013723	1.094367	0.000069
4	C	4.534478	-0.200414	0.000054
5	C	3.670901	-1.303399	0.000023
6	C	2.293667	-1.119263	-0.000019
7	H	-2.197991	-2.280393	0.000001
8	H	4.080235	-2.309615	0.000034
9	H	5.609618	-0.354361	0.000188
10	H	4.680682	1.951187	0.000134
11	H	2.197921	2.280371	0.000000
12	N	0.384697	0.499192	-0.000087
13	N	-0.384716	-0.499264	-0.000093
14	C	-1.768030	-0.184554	-0.000089
15	C	-2.293628	1.119246	-0.000016
16	C	-3.670857	1.303427	0.000022
17	C	-4.534467	0.200469	0.000051
18	C	-4.013756	-1.094329	0.000070
19	C	-2.633443	-1.286305	0.000025
20	H	1.608081	-1.958582	-0.000086
21	H	-4.680741	-1.951128	0.000135
22	H	-5.609603	0.354451	0.000181
23	H	-4.080158	2.309656	0.000033
24	H	-1.608014	1.958543	-0.000083

2. Cartesian coordinates for *cis*-AB optimised at the B3LYP/6-31G(d,p) level of theory

Atom Number	Atom	X Coordinate	Y Coordinate	Z Coordinate
1	C	1.430503	0.755148	-0.065905
2	C	2.542349	0.696962	0.784720
3	C	3.438073	-0.365326	0.687793
4	C	3.263821	-1.341936	-0.295797
5	C	2.184003	-1.253700	-1.177799
6	C	1.261254	-0.216165	-1.063615
7	H	-2.682985	1.487241	-1.515535
8	H	2.057236	-1.998479	-1.958051
9	H	3.974360	-2.157968	-0.385609
10	H	4.284726	-0.419310	1.365701
11	H	2.683476	1.487329	1.515298
12	N	0.624543	1.940722	0.015464
13	N	-0.624429	1.940697	-0.015568
14	C	-1.430394	0.755137	0.065980
15	C	-1.261444	-0.216068	1.063858
16	C	-2.184312	-1.253505	1.177982
17	C	-3.263938	-1.341770	0.295748
18	C	-3.437908	-0.365272	-0.688003
19	C	-2.542084	0.696931	-0.784853
20	H	0.423316	-0.148140	-1.748415
21	H	-4.284423	-0.419271	-1.366079
22	H	-3.974560	-2.157736	0.385512
23	H	-2.057792	-1.998183	1.958369
24	H	-0.423693	-0.148032	1.748875

3. Cartesian coordinates for transition state of AB (Dihedral Rotation) optimised at the B3LYP/6-31G(d,p) level of theory

Atom Number	Atom	X Coordinate	Y Coordinate	Z Coordinate
1	C	-1.572553	-1.175767	-0.038009
2	C	-2.813026	-1.284179	0.655350
3	C	-3.812149	-0.356815	0.437609
4	C	-3.620586	0.697903	-0.474390
5	C	-2.415353	0.803718	-1.173409
6	C	-1.398916	-0.125533	-0.985714
7	H	2.934713	-2.098294	-1.361753
8	H	-2.267392	1.620908	-1.873815
9	H	-4.403976	1.434075	-0.624894
10	H	-4.750509	-0.439171	0.978055
11	H	-2.934657	-2.097316	1.363184
12	N	-0.560056	-2.001957	0.327690
13	N	0.560105	-2.002252	-0.326623
14	C	1.572572	-1.175815	0.038759
15	C	1.398783	-0.124811	0.985570
16	C	2.415192	0.804595	1.172671
17	C	3.620494	0.698245	0.473853
18	C	3.812135	-0.357097	-0.437402

19	C	2.813041	-1.284643	-0.654517
20	H	-0.460402	-0.049555	-1.520080
21	H	4.750543	-0.439833	-0.977706
22	H	4.403860	1.434542	0.623877
23	H	2.267177	1.622308	1.872454
24	H	0.460224	-0.048439	1.519791

4. Cartesian coordinates for transition state of AB (β-Inversion) optimised at the B3LYP/6-31G(d,p) level of theory

Atom Number	Atom	X Coordinate	Y Coordinate	Z Coordinate
1	C	1.557451	0.694374	0.430881
2	C	1.411488	1.906161	1.159206
3	C	2.169406	3.014539	0.802935
4	C	3.076718	2.974744	-0.258936
5	C	3.216499	1.780438	-0.970542
6	C	2.480028	0.647154	-0.649338
7	H	2.599364	-0.275662	-1.205693
8	H	3.916791	1.721349	-1.799705
9	H	3.660336	3.849706	-0.523223
10	H	2.042700	3.930138	1.374790
11	H	0.713050	1.946903	1.987394
12	N	0.850580	-0.387576	0.766497
13	N	0.203091	-1.381628	1.075992
14	C	-1.090816	-1.552553	0.436682
15	C	-1.787051	-2.699544	0.823317
16	C	-3.040402	-2.964282	0.272774
17	C	-3.588064	-2.081277	-0.659447
18	C	-2.884706	-0.932410	-1.043181
19	C	-1.634172	-0.662675	-0.497671
20	H	-1.075226	0.222900	-0.783258
21	H	-3.317109	-0.249952	-1.768819
22	H	-4.564097	-2.284748	-1.089907
23	H	-3.587533	-3.854068	0.568602
24	H	-1.328328	-3.362034	1.550652

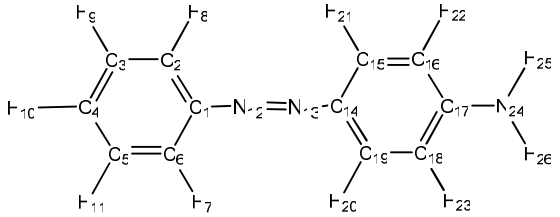

5. Cartesian coordinates for *trans*-AAB optimised at the B3LYP/6-31G(d,p) level of theory

Atom Number	Atom	X Coordinate	Y Coordinate	Z Coordinate
1	C	-2.233802	-0.196589	0.000141
2	C	-2.776326	1.100557	0.000995
3	C	-4.155746	1.270299	0.003102
4	C	-5.008637	0.159431	0.004393
5	C	-4.472165	-1.129043	0.003440
6	C	-3.089860	-1.306224	0.001308
7	H	-2.644462	-2.296031	0.000389
8	H	-2.100269	1.947595	-0.000167
9	H	-4.574828	2.272729	0.003626
10	H	-6.085449	0.301524	0.005988
11	H	-5.129264	-1.993756	0.004312
12	N	-0.847734	-0.495746	-0.001910
13	N	-0.090583	0.517034	-0.001767
14	C	1.287908	0.236289	-0.004890
15	C	1.853758	-1.053698	-0.006835
16	C	3.226935	-1.215895	-0.006596
17	C	4.088456	-0.095734	-0.003860
18	C	3.521319	1.192423	-0.002733
19	C	2.143055	1.348667	-0.003667
20	H	1.695198	2.337408	-0.000496
21	H	1.190491	-1.911060	-0.006225
22	H	3.656558	-2.214812	-0.011914
23	H	4.170472	2.064088	-0.004579
24	N	5.462365	-0.267389	-0.054100
25	H	6.026463	0.512733	0.249968
26	H	5.817385	-1.160595	0.254748

6. Cartesian coordinates for *cis*-AAB optimised at the B3LYP/6-31G(d,p) level of theory

Atom Number	Atom	X Coordinate	Y Coordinate	Z Coordinate
1	C	-1.896902	0.698512	-0.005827
2	C	-1.733614	-0.097388	1.138439
3	C	-2.529136	-1.227253	1.314462
4	C	-3.479919	-1.582189	0.353887
5	C	-3.651351	-0.780277	-0.776789
6	C	-2.882800	0.370106	-0.945843
7	H	-3.029559	1.021877	-1.801541
8	H	-0.994393	0.179559	1.882699
9	H	-2.404714	-1.835048	2.206254
10	H	-4.092830	-2.467406	0.493810
11	H	-4.398746	-1.040596	-1.520783
12	N	-1.236057	1.962932	-0.147449
13	N	0.006013	2.122018	-0.090730
14	C	0.966964	1.067800	-0.089428
15	C	0.873944	-0.143685	-0.799157
16	C	1.942746	-1.026727	-0.825383
17	C	3.133907	-0.746555	-0.126136
18	C	3.232313	0.474548	0.567723
19	C	2.177260	1.373803	0.554011
20	H	2.261866	2.333245	1.054608
21	H	-0.026275	-0.386278	-1.350047
22	H	1.865082	-1.948102	-1.397000
23	H	4.152530	0.722185	1.090339
24	N	4.208979	-1.620532	-0.183258
25	H	4.897057	-1.535386	0.550645
26	H	3.996959	-2.579152	-0.418678

7. Cartesian coordinates for transition state of AAB (Dihedral Rotation) optimised at the B3LYP/6-31G(d,p) level of theory

Atom Number	Atom	X Coordinate	Y Coordinate	Z Coordinate
1	C	-0.153067	0.014597	0.540262
2	C	0.267039	-0.09412	1.895765
3	C	1.619658	-0.029111	2.204456
4	C	2.593015	0.144202	1.216612
5	C	2.177336	0.249536	-0.113695
6	C	0.835895	0.188358	-0.468288
7	H	0.526218	0.266373	-1.504533
8	H	-0.478389	-0.232747	2.67097
9	H	1.914811	-0.117143	3.247106
10	H	3.645068	0.192783	1.475585
11	H	2.913208	0.381745	-0.902954
12	N	-1.444283	-0.061988	0.221612
13	N	-2.639017	-0.13408	-0.061963
14	C	-3.394369	1.086286	-0.078056
15	C	-2.873993	2.358366	0.207416
16	C	-3.696582	3.469546	0.16583
17	C	-5.066139	3.340849	-0.162329
18	C	-5.579193	2.059916	-0.447902
19	C	-4.748299	0.950654	-0.405177
20	H	-5.127992	-0.043356	-0.620621
21	H	-1.823671	2.459398	0.462836
22	H	-3.293025	4.455175	0.383469
23	H	-6.62905	1.948604	-0.705091
24	N	-5.870904	4.459831	-0.247865
25	H	-6.868698	4.315921	-0.205585
26	H	-5.556993	5.2925	0.227766

8. Cartesian coordinates for transition state of AAB (Pure Rotation) optimised at the B3LYP/6-31G(d,p) level of theory

Atom Number	Atom	X Coordinate	Y Coordinate	Z Coordinate
1	C	-2.0047960	0.5553860	-0.1369910
2	C	-3.2217980	0.2510700	-0.8228930
3	C	-4.0589650	-0.7450100	-0.3650020
4	C	-3.7398220	-1.4730880	0.7976260
5	C	-2.5647870	-1.1769610	1.4892940
6	C	-1.7015050	-0.1772090	1.0500080
7	H	-0.7880050	0.0394460	1.5875930
8	H	-3.4538400	0.8167340	-1.7196540
9	H	-4.9735400	-0.9689410	-0.9074220
10	H	-4.3967160	-2.2646210	1.1445400
11	H	-2.3107070	-1.7374660	2.3853670
12	N	-1.1599450	1.4499500	-0.7105040
13	N	-0.0878620	1.7671620	0.0088180
14	C	1.0070090	1.0020680	-0.1808370
15	C	2.2040960	1.3786540	0.5048830

16	C	3.3262230	0.5909770	0.4606100
17	C	3.3247750	-0.6225030	-0.2805150
18	C	2.1525370	-1.0006370	-0.9720300
19	C	1.0219440	-0.2096540	-0.9400390
20	H	0.1246180	-0.4993760	-1.4708590
21	H	2.1901000	2.3041290	1.0712170
22	H	4.2239280	0.8821520	0.9997500
23	H	2.1430330	-1.9390060	-1.5211280
24	N	4.4267740	-1.4406050	-0.2673030
25	H	4.4914760	-2.1716560	-0.9589480
26	H	5.3081580	-1.0575470	0.0378750

9. Cartesian coordinates for transition state of AAB (β-Inversion) optimised at the B3LYP/6-31G(d,p) level of theory

Atom Number	Atom	X Coordinate	Y Coordinate	Z Coordinate
1	C	-2.260634	0.436535	-0.280232
2	C	-3.535840	0.933626	-0.565315
3	C	-4.666483	0.229105	-0.155159
4	C	-4.522503	-0.967414	0.550365
5	C	-3.244771	-1.458380	0.844253
6	C	-2.113360	-0.761548	0.431301
7	H	-1.116362	-1.126966	0.655978
8	H	-3.611013	1.870393	-1.109131
9	H	-5.657238	0.611642	-0.382369
10	H	-5.401547	-1.517012	0.874117
11	H	-3.136264	-2.387173	1.397399
12	N	-1.163717	1.267578	-0.737249
13	N	-0.016678	0.834977	-0.538984
14	C	1.214852	0.368108	-0.325356
15	C	2.236803	1.214993	0.191145
16	C	3.507370	0.726313	0.440867
17	C	3.866213	-0.588365	0.083980
18	C	2.878748	-1.416705	-0.481654
19	C	1.573563	-0.975983	-0.630651
20	H	0.816416	-1.639516	-1.035434
21	H	1.987272	2.245155	0.421173
22	H	4.255300	1.381413	0.881587
23	H	3.134481	-2.435341	-0.763878
24	N	5.148416	-1.074227	0.339947
25	H	5.440472	-1.848524	-0.240354
26	H	5.868885	-0.369241	0.417104

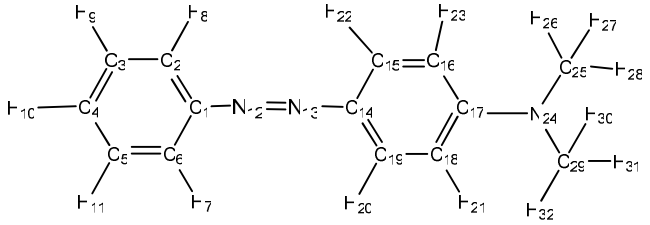

10. Cartesian coordinates for *trans*-MY optimised at the B3LYP/6-31G(d,p) level of theory

Atom Number	Atom	X Coordinate	Y Coordinate	Z Coordinate
1	C	-3.073740	0.202540	-0.000124
2	C	-3.637884	-1.085537	0.000274
3	C	-5.019948	-1.233035	0.000398
4	C	-5.855151	-0.108881	0.000128
5	C	-5.297547	1.170726	-0.000267
6	C	-3.912622	1.325549	-0.000387
7	H	-3.451317	2.308077	-0.000685
8	H	-2.975589	-1.943400	0.000481
9	H	-5.454881	-2.228773	0.000711
10	H	-6.934142	-0.233574	0.000229
11	H	-5.940571	2.046034	-0.000476
12	N	-1.683419	0.479295	-0.000259
13	N	-0.942999	-0.547245	-0.000133
14	C	0.437796	-0.291778	-0.000264
15	C	1.277070	-1.415490	-0.000095
16	C	2.657239	-1.288348	-0.000132
17	C	3.263568	-0.008038	-0.000397
18	C	2.406376	1.126366	-0.000546
19	C	1.031592	0.984809	-0.000499
20	H	0.386879	1.856438	-0.000640
21	H	2.827132	2.124369	-0.000788
22	H	0.814555	-2.397715	0.000146
23	H	3.266125	-2.183458	0.000144
24	N	4.634853	0.135530	-0.000613
25	C	5.489541	-1.039518	0.000231
26	H	6.533304	-0.724889	-0.001239
27	H	5.324067	-1.665426	-0.886871
28	H	5.325773	-1.663428	0.889130
29	C	5.234210	1.459539	0.001689
30	H	6.320011	1.361320	0.002424
31	H	4.947560	2.037815	0.890224
32	H	4.949041	2.040135	-0.885795

11. Cartesian coordinates for *cis*-MY optimised at the B3LYP/6-31G(d,p) level of theory

Atom Number	Atom	X Coordinate	Y Coordinate	Z Coordinate
1	C	-2.677486	0.564327	-0.062146
2	C	-2.407889	-0.073618	1.158887
3	C	-3.023741	-1.286849	1.456846
4	C	-3.899450	-1.881412	0.544376
5	C	-4.178229	-1.238153	-0.663653
6	C	-3.591192	-0.008566	-0.957124
7	H	-3.825878	0.519529	-1.876194
8	H	-1.727616	0.389070	1.866175
9	H	-2.817777	-1.771689	2.406998
10	H	-4.372211	-2.829951	0.780365
11	H	-4.869324	-1.685793	-1.372186
12	N	-2.218321	1.893158	-0.338643
13	N	-1.015860	2.249265	-0.303243
14	C	0.097282	1.367962	-0.196742
15	C	1.246955	1.936492	0.373986
16	C	2.434859	1.230810	0.475307
17	C	2.544632	-0.079581	-0.051119
18	C	1.402067	-0.619329	-0.694522
19	C	0.206454	0.079459	-0.750739
20	H	-0.638495	-0.370606	-1.257189
21	H	1.449210	-1.595744	-1.159931
22	H	1.181297	2.954171	0.746302
23	H	3.287151	1.708882	0.941049
24	N	3.720699	-0.798413	0.045449
25	C	4.916640	-0.160072	0.569953
26	H	5.725833	-0.890237	0.604664
27	H	4.755344	0.204341	1.591144
28	H	5.247743	0.689576	-0.045410
29	C	3.849590	-2.074658	-0.638336
30	H	4.826881	-2.503263	-0.413741
31	H	3.759984	-1.981078	-1.730837
32	H	3.089274	-2.786153	-0.296002

12. Cartesian coordinates for transition state of MY (Dihedral Rotation) optimised at the B3LYP/6-31G(d,p) level of theory

Atom Number	Atom	X Coordinate	Y Coordinate	Z Coordinate
1	C	-2.933080	-0.244055	0.340663
2	C	-3.541537	-0.810596	-0.815310
3	C	-4.677307	-0.221612	-1.355292
4	C	-5.249772	0.924376	-0.795798
5	C	-4.651732	1.477807	0.339904
6	C	-3.515625	0.921905	0.913564
7	H	-3.063803	1.358378	1.797450
8	H	-3.109115	-1.701813	-1.256523
9	H	-5.123337	-0.675111	-2.237050
10	H	-6.137309	1.371251	-1.230420

11	H	-5.077433	2.367236	0.797949
12	N	-1.853210	-0.802261	0.882976
13	N	-0.854456	-1.320980	1.382187
14	C	0.426546	-0.884023	0.914281
15	C	1.532513	-1.501402	1.508239
16	C	2.823882	-1.162314	1.137495
17	C	3.054083	-0.177344	0.143614
18	C	1.919194	0.441283	-0.450931
19	C	0.636559	0.092595	-0.070989
20	H	-0.219288	0.574001	-0.534300
21	H	2.050105	1.198160	-1.213900
22	H	1.352868	-2.255094	2.268981
23	H	3.656181	-1.660402	1.617770
24	N	4.330589	0.170582	-0.234922
25	C	5.476719	-0.476944	0.382862
26	H	6.392642	-0.070304	-0.045826
27	H	5.475009	-1.561313	0.210226
28	H	5.506139	-0.306071	1.467047
29	C	4.544074	1.182066	-1.258141
30	H	5.614953	1.314225	-1.412523
31	H	4.123183	2.153222	-0.966642
32	H	4.097953	0.892883	-2.218790

13. Cartesian coordinates for transition state of MY (β-Inversion) optimised at the B3LYP/6-31G(d,p) level of theory

Atom Number	Atom	X Coordinate	Y Coordinate	Z Coordinate
1	C	-3.122556	0.628481	-0.298706
2	C	-2.872187	-0.553808	0.410689
3	C	-3.938890	-1.342827	0.830228
4	C	-5.255024	-0.960630	0.544808
5	C	-5.502444	0.220170	-0.158708
6	C	-4.437147	1.017080	-0.574414
7	H	-4.593698	1.944986	-1.116167
8	H	-1.846694	-0.834634	0.628593
9	H	-3.749752	-2.259468	1.382153
10	H	-6.083053	-1.581850	0.873621
11	H	-6.523069	0.518771	-0.379735
12	N	-2.102204	1.549410	-0.759641
13	N	-0.920561	1.208009	-0.576687
14	C	0.347178	0.844053	-0.381173
15	C	0.809187	-0.473189	-0.659025
16	C	2.145821	-0.811413	-0.529974
17	C	3.090356	0.099152	0.003375
18	C	2.625537	1.400585	0.319109
19	C	1.315947	1.777476	0.083866
20	H	0.995308	2.793193	0.289928
21	H	3.308931	2.141803	0.714962
22	H	0.101690	-1.204682	-1.036204
23	H	2.451456	-1.810595	-0.815043
24	N	4.411785	-0.268167	0.216612
25	C	4.887298	-1.547347	-0.280929

26	H	5.932258	-1.676044	0.004469
27	H	4.816974	-1.634053	-1.376603
28	H	4.321617	-2.375931	0.159811
29	C	5.393923	0.749942	0.547934
30	H	6.362514	0.273716	0.705956
31	H	5.127220	1.267566	1.476480
32	H	5.508470	1.508582	-0.241728

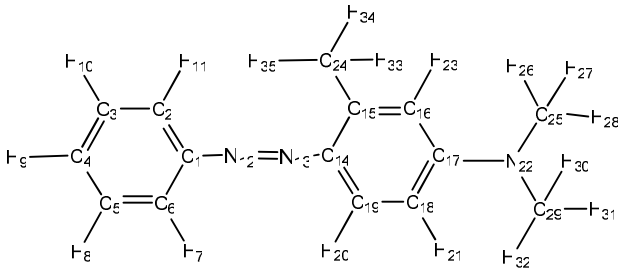

14. Cartesian coordinates for *trans*-MMY optimised at the B3LYP/6-31G(d,p) level of theory

Atom Number	Atom	X Coordinate	Y Coordinate	Z Coordinate
1	C	3.110095	-0.359364	0.000076
2	C	3.676132	0.928133	-0.000856
3	C	5.058269	1.074825	-0.000997
4	C	5.893060	-0.049617	-0.000218
5	C	5.334254	-1.328667	0.000697
6	C	3.949298	-1.482534	0.000823
7	H	3.487518	-2.464835	0.001510
8	H	5.976500	-2.204579	0.001294
9	H	6.972117	0.074409	-0.000347
10	H	5.493694	2.070388	-0.001731
11	H	3.015633	1.787268	-0.001462
12	N	1.720883	-0.637436	0.000261
13	N	0.976598	0.387581	0.000086
14	C	-0.403215	0.135591	0.000088
15	C	-1.257258	1.263602	0.000250
16	C	-2.635235	1.070393	0.000206
17	C	-3.216672	-0.220175	-0.000041
18	C	-2.340204	-1.336679	-0.000208
19	C	-0.972008	-1.151874	-0.000139
20	H	-0.301687	-2.003962	-0.000251
21	H	-2.734873	-2.345080	-0.000373
22	N	-4.585298	-0.387459	-0.000130
23	H	-3.270607	1.947604	0.000327
24	C	-0.692782	2.663831	0.000448
25	C	-5.463448	0.770079	0.000517
26	H	-6.500626	0.434184	0.000855
27	H	-5.312018	1.398596	-0.887250
28	H	-5.311289	1.398071	0.888522

29	C	-5.158976	-1.722878	-0.000815
30	H	-6.246514	-1.645956	-0.001402
31	H	-4.862005	-2.296865	0.887057
32	H	-4.861027	-2.296275	-0.888727
33	H	-1.495182	3.406662	0.000657
34	H	-0.061485	2.836937	-0.876173
35	H	-0.061290	2.836637	0.876983

15. Cartesian coordinates for *cis*-MMY optimised at the B3LYP/6-31G(d,p) level of theory

Atom Number	Atom	X Coordinate	Y Coordinate	Z Coordinate
1	C	2.724484	0.415564	-0.184984
2	C	2.439411	-0.041364	1.111266
3	C	3.091224	-1.167677	1.607600
4	C	4.018138	-1.856106	0.820245
5	C	4.312408	-1.391935	-0.463762
6	C	3.689419	-0.246723	-0.956199
7	H	3.934672	0.147585	-1.937535
8	H	5.043187	-1.911704	-1.076762
9	H	4.518233	-2.737181	1.210835
10	H	2.872829	-1.511199	2.614847
11	H	1.718330	0.491553	1.721835
12	N	2.228993	1.665305	-0.683925
13	N	1.018340	1.995244	-0.682032
14	C	-0.069333	1.119512	-0.415593
15	C	-1.221663	1.709124	0.155082
16	C	-2.369617	0.939412	0.319657
17	C	-2.443399	-0.408177	-0.103425
18	C	-1.299095	-0.956376	-0.731995
19	C	-0.141603	-0.209081	-0.867913
20	H	0.712798	-0.652062	-1.365873
21	H	-1.315790	-1.964443	-1.126120
22	N	-3.591309	-1.157580	0.081054
23	H	-3.231750	1.410479	0.776055
24	C	-1.198448	3.147056	0.610173
25	C	-4.805848	-0.515590	0.555220
26	H	-5.590700	-1.265980	0.656443
27	H	-5.166159	0.267447	-0.128441
28	H	-4.654504	-0.059700	1.540716
29	C	-3.683231	-2.491741	-0.487894
30	H	-4.629140	-2.943875	-0.187227
31	H	-2.876914	-3.134493	-0.116972
32	H	-3.637977	-2.490827	-1.587533
33	H	-2.211649	3.522646	0.777062
34	H	-0.694274	3.774945	-0.129092
35	H	-0.640433	3.260637	1.547224

16. Cartesian coordinates for transition state of MMY (Dihedral Rotation) optimised at the B3LYP/6-31G(d,p) level of theory

Atom Number	Atom	X Coordinate	Y Coordinate	Z Coordinate
1	C	3.020823	0.087757	0.159828
2	C	3.603287	-0.304961	1.399036
3	C	4.776637	-1.047645	1.405320
4	C	5.412658	-1.431426	0.221130
5	C	4.839245	-1.045980	-0.994014
6	C	3.667838	-0.302022	-1.047849
7	H	3.235877	-0.005589	-1.997325
8	H	5.313133	-1.328622	-1.930907
9	H	6.328560	-2.011838	0.244717
10	H	5.201172	-1.331725	2.365167
11	H	3.121954	-0.010562	2.325113
12	N	1.908228	0.816166	0.131406
13	N	0.877915	1.490716	0.104231
14	C	-0.374598	0.804347	0.076539
15	C	-1.529989	1.614665	0.053099
16	C	-2.776715	0.997811	0.023611
17	C	-2.922265	-0.411457	0.016194
18	C	-1.740276	-1.199328	0.040462
19	C	-0.500268	-0.592800	0.069671
20	H	0.400678	-1.198725	0.087938
21	H	-1.799090	-2.280254	0.036113
22	N	-4.166108	-0.999183	-0.014114
23	H	-3.655928	1.629896	0.006046
24	C	-1.427048	3.121114	0.062405
25	C	-5.365302	-0.176920	-0.030766
26	H	-6.242779	-0.823119	-0.056042
27	H	-5.399992	0.474721	-0.913639
28	H	-5.438054	0.458036	0.862166
29	C	-4.291976	-2.448354	-0.011386
30	H	-5.348251	-2.716017	-0.040162
31	H	-3.854771	-2.895690	0.890964
32	H	-3.805620	-2.901813	-0.884764
33	H	-2.419533	3.577496	0.019585
34	H	-0.839984	3.484221	-0.785731
35	H	-0.920757	3.477583	0.964331

17. Cartesian coordinates for transition state of MMY (β-Inversion) optimised at the B3LYP/6-31G(d,p) level of theory

Atom Number	Atom	X Coordinate	Y Coordinate	Z Coordinate
1	C	3.163936	0.314969	-0.164703
2	C	2.952532	-0.852716	0.581378
3	C	4.043735	-1.592710	1.027273
4	C	5.347280	-1.177626	0.731404
5	C	5.556735	-0.011310	-0.008010
6	C	4.466911	0.737387	-0.448379
7	H	4.594803	1.653666	-1.016908
8	H	6.567459	0.313918	-0.237191
9	H	6.194549	-1.760793	1.080301
10	H	3.883059	-2.496666	1.608510
11	H	1.937116	-1.160052	0.809771
12	N	2.116773	1.190599	-0.649908
13	N	0.942274	0.806065	-0.483400
14	C	-0.306158	0.373863	-0.298668
15	C	-1.348440	1.293034	0.056817
16	C	-2.641491	0.823365	0.234357
17	C	-3.006247	-0.524175	-0.010968
18	C	-1.981770	-1.412171	-0.419306
19	C	-0.667993	-0.987450	-0.498786
20	H	0.109127	-1.689352	-0.783990
21	H	-2.207564	-2.446853	-0.645430
22	N	-4.312830	-0.955380	0.150528
23	H	-3.398533	1.537813	0.535883
24	C	-1.006148	2.741030	0.270707
25	C	-5.370790	0.013678	0.379952
26	H	-6.317555	-0.513281	0.504341
27	H	-5.481700	0.727393	-0.450281
28	H	-5.189963	0.587848	1.296210
29	C	-4.678866	-2.304573	-0.244937
30	H	-5.731560	-2.472197	-0.014056
31	H	-4.096343	-3.050191	0.308302
32	H	-4.530172	-2.488408	-1.320070
33	H	-1.905398	3.361809	0.304048
34	H	-0.352389	3.094626	-0.533411
35	H	-0.455675	2.895339	1.206991

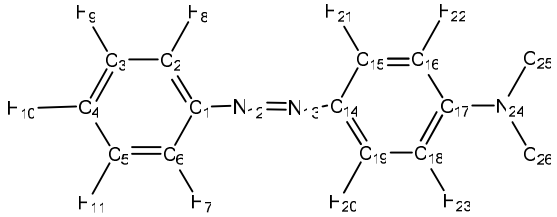

18. Cartesian coordinates for *trans*-NAB optimised at the B3LYP/6-31G(d,p) level of theory

Atom Number	Atom	X Coordinate	Y Coordinate	Z Coordinate
1	C	2.948921	-0.187654	-0.000215
2	C	3.765839	-1.326811	-0.000210
3	C	5.152447	-1.192859	0.000003
4	C	5.725666	0.079765	0.000295
5	C	4.910547	1.219706	0.000427
6	C	3.527487	1.094471	0.000212
7	H	2.878729	1.962435	0.000378
8	H	3.288666	-2.301404	-0.000247
9	H	5.783428	-2.076184	0.000058
10	H	6.806218	0.188244	0.000521
11	H	5.362859	2.207019	0.000738
12	N	1.557559	-0.444242	-0.000108
13	N	0.824234	0.581870	-0.000386
14	C	-0.567749	0.304662	-0.000221
15	C	-1.402382	1.431542	-0.000421
16	C	-2.784854	1.284849	-0.000363
17	C	-3.314874	-0.003617	-0.000179
18	C	-2.504468	-1.142626	-0.000025
19	C	-1.126864	-0.986461	-0.000083
20	H	-0.464951	-1.843780	0.000115
21	H	-0.942295	2.413654	-0.000665
22	H	-3.452587	2.136672	-0.000444
23	H	-2.967509	-2.121289	0.000250
24	N	-4.776239	-0.171068	0.000075
25	O	-5.219940	-1.319460	0.000262
26	O	-5.468777	0.846823	0.000600

19. Cartesian coordinates for *cis*-NAB optimised at the B3LYP/6-31G(d,p) level of theory

Atom number	Atom	X Coordinate	Y Coordinate	Z Coordinate
1	C	2.553278	0.537214	-0.018870
2	C	3.614534	0.068523	-0.805741
3	C	4.152339	-1.193058	-0.566228
4	C	3.678457	-1.964906	0.497697
5	C	2.659776	-1.472216	1.317207
6	C	2.086820	-0.228765	1.060211
7	H	1.302762	0.155309	1.702562
8	H	3.994304	0.702839	-1.600278
9	H	4.956197	-1.564781	-1.194129

10	H	4.113686	-2.938784	0.699453
11	H	2.308661	-2.059042	2.160559
12	N	2.127460	1.879257	-0.286066
13	N	0.935704	2.249018	-0.252709
14	C	-0.185686	1.366354	-0.153472
15	C	-0.399655	0.334488	-1.082854
16	C	-1.590363	-0.380198	-1.061595
17	C	-2.553205	-0.063220	-0.103369
18	C	-2.367032	0.969370	0.816213
19	C	-1.188056	1.701733	0.769975
20	H	-1.025449	2.535054	1.445258
21	H	0.362198	0.103390	-1.818592
22	H	-1.785317	-1.179674	-1.765158
23	H	-3.147507	1.190813	1.533004
24	N	-3.804118	-0.830231	-0.070676
25	O	-3.948043	-1.726316	-0.903227
26	O	-4.634471	-0.534102	0.789282

20. Cartesian coordinates for transition state of NAB (Dihedral Rotation) optimised at the B3LYP/6-31G(d,p) level of theory

Atom number	Atom	X Coordinate	Y Coordinate	Z Coordinate
1	C	2.888658	0.225413	-0.046432
2	C	4.237785	0.569062	-0.168208
3	C	5.216484	-0.388112	0.093312
4	C	4.839812	-1.677050	0.474763
5	C	3.485336	-2.014302	0.596654
6	C	2.502804	-1.066330	0.336131
7	H	1.449657	-1.312400	0.426728
8	H	4.490576	1.581602	-0.465632
9	H	6.266756	-0.131026	0.000357
10	H	5.600371	-2.424299	0.679895
11	H	3.201822	-3.018705	0.895431
12	N	1.967463	1.297126	-0.341019
13	N	0.770301	1.054211	-0.274088
14	C	-0.522364	0.792272	-0.200517
15	C	-1.236000	0.341953	-1.354267
16	C	-2.587818	0.084289	-1.264231
17	C	-3.266117	0.264318	-0.052350
18	C	-2.581587	0.710806	1.085021
19	C	-1.229256	0.974961	1.028767
20	H	-0.691590	1.324083	1.902233
21	H	-0.703492	0.209711	-2.288518
22	H	-3.142758	-0.259054	-2.128769
23	H	-3.131884	0.843334	2.008557
24	N	-4.680918	-0.013484	0.025512
25	O	-5.255825	-0.399545	-1.000378
26	O	-5.246641	0.146860	1.114669

21. Cartesian coordinates for transition state of NAB (β-Inversion) optimised at the B3LYP/6-31G(d,p) level of theory

Atom number	Atom	X Coordinate	Y Coordinate	Z Coordinate
1	C	-2.869478	0.327841	-0.442077
2	C	-3.266261	-1.020148	-0.657193
3	C	-4.503105	-1.452397	-0.195359
4	C	-5.339619	-0.610285	0.542308
5	C	-4.932235	0.705691	0.781069
6	C	-3.736977	1.197103	0.273244
7	H	-3.438473	2.226924	0.432988
8	H	-2.611630	-1.684341	-1.210612
9	H	-4.803651	-2.477255	-0.394989
10	H	-6.289741	-0.970738	0.921266
11	H	-5.570218	1.376454	1.349866
12	N	-1.703828	0.777630	-0.916911
13	N	-0.642479	1.206195	-1.364751
14	C	0.575010	0.684664	-0.757824
15	C	1.759564	1.207349	-1.283158
16	C	2.987065	0.797502	-0.771797
17	C	2.993590	-0.132005	0.265965
18	C	1.819181	-0.662954	0.805446
19	C	0.599824	-0.247903	0.287330
20	H	-0.332839	-0.638305	0.680820
21	H	1.694761	1.930539	-2.089327
22	H	3.925717	1.176983	-1.154633
23	H	1.884074	-1.383309	1.611116
24	N	4.288260	-0.572654	0.815772
25	O	4.268225	-1.393659	1.731781
26	O	5.308733	-0.092552	0.324565

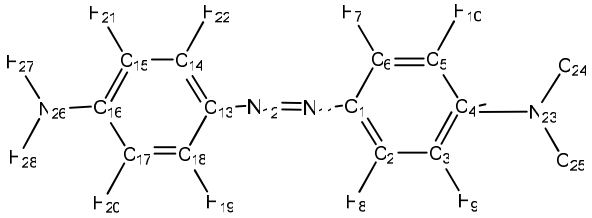

22. Cartesian coordinates for *trans*-DO3 optimised at the B3LYP/6-31G(d,p) level of theory

Atom number	Atom	X Coordinate	Y Coordinate	Z Coordinate
1	C	-1.025193	-0.308468	-0.001573
2	C	-1.590826	0.981438	-0.005793
3	C	-2.968183	1.135201	-0.004440
4	C	-3.779073	-0.004070	0.000974
5	C	-3.243928	-1.291464	0.004833
6	C	-1.862212	-1.435649	0.003213
7	H	-1.401114	-2.417372	0.005692
8	H	-0.931073	1.840346	-0.010117
9	H	-3.432107	2.113532	-0.007740
10	H	-3.909566	-2.144999	0.008798
11	N	0.362903	-0.582549	-0.002911
12	N	1.094941	0.452532	0.000329
13	C	2.473791	0.216883	-0.002424
14	C	3.293334	1.358627	0.003378
15	C	4.673667	1.247756	0.003815
16	C	5.281990	-0.023878	-0.002549
17	C	4.456699	-1.174076	-0.009541
18	C	3.081303	-1.056735	-0.009199
19	H	2.446559	-1.935274	-0.012381
20	H	4.919545	-2.157691	-0.018679
21	H	5.294906	2.139122	0.005731
22	H	2.813195	2.331908	0.009997
23	N	-5.237187	0.160134	0.002300
24	O	-5.929995	-0.858915	0.007446
25	O	-5.685707	1.307834	-0.001748
26	N	6.653165	-0.150663	-0.048178
27	H	7.208347	0.649156	0.215436
28	H	7.051941	-1.039657	0.212730

23. Cartesian coordinates for *cis*-DO3 optimised at the B3LYP/6-31G(d,p) level of theory

Atom number	Atom	X Coordinate	Y Coordinate	Z Coordinate
1	C	-0.684677	1.493771	0.021824
2	C	-0.862045	0.605488	1.099281
3	C	-1.968304	-0.231299	1.135974
4	C	-2.892438	-0.182240	0.090548
5	C	-2.746152	0.704930	-0.977022
6	C	-1.651318	1.558612	-0.996204
7	H	-1.526258	2.280895	-1.795960
8	H	-0.132084	0.583323	1.900806
9	H	-2.128082	-0.923897	1.952764
10	H	-3.493357	0.719797	-1.760381
11	N	0.325772	2.495498	0.051777
12	N	1.557213	2.283023	0.153033
13	C	2.176369	1.012928	0.023744
14	C	3.427651	0.910191	0.657873
15	C	4.180162	-0.249091	0.580683
16	C	3.731169	-1.336781	-0.195711
17	C	2.506407	-1.210610	-0.886268
18	C	1.737766	-0.064457	-0.771692
19	H	0.812481	0.005348	-1.329577
20	H	2.164221	-2.026925	-1.516901
21	H	5.130828	-0.318032	1.102331
22	H	3.783790	1.765632	1.222812
23	N	-4.050067	-1.078114	0.120014
24	O	-4.847376	-1.017835	-0.818130
25	O	-4.159592	-1.844233	1.079467
26	N	4.456616	-2.507965	-0.259652
27	H	5.430123	-2.467939	0.002087
28	H	4.259787	-3.137407	-1.023062

24. Cartesian coordinates for transition state of DO3 (Dihedral Rotation) optimised at the B3LYP/6-31G(d,p) level of theory

Atom number	Atom	X Coordinate	Y Coordinate	Z Coordinate
1	C	-0.978179	0.853356	0.364072
2	C	-1.676565	0.188102	1.423033
3	C	-3.003404	-0.149109	1.266041
4	C	-3.679608	0.155534	0.076511
5	C	-3.014053	0.813091	-0.967406
6	C	-1.687122	1.162680	-0.841385
7	H	-1.166525	1.674158	-1.642437
8	H	-1.147915	-0.039689	2.341167
9	H	-3.542672	-0.653610	2.058544
10	H	-3.561469	1.040407	-1.874067
11	N	0.287716	1.189069	0.503005
12	N	1.468437	1.499438	0.638898
13	C	2.464745	0.570305	0.233198
14	C	3.789588	0.992359	0.414738

15	C	4.845424	0.170962	0.059673
16	C	4.597801	-1.104833	-0.491289
17	C	3.256225	-1.523640	-0.671939
18	C	2.207869	-0.699129	-0.315453
19	H	1.182271	-1.026110	-0.455271
20	H	3.058447	-2.503517	-1.097973
21	H	5.869709	0.504050	0.200205
22	H	3.963046	1.975218	0.841164
23	N	-5.065036	-0.209315	-0.074111
24	O	-5.632890	0.077221	-1.137514
25	O	-5.621567	-0.793612	0.866289
26	N	5.633934	-1.913906	-0.882275
27	H	6.564840	-1.703056	-0.558861
28	H	5.448883	-2.887042	-1.067703

25. Cartesian coordinates for transition state of DO3 (Pure Rotation) optimised at the B3LYP/6-31G(d,p) level of theory

Atom number	Atom	X Coordinate	Y Coordinate	Z Coordinate
1	C	-0.9139210	1.1345550	-0.2733610
2	C	-1.1554380	0.3241810	0.8818140
3	C	-2.4185750	-0.1656050	1.1373610
4	C	-3.4727450	0.1008640	0.2521200
5	C	-3.2589550	0.8871910	-0.8933990
6	C	-2.0085850	1.4010690	-1.1515080
7	H	-1.8326750	2.0170680	-2.0266720
8	H	-0.3416890	0.1384210	1.5743750
9	H	-2.6174290	-0.7637920	2.0185600
10	H	-4.0931240	1.0790040	-1.5567540
11	N	0.2830540	1.7042520	-0.5119500
12	N	1.3532280	1.5727230	0.1835970
13	C	2.3094240	0.6249510	0.0056860
14	C	3.4634440	0.7367730	0.8265060
15	C	4.4883130	-0.1748610	0.7323110
16	C	4.4200850	-1.2280730	-0.2164200
17	C	3.2787210	-1.3308390	-1.0624610
18	C	2.2459620	-0.4360120	-0.9459780
19	H	1.3773630	-0.5019050	-1.5931390
20	H	3.2406940	-2.1245170	-1.8037520
21	H	5.3631190	-0.0891740	1.3701980
22	H	3.4994580	1.5583400	1.5339790
23	N	-4.7824830	-0.4326150	0.5216700
24	O	-5.6930400	-0.1847080	-0.2825920
25	O	-4.9383580	-1.1192120	1.5429820
26	N	5.4403170	-2.1131530	-0.3394660
27	H	6.2423250	-2.0697250	0.2676790
28	H	5.3834410	-2.8858170	-0.9825290

26. Cartesian coordinates for transition state of DO3 (β-Inversion) optimised at the B3LYP/6-31G(d,p) level of theory

Atom number	Atom	X Coordinate	Y Coordinate	Z Coordinate
1	C	-1.065837	1.191569	-0.348775
2	C	-1.241833	-0.058694	0.264487
3	C	-2.520768	-0.530847	0.523708
4	C	-3.616598	0.258270	0.163500
5	C	-3.464675	1.507959	-0.438597
6	C	-2.178822	1.974092	-0.682850
7	H	-2.005972	2.944054	-1.137642
8	H	-0.370227	-0.642701	0.539229
9	H	-2.693104	-1.490224	0.995385
10	H	-4.343893	2.083373	-0.698882
11	N	0.216047	1.806485	-0.615472
12	N	1.223152	1.089717	-0.445634
13	C	2.297280	0.322397	-0.264154
14	C	3.508035	0.876017	0.248409
15	C	4.619020	0.086116	0.469722
16	C	4.628406	-1.273002	0.086031
17	C	3.456863	-1.822294	-0.478077
18	C	2.307130	-1.064494	-0.598749
19	H	1.403148	-1.507459	-1.003890
20	H	3.450281	-2.866606	-0.780108
21	H	5.514443	0.521811	0.906024
22	H	3.522912	1.931903	0.496395
23	N	-4.969911	-0.243503	0.429834
24	O	-5.920626	0.469680	0.105440
25	O	-5.077791	-1.350376	0.960781
26	N	5.742946	-2.059479	0.303498
27	H	6.622333	-1.584281	0.443152
28	H	5.819989	-2.910096	-0.233909

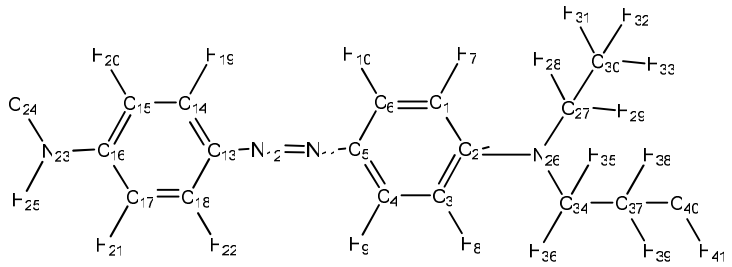

27. Cartesian coordinates for *trans*-DR1 optimised at the B3LYP/6-31G(d,p) level of theory

Atom number	Atom	X Coordinate	Y Coordinate	Z Coordinate
1	C	2.428592	-1.427104	-0.180228
2	C	3.326516	-0.323762	-0.131805
3	C	2.750814	0.971425	-0.068186
4	C	1.378246	1.143980	-0.039884
5	C	0.503084	0.046411	-0.072210
6	C	1.059957	-1.245578	-0.146268
7	H	2.805697	-2.436463	-0.280066
8	H	3.383699	1.847550	-0.010308
9	H	0.949227	2.139349	0.019240
10	H	0.391472	-2.097608	-0.194104
11	N	-0.862172	0.341014	-0.035748
12	N	-1.638602	-0.662352	-0.054049
13	C	-3.012587	-0.329553	-0.019976
14	C	-3.521919	0.982859	0.030948
15	C	-4.890988	1.195643	0.061492
16	C	-5.750848	0.092929	0.040955
17	C	-5.272103	-1.215627	-0.009295
18	C	-3.898290	-1.419111	-0.039533
19	H	-2.825337	1.812084	0.045449
20	H	-5.311777	2.192549	0.100558
21	H	-5.974210	-2.039342	-0.023611
22	H	-3.480585	-2.419319	-0.078701
23	N	-7.199805	0.319444	0.072690
24	O	-7.598206	1.484871	0.115203
25	O	-7.936372	-0.668441	0.054948
26	N	4.702748	-0.487507	-0.148198
27	C	5.307950	-1.823940	-0.120185
28	H	5.446019	-2.204283	-1.145304
29	H	4.613205	-2.497740	0.380505
30	C	6.636120	-1.892001	0.637336
31	H	6.512076	-1.570226	1.675512
32	H	7.419685	-1.284055	0.177414
33	H	6.989639	-2.927726	0.642703
34	C	5.559144	0.609662	-0.603705
35	H	4.998887	1.236831	-1.307789
36	H	6.398094	0.192355	-1.169698
37	C	6.132601	1.490255	0.520216
38	H	6.737925	0.883289	1.197809
39	H	5.319698	1.925517	1.119380

40	O	7.000687	2.483970	-0.003745
41	H	6.464807	3.130918	-0.481123

28. Cartesian coordinates for *cis*-DR1 optimised at the B3LYP/6-31G(d,p) level of theory

Atom number	Atom	X Coordinate	Y Coordinate	Z Coordinate
1	C	1.226947	-0.011057	-1.125843
2	C	2.514592	0.247880	-0.582144
3	C	2.668644	1.457492	0.144410
4	C	1.612418	2.337474	0.297089
5	C	0.328303	2.045065	-0.193607
6	C	0.166166	0.855812	-0.930980
7	H	1.051516	-0.902780	-1.712905
8	H	3.624077	1.721519	0.578232
9	H	1.753194	3.275411	0.824987
10	H	-0.787161	0.615718	-1.384401
11	N	-0.627141	3.068708	0.012577
12	N	-1.871493	2.904154	0.017854
13	C	-2.537908	1.649274	0.056780
14	C	-2.362657	0.766095	1.139539
15	C	-3.162151	-0.361783	1.254550
16	C	-4.133738	-0.608579	0.282316
17	C	-4.338677	0.264697	-0.787279
18	C	-3.553003	1.405161	-0.884535
19	H	-1.602584	0.977090	1.883631
20	H	-3.047104	-1.056792	2.076822
21	H	-5.112208	0.043121	-1.511691
22	H	-3.708200	2.117627	-1.687788
23	N	-4.963589	-1.808855	0.392769
24	O	-4.761267	-2.561968	1.347866
25	O	-5.815121	-2.001511	-0.477651
26	N	3.569479	-0.620713	-0.783753
27	C	3.383418	-1.882315	-1.507815
28	H	4.370105	-2.200164	-1.855596
29	H	2.794167	-1.691797	-2.411690
30	C	2.742695	-3.008596	-0.687042
31	H	1.760850	-2.717473	-0.304294
32	H	3.369432	-3.282700	0.166667
33	H	2.613669	-3.899582	-1.310409
34	C	4.893606	-0.345528	-0.233647
35	H	5.132500	0.717967	-0.357399
36	H	5.632875	-0.892132	-0.825167
37	C	5.071121	-0.745473	1.242636
38	H	4.916089	-1.822648	1.352839
39	H	4.319398	-0.243685	1.868621
40	O	6.394622	-0.489304	1.686594
41	H	6.504068	0.466800	1.772371

29. Cartesian coordinates for transition state of DR1 (Dihedral Rotation) optimised at the B3LYP/6-31G(d,p) level of theory

Atom number	Atom	X Coordinate	Y Coordinate	Z Coordinate
1	C	0.594382	-0.413990	0.029485
2	C	-0.037931	-1.239521	1.005986
3	C	0.752014	-2.261686	1.598550
4	C	2.067160	-2.457157	1.217943
5	C	2.665264	-1.644897	0.245694
6	C	1.908086	-0.616804	-0.341347
7	H	0.048110	0.394544	-0.437143
8	H	0.334834	-2.904834	2.361384
9	H	2.663613	-3.243348	1.670158
10	H	2.363232	0.024066	-1.090199
11	N	4.019067	-1.940759	-0.055775
12	N	4.596463	-1.256326	-0.898276
13	C	5.218084	-0.516209	-1.791821
14	C	5.936477	0.658095	-1.394091
15	C	6.591846	1.416985	-2.339043
16	C	6.563762	1.050077	-3.691913
17	C	5.871701	-0.099330	-4.098751
18	C	5.206488	-0.878974	-3.177805
19	H	5.957217	0.932606	-0.345938
20	H	7.137607	2.307277	-2.050967
21	H	5.869472	-0.362187	-5.149607
22	H	4.672896	-1.771082	-3.484089
23	N	7.247327	1.858239	-4.668235
24	O	7.847618	2.868562	-4.274660
25	O	7.201049	1.505945	-5.855586
26	N	-1.360315	-1.059020	1.346233
27	C	-2.165357	0.005497	0.734708
28	H	-3.213013	-0.293492	0.826147
29	H	-1.955499	0.036881	-0.339451
30	C	-1.972686	1.394728	1.355049
31	H	-0.929184	1.716913	1.303016
32	H	-2.276837	1.405321	2.405585
33	H	-2.582777	2.130253	0.820665
34	C	-2.003634	-1.894101	2.358774
35	H	-1.695540	-2.938456	2.227021
36	H	-3.082663	-1.872071	2.186987
37	C	-1.741661	-1.456044	3.811943
38	H	-2.121689	-0.441696	3.964033
39	H	-0.661958	-1.431543	4.017480
40	O	-2.442974	-2.282799	4.726659
41	H	-1.997736	-3.139305	4.765015

30. Cartesian coordinates for transition state of DR1 (β-Inversion) optimised at the B3LYP/6-31G(d,p) level of theory

Atom number	Atom	X Coordinate	Y Coordinate	Z Coordinate
1	C	0.136878	-0.493318	-0.267313
2	C	-0.204643	-1.209714	0.912428
3	C	0.748416	-2.152315	1.387342
4	C	1.913689	-2.413243	0.695202
5	C	2.282408	-1.665940	-0.460685
6	C	1.351203	-0.678551	-0.898273
7	H	-0.542259	0.244176	-0.675391
8	H	0.556724	-2.715719	2.291512
9	H	2.601256	-3.172634	1.052869
10	H	1.591137	-0.094641	-1.781146
11	N	3.426800	-1.905536	-1.096121
12	N	4.501497	-2.128571	-1.693801
13	C	5.159202	-0.986031	-2.284765
14	C	4.798852	0.351988	-2.058447
15	C	5.536900	1.377429	-2.632109
16	C	6.635178	1.052039	-3.432
17	C	7.017020	-0.270468	-3.664380
18	C	6.277091	-1.287358	-3.074578
19	H	3.946289	0.571695	-1.425190
20	H	5.286827	2.419646	-2.477549
21	H	7.875426	-0.474093	-4.291751
22	H	6.540318	-2.331003	-3.212811
23	N	7.411388	2.134998	-4.046188
24	O	7.056349	3.294190	-3.823066
25	O	8.373226	1.824658	-4.751102
26	N	-1.412077	-1.010401	1.554872
27	C	-2.369644	-0.012559	1.070592
28	H	-3.351700	-0.293497	1.460984
29	H	-2.445474	-0.091795	-0.019690
30	C	-2.053750	1.433402	1.474108
31	H	-1.067080	1.742143	1.118237
32	H	-2.072335	1.553691	2.561143
33	H	-2.798232	2.113298	1.046622
34	C	-1.760716	-1.752742	2.762587
35	H	-1.450857	-2.799578	2.656523
36	H	-2.849931	-1.767541	2.855573
37	C	-1.178218	-1.171486	4.064436
38	H	-1.553135	-0.154706	4.213525
39	H	-0.082693	-1.106810	3.998966
40	O	-1.603614	-1.918838	5.193632
41	H	-1.135397	-2.763901	5.190017

Appendix C: DFT Potential Energy Curves; Bond Parameter *vs.* Energy

This appendix contains the coordinates of the potential energy curves for the proposed mechanism of the thermal *cis-trans* isomerisation process; this includes the dihedral rotation, pure rotation, α-inversion, and β-inversion pathways, presented within Chapter 5 of this thesis.

Dihedral/Pure Rotation Pathway

31. Potential Energy Curve of AB at B3LYP/6-31G(d,p) level of theory/basis; CN=NC dihedral angle *vs.* Energy. Relative energy is respect to the *trans* isomer (CN=NC is 180^0)

CN=NC Dihedral angle /deg	Energy /HF	Energy /kJmol^{-1}	Relative energy /kJ
180	-572.777856200	-1.5038120E+06	0
170	-572.776619500	-1.5038087E+06	3
160	-572.773028500	-1.5037993E+06	13
150	-572.767092100	-1.5037837E+06	28
140	-572.759054000	-1.5037626E+06	49
130	-572.749107900	-1.5037365E+06	75
120	-572.737687500	-1.5037065E+06	105
110	-572.725255600	-1.5036739E+06	138
100	-572.712255400	-1.5036397E+06	172
90	-572.699166900	-1.5036054E+06	207
80	-572.713449700	-1.5036429E+06	169
70	-572.722650600	-1.5036670E+06	145
60	-572.731802100	-1.5036911E+06	121
50	-572.739607000	-1.5037115E+06	100
40	-572.745772400	-1.5037277E+06	84
30	-572.750175100	-1.5037393E+06	73
20	-572.752808700	-1.5037462E+06	66
10	-572.753709100	-1.5037486E+06	63
0	-572.752903900	-1.5037465E+06	66

32. Potential Energy Curve of AAB at B3LYP/6-31G(d,p) level of theory/basis in the gas phase; CN=NC dihedral angle *vs.* Energy. Relative energy is respect to the *trans* isomer(CN=NC is 180^0)

CN=NC Dihedral angle /deg	Energy /HF	Energy /kJmol^{-1}	Relative energy /kJ
180	-628.1393367	-1.64916196E+06	0.000
170	-628.1381195	-1.64915877E+06	3.196
160	-628.1345624	-1.64914943E+06	12.535
150	-628.1287427	-1.64913415E+06	27.814
140	-628.1208440	-1.64911341E+06	48.552
130	-628.1111600	-1.64908799E+06	73.977
120	-628.1000591	-1.64905884E+06	103.122
110	-628.0880720	-1.64902737E+06	134.594
100	-628.0758683	-1.64899533E+06	166.634
90	-628.0759449	-1.64899553E+06	166.433
80	-628.0759512	-1.64899555E+06	166.417
70	-628.0845004	-1.64901799E+06	143.971
60	-628.0931892	-1.64904081E+06	121.159
50	-628.1006057	-1.64906028E+06	101.687
40	-628.1064495	-1.64907562E+06	86.344
30	-628.1105906	-1.64908649E+06	75.472
20	-628.1130112	-1.64909285E+06	69.117
10	-628.1137625	-1.64909482E+06	67.144
0	-628.1129304	-1.64909264E+06	69.329

33. Potential Energy Curve of AAB at B3LYP/6-31G(d,p) level of theory/basis in benzene; CN=NC dihedral angle *vs.* Energy. Relative energy is respect to the *trans* isomer(CN=NC is 180^0)

CN=NC Dihedral angle /deg	Energy /HF	Energy /kJmol^{-1}	Relative energy /kJ
180	-628.146629	-1.64918111E+06	0.000
170	-628.145491	-1.64917812E+06	2.988
160	-628.142022	-1.64916901E+06	12.095
150	-628.136381	-1.64915421E+06	26.905
140	-628.128621	-1.64913383E+06	47.281
130	-628.119167	-1.64910901E+06	72.100
120	-628.108380	-1.64908069E+06	100.423
110	-628.096776	-1.64905022E+06	130.888
100	-628.084069	-1.64901686E+06	164.249
90	-628.084082	-1.64901689E+06	164.217
80	-628.084094	-1.64901693E+06	164.184
70	-628.093754	-1.64904229E+06	138.822
60	-628.102300	-1.64906473E+06	116.385
50	-628.109604	-1.64908390E+06	97.209
40	-628.115392	-1.64909910E+06	82.011
30	-628.119426	-1.64910969E+06	71.421
20	-628.121826	-1.64911599E+06	65.119
10	-628.122510	-1.64911779E+06	63.323
0	-628.121721	-1.64911572E+06	65.395

34. Potential Energy Curve of AAB at B3LYP/6-31G(d,p) level of theory/basis in DMSO; CN=NC dihedral angle *vs.* Energy. Relative energy is respect to the *trans* isomer(CN=NC is 180^0)

CN=NC Dihedral angle /deg	Energy /HF	Energy /kJmol^{-1}	Relative energy /kJ
179.99	-628.157968	-1.64921088E+06	0.000
170	-628.156856	-1.64920796E+06	2.919
160	-628.153625	-1.64919948E+06	11.401
150	-628.148166	-1.64918515E+06	25.734
140	-628.140772	-1.64916573E+06	45.149
130	-628.131727	-1.64914198E+06	68.896
120	-628.121488	-1.64911510E+06	95.777
110	-628.110907	-1.64908732E+06	123.556
100	-628.100456	-1.64905988E+06	150.996
90	-628.100406	-1.64905975E+06	151.127
80	-628.100276	-1.64905941E+06	151.468
70	-628.108203	-1.64908022E+06	130.656
60	-628.116198	-1.64910121E+06	109.666
50	-628.123293	-1.64911984E+06	91.038
40	-628.128902	-1.64913457E+06	76.313
30	-628.132718	-1.64914459E+06	66.293
20	-628.135047	-1.64915070E+06	60.178
10	-628.135583	-1.64915211E+06	58.770
0	-628.134777	-1.64914999E+06	60.887

35. Potential Energy Curve of AAB at B3LYP/6-31G(d,p) level of theory/basis in gas phase; CN=NC dihedral angle *vs.* Energy (α-CN=N equals 115.5^0 and N β-N=NC equals 116.3^0). Relative energy is respect to the *trans* isomer(CN=NC is 180^0)

CN=NC Dihedral angle /deg	Energy /HF	Energy /kJmol^{-1}	Relative energy /kJ
180	-628.127326	-1.64913043E+06	0.000
170	-628.126429	-1.64912807E+06	2.357
160	-628.123558	-1.64912054E+06	9.894
150	-628.118803	-1.64910805E+06	22.379
140	-628.112193	-1.64909070E+06	39.733
130	-628.103929	-1.64906900E+06	61.429
120	-628.094279	-1.64904367E+06	86.765
110	-628.083635	-1.64901572E+06	114.710
100	-628.072463	-1.64898639E+06	144.043
90	-628.061336	-1.64895718E+06	173.256
80	-628.069284	-1.64897804E+06	152.390
70	-628.078850	-1.64900316E+06	127.273
60	-628.087290	-1.64902532E+06	105.114
50	-628.094107	-1.64904322E+06	87.216
40	-628.099075	-1.64905626E+06	74.173
30	-628.102201	-1.64906447E+06	65.966
20	-628.103675	-1.64906833E+06	62.097
10	-628.103801	-1.64906867E+06	61.765
0	-628.102882	-1.64906625E+06	64.180

36. Potential Energy Curve of MY at B3LYP/6-31G(d,p) level of theory/basis; CN=NC dihedral angle *vs.* Energy. Relative energy is respect to the *trans* isomer(CN=NC is 180^0)

CN=NC Dihedral angle /deg	Energy /HF	Energy /kJmol^{-1}	Relative energy /kJ
180	-706.54279160	-1.85501E+06	0.000
170	-706.54165780	-1.85501E+06	2.977
160	-706.53819690	-1.85500E+06	12.063
150	-706.53253310	-1.85498E+06	26.933
140	-706.52488960	-1.85496E+06	47.001
130	-706.51551390	-1.85494E+06	71.617
120	-706.50478370	-1.85491E+06	99.789
110	-706.49317910	-1.85488E+06	130.256
100	-706.48344450	-1.85485E+06	155.814
90	-706.48344400	-1.85485E+06	155.815
80	-706.48344380	-1.85485E+06	155.816
70	-706.48344410	-1.85485E+06	155.815
60	-706.49718070	-1.85489E+06	119.750
50	-706.50413490	-1.85491E+06	101.492
40	-706.50958810	-1.85492E+06	87.175
30	-706.51339290	-1.85493E+06	77.185
20	-706.51554120	-1.85494E+06	71.545
10	-706.51610900	-1.85494E+06	70.054
0	-706.51523840	-1.85494E+06	72.340

37. Potential Energy Curve of MMY at B3LYP/6-31G(d,p) level of theory/basis; CN=NC dihedral angle *vs.* Energy. Relative energy is respect to the *trans* isomer(CN=NC is 180^0)

CN=NC Dihedral angle /deg	Energy /HF	Energy /kJmol^{-1}	Relative energy /kJ
180	-746.0748608	-1.95880E+06	0.000
170	-746.0738157	-1.95880E+06	2.744
160	-746.0705553	-1.95879E+06	11.304
150	-746.0651746	-1.95877E+06	25.431
140	-746.0577996	-1.95875E+06	44.794
130	-746.0486641	-1.95873E+06	68.779
120	-746.0381808	-1.95870E+06	96.302
110	-746.0268743	-1.95867E+06	125.987
100	-746.0152545	-1.95864E+06	156.495
90	-746.0120495	-1.95863E+06	164.909
80	-746.0137535	-1.95864E+06	160.436
70	-746.0227129	-1.95866E+06	136.913
60	-746.0309803	-1.95868E+06	115.207
50	-746.0380494	-1.95870E+06	96.647
40	-746.0436082	-1.95872E+06	82.053
30	-746.0474981	-1.95873E+06	71.840
20	-746.0496827	-1.95873E+06	66.104
10	-746.0465175	-1.95872E+06	74.414
0	-746.0491150	-1.95873E+06	67.595

38. Potential Energy Curve of NAB at B3LYP/6-31G(d,p) level of theory/basis; CN=NC dihedral angle *vs.* Energy. Relative energy is respect to the *trans* isomer(CN=NC is 180^0)

CN=NC Dihedral angle /deg	Energy /HF	Energy /kJmol^{-1}	Relative energy /kJ
180	-777.2769475	-2.040719E+06	0.000
170	-777.2757825	-2.040715E+06	3.059
160	-777.2723220	-2.040706E+06	12.144
150	-777.2665745	-2.040691E+06	27.234
140	-777.2587845	-2.040671E+06	47.686
130	-777.2492746	-2.040646E+06	72.654
120	-777.2384458	-2.040617E+06	101.085
110	-777.2226394	-2.040576E+06	142.584
100	-777.2226512	-2.040576E+06	142.553
90	-777.2226455	-2.040576E+06	142.568
80	-777.2226499	-2.040576E+06	142.557
70	-777.2247728	-2.040582E+06	136.983
60	-777.2329630	-2.040603E+06	115.480
50	-777.2401489	-2.040622E+06	96.614
40	-777.2459036	-2.040637E+06	81.505
30	-777.2500373	-2.040648E+06	70.652
20	-777.2524942	-2.040654E+06	64.202
10	-777.2500107	-2.040648E+06	70.722
0	-777.2524331	-2.040654E+06	64.362

39. Potential Energy Curve of DO3 at B3LYP/6-31G(d,p) level of theory/basis; CN=NC dihedral angle *vs.* Energy. Relative energy is respect to the *trans* isomer (CN=NC is 180^0)

CN=NC Dihedral angle /deg	Energy /HF	Energy /kJmol^{-1}	Relative energy /kJ
180	-832.6404400	-2.186074E+06	0.000
170	-832.6393306	-2.186071E+06	2.913
160	-832.6359979	-2.186029E+06	45.132
150	-832.6305615	-2.186005E+06	68.409
140	-832.6232499	-2.185979E+06	94.324
130	-832.6143842	-2.185935E+06	139.024
120	-832.6045136	-2.185935E+06	139.038
110	-832.5874878	-2.185935E+06	139.045
100	-832.5874828	-2.185935E+06	139.049
90	-832.5874799	-2.185945E+06	129.078
80	-832.5874783	-2.185963E+06	110.961
70	-832.5912763	-2.185979E+06	94.649
60	-832.5981767	-2.185992E+06	81.527
50	-832.6043896	-2.186002E+06	72.185
40	-832.6093878	-2.185992E+06	81.527
30	-832.6129460	-2.186002E+06	72.185
20	-832.6149783	-2.186007E+06	66.849
10	-832.6155000	-2.186008E+06	65.479
0	-832.6146624	-2.186006E+06	67.678

40. Potential Energy Curve of DO3 at B3LYP/6-31G(d,p) level of theory/basis in gas phase; CN=NC dihedral angle *vs*. Energy (α-CN=N equals 127.0^0 and N β-N=NC equals 126.0^0). Relative energy is respect to the *trans* isomer(CN=NC is 180^0)

CN=NC Dihedral angle /deg	Energy /HF	Energy /kJmol^{-1}	Relative energy /kJ
180	-832.6258893	-2.186036E+06	0.000
170	-832.6255156	-2.186035E+06	0.981
160	-832.6234883	-2.186005E+06	30.766
150	-832.6196894	-2.185986E+06	49.150
140	-832.6141709	-2.185965E+06	70.445
130	-832.6071688	-2.185942E+06	93.445
120	-832.5990580	-2.185919E+06	116.361
110	-832.5902974	-2.185905E+06	130.146
100	-832.5815694	-2.185923E+06	112.382
90	-832.5763186	-2.185943E+06	92.746
80	-832.5830848	-2.185962E+06	73.983
70	-832.5905639	-2.185978E+06	57.528
60	-832.5977102	-2.185991E+06	44.306
50	-832.6039779	-2.186001E+06	34.815
40	-832.6090138	-2.185991E+06	44.306
30	-832.6126290	-2.186001E+06	34.815
20	-832.6147367	-2.186006E+06	29.281
10	-832.6153478	-2.186008E+06	27.676
0	-832.6146145	-2.186006E+06	29.602

41. Potential Energy Curve of DR1 at B3LYP/6-31G(d,p) level of theory/basis; CN=NC dihedral angle *vs*. Energy. Relative energy is respect to the *trans* isomer (CN=NC is 180^0)

CN=NC Dihedral angle /deg	Energy /HF	Energy /kJmol^{-1}	Relative energy /kJ
180	-1065.09582260	-2.79638E+06	0.000
170	-1065.09470820	-2.79638E+06	2.926
160	-1065.09138600	-2.79637E+06	11.648
150	-1065.08596700	-2.79635E+06	25.876
140	-1065.07870780	-2.79633E+06	44.934
130	-1065.07309570	-2.79632E+06	59.669
120	-1065.06336410	-2.79629E+06	85.219
110	-1065.05332520	-2.79627E+06	111.576
100	-1065.04599160	-2.79625E+06	130.830
90	-1065.04599032	-2.79625E+06	130.833
80	-1065.04598966	-2.79625E+06	130.835
70	-1065.04598931	-2.79625E+06	130.836
60	-1065.04598930	-2.79625E+06	130.836
50	-1065.06323340	-2.79629E+06	85.562
40	-1065.07145200	-2.79631E+06	63.984
30	-1065.07336800	-2.79632E+06	58.954
20	-1065.07380750	-2.79632E+06	57.800
10	-1065.07292640	-2.79632E+06	60.113
0	-1065.09582260	-2.79638E+06	0.000

α-Inversion Pathway

42. Potential Energy Curve of AB at B3LYP/6-31G(d,p) level of theory/basis; α-CN=N angle *vs.* Energy. Relative energy is respect to the *trans* isomer

α-CN=N angle /deg	Energy /HF	Energy /kJmol^{-1}	Relative energy /kJ
100.00	-572.762848	-1.503773E+06	35.589
110.00	-572.776403	-1.503808E+06	0.000
120.00	-572.776335	-1.503808E+06	0.178
130.00	-572.766628	-1.503782E+06	25.665
140.00	-572.751143	-1.503742E+06	66.319
150.00	-572.733299	-1.503695E+06	113.169
160.00	-572.723652	-1.503670E+06	138.497
170.00	-572.715909	-1.503649E+06	158.825
179.99	-572.713448	-1.503643E+06	165.288
190.00	-572.716417	-1.503651E+06	157.493
200.00	-572.723874	-1.503670E+06	137.914
210.00	-572.733871	-1.503696E+06	111.668
220.00	-572.744393	-1.503724E+06	84.042
230.00	-572.752207	-1.503745E+06	63.526
240.00	-572.752949	-1.503747E+06	61.579
250.00	-572.743780	-1.503723E+06	85.651
260.00	-572.723161	-1.503668E+06	139.786

43. Potential Energy Curve of AAB at B3LYP/6-31G(d,p) level of theory/basis; α-CN=N angle *vs.* Energy. Relative energy is respect to the *trans* isomer

α-CN=N angle /deg	Energy /HF	Energy /kJmol^{-1}	Relative energy /kJ
100.00	-628.1240775	-1.649122E+06	37.777
110.00	-628.1372416	-1.649156E+06	3.215
115.50	-628.1384661	-1.649160E+06	0.000
120.00	-628.1369025	-1.649156E+06	4.105
130.00	-628.1270402	-1.649130E+06	29.998
140.00	-628.1113267	-1.649088E+06	71.254
150.00	-628.0975409	-1.649052E+06	107.448
160.00	-628.0858825	-1.649022E+06	138.057
170.00	-628.0783944	-1.649002E+06	157.717
179.99	-628.0759350	-1.648996E+06	164.174
190.00	-628.0788684	-1.649003E+06	156.472
200.00	-628.0862516	-1.649023E+06	137.088
210.00	-628.0960569	-1.649048E+06	111.344
220.00	-628.1056979	-1.649074E+06	86.032
230.00	-628.1126317	-1.649092E+06	67.828
234.60	-628.1139032	-1.649095E+06	64.489
240.00	-628.1130614	-1.649093E+06	66.699
250.00	-628.1036504	-1.649068E+06	91.408
260.00	-628.0818704	-1.649011E+06	148.590

44. Potential Energy Curve of AAB at B3LYP/6-31G level of theory/basis; α-CN=N angle *vs.* Energy. Relative energy is respect to the *trans* isomer

α-CN=N angle /deg	Energy /HF	Energy /kJmol^{-1}	Relative energy /kJ
110.0	-627.95233058	-1.648671E+06	4.803
115.5	-627.95416007	-1.648676E+06	0.000
121.0	-627.95256240	-1.648672E+06	4.195
126.5	-627.94820123	-1.648660E+06	15.645
132.0	-627.94169597	-1.648643E+06	32.724
137.5	-627.93365088	-1.648622E+06	53.846
143.0	-627.92468287	-1.648598E+06	77.392
148.5	-627.91539736	-1.648574E+06	101.770
154.0	-627.91053029	-1.648561E+06	114.549
159.5	-627.90476432	-1.648546E+06	129.687
165.0	-627.90021225	-1.648534E+06	141.638
170.5	-627.89693042	-1.648526E+06	150.255
176.0	-627.89505507	-1.648521E+06	155.178
181.5	-627.89523832	-1.648521E+06	154.697
187.0	-627.89725218	-1.648526E+06	149.410
192.5	-627.90050242	-1.648535E+06	140.877
198.0	-627.90470774	-1.648546E+06	129.836
203.5	-627.90951069	-1.648559E+06	117.226
209.0	-627.91449945	-1.648572E+06	104.128
214.5	-627.91924651	-1.648584E+06	91.665
220.0	-627.92336357	-1.648595E+06	80.855
225.5	-627.92629190	-1.648603E+06	73.167
231.0	-627.92740717	-1.648606E+06	70.239
236.5	-627.92615156	-1.648602E+06	73.536

45. Potential Energy Curve of protonated AAB at B3LYP/6-31G level of theory/basis; α-CN=N angle *vs.* Energy. Relative energy is respect to the *trans* isomer

α-CN=N angle /deg	Energy /HF	Energy /kJmol^{-1}	Relative energy /kJ
115	-628.3451322	-1.649702E+06	4.042
120	-628.3466716	-1.649706E+06	0.000
125	-628.3459770	-1.649704E+06	1.824
130	-628.3433120	-1.649697E+06	8.821
135	-628.3391642	-1.649687E+06	19.710
140	-628.3339962	-1.649673E+06	33.279
145	-628.3282296	-1.649658E+06	48.419
150	-628.3222535	-1.649642E+06	64.109
155	-628.3164326	-1.649627E+06	79.392
160	-628.3111012	-1.649613E+06	93.389
165	-628.3065550	-1.649601E+06	105.325
170	-628.3030288	-1.649592E+06	114.583
175	-628.3006873	-1.649586E+06	120.730
185	-628.2997568	-1.649583E+06	123.173
190	-628.3011522	-1.649587E+06	119.510
195	-628.3037048	-1.649594E+06	112.808
200	-628.3072112	-1.649603E+06	103.602
205	-628.3114021	-1.649614E+06	92.599

210	-628.3159410	-1.649626E+06	80.682
215	-628.3204414	-1.649637E+06	68.867
220	-628.3244781	-1.649648E+06	58.268
225	-628.3276007	-1.649656E+06	50.070
230	-628.3293941	-1.649661E+06	45.362
235	-628.3295116	-1.649661E+06	45.053
240	-628.3276905	-1.649656E+06	49.834

46. Potential Energy Curve of protonated AAB at B3LYP/6-31G level of theory/basis in gas phase; α-CN=N+H angle *vs.* Energy. Relative energy is respect to the *trans* isomer

α-CN=N^+H angle /deg	Energy /HF	Energy /kJmol^{-1}	Relative energy /kJ
115	-628.345132	-1.649702E+06	4.042
120	-628.346672	-1.649706E+06	0.000
125	-628.345977	-1.649704E+06	1.824
130	-628.343312	-1.649697E+06	8.821
135	-628.339164	-1.649687E+06	19.710
140	-628.333996	-1.649673E+06	33.279
145	-628.328230	-1.649658E+06	48.419
150	-628.322254	-1.649642E+06	64.109
155	-628.316433	-1.649627E+06	79.392
160	-628.311101	-1.649613E+06	93.389
165	-628.306555	-1.649601E+06	105.325
170	-628.303029	-1.649592E+06	114.583
175	-628.300687	-1.649586E+06	120.730
185	-628.299757	-1.649583E+06	123.173
190	-628.301152	-1.649587E+06	119.510
195	-628.303705	-1.649594E+06	112.808
200	-628.307211	-1.649603E+06	103.602
205	-628.311402	-1.649614E+06	92.599
210	-628.315941	-1.649626E+06	80.682
215	-628.320441	-1.649637E+06	68.867
220	-628.324478	-1.649648E+06	58.268
225	-628.327601	-1.649656E+06	50.070
230	-628.329394	-1.649661E+06	45.362
235	-628.329512	-1.649661E+06	45.053
240	-628.327691	-1.649656E+06	49.834

47. Potential Energy Curve of MY at B3LYP/6-31G(d,p) level of theory/basis; α-CN=N angle *vs.* Energy. Relative energy is respect to the *trans* isomer

α-CN=N angle /deg	Energy /HF	Energy /kJmol^{-1}	Relative energy /kJ
100.00	-706.7403388	-1.855527E+06	34.421
110.00	-706.7534492	-1.855561E+06	0.000
120.00	-706.7531198	-1.855560E+06	0.865
130.00	-706.7432037	-1.855534E+06	26.899
140.00	-706.7278292	-1.855494E+06	67.265
150.00	-706.7130900	-1.855455E+06	105.962
160.00	-706.7015754	-1.855425E+06	136.193
170.00	-706.6941616	-1.855405E+06	155.658
179.99	-706.6917359	-1.855399E+06	162.027
190.00	-706.6946381	-1.855407E+06	154.407
200.00	-706.7019518	-1.855426E+06	135.205
210.00	-706.7117096	-1.855451E+06	109.586
220.00	-706.7212517	-1.855477E+06	84.534
230.00	-706.7281107	-1.855495E+06	66.526
240.00	-706.7285210	-1.855496E+06	65.448

48. Potential Energy Curve of MMY at B3LYP/6-31G(d,p) level of theory/basis; α-CN=N angle *vs.* Energy. Relative energy is respect to the *trans* isomer

α-CN=N angle /deg	Energy /HF	Energy /kJmol^{-1}	Relative energy /kJ
100.00	-746.0610501	-1.958762E+06	32.731
110.00	-746.0735167	-1.958795E+06	0.000
120.00	-746.0732913	-1.958794E+06	0.592
130.00	-746.0634273	-1.958768E+06	26.489
140.00	-746.0480852	-1.958728E+06	66.770
150.00	-746.0333683	-1.958689E+06	105.408
160.00	-746.0219284	-1.958659E+06	135.444
170.00	-746.0145121	-1.958640E+06	154.915
179.99	-746.0120954	-1.958634E+06	161.260
190.00	-746.0149074	-1.958641E+06	153.877
200.00	-746.0221675	-1.958660E+06	134.816
210.00	-746.0318196	-1.958685E+06	109.475
220.00	-746.0415913	-1.958711E+06	83.819
230.00	-746.0488456	-1.958730E+06	64.773
240.00	-746.0494100	-1.958732E+06	63.291

49. Potential Energy Curve of NAB at B3LYP/6-31G(d,p) level of theory/basis; α-CN=N angle *vs.* Energy. Relative energy is respect to the *trans* isomer

α-CN=N angle /deg	Energy /HF	Energy /kJmol^{-1}	Relative energy /kJ
110.00	-777.2757972	-2.040715E+06	0.000
120.00	-777.2751471	-2.040714E+06	1.707
130.00	-777.2649834	-2.040687E+06	28.391
140.00	-777.2520031	-2.040653E+06	62.471
150.00	-777.2406717	-2.040623E+06	92.221
160.00	-777.2312999	-2.040599E+06	116.826
170.00	-777.2249165	-2.040582E+06	133.586
179.99	-777.2226544	-2.040576E+06	139.525
190.00	-777.2247600	-2.040582E+06	133.997
200.00	-777.2305556	-2.040597E+06	118.781
210.00	-777.2383834	-2.040617E+06	98.229
220.00	-777.2461001	-2.040638E+06	77.969
230.00	-777.2521760	-2.040653E+06	62.017
240.00	-777.2523616	-2.040654E+06	61.530

50. Potential Energy Curve of DO3 at B3LYP/6-31G(d,p) level of theory/basis; α-CN=N angle *vs.* Energy. Relative energy is respect to the *trans* isomer

α-CN=N angle /deg	Energy /HF	Energy /kJmol^{-1}	Relative energy /kJ
110.00	-832.6393877	-2.186071E+06	0.000
120.00	-832.6385236	-2.186069E+06	2.269
130.00	-832.6282377	-2.186042E+06	29.274
140.00	-832.6155972	-2.186009E+06	62.461
150.00	-832.6047970	-2.185980E+06	90.817
160.00	-832.5958136	-2.185957E+06	114.403
170.00	-832.5896879	-2.185941E+06	130.485
179.99	-832.5874709	-2.185935E+06	136.306
190.00	-832.5894548	-2.185940E+06	131.097
200.00	-832.5950202	-2.185955E+06	116.486
210.00	-832.6026321	-2.185975E+06	96.501
220.00	-832.6098994	-2.185994E+06	77.421
230.00	-832.6148171	-2.186007E+06	64.509
240.00	-832.6143007	-2.186005E+06	65.865

β-Inversion Pathway

51. Potential Energy Curve of AAB at B3LYP/6-31G(d,p) level of theory/basis; β-CN=N angle *vs.* Energy. Relative energy is respect to the *trans* isomer

β-CN=N angle /deg	Energy /HF	Energy /kJmol^{-1}	Relative energy /kJ
100.00	-628.122465	-1.649118E+06	42.009
110.00	-628.136767	-1.649155E+06	4.461
115.50	-628.138466	-1.649160E+06	0.000
120.00	-628.137338	-1.649157E+06	2.962
130.00	-628.128241	-1.649133E+06	26.846
140.00	-628.113789	-1.649095E+06	64.790
150.00	-628.096466	-1.649049E+06	110.270
160.00	-628.081404	-1.649010E+06	149.814
170.00	-628.071704	-1.648984E+06	175.281
179.99	-628.068605	-1.648976E+06	183.420
190.00	-628.072089	-1.648985E+06	174.272
200.00	-628.080881	-1.649008E+06	151.188
210.00	-628.092952	-1.649040E+06	119.495
220.00	-628.104983	-1.649072E+06	87.909
230.00	-628.112807	-1.649092E+06	67.367
234.60	-628.113903	-1.649095E+06	64.489
240.00	-628.112771	-1.649092E+06	67.462

52. Potential Energy Curve of MY at B3LYP/6-31G(d,p) level of theory/basis; β-CN=N angle *vs.* Energy. Relative energy is respect to the *trans* isomer

β-CN=N angle /deg	Energy /HF	Energy /kJmol^{-1}	Relative energy /kJ
110.00	-706.7530173	-1.855560E+06	1.446
120.00	-706.7535679	-1.855561E+06	0.000
130.00	-706.7444503	-1.855537E+06	23.938
140.00	-706.7294661	-1.855498E+06	63.279
150.00	-706.7121655	-1.855453E+06	108.701
160.00	-706.6969550	-1.855413E+06	148.636
170.00	-706.6871462	-1.855387E+06	174.388
179.99	-706.6840241	-1.855379E+06	182.585
190.00	-706.6874831	-1.855388E+06	173.504
200.00	-706.6963655	-1.855411E+06	150.183
210.00	-706.7085209	-1.855443E+06	118.270
220.00	-706.7205401	-1.855475E+06	86.714
230.00	-706.7283207	-1.855495E+06	66.286
240.00	-706.7281667	-1.855495E+06	66.690

53. Potential Energy Curve of MMY at B3LYP/6-31G(d,p) level of theory/basis; β-CN=N angle *vs.* Energy. Relative energy is respect to the *trans* isomer

β-CN=N angle /deg	Energy /HF	Energy /kJmol^{-1}	Relative energy /kJ
110.00	-746.0728842	-1.958793E+06	2.404
120.00	-746.0737997	-1.958796E+06	0.000
130.00	-746.0647111	-1.958772E+06	23.862
140.00	-746.0494126	-1.958732E+06	64.028
150.00	-746.0327796	-1.958688E+06	107.697
160.00	-746.0185173	-1.958650E+06	145.142
170.00	-746.0087457	-1.958625E+06	170.797
179.99	-746.0064499	-1.958619E+06	176.825
190.00	-746.0100440	-1.958628E+06	167.389
200.00	-746.0188386	-1.958651E+06	144.299
210.00	-746.0304848	-1.958682E+06	113.722
220.00	-746.0418612	-1.958712E+06	83.854
230.00	-746.0492247	-1.958731E+06	64.521
240.00	-746.0489608	-1.958730E+06	65.214

54. Potential Energy Curve of NAB at B3LYP/6-31G(d,p) level of theory/basis; β-CN=N angle *vs.* Energy. Relative energy is respect to the *trans* isomer

β-CN=N angle /deg	Energy /HF	Energy /kJmol^{-1}	Relative energy /kJ
100.00	-777.2620167	-2.040679E+06	35.683
110.00	-777.2753624	-2.040714E+06	0.644
120.00	-777.2756078	-2.040715E+06	0.000
130.00	-777.2661812	-2.040690E+06	24.749
140.00	-777.2508913	-2.040650E+06	64.892
150.00	-777.2345273	-2.040607E+06	107.856
160.00	-777.2213192	-2.040572E+06	142.533
170.00	-777.2128129	-2.040550E+06	164.866
179.99	-777.2100668	-2.040543E+06	172.076
190.00	-777.2131428	-2.040551E+06	164.000
200.00	-777.2209084	-2.040571E+06	143.612
210.00	-777.2316837	-2.040600E+06	115.321
220.00	-777.2432868	-2.040630E+06	84.858
230.00	-777.2516402	-2.040652E+06	62.926
240.00	-777.2526133	-2.040655E+06	60.371

55. Potential Energy Curve of DO3 at B3LYP/6-31G(d,p) level of theory/basis; β-CN=N angle *vs.* Energy. Relative energy is respect to the *trans* isomer

β-CN=N angle /deg	Energy /HF	Energy /kJmol^{-1}	Relative energy /kJ
100.00	-832.6239558	-2.186031E+06	40.414
110.00	-832.6385453	-2.186069E+06	2.110
120.00	-832.6393488	-2.186071E+06	0.000
130.00	-832.6304232	-2.186047E+06	23.434
140.00	-832.6156174	-2.186009E+06	62.306
150.00	-832.5984150	-2.185963E+06	107.471
160.00	-832.5828110	-2.185922E+06	148.438
170.00	-832.5724840	-2.185895E+06	175.552
179.99	-832.5690621	-2.185886E+06	184.536
190.00	-832.5725061	-2.185895E+06	175.494
200.00	-832.5816524	-2.185919E+06	151.480
210.00	-832.5941882	-2.185952E+06	118.568
220.00	-832.6064867	-2.185985E+06	86.279
230.00	-832.6144143	-2.186005E+06	63.355
240.00	-832.6143599	-2.186005E+06	65.608

Courses and Conferences

Postgraduate Courses and Lectures

- Introduction to Unix
- Introduction to Excel
- Effective Writing
- Academic Paper Writing
- Thesis Writing Workshop
- Bibliography with Endnote
- Nuclear Magnetic Resonance
- Computational Chemistry
- Quantum Mechanics
- Chemical Kinetics
- Postgraduate NMR Workshop
- Departmental Colloquium

Conferences and Meetings

- Attendance of EaStCHEM 2007 Computational Chemistry Symposium 1, The University of St. Andrews.
- Oral presentation at the Royal Society of Chemistry Photochemistry Group 2007, Loughborough University.
- Poster presentation at the EaStCHEM 2008 Computational Chemistry Symposium 2, The University of Glasgow.
- Poster presentation at the EDIKT 2008 Using Computing in your Research, The University of Edinburgh.
- Poster presentation at the Computational Molecular Science CMS 2008, The Royal Agricultural College, Cirencester.
- Annual oral presentation to the Materials and Physical Chemistry Section 2007 and 2008; School of Chemistry, The University of Edinburgh.
- Attendance of 42nd IUPAC Congress 2009 Chemistry Solutions, The University of Glasgow.